UNIVERSITY OF POTSDAM
Faculty of Sciences

UNIVERSITY OF BUENOS AIRES
Faculty of Exact and Natural Sciences

The role of the upper plate in the Andean tectonic evolution (33-36°S): insights from structural geology and numerical modeling

Thesis presented to opt for the degree of Doctor de la Universidad de Buenos Aires, Geosciences and Dr. rer. nat. from the University of Potsdam

Matías Barrionuevo

Supervisor UBA: Dr Daniel Yagupsky
Supervisor UP**:** Dr Stephan Sobolev

Workplace: Instituto de Nivología, Glaciología y Ciencias Ambientales. IANIGLA, CCT – Mendoza, CONICET

Buenos Aires, 17th March, 2020

UNIVERSIDAD DE BUENOS AIRES
Facultad de Ciencias Exactas y Naturales
Departamento de Ciencias Geológicas

El rol de la placa superior en la evolución tectónica andina (33-36°S): aportes desde la geología estructural y el modelado numérico

Tesis presentada para optar por el título de Doctor de la Universidad de Buenos Aires en el área Ciencias Geológicas

Matías Barrionuevo

Director: Dr. Daniel Yagupsky
Co-director: Dr. José Mescua
Consejero de Estudios: Dr. Ernesto Cristallini

Lugar de trabajo: Instituto de Nivología, Glaciología y Ciencias Ambientales. IANIGLA, CCT – Mendoza, CONICET
Lugar y fecha de defensa: Buenos Aires, 17/03/2020

The role of the upper plate in the Andean tectonic evolution (33-36°S): insights from structural geology and numerical modeling

Matías Barrionuevo

Univ.-Diss.

zur Erlangung des akademischen Grades
"doctor rerum naturalium"
(Dr. rer. nat.)
in der Wissenschaftsdisziplin "Geologie"

eingereicht an der
Mathematisch-Naturwissenschaftlichen Fakultät
Institut für Geowissenschaften
der Universität Potsdam
und
der Universität Buenos Aires

Ort und Tag der Disputation: Buenos Aires, Argentinien, 17. Marz 2020

Hauptbetreuer: Prof. Dr. Stephan V. Sobolev
Betreuer: Prof. Dr. Manfred Strecker
Mentor: Dr. Javier Quinteros
Gutachter: Prof. Dr. Bodo Bookhagen
Dr. Facundo Fuentes
Dr. Juan Franzese

Published online on the
Publication Server of the University of Potsdam:
https://doi.org/10.25932/publishup-51590
https://nbn-resolving.org/urn:nbn:de:kobv:517-opus4-515909

Table of contents

El rol de la placa superior en la evolución tectónica andina (33-36°S): aportes desde la geología estructural y el modelado numérico

Resumen

Los Andes Centrales del Sur (33-36°S) son un gran laboratorio para el estudio de los procesos de deformación orogénica, donde las condiciones de borde, como la geometría de la placa subductada, imponen un importante control sobre la deformación andina. Por otro lado, la Placa Sudamericana presenta una serie de heterogeneidades que también imparten un control sobre el modo de deformación. El objetivo de esta tesis es probar el control de este último factor sobre la construcción del sistema orogénico andino.

A partir de la integración de la información superficial y de subsuelo en el área sur (34°-36°S), se estudió la evolución de la deformación andina sobre el segmento de subducción normal. Se desarrolló un modelo estructural que evalúa el estado de esfuerzos desde el Mioceno hasta la actualidad, el rol de estructuras previas y su influencia en la migración de fluidos. Con estos datos y publicaciones previas de la zona norte del área de estudio (33°-34ºS), se realizó un modelado numérico geodinámico para probar la hipótesis del papel de las heterogeneidades de la placa superior en la evolución andina. Se utilizaron dos códigos (LAPEX-2D y ASPECT) basados en elementos finitos/diferencias finitas, que simulan el comportamiento de materiales con reologías elastoviscoplásticas bajo deformación. Los resultados del modelado sugieren que la deformación contraccional de la placa superior está significativamente controlada por la resistencia de la litósfera, que está definida por la composición de la corteza superior e inferior y por la proporción del manto litosférico, que a su vez está definida por eventos tectónicos previos. Estos eventos previos también definieron la composición de la corteza y su geometría, que es otro factor que controla la localización de la deformación. Con una composición de corteza inferior más félsica, la deformación sigue un modo de cizalla pura mientras que las composiciones más máficas provocan un modo de deformación tipo cizalla simple. Por otro lado, observamos que el espesor inicial de la litósfera controla la localización de la deformación, donde zonas con litósfera más fina es propensa a concentrar la deformación. Un límite litósfera-astenósfera asimétrico, como resultado del flujo de la cuña mantélica tiende a generar despegues vergentes al E.

Palabras clave: geología estructural; tectónica, subducción; modelado geodinámico; Andes.

The role of the upper plate in the Andean tectonic evolution (33-36°S): insights from structural geology and numerical modeling

Abstract

The Southern Central Andes (33°-36°S) are an excellent natural laboratory to study orogenic deformation processes, where boundary conditions, such as the geometry of the subducted plate, impose an important control on the evolution of the orogen. On the other hand, the South American plate presents a series of heterogeneities that additionally impart control on the mode of deformation. This thesis aims to test the control of this last factor over the construction of the Cenozoic Andean orogenic system.

From the integration of surface and subsurface information in the southern area (34-36°S), the evolution of Andean deformation over the steeply dipping subduction segment was studied. A structural model was developed evaluating the stress state from the Miocene to the present-day and its influence in the migration of magmatic fluids and hydrocarbons. Based on these data, together with the data generated by other researchers in the northern zone of the study area (33-34°S), geodynamic numerical modeling was performed to test the hypothesis of the decisive role of upper-plate heterogeneities in the Andean evolution. Geodynamic codes (LAPEX-2D and ASPECT) which simulate the behavior of materials with elasto-visco-plastic rheologies under deformation, were used. The model results suggest that upper-plate contractional deformation is significantly controlled by the strength of the lithosphere, which is defined by the composition of the upper and lower crust, and by the proportion of lithospheric mantle, which in turn is determined by previous tectonic events. In addition, the previous regional tectono-magmatic events also defined the composition of the crust and its geometry, which is another factor that controls the localization of deformation. Accordingly, with more felsic lower crustal composition, the deformation follows a pure-shear mode, while more mafic compositions induce a simple-shear deformation mode. On the other hand, it was observed that initial lithospheric thickness may fundamentally control the location of deformation, with zones characterized by thin lithosphere are prone to concentrate it. Finally, it was found that an asymmetric lithosphere-astenosphere boundary resulting from corner flow in the mantle wedge of the eastward-directed subduction zone tends to generate east-vergent detachments.

Keywords: structural geology; tectonics, subduction; geodynamic modeling; Andes.

Die Rolle der oberen Platte in der tektonischen Entwicklung der Anden (33-36°S): Erkenntnisse aus der Strukturgeologie und der numerischen Modellierung

Zusammenfasung

Die südlichen Zentralanden (33°-36°S) sind eine ausgezeichnete, natürliche Forschungsumgebung zur Untersuchung gebirgsbildender Deformationsprozesse, in der Randbedingungen, wie die Geometrie der subduzierten Platte, einen starken Einfluss auf die Evolution des Gebirges besitzen. Anderseits sind die Deformationsmechanismen geprägt von der Heterogenität der Südamerikanischen Platte. In dieser Arbeit wird die Bedeutung dieses Mechanismus für die Herausbildung der Anden während des Känozoikums untersucht.

Im südlichen Teil (34-36°S), in dem die subduzierte Platte in einem steileren Winkel in den Erdmantel absinkt, wird die Entwicklung der Andendeformation mithilfe von oberflächlich aufgezeichneten und in tiefere Erdschichten reichenden Daten untersucht. Das darauf aufbauende Strukturmodell ermöglicht die Abschätzung der tektonischen Spannungen vom Miozän bis in die Neuzeit und den Einfluss der Bewegungen von magmatischen Fluiden, sowie Kohlenwasserstoffen. Auf Grundlage dieser Daten und solcher, die von Wissenschaftlern im nördlichen Bereich des Untersuchungsgebietes (33-34°S) erfasst wurden, wurde eine geodynamische, numerische Modellierung durchgeführt, um die Hypothese des Einflusses der Heterogenität der oberen Platten auf die Gebirgsbildung der Anden zu überprüfen. Die genutzte geodynamische Softwares (LAPEX-2D und ASPECT) simulieren das Verhalten von elasto-viskoplastischen Materialien, wenn diese unter Spannung stehen. Die Modellierungsergebnisse zeigen, dass die Kontraktionsprozesse hauptsächlich durch die Stärke der Lithosphäre beeinflusst werden. Diese Kenngröße wird aus der Zusammensetzung von Ober- und Unterkruste und dem Anteil des lithosphärischen Mantels, der durch vorhergehende tektonische Vorgänge überprägt ist, bestimmt. Diese räumlich begrenzten tektono-magmatischen Events definieren ebenfalls die Zusammensetzung und die Geometrie der Erdkruste, welche einen großen Einfluss auf das räumliche Auftreten von Deformationsprozessen hat. Eine eher felsische Unterkruste führt vorrangig zu pure-shear, während eine eher mafisch zusammengesetzte Unterkruste primär zu einem Deformationsmechanismus führt, der simple-shear genannt wird. Weiterhing wurde beobachtet, dass die Dicke der Lithosphäre vor der Deformation einen fundamentalen Einfluss auf die räumliche

Eingrenzung von Deformation hat, wobei Regionen mit einer dünnen Lithosphärenschicht verstärkt Deformation aufweisen. Eine asymmetrische Grenzschicht zwischen Lithosphäre und Asthenosphäre ist das Resultat von Fließprozessen im Erdmantel, im Keil zwischen der obenliegenden Platte und der sich ostwärts absinkenden Subduktionszone, und verstärkt die Herausbildung von nach Osten gerichteten Abscherungen in der Erdkruste.

Acknowledgements

To my parents, Linda and Carlos, and to my siblings, Rocío and Benja, who always supported me, with love, through these years. With them, I started enjoying the mountains and nature. To my goddaughter, Valentina and to Justina, whose laughs and love rejoice me. To Sole for letting me be part of her family.

To Laura and Jose, who guided me closely during my doctorate. Their generosity, humility and help were very important during this stage.

To Valeria who accompanied me much of the time of this project, who supported me when I was abroad and whose words and love really made me feel good.

To my friends in the institute, Sebis, Tuqui, Albertini, Marcos, Clari, Mari, Andre, Aldi, Valen, Juli, Manu, Javi, Fer, Diego, Rodri.

And among them, especially to Pili, who in the last months appeared as a great and lovely companion to walk through the last steps of the doctorate.

To my friends in the choir, with whom I shared these years of singing, and particularly to Natu, Tango, Flor, Tincho, Mati, Titi, Nati, Ceci, Nico, Eric. Especially to Lili for teaching me to enjoy group music.

To my friends in Córdoba, Chancha, Popi, Carlitos, Juan P, Mateo, Vere, Lu, Ine, Gordo Franco, Enano, Tata and especially to Fer who accompanies us from above and whose passion for geology and the Andes always inspired us. For so much “asados” and happy moments.

To Stephan, Andrey and Javier who introduced me into the subject of numerical models and taught me a lot. To Dani Yag and Manfred for their great help with the manuscript corrections and their support during the PhD project.

To the reviewers Dr. Facundo Fuentes, Dr. Juan Franzese and Dr. Bodo Bookhagen whose suggestions improved this manuscript.

To the StRATEGy project here in Argentina and in Germany that let me work in cooperation with many colleagues, and particularly with Sibiao Liu. To Veronica Acosta who assisted me to accomplish the binational doctorate. To Martin Zeckra and Sarah Zobel, who helped me with the translation to German and to Michaël Pons who helped me to submit the thesis in Germany.

To the Argentinean State, the public University of Córdoba and the University of Buenos Aires and to all those who contributed to my education. To CONICET that provided me with financial support through the doctoral grant and with the opportunity to stay and learn in Germany.

Chapter I

1. Introduction

1.1 Research hypothesis

The Andes are the type locality of a non-collisional subduction orogen, where the oceanic Nazca Plate is subducted underneath the South American continental plate (Oncken et al., 2006). While the Andean orogenic evolution appears to be largely controlled by the behaviour of the subduction system (Jarrard, 1986; Sobolev and Babeyko, 2005; Oncken et al., 2006; Ramos, 2010), the mountain belt comprises segments with variable structural characteristics and tectono-magmatic evolution (Gansser, 1973; Ramos, 1999; Tassara and Yáñez, 2003; McGroder et al., 2015). This segmentation is the result of the interplay between subduction dynamics and upper-plate characteristics (Gansser, 1973), and this includes crustal anisotropies inherited from past geological processes in deep time.

Therefore, inherited geological characteristics (structures, composition, lower and upper crustal thickness, among others) of the continental plate of the subduction system exert an important control on deformation processes during orogenesis. Mesozoic pre-Andean extensional events between 33° and 36°S modified the crustal architecture of the South American plate significantly and generated segments with different characteristics (e.g., Franzese and Spalletti, 2001, Mosquera and Ramos, 2006; Bechis et al., 2014) that later, during Cenozoic Andean compression, have responded differently and influenced deformation processes until the present day (e.g., Manceda and Figueroa, 1995; Cristallini and Ramos, 2000; Mescua et al., 2016). For example, north of 35°S, the strength of the lithosphere is inferred to be lower compared to the lithosphere south of 35°S (Giambiagi et al., 2012). This has been explained with differences in crustal extension during the Mesozoic, when the area south of 35°S experienced more crustal extension, resulting in a lower ratio of thickness between the crust and lithospheric mantle, thus rendering it more resistant to compressional deformation. Such a scenario would be susceptible to a decoupling of deformation between the upper and lower crust and thus be similar to the simple-shear model proposed for deformation processes in the intraorogenic Andean Plateau (Altiplano) between 19° and 23°S (Isacks, 1988; Allmendinger and Gubbels, 1996); there, upper-crustal deformation is located eastward with respect to the maximum thickness of the crustal root. This contrasts with a pure-shear model, where the deformation of the upper and lower crust is coupled, as has been proposed for the southern sector of the Andean Plateau in the Argentine Puna between 23° and 26°S (Isacks, 1988; Allmendinger and Gubbels, 1996). The fundamental difference in tectonic deformation characteristics of the Andean Plateau is linked with the presence of a thick sedimentary sequence underlying the Subandes foreland fold-and thrust belt in the foreland of the Bolivian Altiplano, where deformation is focused, due to lower strength as compared to the arc and orogen interior (Babeyko and Sobolev, 2005). In contrast, deformation in the regions east of the Puna Plateau is accommodated by temporally and spatially disparate reverse-fault bounded mountain ranges in the broken foreland of Northwest Argentina, which does not coincide with deep-seated sedimentary basins.

These examples illustrate that the characteristics of the continental crust play a pivotal role in determining deformational styles and that crustal anisotropies may be more important in the overall deformation characteristics compared to the geometry of subducting plates. In the area that is the focus of my study (33-36°S), sedimentary successions of the Neuquén Basin do not show major thickness variations. The study area is located south of the flat subduction segment that underlies Central Argentina. The principal research hypothesis that drives this work is that the pre-Andean tectono-magmatic history is a fundamental condition that controls crustal strength and thus the locus of Cenozoic Andean deformation.

1.2 Research questions

The main questions that guide this research are summarized below:

- How is deformation in the upper plate of the subduction system distributed and what controls this spatial distribution?
- How does the presence of a mafic vs. more felsic lower crust condition the mode of deformation?
- Does the crustal geometry of the upper plate (basins or thickened areas) influence how deformation is distributed?

In order to answer these questions, I compiled structural data across the study area focusing on transects at 33°30 and at 36°S in the steep subduction segment. This sector of the Andes is also important in that it is located south of the proposed transition between pure and simple-shear orogen development at 35°S (Giambiagi et al. 2012). In the transect at 36°S, I was confronted with a lack of detailed geological structural information and additional fieldwork was necessary to improve the knowledge of the tectonic evolution in this region.

1.3 Objectives

1.3.1 General objectives

In the context of the research questions outlined above the main goals of this research are: (i) to analyse the Cenozoic tectonic evolution of the Andean orogen in the southern-central sector of the orogen; (ii) to test conceptual geodynamic models (pure vs. simple shear) for the evolution of the Andes north and south of 35°S, using thermomechanical numerical models; and (iii) to compare the obtained results with the tectonic evolutionary models that have been inferred for these regions. Thermomechanical numerical modeling will help to validate these tectonic evolution models and advance our understanding of Andean mountain building.

1.3.2 Specific objectives

- Examine the role of pre-existing Mesozoic structures in Andean deformation in selected transects along the study area, i.e., the 33° and 36°S transect.
- Evaluate the evolution of the deformation structures and related tectonic stress field at the orogenic front (i.e., from Miocene to the present-day) and impacts on fluid migration.
- Verify if the conceptual models proposed by different authors for the evolution of the Southern Central Andes are consistent with numerical modeling results of the physical processes that have been driving mountain building, using different initial crustal configurations.
- Compare my own conclusions to those obtained for other latitudes by other researchers, exploring the idea of different stages in evolution throughout the Andes.

1.4 Structure of the thesis and preliminary considerations

This thesis is part of a cotutelle-de-these agreement between the University of Buenos Aires (Argentina) and the University of Potsdam (Germany) to obtain a doctoral degree between both universities. The dissertation is also part of the International Cooperation project StRATEGy (Surface processes, Tectonics and Georesources: The Andean foreland basin of Argentina) between CONICET of Argentina and DFG of Germany whose objective is to study the Andes from a multi-temporal (involving very different time scales), multi-disciplinary and multi-spatial (involving very different areas) point of view, considering climate-tectonic relationships, the influence of inherited crustal structures, basin modeling, resource generation, and geological hazards, among other topics.

The thesis is organized as a series of chapters that can be read in a relatively independent way since some are part of accepted publications and others pertain to manuscripts in preparation. Chapter I is an introduction to the research topic, including methodology and the geological framework of the area. Chapter II is based on a manuscript published in Tectonophysics (Barrionuevo et al., 2019) focussed on the evolution of the orogenic front in the Malargüe fold-and-thrust belt. Chapter III is based on a published paper in Tectonophysics (Mescua, Barrionuevo, et al., 2019) that investigates the current state of stress and its relation to active faults and seismic hazard in the Malargüe fold-and-thrust belt. This chapter results from the recognition of active faults during the fieldwork, which was initially aimed to expand the structural database for the study area. Chapter IV presents the numerical modeling techniques applied and attempts to model the entire subduction system using LAPEX-2D. Chapter V constitutes a first-author manuscript in preparation; in this manuscript I present the results of numerical modeling experiments between 33°S and 36°S and their comparison with the study area, based on variations in the initial conditions of the upper plate. Finally, Chapter VI summarizes the conclusions and potential future avenues of research related to the results of this thesis.

1.5 General methodology

First, this study is based on the compilation of the bibliographic information of the study area regarding geology and tectonic evolution. The northern and central zones (33°-34°S) are areas with the highest data density regarding the geologic evolution, with detailed analyses on structural geology (see Giambiagi et al., 2015 and 2016 for a review).

Secondly, in the southern zone (34-36°S) additional fieldwork was carried out, including structural mapping and analysis of kinematic indicators of faults to allow to better constrain the structural evolution of the area. In particular, during fieldwork in the Malargüe fold-and-thrust belt (35°-36°S), geological units, their attitude and structural overprints by faults and folds were surveyed. Kinematic data were analysed using FaultKin software (Allmendinger et al., 2001, 2012) to estimate P and T axes in representative survey stations of mesoscale faults.

Thirdly, the combination of this information was used to generate a map base with QGIS open software that was used subsequently as input data to construct local structural sections in the commercial program MOVE. In order to make the sections, subsurface data was also used, such as 2D and 3D seismic, along with logging information from hydrocarbon wells provided by ROCH SA. This enabled me to tie up the surface structures and outcropping units with their subsurface manifestations.

The fourth step involved thermomechanical numerical. For this purpose, I visited the Geodynamic Modeling Section of the GFZ (Deutsches GeoForschungsZentrum, Potsdam, Germany) twice. At GFZ Dr. Stephan Sobolev, Dr. Andrey Babeyko and Dr. Javier Quinteros guided me in carrying out the simulations. For the numerical models, it was proposed to use the geodynamic code LAPEX-2D, developed by Dr. Babeyko. Modifications were made to this code in order to simulate an oceanic slab that subducts with a prescribed geometry and speed, to avoid the variability that can occur if dynamically developed. The first stage of this modeling effort lead to unrealistic results. Therefore, a new series of models, without imposing restrictions on the slab, were designed. These models are still running. The simulations were run in the GMOD2 cluster of the GFZ and in TUPAC of the CSC CONICET. At the same time, simulations were carried out using a newer code. This code is called ASPECT (Kronbichler et al., 2012; Heister et al., 2017) and our analyses of the different data sets was carried in cooperation with Sibiao Liu, MSc of Potsdam University. In these simulations we tested the behaviour of the continental lithosphere under compression, but without subduction of an oceanic plate. The simulations were performed at the HLRN (North-German Supercomputing Alliance) in Germany. These sets of experiments are presented in Chapter 5. The obtained results can be exported and visualized in Paraview, which allows analysing the temporal evolution of the different variables.

1.6 Geological setting

The Andes mountain range with a length of about 7000 km results from the subduction of different Pacific oceanic plates (Cocos, Nazca and Antarctica plates) under the South American plate. This orogenic system presents a shortening pattern characterized by a central sector (~20°S) where it is maximum (between 280 and 320 km, Isacks, 1988; Allmendinger et al., 1997; Kley et al., 1999; Ramos, 1999 a; McQuarrie, 2002); towards the north and the south shortening decreases. The origin of these variations in shortening is debated, and multiple factors may be responsible for this (see Oncken et al., 2006 for a review). Among these factors are: (i) the weakening of the lithosphere by the asthenospheric wedge (Isacks, 1988); (ii) the age of the subducted slab (Ramos et al., 2004; Yañez and Cembrano, 2004); (iii) the existence of zones with flat subduction (Isacks, 1988; Jordan et al., 1983 a); (iv) the subduction of oceanic ridges (Yañez et al., 2001); (v) the existence of crustal heterogeneities and variations in the resistance of the upper plate

(Tassara and Yañez, 2003; Babeyko and Sobolev, 2005; Oncken et al, 2006), as well as the presence of thick sedimentary basins that promote the formation of thin-skinned fold-and-thrust belts (Allmendinger and Gubbels, 1996; Kley et al., 1999); (vi) different climate zones and their relation with the contribution of sediments to the trench, which may modify the degree of plate coupling in the subduction zone (Lamb and Davis, 2003; Strecker et al., 2007, 2009); and (vii) lithospheric-scale dynamics and mantle flow in the subduction zone (Russo and Silver, 1996; Schellart et al., 2007; Faccenna et al., 2013). In addition to these large-scale, first-order factors, there are additional second-order factors that may promote variations in shortening. These may include differences in inherited crustal thickness and lower crustal composition (Giambiagi et al., 2012), basement characteristics and geometry of extensional sedimentary basins (Kley et al., 1999; Ramos et al., 2004; McGroder et al., 2015).

The Andean orogenic system can be divided into different segments (Fig.1.1) according to geological characteristics, geometry of the subduction zone, and topography. There are several proposals, the first by Gansser (1973) that distinguish the Northern Andes (10ºN-4ºS), Central Andes (4ºS-46º30'S) and Southern Andes (46º30'-52ºS), according to tectonic criteria (Fig. 1.1). Ramos (1999a), based on this proposal, introduced a further subdivision into the Central Andes according to variations in the geometry of the Wadati-Benioff zone; he differentiated a northern sector (4ºS-14ºS), a central sector (14ºS-27ºS) ,and a southern sector (27ºS-46º30'S).

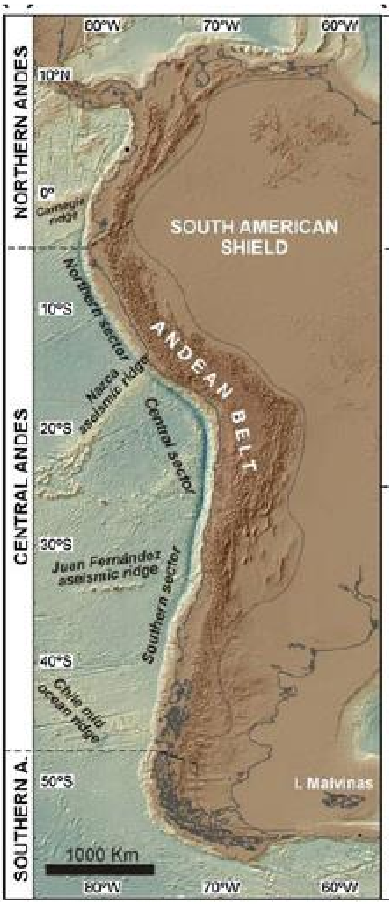

Figure 1.1: Andean segmentation into principal structural provinces, according to Gansser (1973) and Ramos (1999). From Folguera et al., 2016.

Here, I focus on the portion of the Southern Central Andes that is located between 33° and 36°S. In this area, the oceanic Nazca plate is being subducted below the South American plate. Although it is considered that the Andes are the result of shortening and uplift at this latitude from the Cretaceous to the present-day (e.g., Mpodozis and Ramos, 1989), most of the crustal thickening and topographic uplift took place during the Miocene-Quaternary (Ramos et al., 1996; Giambiagi et al., 2012; Suriano et al., 2017). Between 30° and 36°S, there are variations in the subduction angle of the oceanic slab, with a sub-horizontal segment between 27° and

33°S and an inclined subduction zone south of 33°S (Barazangi and Isacks, 1976; Cahill and Isacks, 1992). This overall geodynamic setting defines very different characteristics to the north and south of 33°S (Isacks et al., 1982; Jordan et al., 1983 a).

In the sub-horizontal or flat-subduction segment, the Andean orogen (Fig. 1.2) comprises, from West to East, the Coastal Range, the Principal or Main and Frontal cordilleras, the Precordillera thin-skinned thrust belt, and a sector with thick-skinned deformation corresponding to the Sierras Pampeanas basement uplifts. The Sierras Pampeanas have been inferred to be linked to the shallowing of the Nazca slab during the Late Miocene, which also caused a migration of the magmatic arc towards the foreland, resulting in arc volcanism 500 km away from the highest peaks of Andes (Ramos, 1988; Kay et al., 1991). Limited recent thermochronological data suggest an uplift history which may have started

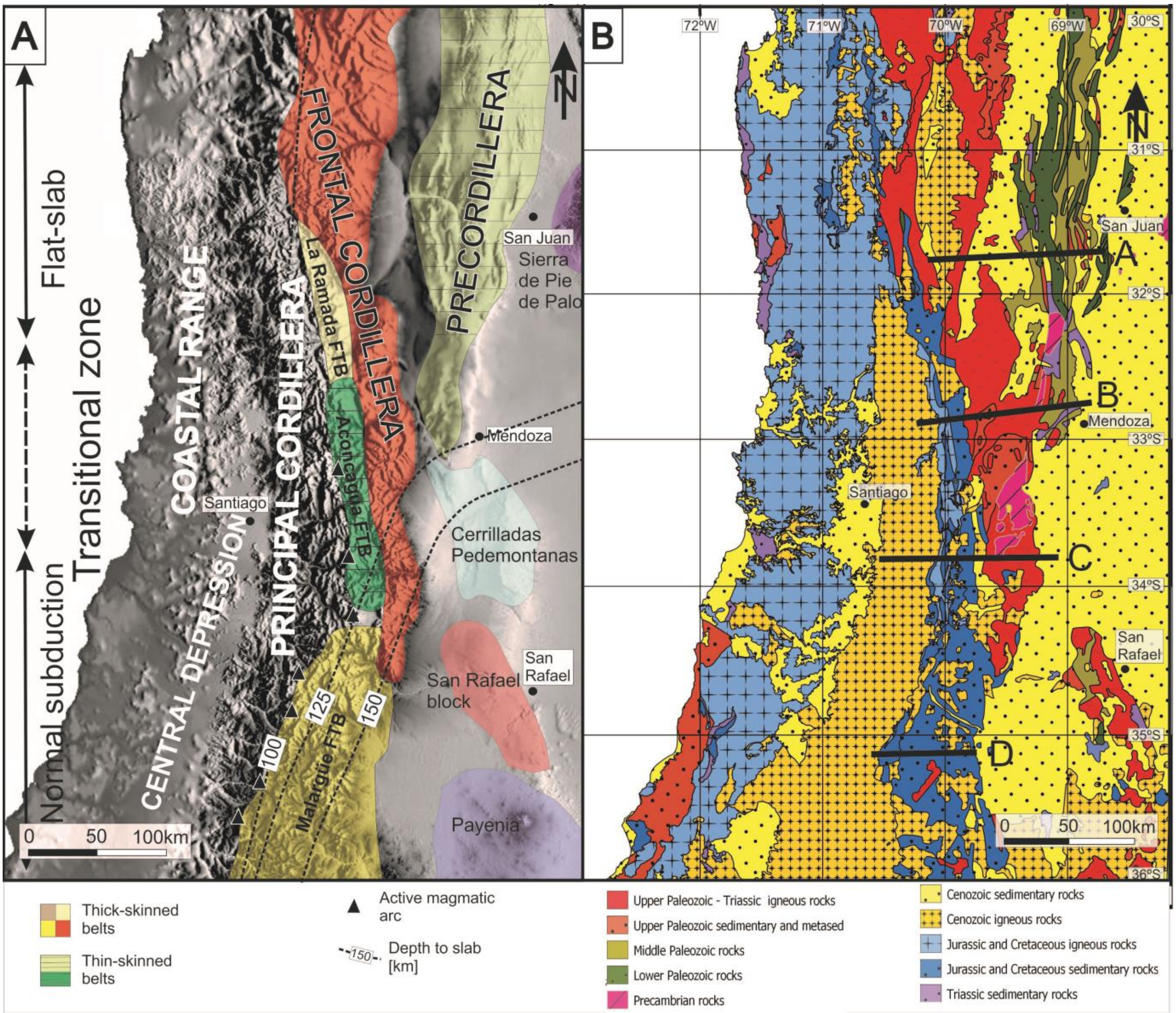

Figure 1.2: A: Morphostructural provinces of the study area. B: Simplified geological map based on SERNAGEOMIN (2003) and SEGEMAR (1997) with location of the transects (Fig. 1.7) indicated by upper-case letters. Modified from Mescua et al. (2016).

earlier, perhaps accentuated by the effects of Neogene flat-slab subduction (Löbens et al., 2011; Bense et al., 2013). This flat-subduction segment is characterized by the absence of an active volcanic arc.

Between 33° and 34°S a transition zone exists between the flat-subduction segment to the north and the normal subduction zone to the south. Here, the abrupt disappearance of the Precordillera and the Sierras Pampeanas occurs and the orogenic system becomes narrower. The morphostructural units in this sector are, from West to East, the Coastal Range (Cordillera de la Costa), Central Depression (Depresión Central), Principal Cordillera (Cordillera Principal), Frontal Cordillera (Cordillera Frontal) and Cerrilladas Pedemontanas. In this region, an active volcanic arc appears again, which corresponds to the Southern Volcanic Zone (SVZ, Hildreth and Moorbath, 1988; Stern et al., 2007).

To the south of 34°, the topographic expression of the Frontal Cordillera disappears under the Cenozoic sediments, only leaving the Coastal Cordillera and the Main Cordillera as the sole morphostructural units in the orogen interior and the uplifted San Rafael basement block in the foreland.

1.6.1 Paleozoic and Mesozoic evolution of the western margin of South America

The western margin of Gondwana records a protracted history of subduction, which resulted in structural heterogeneity of the crust, prior to the development of the Cenozoic Andean orogen (Ramos et al., 1986); these crustal anisotropies have been recognized as a major control on the deformation associated with the Andean shortening. Contractional events in the Paleozoic and extensional events in the Mesozoic created anisotropies and zones of weakness that affected lithospheric strength and the emergence of structural styles during the Neogene compressive deformation (Giambiagi et al., 2012).

The geological evolution of the Lower Paleozoic was characterized by the accretion of allochthonous or para-autochthonous terranes to the western margin of Gondwana. According to several authors, during the Middle to Late Ordovician the accretion of the Cuyania terrane (Fig. 1.3) of Laurentian origin occurred (Ramos et al., 1998; Thomas and Astini, 1996). Subsequently, during the Late Devonian the Chilenia terrane, whose origin is still debated, accreted to the margin (Ramos et al., 1986; López and Grégori, 2004; Massone and Calderón, 2008).

In the late Paleozoic, a subduction zone developed along the continental margin and contractional deformation took place, known as the Gondwana orogeny (Keidel, 1916; Du Toit, 1937; Cawood, 2005) or the San Rafael Phase (Azcuy and Caminos, 1987). This

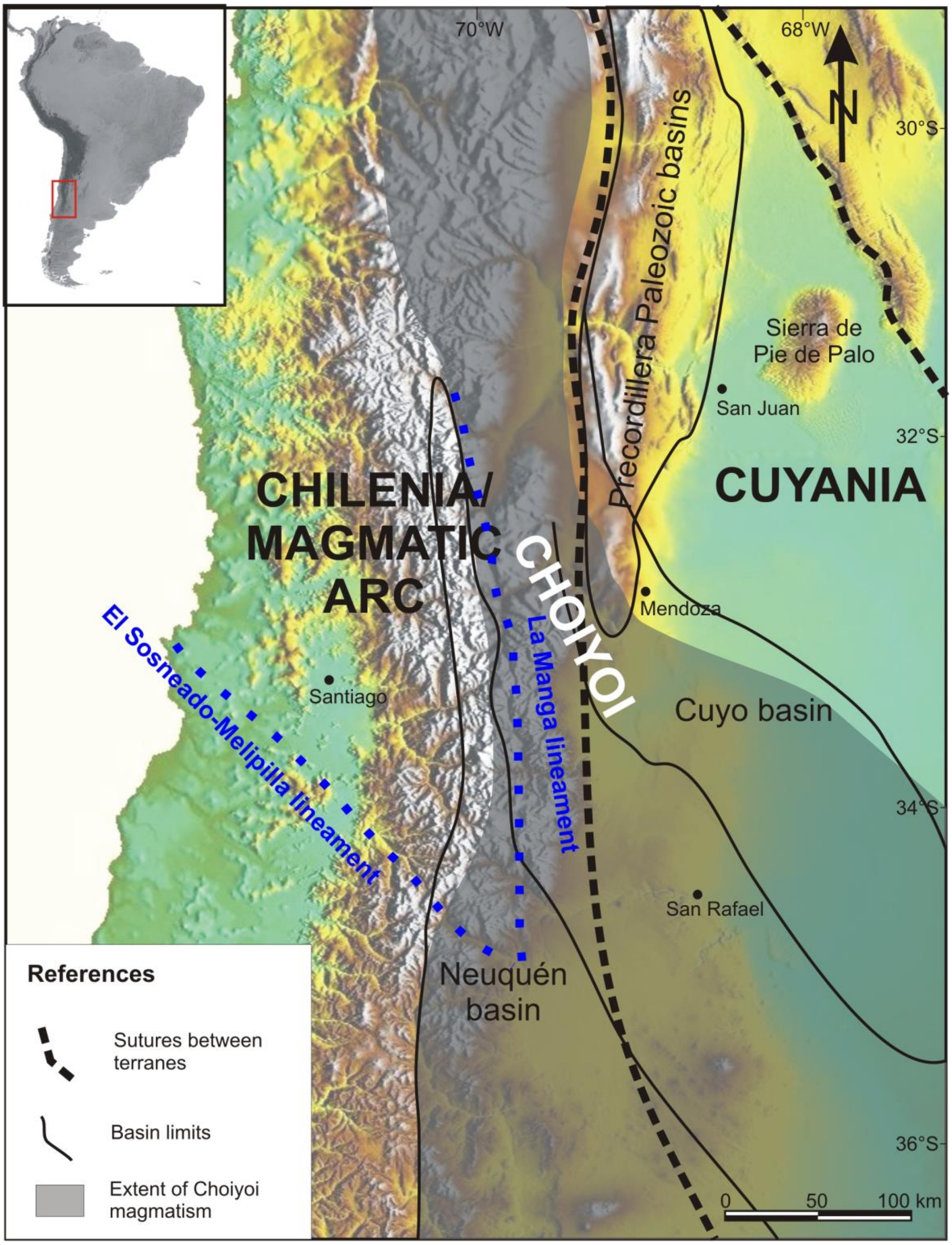

Figure 1.3: Pre-Andean features, including terranes, basins, and volcanic belts that comprise the South American Plate between 30°-36°S (modified from Mescua et al., 2016).

mountain belt with thickened crust had a curved shape trending NW to NNW (Llambías and Sato, 1990). Retroarc basins of Early Carboniferous-Permian age (Limarino and Spalletti, 2006) were deformed during this event.

In the study region two important structures were formed during the Paleozoic that probably impacted the Cenozoic orogeny: the NNW-striking La Manga lineament, which is interpreted as an anisotropy of lithospheric scale with evidence of successive reactivation during the late Paleozoic and the Mesozoic (Bechis et al., 2010); and the WNW-striking Sosneado-Melipilla lineament. This structure is associated with the Melipilla anomaly, a rigid crustal block south of the Melipilla sinistral shear zone (Yáñez et al., 1998).

The transition from the Late Permian to Early Triassic is characterized by a widespread extensional event associated with the initial break-up of Gondwana (Charrier, 1979; Llambías et al., 1993). During this time, the post-orogenic plutonism and acidic volcanism of the Choiyoi Group, which covers a large part of the study area (Fig. 1.3), was associated with the gravitational collapse of the San Rafael orogen (Llambías et al., 1993; Sato et al., 2015).

During the Early to Middle Triassic the extensional processes continued, generating the NNW-oriented halfgrabens of the Cuyo basin and other basins, which were filled with continental clastics (Kokogián et al., 1993; Franzese et al., 2003). Later, during the Late Triassic-Early Jurassic the extension shifted westward and the early depocenters of the Neuquén basin developed (Legarreta and Gulisano, 1989; Vergani et al., 1995). As extension continued the depocenters of the Neuquén basin coalesced in the Middle Jurassic and by Middle Jurassic to Early Cretaceous the basin fill records a sag stage with more than 5000 m of marine and continental deposits (Vergani et al., 1995).

Finally, in the Late Cretaceous the Andean uplift started at this latitude and the continental foreland deposits of the Neuquén Group were deposited (Tunik et al., 2010; Di Giulio et al., 2012; Mescua et al., 2013).

1.6.2 Morphostructural units

In the area between 30° and 36°S, three morphostructural sectors with different tectonic characteristics can be defined (Fig. 1.2). The northern sector, between 30°-33°S, in the flat-subduction segment; a transitional sector between 33°-34°S, and a southern sector, between 34°-36°S, with a normal, steeply dipping subduction zone (Barazangi and Isacks, 1976; Cahill and Isacks, 1992; Tassara et al., 2006). According to Jordan et al. (1983a) this variation in the geometry of the subduction zone may be partly responsible for the presence or absence of certain morphostructural provinces. In the flat-subduction segment, there is no Central Depression that separates the Coastal Range from the Principal Cordillera, as observed in Chile (Charrier et al., 2015). To the east of the Principal Cordillera, the principal morphostructural provinces include the Frontal Cordillera, the Precordillera, and the Sierras Pampeanas. The latter two provinces are no longer present in the transition zone, and in the normal subduction segment, the Frontal Cordillera is absent.

Coastal Range

This range (Fig. 1.2) consists of a series of upper Paleozoic to Cretaceous outcrops, arranged in a gently, E-dipping homocline (Wall et al., 1999). No major Andean thrusts have been identified. Instead, this region exhibits NW to-NNW-striking faults, such as the Melipilla fault (Yáñez et al., 2002). Cenozoic Andean deformation in this mountain range is related to flexural folding and uplift, without negligible movement along the contractional structures (Giambiagi et al., 2015).

Central Depression

The Central Depression (Fig. 1.2) separates the Coastal Range from the Principal Cordillera south of Santiago de Chile; the depression hosts Quaternary sedimentary and pyroclastic deposits, up to 500 m thick (Araneda et al., 2000). Locally, basement rocks emerge from the fill as isolated highs that reach 1600 m elevation (Rodríguez et al., 2012).

Principal Cordillera

The Principal Cordillera (Fig. 1.2) comprises a Western sector (WPC) and an Eastern sector (EPC). The WPC corresponds to the Oligocene to Miocene volcanic arc and is characterized by the inversion of the Abanico basin, a Late Eocene to Early Miocene intra-arc extensional basin (Godoy et al., 1999; Charrier et al., 2002; Fock et al., 2006). The Abanico Formation is deformed by long-wavelength (102-103 m), vergent folds (Rivano et al., 1990). These rocks are overlain by the Farellones Formation which is linked to the activity of the Middle Miocene arc; this unit is gently folded with stratal dips <15° (Vergara et al., 1988).

The EPC is divided into three fold-and-thrust belts (FTB) that are characterized by different structural styles: the La Ramada FTB, Aconcagua FTB, and Malargüe FTB.

North of 32°30'S the La Ramada FTB corresponds to a region with thin- and thick-skinned deformation. This is a consequence of the tectonic inversion of the Permo-Triassic extensional structures (Cristallini et al., 1995; Jara and Charrier, 2014) and those of the Late Triassic-Early Jurassic rift (Álvarez et al., 1996; Ramos et al., 1996a; Mackaman Loflad et al., 2020). Initially, a period of thin-skinned deformation occurred that affected the Neuquén Basin deposits; thin-skinned deformation was associated with a detachment level in the evaporites of the Jurassic Auquilco Formation. This early deformation was superseded by the inversion of extensional faults in the Permo-Triassic basement (Cristallini and Ramos, 2000). At this latitude the orogen records a low amount of shortening (~18 km) in Principal Cordillera since the deformation is concentrated in the Precordillera (Cristallini et al., 1995; Cristallini and Ramos, 2000).

The Aconcagua FTB (32°30'-34°S) is a thin-skinned thrust belt in its northern part with shortening values of ~60 km. The thrust belt comprises east-vergent folds and thrusts that are detached from Jurassic shales and evaporites of the Neuquén Basin (Kozlowski et al., 1993; Cegarra and Ramos, 1996). In the southern sector of the belt changes into a thick-skinned deformation regime as shortening is additionally accommodated by the inversion of Mesozoic normal faults (Giambiagi et al., 2003a).

The Malargüe FTB (south of 34°S) is a hybrid belt with thick- and thin-skinned deformation characteristics, with deep-seated faults affecting the basement and shallow faults deforming Mesozoic to Cenozoic sedimentary cover rocks (Kozlowski et al., 1993; Manceda and Figueroa, 1995; Giambiagi et al., 2008; Silvestro and Atencio, 2009; Fuentes et al., 2016). In the northern zone, the belt shares structural characteristics with the southern portion of the Aconcagua FTB, marking a transition to thick-skinned deformation south of 35°S (Giambiagi et al., 2016). In places, Triassic-Jurassic normal faults, such as the La Manga and Río del Cobre faults, were inverted, (Mescua and Giambiagi, 2012) or exerted an influence on the development of Cenozoic thrusts (Manceda and Figueroa, 1995; Giambiagi et al., 2008; Yagupsky et al., 2008; Bechis et al., 2014). Shortening decreases towards the south, from ~30 km at 34°S to ~10 km at 36ºS (Giambiagi et al., 2012; Mescua et al., 2014).

Frontal Cordillera

This morphostructural province (Fig. 1.2) is composed of Proterozoic metamorphic rocks, lower Paleozoic metasedimentary and metavolcanic rocks, upper Paleozoic marine sedimentary rocks, Carboniferous to Permian granitoids, and Permo-Triassic volcanic rocks (Polanski, 1964, 1972; Heredia et al., 2012). These rocks crop out in the following ranges that conform the Frontal Cordillera: Cajón de la Brea, Colangüil, Ansilta, Cordón de la Ramada, Cordillera del Tigre, Cordón del Plata, Cordón del Portillo, and Cordillera de las Yaretas (Ramos, 1999b; Giambiagi et al., 2016). North of 33°S, the Frontal Cordillera is uplifted along a blind ramp, which ramp up below the Precordillera FTB (Allmendinger et al., 1990). South of 33°S, the Frontal Cordillera is delimited by the La Carrera fault system, which corresponds to reactivated N- to NNE-striking faults (Caminos, 1965; Folguera et al., 2004; Casa et al., 2010).

Precordillera

The Precordillera FTB (Fig. 1.2) is located between 29° and 33°S; from north to south it can subdivided into two zones, the northern zone between 29° and 32°S, and the southern zone, between 32° and 33°S. The northern zone can be sub-divided, according to stratigraphic and structural characteristics, into three subunits: the Western, Central, and Eastern Precordillera (Ortiz and Zambrano, 1981). In its western and central sectors the Precordillera is a thin-skinned, E-vergent thrust belt; the eastern sector involves basement faults, with mainly W-vergent structures, similar to the Sierras Pampeanas style of deformation (Bracaccini, 1946, 1960; Rolleri, 1969). The thrusts of the Western and Central zones are detached along a *décollement* in Cambrian to Ordovician limestones and mudstones (Baldis and Chebli, 1969; Ortiz and Zambrano, 1981). The stratigraphy comprises lower to middle Paleozoic continental and marine deposits (evaporites, limestones and clastic rocks), upper Paleozoic continental, marine and volcanic rocks, Triassic continental sediments, and Mio-Pliocene synorogenic deposits (Jordan et al., 1983b; Kokogian et al., 1999; Ramos, 1999b).

In contrast, the southern Precordillera exhibits a thick-skinned deformation style and involves middle Paleozoic to Triassic rocks that were reactivated during Andean shortening (Giambiagi et al., 2011). The absence of the complete Paleozoic sequence distinguishes this part of the morphostructural province from the northern Precordillera.

Sierras Pampeanas

This morphostructural province (e.g. Sierra de Pie de Palo in Fig. 1.2) corresponds to a series of basement blocks delimited by reverse faults (Stelzner, 1873; Gonzalez Bonorino, 1950), and elevations in excess of 5000 m in some sectors. The basement consists of Proterozoic to the early Paleozoic metamorphic and igneous rocks, superseded by Neopaleozoic continental sediments (Bodenbender, 1911; Salfity and Gorustovich, 1984). This region was affected during Mesozoic extension with the deposition of continental deposits and mafic volcanics (López and Solá, 1981; Kay and Ramos, 1996; Lagorio, 2008). In the greater study area, asymmetrically uplifted basement blocks are inferred to be associated with listric reverse faults, usually with a westward vergence (González Bonorino, 1950) and associated with the compressional reactivation of Mesozoic normal faults and Paleozoic anisotropies (Gordillo and Lencinas, 1979; Jordan and Allmendinger, 1986; Jordan et al., 1983b; Ramos, 1999 b).

Cerrilladas Pedemontanas

The Cerrilladas Pedemontanas (Fig. 1.2) present a series of elongated folds, with W- and E-vergent reverse faults (Dellapé and Hegedus, 1995), striking to the NNW. This is due to the reactivation of Triassic normal faults of the Cuyo basin, which were partially inverted during the Cenozoic (Legarreta et al., 1992). Here, Triassic continental deposits are covered by Neogene to Quaternary synorogenic sediments of the Cacheuta sub-basin (Irigoyen et al., 2000; Buelow et al., 2018).

San Rafael Block

The San Rafael Block (Fig. 1.2) corresponds to an uplifted basement range, located in the center-south of Mendoza, between 34° and 36°S. This morphotectonic feature, whose basement corresponds to Proterozoic (Grenvillian) metamorphic rocks, is covered by Ordovician calcareous, siliciclastic and low-grade metamorphic rocks; these units are superseded by Silurian-Devonian and Carboniferous sediments and Permian-Triassic volcanic and sedimentary rocks (González Díaz, 1964; Bordonaro, 1999; Baldis and Peralta, 1999; Cortés et al., 1999; Kleiman and Japas, 2009). Retroarc volcanism developed on this block during Pliocene to Quaternary (Folguera et al., 2009).

The San Rafael Block rises about 100-200 m over the Alvear basin and the Pampean plain (Folguera and Zárate, 2011). It was uplifted by the Las Malvinas fault system (Folguera et al., 2009) and the Santa Isabel fault, both reverse faults, which were active in the Pliocene (~3 Ma; Folguera and Zárate, 2009). In the eastern zone, neotectonics characterized by an active fault system is documented (Folguera et al., 2009) – the data include activity along the Las Malvinas fault associated with the 1929 M 6.0 earthquake (Bastías et al., 1993; Cisneros and Bastías, 1993; Cortéz et al., 2006). It has been speculated that this neotectonic activity may be influenced, as a second order factor, by the impact of mantle anomalies in the lower crust (Burd et al., 2014; Folguera et al., 2015).

1.6.3 Andean tectonic cycle - from the Late Cretaceous to the present

The Andean tectonic cycle began during the Late Cretaceous, although subduction of an oceanic plate below the western margin of South America had probably already been established during the Triassic (Vázquez et al., 2011; Del Rey et al 2016, Oliveros et al., 2018); related magmatism developed in the locations of the present-day Principal Cordillera and the Coastal Range (Oliveros et al., 2018). This magmatic arc was parallel to the western margin of Gondwana, with extensional backarc basins to the east of the arc, including the Neuquén basin. This was probably due to a low degree of plate coupling at the beginning of the cycle, when old, cold oceanic crust was subducted below western Gondwana (Charrier et al., 2007). This extensional setting was maintained during most of the Jurassic and Early Cretaceous.

Shortening began in the Late Cretaceous, although the current topography of the Andes between 30° and 36°S results primarily from the deformation that has characterized this region from the Miocene to the present-day (Ramos, 1999 b; Giambiagi et al., 2012; Suriano et al., 2017). The different deformational stages since the Late Cretaceous are described below.

1.6.4 Initiation of Andean deformation – from the Late Cretaceous to Paleocene

The Andean orogeny began with episodes of contractional deformation during the Late Cretaceous (Fig.1.4) and involved the inversion of retroarc basins (Mpodozis and Ramos, 1989). This Cretaceous shortening event is recorded by synorogenic continental deposits of the Neuquén Group (and equivalent Diamante Formation) in the Principal Cordillera, between 34° and 36°S during the Aptian-Cenomanian (Tunik et al., 2010; Orts et al., 2012; Tapia et al., 2012; Mescua et al., 2013; Balgord and Carrapa, 2016; Horton and Fuentes, 2016; Fennell et al., 2017; Gómez et al., 2019). Flexural subsidence in the foreland increased during the Maastrichtian, culminating during the first Atlantic ingression, which reached the Cretaceous orogenic front (Tunik, 2003; Aguirre-Urreta et al., 2011). Recent studies, however, proposed an extensional phase for the latest part of this last event (Fennell et al., 2019). The classic foreland basin (i.e. due to the orogen flexural loading) stage recorded by the Neuquén Group has been challenged recently by Fuentes and Horton (2020) proposing that the remaining thermal subsidence from the former postextensional stage and the loading by the magmatic arc were important in the generation of accommodation rather than a shortened crust. During the Paleocene, a phase of reduced accumulation in the foreland is related to low or null shortening in the arc (Horton et al. 2016; Horton and Fuentes, 2016).

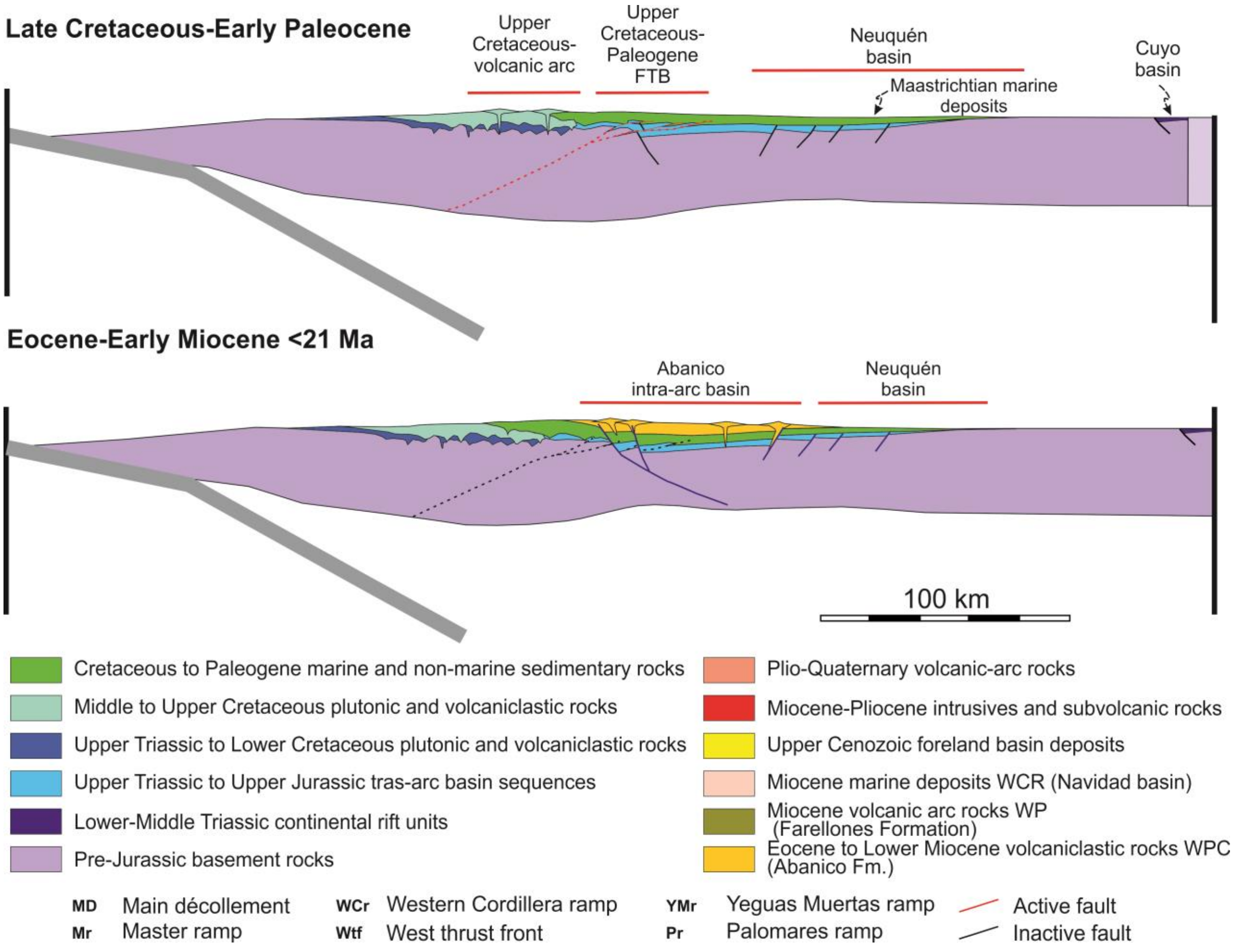

Figure 1.4: Kinematic model for the Andes at 33°40’S from Late Cretaceous to Early Miocene (Giambiagi et al., 2015).

1.6.5 Initial uplift of the Frontal Cordillera at 30°S during the Late Eocene

According to new thermocronological data from the Frontal Cordillera at 30°S (e.g., Lossada et al., 2017), the central sector of the Frontal Cordillera began to be uplifted during the Late Eocene to Early Oligocene (~35 Ma). This agrees with structural evidence (Pineda and Emparán, 2006), thermochronological data from the western slope (Cembrano et al., 2003; Rodríguez, 2013), and retroarc provenance analysis (Fosdick et al., 2017). This tectonic phase is widely recognized to the north, in the Puna/Altiplano region (i.e., the Incaic deformation phase between 45 and 35 Ma), but there is no evidence of this pre-Miocene contractional phase to the south of 30°S.

1.6.6 Late Eocene to Early Miocene extension

During the Late Eocene to Early Miocene (Fig. 1.4), a prolonged extensional event took place, that affected the western slope of the Principal Cordillera (Charrier et al., 2002) and that has been linked to trench rollback of the Nazca Plate (Mpodozis and Cornejo between 35 and 21 Ma (Muñoz et al., 2006). This event led to normal faulting, crustal thinning (30-35 km) and tholeiitic magmatism, represented by the deposits of the Abanico/Coya Machalí Formation (Nyström et al., 1993; Kay and Kurtz, 1995; Zurita et al., 2000; Muñoz et al., 2006). This basin was filled by up to 3000 m of volcaniclastic deposits, acid to intermediate lavas, and sedimentary intercalations (Charrier et al., 2002). The magmatism reflected by the Abanico Formation is contemporaneous with that recorded farther north, between ~29°S and 30°30'S. There, the Doña Ana Group of Late Eocene to Late Miocene age was also deposited in an extensional environment (Charrier et al., 2007; Litvak et al., 2007; Winocur et al., 2015). To the south (35-36°S) the Coya Machalí Formation represents the equivalent of the Abanico Formation (Charrier et al., 2007).

During this period, it is expected that the Coastal Range would have corresponded to a topographic high due to crustal thickening (from the Late Cretaceous-Paleocene event) and isostatic compensation (Giambiagi et al., 2016). Locally, isostatic rebound close to the W-vergent Abanico master fault may have also affected this area (Charrier et al., 2009). Towards the east, in the Neuquén Basin, distal continental sediments were deposited, tapering towards the east (Melchor and Casadío, 2000). An important hiatus that lasted 20 Ma is registered in the foreland (Horton et al., 2016; Horton and Fuentes, 2016) coeval with the extension I the hinterland.

1.6.7 Early Miocene main-shortening event (21-16 Ma)

The last major shortening event began in the Early Miocene (Fig. 1.5) with the inversion of the Abanico basin (Godoy et al., 1999; Charrier et al., 2002; Fock et al., 2006). The onset of deformation on the present-day western slope of the Andes is marked by a changeover from the low-K tholeiites of the Abanico Formation to the calc-alkaline dacites of the Teniente Volcanic Complex (~34ºS) (Kay et al., 2005; 2006) between 21 and 19 Ma (Charrier et al., 2002; 2005). This deformation is contemporaneous with volcanism between 29° and 30°S, represented by Las Tórtolas, (Mpodozis and Cornejo, 1988; Nasi et al., 1990; Martin et al., 1995; Murillo et al., 2017), the development of the Farellones volcanic arc (Vergara et al., 1999) in the northern zone (32°-34°S), and the magmatic activity of the Cordón del Burrero Volcanic Complex (~ 18 Ma) in the southern zone of the study area (~35°S) (Sruoga et al., 2008). In the northern zone, the geochemical signatures of the Late Oligocene to Early Miocene lavas indicates an increase in crustal thickness with respect to the lower part of Doña Ana Group (Kay and Abruzzi, 1996; Litvak et al., 2007) and the Abanico Formation (Charrier et al., 2007).

During this period, retroarc magmatism in the Precordillera was represented by volcanic and subvolcanic complexes, such as the La Peña alkaline complex (Villar and Zappettini, 2000; Zappettini et al., 2013). The La Peña complex was emplaced in a transtensional tectonic environment, developed locally in the Precordillera during the Early Miocene (19 Ma) (Pagano et al., 2014).

The deformation and uplift of the Western Principal Cordillera (WPC) is related to the generation of a main crustal *decóllement*, which roots under the arc at the contact between the Moho and the lithospheric mantle, about 40 km deep and corresponding to the lowermost tip of the locked subduction (Giambiagi et al., 2015). The eastward movement of the upper crust with respect to the stable and long-lived lower crustal MASH zone (Muñoz et al., 2012) may explain the up to 40-km-width of the Farellones volcanic arc. The main sectors that were passively elevated during this period are the Eastern Coastal Range and the Western Principal Cordillera (Giambiagi et al., 2016). Passive uplift in both sectors agrees with provenance studies for the lower part of the Navidad Formation (Rodríguez et al., 2012) whose radiometric ages indicate a deposition during 23-18 Ma (Gutiérrez et al., 2013); an apatite fission-track (AFT) age of 18,3+2,6 Ma reflects exhumation during the sedimentation of the Upper Cretaceous deposits (Fock, 2005). The coeval uplift of the Eastern Coastal Range and the Principal Cordillera resulted in the formation of a depocenter filled with 3000 m of volcanic rocks that are represented by the Farellones Formation volcanic rocks (Vergara et al., 1988; Elgueta et al., 1999; Godoy et al., 1999). The onset of deformation (20-18 Ma) in the foreland fold-and-thrust belts (FTB) (e.g., Cegarra and Ramos, 1996; Cristallini and Ramos, 2000; Perez, 2001; Giambiagi and Ramos, 2002; Silvestro et al., 2005; Mescua et al., 2014) is linked to the eastward propagation of the main *décollement* (Giambiagi et al., 2015). Between 18 and 15 Ma, however, the driving forces were apparently not strong enough to cause the uplift the WPC; as a consequence, the orogen widened and propagated toward the foreland to maintain critical taper (Giambiagi et al., 2016). The change in the location of the deformation might be related to the rapid ascent of magmas derived from the mantle and with little interaction with the upper sectors of the lithosphere in the Western Principal Cordillera (Muñoz et al., 2012). During this period the northern sector of the Aconcagua FTB accommodated most of the shortening (Cegarra and Ramos, 1996; Cristallini and Ramos, 2000) prior to the volcanism of the Aconcagua Complex (15,8-8,6 Ma) (Ramos et al., 1996b). The synorogenic deposits that record this stage of deformation are preserved in the Eastern Principal Cordillera (EPC) (Manantiales, Penitentes and Alto Tunuyán basins) and in the foreland along the orogenic front (Cacheuta, Atuel, Las Peñas and Río Grande-Palauco basins) (Giambiagi et al., 2016).

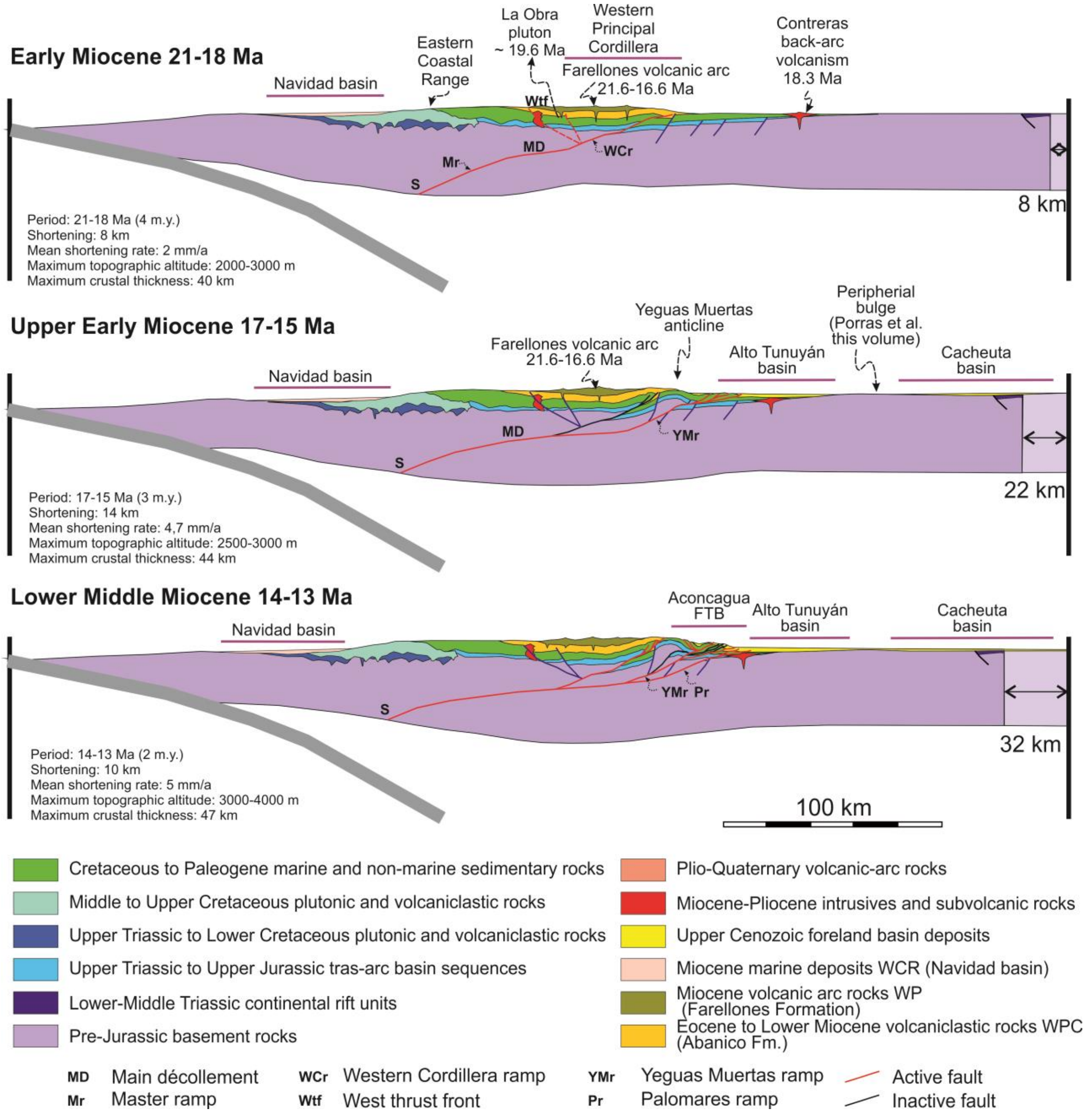

Figure 1.5: Kinematic model for the Andes at 33°40'S from Early to lower Middle Miocene (Giambiagi et al., 2015).

The Frontal Cordillera uplift, which occurred during the Miocene, records a diachronous evolution, starting first (i.e. ~18 Ma, Lossada et al., 2018) in the northern zone of the study area (30°S), at ~16 Ma in the central zone (32°-33°S; Suriano et al., 2018) and between 10-5 Ma to the south of 33°S (Lossada et al., under review). This cannot be correlated with the change in subduction dynamics, because the onset of Miocene contraction predates the collision of Juan Fernández ridge, which has been considered by some authors to cause the flat-slab subduction between 27° and 33°S (Yáñez et al., 2001; Ramos et al.,2002).

1.6.8 Middle Miocene eastward-directed deformation and flat-slab subduction (15-12 Ma)

During this period important crustal shortening occurred in the northern segment, concentrated in the EPC and in the Cordón de La Ramada (Frontal Cordillera) (Cristallini and Ramos, 2000). The crustal thickness reached a value close to the present and associated with an eastward migration of the crustal root (Giambiagi et al., 2015). Due to tectonic loading, accommodation was generated in the foreland basins to the east of the La Ramada and Aconcagua FTBs (Irigoyen et al., 2000; Pérez, 2001; Mazzitelli, 2019).

At 30° S the crust achieved its maximum thickness at ~14 Ma, which was accompanied by an increase in the relative magnitude of the vertical stress component, which caused a permutation between $\sigma 3$ and $\sigma 2$, and a corresponding changeover to a strike-slip regime (Giambiagi et al., 2017).

In the Middle-Late Miocene (14-10 Ma, Yánez et al., 2001; Kay and Mpodozis, 2002), the oceanic slab started flattening north of 33°S and volcanism migrated from the Principal Cordillera, where it was active between 15 and 9 Ma (i.e., Aconcagua and La Ramada volcanic complexes; Ramos et al., 1996b; Pérez and Ramos, 1996), toward the Sierras Pampeanas (Kay and Abbruzzi, 1996). To the south of 33°S, the volcanic activity decreased and it is manifested in the form of localized centers from the Middle-Late Miocene to the Pliocene (Giambiagi et al., 2016). Subsequently, the active volcanic arc was established in the Late Pliocene (Giambiagi et al., 2016).

In the southern segment (34°-36°S), the eastern Malargüe FTB was deformed during this period (Kozlowski et al., 1993; Silvestro et al., 2005; Giambiagi et al., 2008; Turienzo et al., 2012; Mescua et al., 2014), with significant shortening and a complex structural style, which involved the inversion of Mesozoic normal faults and the formation of thrusts (Giambiagi et al., 2012; Mescua et al., 2014; Fuentes et al., 2016). The orogenic front expanded towards the east, resulting in a wide deformation zone that includes the Sierra Azul and Sierra de Palauco (Yagupsky et al., 2008; Silvestro and Atencio, 2009, Giambiagi et al., 2009). The eastward advance of deformation in the Principal Cordillera was accompanied by synorogenic sedimentation leading to the formation of the Pincheira-Ventana basin between 16 and 7 Ma (Silvestro et al., 2005; Horton et al., 2016). In this context the calc-alkaline synorogenic magmatism of the Huincán cycle began at ~14 Ma

(Baldauf, 1997; Nullo et al., 2002; Sruoga et al., 2009) and reflects an important widening of the arc towards the east, contemporary with crustal deformation. The geochemical signature of these volcanic rocks indicates crustal thickening in this period (e.g., Nullo et al., 2002).

1.6.9 Middle-Late Miocene uplift of the Precordillera (12-6 Ma)

The uplift of the Precordillera began between the Middle to Late Miocene. Previous studies proposed that it began at 20 Ma in its western part with the La Tranca thrust (Jordan et al., 1993); however, recent investigations have proposed that the beginning of deformation may have taken place been between 12 and 11 Ma, virtually with an uninterrupted migration of the orogenic front towards the foreland (Suriano et al., 2017). In addition, it has been suggested that the Precordillera uplift was largely synchronous latitudinally, according to new geochronological data obtained in the north and south of the range (Walcek and Hoke, 2012; Levina et al., 2014; Suriano et al., 2017; Buelow et al., 2018).

Between 10 and 9 Ma, the crust thickness in the Aconcagua FTB had reached its current maximum thickness of 50 km (Giambiagi et al., 2015), as isotopic analyses suggest (Kay et al., 2005). At this point, the driving forces of uplift failed to provide the energy needed to thicken the crust more and it appears that the crustal root started growing laterally rather than vertically. This process appears to have been associated with a reduction in shortening rates (Giambiagi et al., 2016). This scenario corresponds to the deep crustal hot zones proposed by Muñoz et al (2012), which develop due to repeated basaltic intrusions in the lower crust that impact the thermal field, thus increasing the production of melts. This in turn may have promoted the ductile behavior of the lower crust and the widening of the crustal root (Giambiagi et al., 2015).

In the northern sector the volcanic arc migrated eastward from the Precordillera to the Sierras Pampeanas during this period, probably associated with the shallowing of the oceanic slab (Ramos et al., 2002). This volcanism took place between 9.5 and 2 Ma (Ramos et al., 2002), it has a clear geochemical signature related to subduction (Kay et al., 1991), and it is restricted to the southern Sierras Pampeanas between 31°-33°S. In contrast, to the south of 33°S, on the western slope of the Principal Cordillera, the Teniente Volcanic Complex (34°S) intruded the Abanico and Farellones formations, bracketed by radiometric ages between 12 and 7 Ma (Kay and Kurtz, 1995; Kurtz et al., 1997; Kay et al., 2005).

The Southern Precordillera uplift (32-33°S) began at ~14 Ma (Walcek and Hoke, 2012; Buelow et al., 2018). Immediately afterwards, the migration of the arc to the Sierras Pampeanas took place (Kay et al., 1991; Ramos et al., 2002).

During the Late Miocene (8-6 Ma), the sedimentary record documents an important uplift event in the Frontal Cordillera between 33°30' and 34°30'S (Irigoyen et al., 2000; Giambiagi et al., 2003b). From (U-Th)/He apatite thermochronology in the Frontal Cordillera it has been inferred that exhumation rates were ~10 m/Ma in the region between 32°50' and 33°40'S prior to the Miocene and 100-60 m/Ma during the Early Miocene (Hoke et al., 2015).

Based on thermochronology on the Chilean sector of the Principal Cordillera between 34° and 36° S, a period of high exhumation at 8 Ma is inferred (Spikings et al., 2008), which may have been associated with out-of-sequence thrusting of the El Fierro and Las Leñas thrusts (Godoy et al., 2009; Kozlowski et al., 1993; Mescua et al., 2014), or the inversion of the eastern master faults of the Abanico basin (Piquer et al., 2010; Tapia et al., 2012). According to Maksaev et al. (2009), this period of high exhumation occurred between 6 and 3 Ma. The frontal structures of this part of the range, such as the Malargüe anticline, were also active during this period, as recorded by the foreland deposits of the Loma Fiera Formation, with ages younger than 10 Ma (Baldauf, 1997; Silvestro et al., 2005; Horton et al., 2016; Fuentes et al., 2016).

In the south of the study zone (34°-36°S), the Huincán volcanic arc reached the orogenic front with eruptions along the Sosneado thrust, with ages between 10 and 5 Ma (Baldauf, 1997; Nullo et al., 2002). In the internal part of the FTB there was coeval volcanism, dated between 10 and 6 Ma (Sruoga et al., 2009). In the retroarc the volcanism reached the eastern zone of the San Rafael Block at ~4 Ma and then recedes to the west, reaching the eastern zone of the Malargüe FTB at 0.1 Ma (Folguera et al., 2009). This migration could have been related to the increase of the subduction angle of the Nazca Plate following a shallow-subduction cycle (Kay et al., 2006; Folguera et al., 2009), although alternative explanations are possible, such as those that involve variations in the tectonic stress field and crustal thickness that conditioned arc expansion during upper-plate contraction (Mescua et al., 2019).

1.6.10 Pliocene deformation in the foreland (5-2.5 Ma)

During the Pliocene the deformation processes migrated to the east toward the Sierras Pampeanas in the flat-slab segment north of 33°30'S (Ramos et al., 1996 a,b). Based on morphometric analysis, regional stratigraphic relationships and cosmogenic nuclide geochronology Siame et al. (2015) determined that the Sierra de Pie de Palo (Fig. 1.2) began to uplift between 6-4 Ma although a previous uplift is also reported by Löbens et al. (2013), while the Sierras de Córdoba and the Sierra de Chepes uplifted between 6-5.5 Ma (Ramos et al., 2002).

In the Andes tectonic activity was sustained along the orogenic front of the Frontal Cordillera and the Precordillera, and strike-slip faults were active in the eastern Principal Cordillera. Magmatic activity decreased significantly and ceased altogether at 2 Ma. South of this latitude, however, magmatic activity resumed along the watershed of the Andes, and volcanoes such as Tupungato, San Jose, Marmolejo, Maipo, Sosneado, Risco Plateado, Tinguiririca, Planchón-Peteroa among others were formed (Stern, 2004).

In the transition zone between the flat-slab and the steeper subduction segments, contractional deformation occurred only in the eastern zone of the Frontal Cordillera associated with the generation of thrusts that affected the Lower Miocene-Pliocene synorogenic deposits of the Cacheuta basin, and the development of an angular unconformity in the synorogenic units in the Cerrilladas Pedemontanas (Yrigoyen, 1993; Irigoyen et al., 2000).

During this stage, there was a widening of the crustal root, which would have favoured the uplift of the Coastal Range by isostatic rebound (Giambiagi et al., 2015). This is inferred through emerged marine deposits in the interval between 4.4 and 2.7 Ma (Encinas et al., 2006) and accelerated erosion, related to the increased relief conditions between 6 and 3 Ma (Maksaev et al., 2009).

The Malargüe FTB records minor deformation during the Pliocene, with minor thrusts and strike-slip faults along the orogenic front (Giambiagi et al., 2008; Mescua et al., 2019). Exhumation in the southern part of the Western Principal Cordillera has been attributed to fault activity between 5 and 1 Ma (Spikings et al., 2008). At this latitude in the foreland, extensional tectonics related to orogen relaxation, coeval with volcanism in the Payenia area (Folguera et al., 2009; Ramos et al., 2014), evolved over the last 2 Ma (Ramos and Folguera, 2011).

1.6.11 Quaternary (2.5 Ma to the present-day)

In the Quaternary the active orogenic front has been located in the foothills of the Andes (Costa et al., 2000) where strong historical earthquakes were repeatedly recorded between 30-34°S (Alvarado et al., 2005). Between 31° and 33°S, faults affected

Pleistocene deposits on the border between the Frontal Cordillera and the Precordillera (Cortés and Cegarra, 2004; Terrizzano et al., 2010), while on the eastern limit of the Precordillera and on both sides of the Meseta del Guadal (Cerrilladas Pedemontanas), faults affect Pleistocene-Holocene deposits (Bastías et al., 1993; Ahumada and Costa, 2009; Moreiras et al., 2014; García and Casa, 2015) (Fig. 1.6). These structures unambiguously show that the deformation front of the orogen has been propagating toward the foreland during the Quaternary (Giambiagi et al., 2016). This style of deformation is furthermore confirmed by the recent activity of the eastern thrust of the Barrancas anticline (68.75ºW) related to the 1985 Mb = 6.0 Mendoza earthquake (INPRES, 1985; Triep, 1987; Chiaramonte et al., 2000).

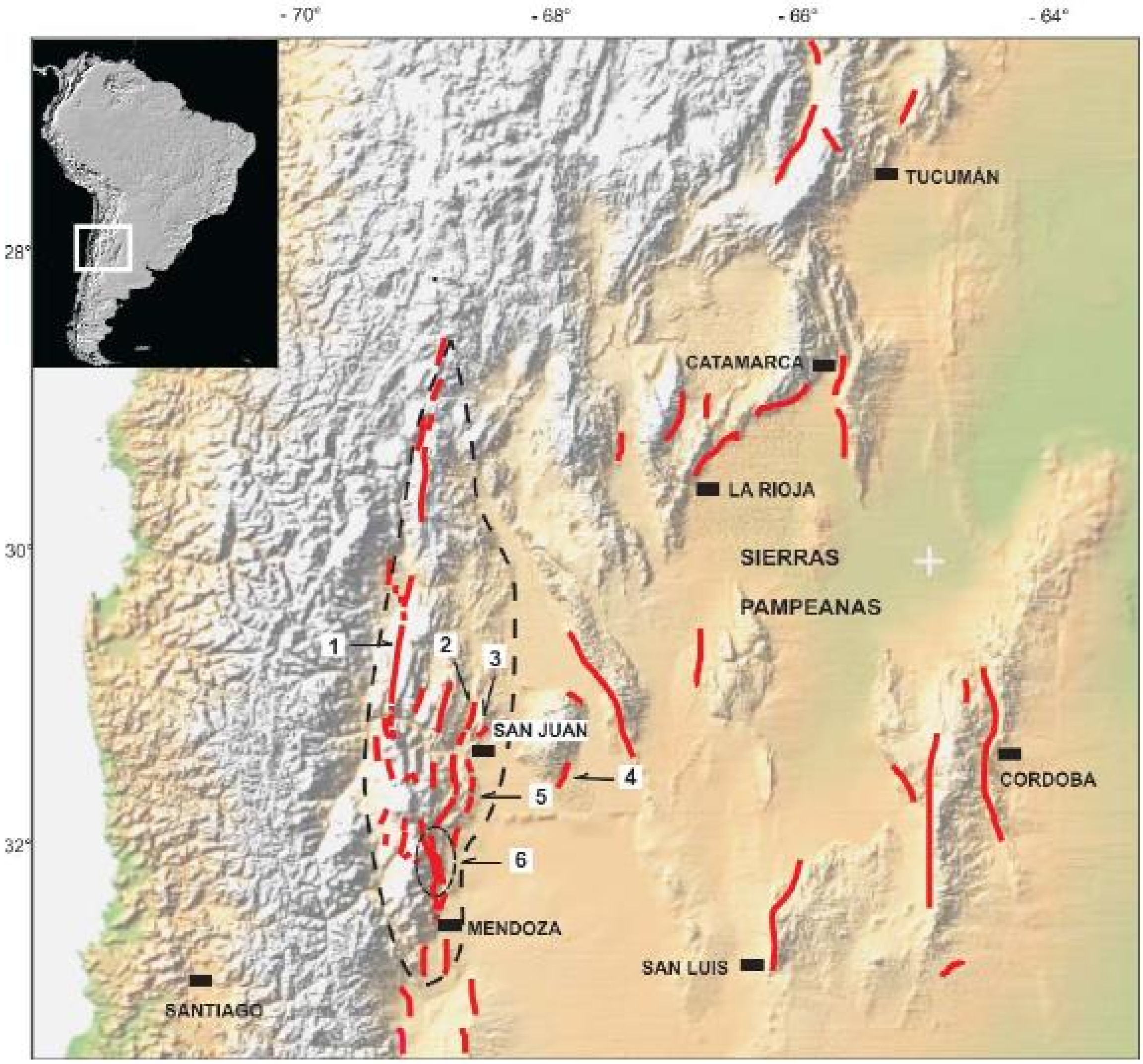

Figure 1.6: Neotectonic structures in the Andes and their foreland between 27°-33°S (Costa et al., 2006). 1. El Tigre, 2. Villicum-Zonda-Pedernal, 3. La Laja-Marquezado-Cerro Salinas, 4. Ampacama-Niquizanga, 5. La Rinconada , 6. Las Peñas-Las Higueras. Precordillera within dashed lines.

Evidence for Quaternary seismic activity is widely distributed across the major faults of the Sierra de San Luis and the Sierra Comechingones in the southern zone of the Sierras Pampeanas, (Fig. 1.6; Costa and Vita-Finzi, 1996; Costa et al., 2000; 2001).

In the northern sector of the study area, earthquakes with shallow focal mechanisms frequently occur in the longitudinal valley separating the Principal and Frontal Cordilleras, and in the eastern Sierras Pampeanas (Giambiagi et al., 2016). During the last 250 years there has been a concentration of large earthquakes in the western Sierras Pampeanas, some of the most recent and destructive events being the 1944 Mw7.0 San Juan earthquake, the 1952 Mw 6.8 San Juan earthquake, and the 1977 Mw 7.4 Caucete earthquake, all of them close to the Sierra de Pie de Palo (Kadinsky-Cade et al., 1985; Langer and Hartzell, 1996; Alvarado et al., 2005; INPRES, 2016).

In the southern sector, seismicity is concentrated along the Malargüe FTB (Giambiagi et al., 2016). Following the Maule earthquake in 2010 (Mw 8.8), there was an increase in seismicity in the arc region at 35°S, related to a change in the regional state of stress (Spagnotto et al., 2015). In this zone, Quaternary faults are recognized which can generate moderate earthquakes (Mescua et al., 2019).

On the Chilean flank of the Andes shallow-seated seismicity is distributed along the western flank of the Principal Cordillera, at depths of 12-15 km (Barrientos et al., 2004); under the Central Depression seismicity typically occurs at depths of <20 km (Farías et al., 2010). This suggests that at least the western portion of the main *décollement* underlying the Principal Cordillera is active today (Giambiagi et al., 2016). This is consistent with data indicating minor amounts of Quaternary motion of the San Ramón fault, whose scarp is linked to vertical displacements of 0.7-1.1 km (before 2.3 Ma) of the peneplains in the western Principal Cordillera (Farías et al., 2008; Armijo et al., 2010).

In the high Andes, near the crest line, most shallow-seated earthquakes with magnitudes >Mw 5 have strike-slip focal mechanism (Barrientos et al., 2004, Sielfeld et al., 2019). Under the eastern part of the Frontal Cordillera and the Cuyo basin, shallow-seated earthquakes display focal mechanisms that indicate ongoing shortening (Alvarado et al., 2007). The neotectonics in the foreland are characterized by motion along blind faults that have folded Quaternary deposits (García and Casa, 2015).

1.6.12 Analysis of crustal shortening

This section presents four transects (Fig. 1.7; Mescua et al., 2016) corresponding to the segments of the Wadati-Benioff area, which have different geometries. The first and second segments (A, 32°S and B, 33°S) correspond to the flat-slab zone, the third (C, 33°40'S) to the transition zone, and the fourth (D, 35°S) to the normal subduction zone.

The first transect (A) located at 32°S displays shortening of 15 km in the La Ramada FTB in the eastern Principal Cordillera, while in the Frontal Cordillera, the values center around 4-6 km (Cristallini and Ramos, 2000). In this transect, the shortening is concentrated mainly in the Precordillera where previous studies estimated high values, between 88 and 136 km (Von Gosen, 1992; Cristallini and Ramos, 1995) although pre-Andean shortening was probably important. Recent studies estimated 40 km at latitude 32° S (Mazzitelli, 2019) and around 60 km at 30°S latitude (Mardonez, 2019).

The following transect (B) at 33°S presents a different spatial distribution of shortening, with respect to the previous transect. The Aconcagua FTB in the Principal Cordillera, with a thin-skinned structural style, absorbs most of the shortening in this section, with values of ~63 km (Cegarra and Ramos, 1996). In the western Principal Cordillera, less than 10 km of shortening is estimated (Jara et al., 2015), while in the Frontal Cordillera, a shortening of 15-20 km is estimated, and in the Precordillera about 10 km (Giambiagi et al., 2011).

The Maipo-Tunuyán transect (C, 33°40'S) has lower shortening values in each morphotectonic unit than the previous transect (Giambiagi et al., 2015). In the Principal Cordillera, ~50 km of shortening is estimated, while in Frontal Cordillera, it is ~15 km. At this latitude, the Precordillera is no longer present, but limited inversion in the Cuyo basin with less than 5 km of shortening can be observed (Giambiagi et al., 2015).

Finally, in the southern transect (D) at 35°S, the Frontal Cordillera is no longer present, and the Principal Cordillera comprises the Miocene to present magmatic arc and the Malargüe FTB. On the eastern slope of this structural province, a shortening of 27 km in the northern zone, decreasing to 10 km in the southern zone is estimated (Giambiagi et al., 2012).

The variation in shortening along the orogen, decreasing from north to south, is probably related to the change in the subduction angle, with greater shortening values related to the greater coupling between the slab and the upper plate in the horizontal subduction zone (Jordan et al., 1983 a; Ramos et al., 2002).

Alternatively, variations of shortening throughout the orogen could be related to changes in the composition of the basement and, consequently to its strength to deformation in contrast to the strength of the sedimentary rocks that cover it (Mescua et al., 2016). The highest shortening values correspond to those areas with the highest contrast in resistance between the basement and the sedimentary cover (Mescua et al., 2016).

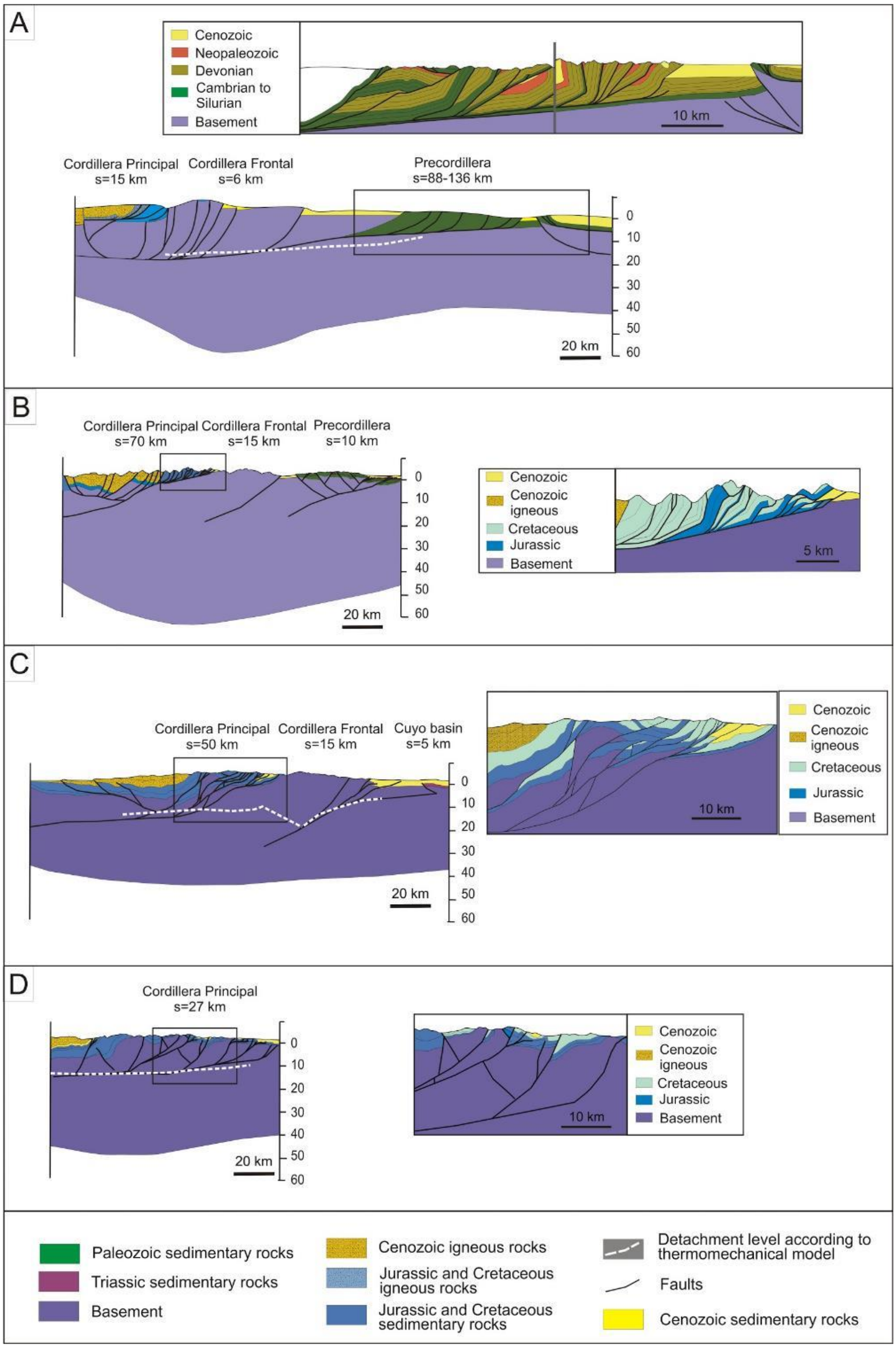

Figure 1.7: Cross sections between 30° and 36°S with shortening estimates (Mescua et al., 2016).

Chapter II

2. Miocene deformation in the orogenic front of the Malargüe fold-and-thrust belt (35º30'- 36° S): controls on the migration of magmatic and hydrocarbon fluids.

Resumen

La integración de observaciones de superficie y de subsuelo (perfilaje de pozos y sísmica de reflexión) del frente orogénico de la faja plegada y corrida de Malargüe nos permite estudiar su cinemática e interpretar el campo de esfuerzos local y su control sobre la migración de fluidos (magmáticos e hidrocarburíferos). Las fallas inversas corresponden a fallas, con orientación NNO, normales mesozoicas invertidas y a corrimientos cenozoicos de bajo ángulo, con rumbo N-S paralelas al orógeno. También se observan estructuras oblicuas con movimiento de rumbo. La actividad magmática en el área de estudio estuvo fuertemente controlada por el marco estructural y el campo de esfuerzos in-situ. Diques y filones capa miocenos fueron emplazados en relación a fallas de rumbo y fallas inversas, respectivamente. Proponemos una evolución estructural para la región de estudio desde una posición de antefosa (foredeep) en el Mioceno temprano a medio, pasando por un pico de deformación en el Mioceno tardío y finalmente una disminución en la deformación desde el Plioceno al presente. Nuestro modelo estructural sugiere que durante la evolución del frente de corrimientos, el estado de esfuerzos in-situ cambió de uno compresivo a de rumbo/compresivo favoreciendo el emplazamiento sincrónico de filones y diques. Esta alternancia entre estados de esfuerzos favorece la migración de hidrocarburos a través de corrimientos y también de fallas de rumbo sub-verticales. Este cambio entre ambos estados de esfuerzos está probablemente relacionado a valores similares del esfuerzo principal mínimo (σ3) y el intermedio (σ2) con un esfuerzo principal máximo (σ1) orientado E-O de acuerdo al vector de convergencia entre las placas Sudamericana y de Nazca.

Abstract

The integration of surface observations and sub-surface data (wellbore and seismic) from the orogenic front of the Malargüe fold-and-thrust belt allows us to study its kinematics, and to interpret the local stress field and its control over fluid (magmatic and hydrocarbon) migration. Reverse faults correspond to inverted NNW-striking Mesozoic normal faults and N-S striking Cenozoic low-angle thrusts parallel to the orogen. Oblique structures with strike-slip movement are also present. The magmatic activity in the study area was strongly controlled by this structural framework and the in-situ stress field. Miocene dykes and sills were emplaced in relation to strike-slip and reverse faults, respectively. We propose an evolution of the study region from a foredeep sector, in the early-middle Miocene, to a peak in deformation in the late Miocene, and finally a waning of deformation from the Pliocene to the present. Our structural model suggests that during the evolution of the thrust front, the in-situ stress field changed from a compressional to strike-slip/compressional stress field, favouring the synchronous emplacement of sills and dykes. This alternation of stress regimes favours hydrocarbon migration through both thrusts and subvertical strike-slip faults. This exchange between both stress regimes is likely related to the similar values of the minimum ($\sigma 3$) and intermediate ($\sigma 2$) principal stress with an E-W oriented maximum principal stress ($\sigma 1$) according to the plate convergence vector.

A version of this chapter was published in Tectonophysics as Barrionuevo, M., Giambiagi, L., Mescua, J., Suriano, J., de la Cal, H., Soto, J.L., Lossada, A.C., 2019. Miocene deformation in the orogenic front of the Malargüe fold-and-thrust belt (35°30'–36° S): Controls on the migration of magmatic and hydrocarbon fluids.

2.1 Introduction

Fluid migration in fold-and-thrust belts is a complex process with implications for magmatic activity and the emplacement of mineral resources, including economic mineralization and hydrocarbon deposits (Aydin, 2000; Haney et al., 2005; Cox, 2005). The development of fluid migration paths is closely linked to active faults and open fractures, in turn, controlled by the stress conditions (Barton et al., 1995). The Southern Central Andes provide a natural laboratory for the study of fault reactivation and its relationship with fluid migration during the ongoing migration of the foreland fold-and-thrust belts, due to the combination of inherited pre-Andean structures, magmatic arc activity and the development of the Mesozoic Neuquén basin where one of the main hydrocarbon systems in Argentina is located (Boll et al., 2014, and references therein).

The Malargüe fold-and-thrust belt (Fig. 2.1) extends between 34º and 36ºS in the normal subduction (i.e. steeper subduction angle compared to subhorizontal or flat-slab zone) segment of the Southern Central Andes, where the Nazca plate subducts beneath the South American plate with an angle of 30° (Barazangi and Isacks, 1976). This area was part of the Neuquén basin, an extensional retroarc basin developed during the Mesozoic (Uliana and Legarreta, 1993). The initial setup of the basin consisted on normal fault-bounded depocenters developed as a result of extension from the Late Triassic to the Early Jurassic (Vergani et al., 1995) during the synrift stage (Fig. 2.2). These depocenters, filled with clastic, volcaniclastic and volcanic deposits, were initially isolated and were linked as the extension progressed (Manceda and Figueroa, 1995). The master faults that bounded the depocenters have different polarities and orientations, with NNW and NNE strikes (Giambiagi et al., 2009a).

The Malargüe fold-and-thrust belt has a basement-involved structural style (Kozlowski et al., 1993; Manceda and Figueroa, 1995; Giampaoli et al., 2002; Silvestro et al., 2005, Giambiagi et al., 2009b; Silvestro and Atencio, 2009; Turienzo et al., 2012). Different structural models have been proposed, some related to inversion of Mesozoic normal faults (Manceda and Figueroa 1995; Uliana et al., 1995; among others), others to the development of new thrusts during Andean contraction (Dimieri, 1997; Turienzo, 2010), and finally “hybrid” models which include both inversion and new faults (Yagupsky et al., 2008; Giambiagi et al., 2009b; Orts et al., 2012; Mescua et al., 2014; Branellec et al. 2015a, 2016; Fuentes et al., 2016; Seoane Borracer et al., 2018; Granado & Ruh, 2019).

Here we present the results from a structural study in the orogenic front of the Southern Central Andes, between 35º30’ and 36ºS, where the Andean orogeny was superimposed to the previous structures developed during the opening of the Mesozoic Neuquén basin. We focus our analysis in the Agua Botada oil field (Fig. 2.1), where we integrate surface and subsurface information into a 3D structural model.

From these observations, we address the subject of: (i) the tectonic inversion of pre-existing faults, (ii) the control by the local stress field and active structures over the emplacement of sills and dykes and over fluid migration, and (iii) how this control varies during the advance of the thrust front.

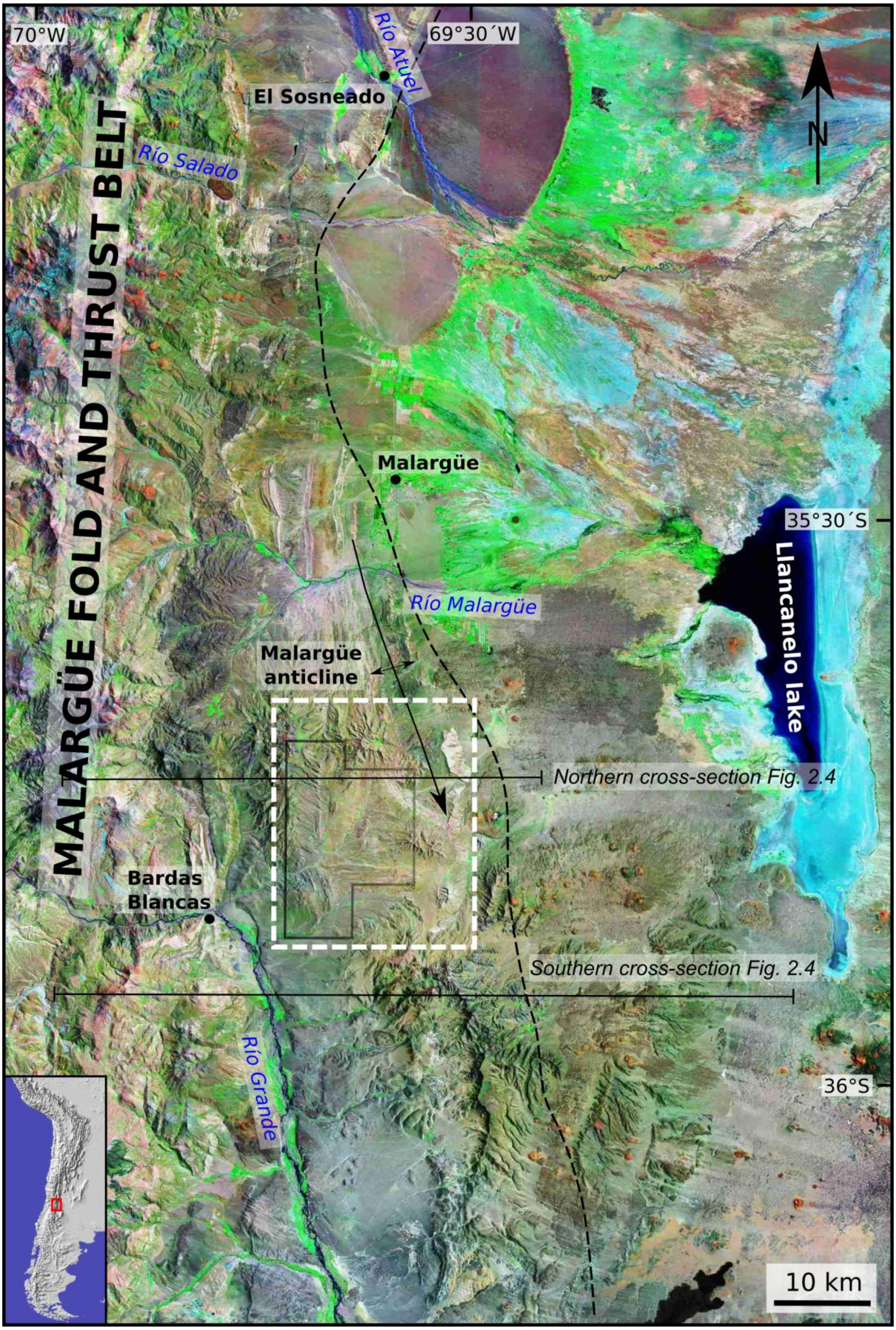

Figure 2.1: Location of the study area (white dashed rectangle), including the Agua Botada oil field (black continuous polygon) and adjacent areas, with indication of the regional balanced cross-sections shown in Fig. 2.4. Map base is a LANDSAT7+ satellite image (RGB741 band combination).

2.2 Geological setting

2.2.1 The northern Neuquén basin

During the Late Triassic to Early Jurassic, extension along the western South American continental margin resulted in the opening of the Neuquén basin (Uliana et al., 1989; Vergani et al., 1995; Franzese and Spalletti, 2001). The basement of this basin, composed mainly of Permian to Triassic volcanic and plutonic rocks of the Choiyoi Group, was affected by structures inherited from previous tectonic stages (Mosquera and Ramos,

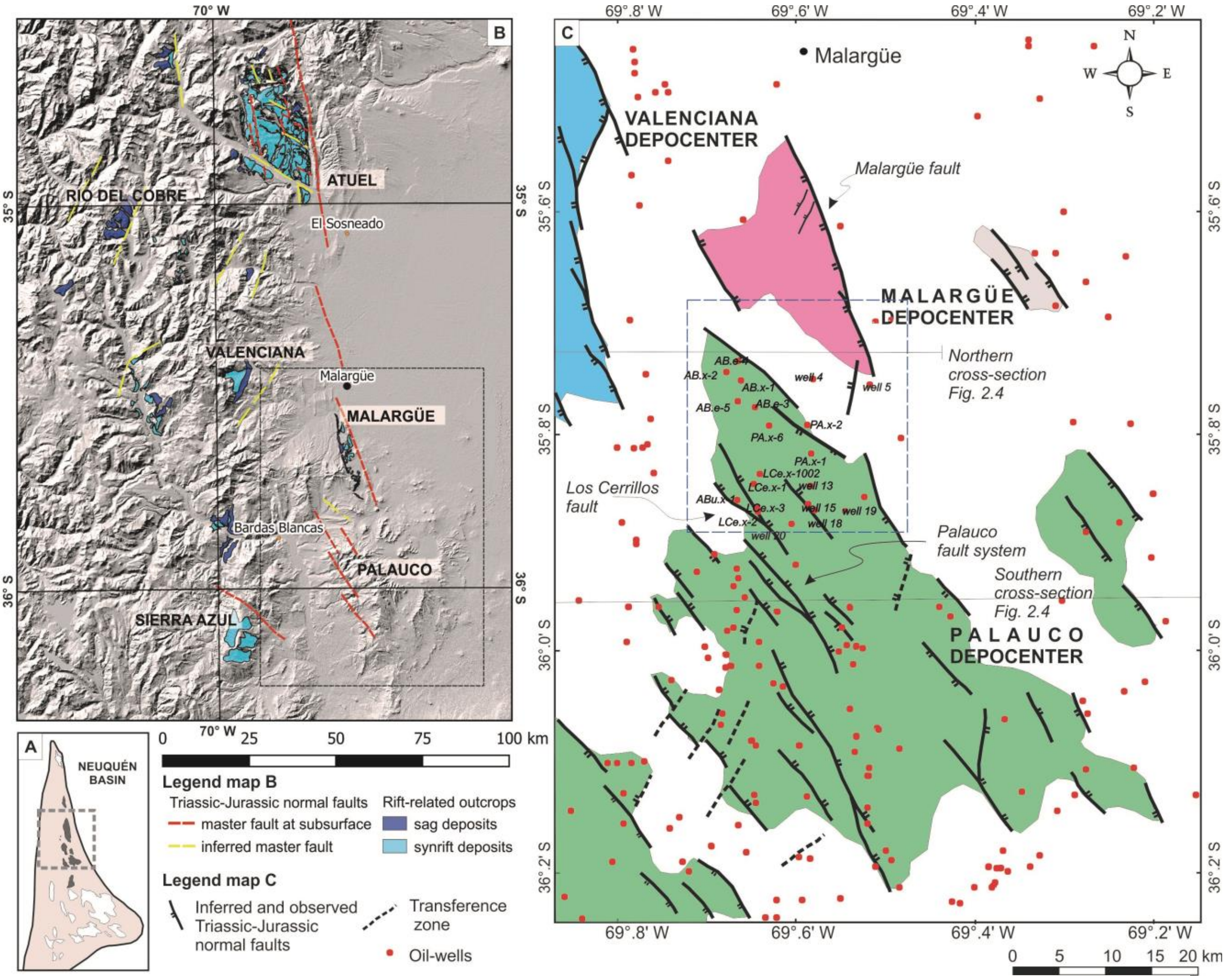

Figure 2.2: A) Areal extension of the Neuquén basin (grey square shows the location of fig 2.2B). B) Map showing the master faults that bounded the Atuel, Río del Cobre, Valenciana, Malargüe, Palauco and Sierra Azul depocenters) of the Neuquén basin with indication of rift-related deposits (modified from Bechis et al., in press). C) Detailed map of the Valenciana (light blue area), Malargüe (pink area) and Palauco (green area) depocenters with the distribution of the Upper Triassic-Lower Jurassic synrift deposits and the main normal faults inferred from subsurface and surface data. The Agua Botada area corresponds to the blue dashed rectangle between Malargüe and Palauco depocenters (modified from Giambiagi et al., 2009a).

2006; Kleiman and Japas, 2009; Bechis et al., 2014). Northeast of the study area, structures related to the Permian San Rafael orogeny are NNW- to NW-striking faults (Kleiman and Japas, 2009).

The Agua Botada area (Figs. 2.1, 2.2) is located in the northern part of this oil-bearing basin, which presents an almost continuous record of up to 7,000 m of Late Triassic to Neogene marine and continental deposits representing different tectonic scenarios from a backarc extensional basin followed by a postextensional setting and finally a retroarc foreland basin (Fig. 2.3, Uliana et al., 1989; Legarreta and Gulisano, 1989; Vergani et al., 1995; Legarreta and Uliana, 1999). In this part, the basin is composed of several NNE- to NNW-trending depocenters, which are from north to south: Atuel, Malargüe, Valenciana, Río del Cobre, Palauco and Sierra Azul (Fig. 2.2B). The Agua Botada oil field (Figs. 2.1, 2.2) is located between the Malargüe and Palauco depocenters (Fig. 2.2C).

The Malargüe depocenter developed at the beginning of extension in the Neuquén basin, affecting the basement, and it is filled with synrift clastic and volcaniclastic, braided-river plain deposits interbedded with lacustrine black shales grouped in the Upper Triassic-Lower Jurassic Pre-Cuyo Cycle (Fig. 2.3, Spalletti, 1997; Artabe et al., 1998; Buchanan et al., 2017). The depocenter was controlled by a NNW-striking, west dipping, master fault called Malargüe fault (Manceda and Figueroa, 1995; Silvestro et al., 2005; Giambiagi et al., 2009a; Fig. 2.2B).

The Palauco depocenter is filled up with volcaniclastic deposits of the Upper Triassic-Lower Jurassic Pre-Cuyo Cycle (Fig. 2.3, Gulisano, 1981; Legarreta and Gulisano, 1989) and it is affected by two master faults controlling the accommodation, the NNW-striking, ENE-dipping, previously proposed Palauco fault (Manceda and Figueroa, 1995; Giambiagi et al., 2009a) and the Los Cerrillos fault (Fig. 2.2C). These previously isolated depocenters were linked during the Middle Jurassic sag phase (Uliana and Biddle, 1988; Uliana and Legarreta, 1993; Vergani et al., 1995).

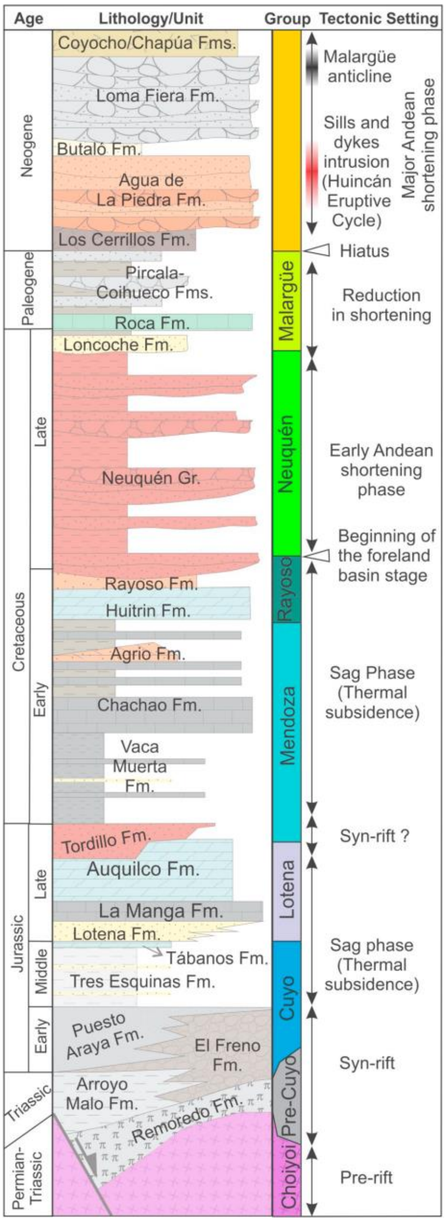

Figure 2.3: Stratigraphic chart showing the main tectonic phases of the Neuquén Basin and Malargüe fold-and-thrust belt (based on Giampaoli et al., 2002; Giambiagi et al., 2008; Mescua et al., 2014; Horton et al., 2016).

During the Middle Jurassic and Early Cretaceous a thick pile of evaporitic, calcareous and clastic marine and continental sedimentary rocks belonging to the Cuyo, Lotena, Mendoza and Rayoso Groups were deposited (Fig. 2.3). A brief episode of extension occurred during the deposition of the Upper Jurassic Tordillo Formation red sandstones at this latitude, subsequently followed by another sag stage during the Early Cretaceous (Fig. 2.3, Mescua et al., 2014). In the Late Cretaceous, coarse continental deposits belonging to the Neuquén Group (Uliana and Legarreta, 1993; Vergani et al., 1995) represent the foreland basin stage related to the beginning of the Andean shortening.

The Oxfordian Auquilco and Aptian-Albian Huitrín anhydrite units (Fig. 2.3) are the main detachment levels for thin-skinned thrust sheets (Kozlowski et al., 1993), and also act as seals for hydrocarbon accumulations (Cobbold and Rossello, 2003). The Neocomian black shales of the Vaca Muerta Formation, which are the main source-rock of the basin, are also an important detachment level for thrusts (Kozlowski et al., 1993).

2.2.2 The Malargüe fold and thrust belt

Deformation of the Malargüe fold-and-thrust belt started in the Late Cretaceous in its western sector (Tunik et al., 2010; Mescua et al., 2013; Balgord and Carrapa, 2016; Fennell et al., 2017). The study area is located in the foredeep sector of the Cretaceous foreland basin, filled with up to 1.5 km thick continental fluvial deposits of the Neuquén Group (Uliana and Legarreta, 1993; Balgord and Carrapa, 2016). The sedimentation rate diminished during the deposition of mudstones and sandstones of the Malargüe Group in the Paleocene-Eocene, probably due to the cessation or reduction in shortening (Legarreta and Gulisano, 1989; Horton et al., 2016), followed by a non-deposition period with a stratigraphical hiatus spanning between 40 and 20 Ma (Horton et al., 2016). Shortening and uplift resumed in the middle to late Miocene (Giambiagi et al., 2003a, b, 2008, 2015; Spagnuolo et al., 2012; Orts et al., 2012, Boll et al., 2014; Fuentes et al., 2016; Horton et al., 2016). During this Miocene shortening phase, predominantly N-striking basement thrusts and reverse faults were active and transferred shortening to the Neuquén basin cover (Manceda and Figueroa, 1995; Uliana et al., 1995; Zapata et al., 1999; Giambiagi et al., 2003a, 2008). The foreland basin related to this orogenic event was filled with 1.5-2 km-thick, clastic rocks of the Agua de la Piedra and Butaló Formations (approx. 16-10 Ma; Silvestro and Atencio, 2009) and volcaniclastic successions of the Loma Fiera Formation (approx. 11-8 Ma; Silvestro and Atencio, 2009). In the northern sector of the study area, a forelandward progression of the deformation has been

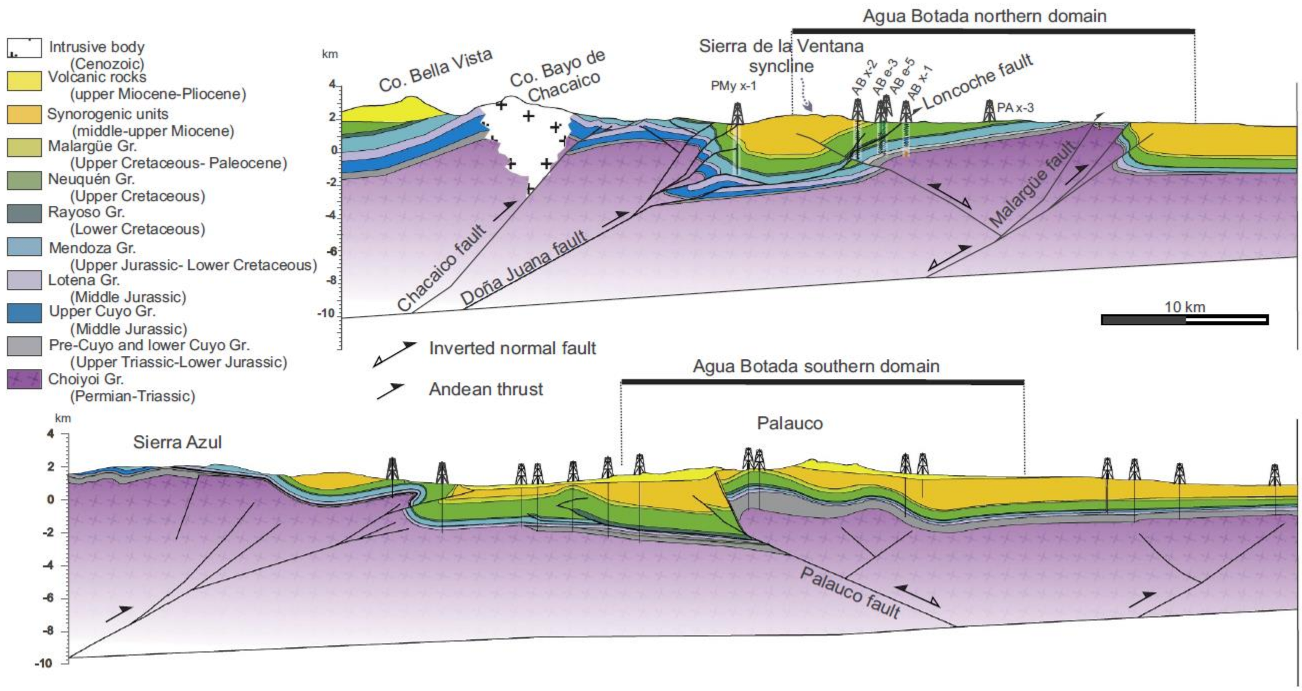

Figure 2.4: Regional balanced cross-sections, modified from Giambiagi et al. (2009b). See location in figure 2.1. The northern section cuts the Agua Botada northern domain. In this domain, the Malargüe fault (and fault-related anticline) is the main basement structure. The southern section crosses close to (~5 km) the Agua Botada southern domain, characterized by the inversion of a Triassic-Jurassic normal fault, the Palauco west-directed fault.

determined, with deformation at the orogenic front represented by the Malargüe anticline (Figs. 2.4, 2.5) since 8-7 Ma (Silvestro et al., 2005). In contrast, in the southern part of the study area, the easternmost structures of the Sierra the Palauco (Fig. 2.4) were uplifted early in the history of the belt (17 Ma, Silvestro and Atencio, 2009) and experienced a reactivation phase between 11-8 Ma, as recorded by angular unconformities in the synorogenic volcaniclastic deposits (Silvestro and Atencio, 2009).

Furthermore, the northern and southern sectors are also differentiated by the vergence of the main structures (Fig. 2.4). The northern and southern sectors are characterized by eastern and western vergence, respectively, which seems to indicate that the Andean structure has been significantly controlled by the inherited geometry of the Late Triassic to Early Jurassic Neuquén extensional basin (Fig. 2.2C).

Active (Pliocene-recent) N-striking reverse faults and oblique strike-slip faults (Spacapan et al., 2016; Stein et al., 2018; Mescua et al., 2019) are documented in the orogenic front of the Malargüe fold-and-thrust belt.

2.2.3 Magmatic activity

The magmatic activity in the eastern Malargüe fold-and-thrust belt has been separated into two cycles: the late Oligocene to middle Miocene Molle Eruptive Cycle and the middle Miocene to Pliocene Huincán Eruptive Cycle (Groeber, 1946; Nullo et al., 2002, Fig. 2.3). The first one associated with retroarc volcanism and the latter to arc volcanism (Bettini, 1982; Baldauf, 1997; Nullo et al., 2002; Sruoga et al., 2009; Combina and Nullo, 2011; Litvak et al., 2015). Both cycles correspond to predominantly basaltic and andesitic magmatism, represented by many lava flow sequences and subvolcanic bodies such as sills, dykes and laccoliths (Baldauf, 1997; Combina and Nullo, 2011; Spacapan et al., 2016, 2017). The Coyocho Basalt (Fig. 2.3), corresponding to the final part of the Huincán Cycle (6.7 to 2.3 Ma, Silvestro and Atencio, 2009), unconformably covers the deformed Neogene strata, cropping out mainly to the west of our study area. The youngest volcanism is located towards the east, in the Quaternary Payenia Basaltic Province (Bermúdez et al., 1993; Ramos and Folguera, 2011).

The Neogene intrusives emplaced in the Mesozoic source rocks are one of the main fractured reservoirs in the hydrocarbon fields in this sector of the basin (Schiuma, 1994; Rodriguez Monreal et al., 2009; Witte et al., 2012; Schiuma and Llambias, 2014; Spacapan et al., 2018). Furthermore, the source rock maturation due to the thermal impact of these intrusives in the Río Grande area, south of Agua Botada, was modelled by Spacapan et al. (2018) suggesting that two pulses of hydrocarbon generation were triggered by the two magmatic cycles mentioned above.

In the Agua Botada sector, Cenozoic intrusives correspond to sills, subvolcanic bodies and dykes with predominantly intermediate compositions (Schiuma, 1994). Available K/Ar ages on dykes in the study area provided early to middle Miocene ages (17.3±0.8 and 14.4±0.7 Ma, Valencio et al., 1969).

Andesitic and basaltic andesite sills are predominantly emplaced in units with fine grained intervals within the study area, particularly in the black shales of the Vaca Muerta and Agrio Formations (Schiuma, 1994; Rodriguez Monreal et al., 2009; Spacapan et al., 2016a, 2018). Scapacan et al. (2016a) studied the mechanism of intrusion of sills in this area, based on detailed observations at Cuesta del Chihuido (Fig. 2.5). They propose a two-stage intrusion history, where magma fingers push away the host rock in the initial stage, followed by brittle and ductile inelastic deformation of the strata as the sill propagates. Their results are in agreement with the viscous indenter model (Donadieu and Merle, 1998; Mathieu et al., 2008), and underscore the role of strength contrast between thin and thick layers in the Agrio Formation with intrusions confined to the thin and weak layers.

Miocene to Quaternary andesitic and basaltic subvertical dykes are abundant in the easternmost Malargüe fold-and-thrust belt and in the Payenia volcanic province developed to the east, where volcano alignments of several tens of kms are interpreted as the surface expression of dykes in depth (Bermúdez and Delpino, 1989; Spacapan et al., 2016b). The most common orientation of dykes is NW; based on this, igneous intrusion in the area has been interpreted as controlled by the presence of pre-existing NW-striking Paleozoic lineaments (Bermúdez and Delpino, 1989; Llambías et al., 2010; Spacapan et al., 2016b), namely strike-slip faults observed in the basement north of the study area (e.g. Kleiman and Japas, 2009). A secondary E-W dyke trend has been interpreted as opening parallel to the maximum horizontal stress (Hernando et al., 2014; Scapacan et al., 2016b). Two of the NW-trending dykes within our study area, at Cuesta del Chihuido, were studied in detail by Spacapan et al. (2016b). The observations made by these authors underscore the association of the dykes with strike-slip faults, which they interpret as pre-existing structures without activity during or after dyke emplacement. We will discuss this interpretation in the light of our own observations below.

2.3 Methods

Our methodology consists of structural mapping of the Agua Botada area (Figs. 2.1, 2.2) based on fieldwork and satellite image interpretation, structural interpretation of 3D seismic data, analysis of oil-well logs, and collection of fault-slip kinematic data. All the data were integrated into a structural model, based on previous chronological constraints (Silvestro and Atencio, 2009, Arcila Gallego, 2010), results of the kinematic analysis of fault-slip data, balanced cross-section forward modeling, pseudo-3D structural model construction, and interpretation of Miocene to Quaternary in-situ stress fields.

Wellbore data available for the study area (Fig. 2.5) was analysed to determine thickness variations of units and to locate faults.

Newly acquired 3D seismic data was provided by the company ROCH SA. The seismic vibroseis survey was carried out in 2017 covering 107 km2 with a bin size of 25 m x 25 m.

The source-point intervals were of 50 m and source line distances of 400 m oriented N-S while the receiver array consisted of W-E oriented lines spaced at 400 m each with receiver point intervals of 50 m; this results in a nominal fold of 64. In each vibrator point (VP) three vibroseis were placed and the source density was 50 VP/km2. The data was migrated through pre-stack time migration.

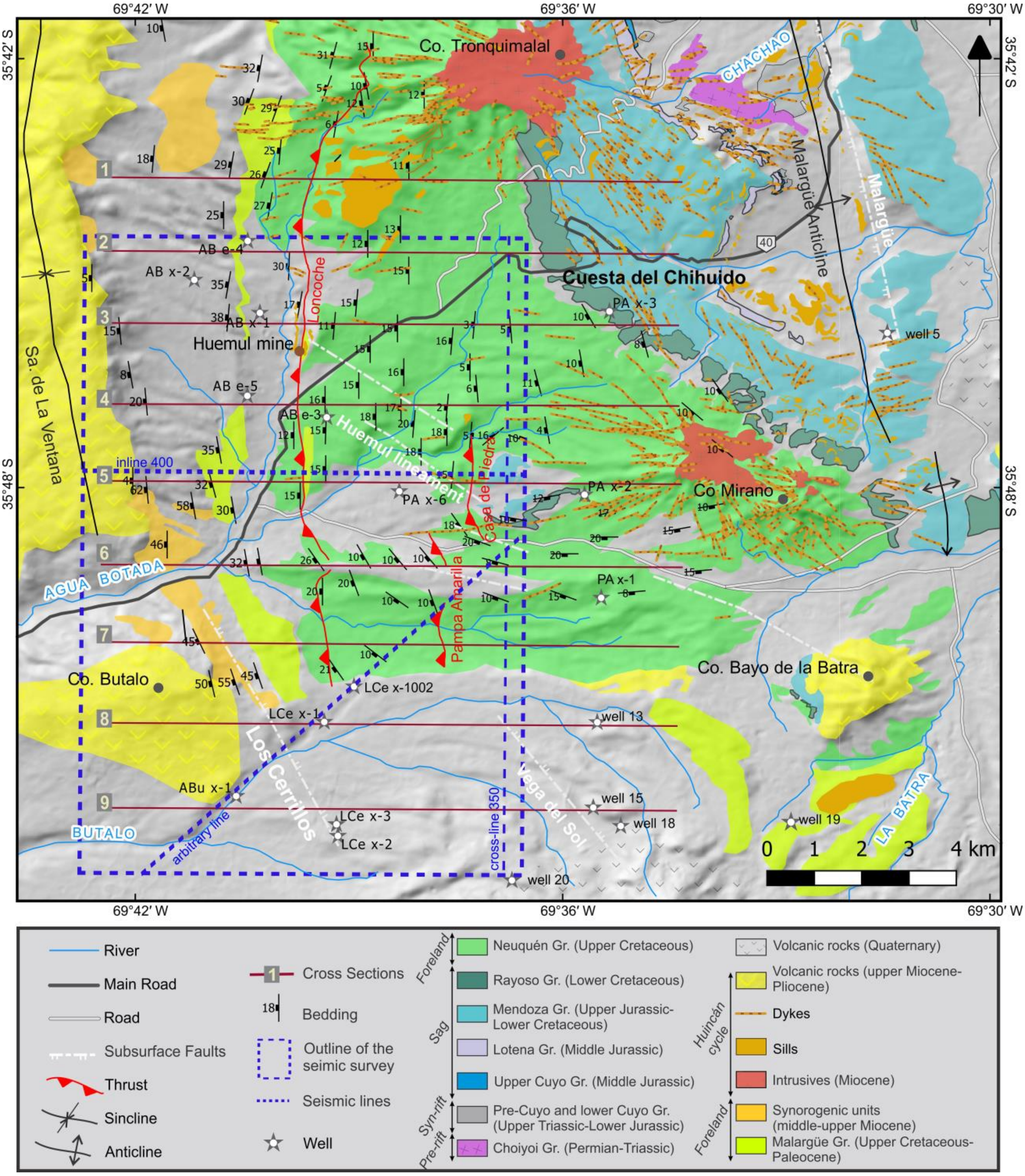

Figure 2.5: Main geologic units and structures in the Agua Botada area. Based on YPF, 1976; Nullo et al., 2005; Arcila Gallego, 2010 and own data

This 3D seismic data was interpreted using the free software OpendTect 6.4.2. Formation tops recognized in wellbore data were used to pick reflectors and trace unit contacts in the subsurface. The main faults were recognized in the seismic data through the structural interpretation of 2D lines and time slices. Finally, we interpolated these lines to create 3D surfaces which provided us the structural array of the area as a constraint for the kinematic modeling. The combination of fault geometries, thickness variations and stratal geometry of the Late Triassic-Early Jurassic synrift units was used to differentiate reactivated pre-Andean faults and Andean thrusts in the structural model.

Selected cross-sections were forward-modelled using 2D area-balancing techniques with the algorithms provided by MOVE© to obtain the best geometric match between the natural example and the model. Fault-parallel-flow, inclined shear or trishear were used depending on the geometry of the fold-related-fault. The nine cross-sections were the base for the construction of a pseudo-3D model, built using the interpolation tools available in the MOVE© software.

During fieldwork, the orientation of dykes and sills was measured, and their relationship with structures assessed. Fault-slip data of outcrop-scale faults affecting the intrusions were obtained from the measurement of mineral fibers on fault planes, Riedel structures, and lineations coupled with marker bed displacements. In addition, Google Earth satellite images were used to determine the orientations and length of dykes.

Fault-slip data was analysed using the FaultKinWin software (Allmendinger et al., 2012). This program determines shortening and extension axes for each fault datum and uses Linked Bingham statistics to define the main deformation axes for the whole fault population.

2.4 Results

2.4.1 Surface structural mapping

The Agua Botada area (Fig. 2.5) is located in the backlimb of the Malargüe anticline, a fault-related fold interpreted as the result of the inversion of a Mesozoic normal fault (Silvestro and Atencio, 2009; Giambiagi et al., 2009b; Branellec et al., 2016). This fault was bounding the Malargüe depocenter during the Late Triassic (Manceda and Figueroa, 1995). Fault inversion took place in the late Miocene (7 Ma to recent, Silvestro et al., 2005) with positive reactivation of the lower reaches of the listric normal fault and the development of a short-cut fault in the steeply-dipping upper reaches of the fault

(Giambiagi et al., 2009b). The NNW-striking anticline is an asymmetric fold with a steep to overturned forelimb and a subdued backlimb. Basement rocks of the Permian-Triassic Choiyoi Group are exposed in the core of this structure; while to the west, in the backlimb, Upper Triassic to Upper Cretaceous sedimentary and volcaniclastic deposits corresponding to the Pre-Cuyo, Cuyo, Mendoza, Rayoso and Neuquén Groups are

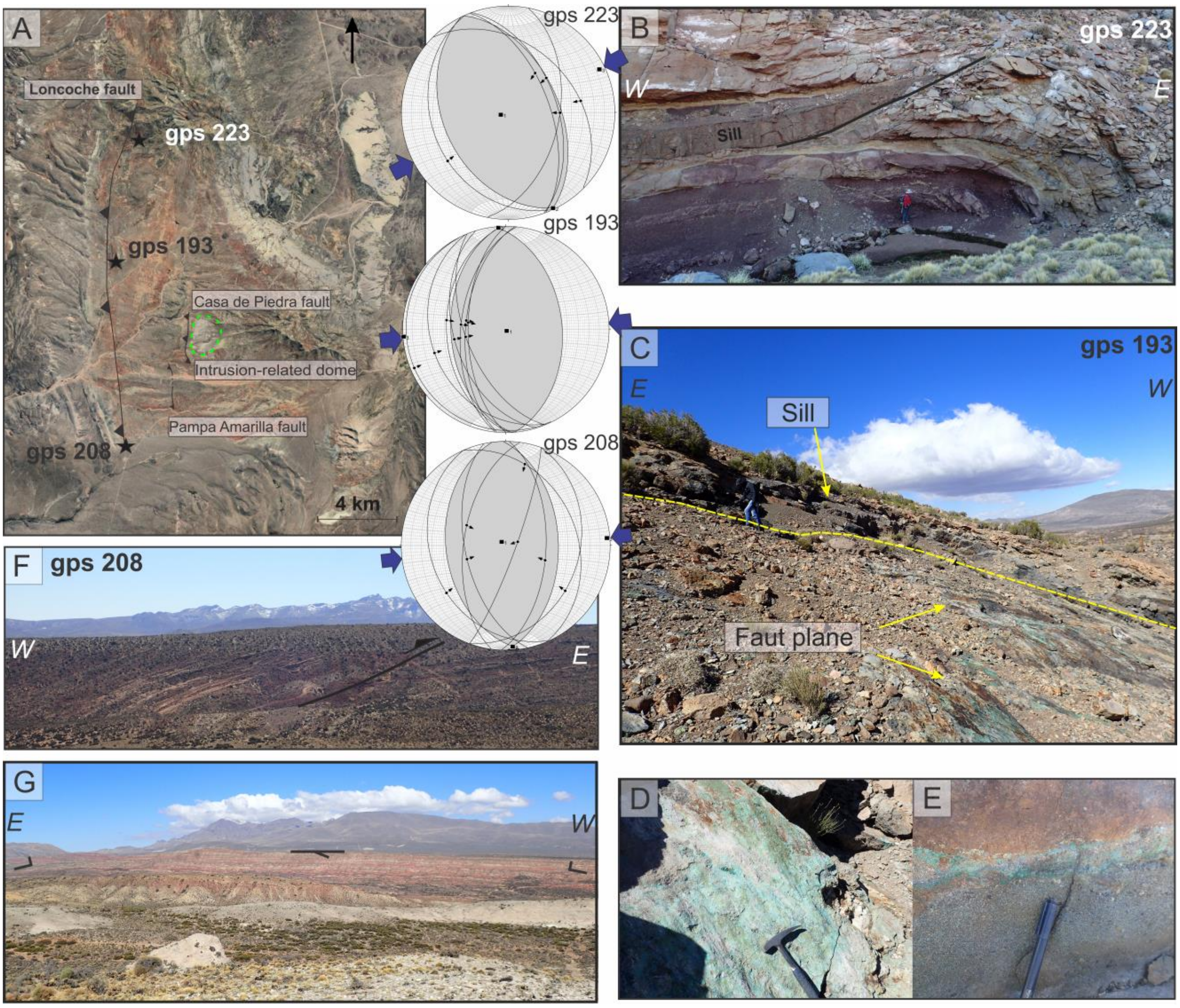

Figure 2.6: A) Aerial image with indication of the Loncoche, Casa de Piedra and Pampa Amarilla faults and the intrusion-related dome. Fault kinematic data displayed in equal area, lower hemisphere stereonets from stations 193, 208 and 223. The striae and sense of movement is represented by small arrows at the fault plane; the shortening axis is shown as blue arrows. B) Station gps 223 (35°43'23.20"S 69°39'9.84"W) where a sheet intrusion probably intrudes a fault splay developed in the Neuquén Group rocks; an alternative is that the fault ramped up at the intrusion tip. C) Station gps 193 (35°45'57.95"S 69°39'38.11"W) near the uranium mine site. Notice a sill intruded concordantly to the fault plane where patinas of secondary minerals of copper and uranium cover the fractures. D) Detail of patinas and striae from Fig. 2.6C. E) Oil-impregnated sandstones of the Neuquén Group with secondary copper and uranium minerals (e.g. malachite, covellite, autunite). F) Station gps 208 (35°50'39.78"S 69°39'24.07"W), the Neuquén Group strata is tilted in the hanging-wall of the Loncoche fault. G) Photo (35°48'S 69°36'W) looking south from the core of the intrusion-related dome that probably causes the buttressing-related Casa de Piedra fault. Notice the radial dipping of the Neuquén Group redbeds and compare it with the dips plotted in the map (Fig. 2.5) that show the radial pattern.

cropping out and gently-dipping (i.e., 10º-20º) to the west.

The Loncoche fault (Figs. 2.5, 2.6) is a NS-trending and E-directed thrust developed in the Neuquén basin cover and probably detached along the Jurassic Auquilco Formation evaporites (Fig. 2.3). In the northern part of the study area (Fig. 2.6A), the Loncoche thrust folds the Upper Cretaceous Neuquén Group and the Neogene strata, including the approx. 10 Ma Loma Fiera deposits, in its hanging-wall. A sill intrudes a fault splay tapering towards the hinge of the fold (Fig. 2.6B). In the central zone (Fig. 2.6C), there is an old uranium mine site, called Mina Huemul, associated with the Loncoche fault zone. Here we report a sheet intrusion, parallel to and in contact with the fault plane. There are secondary copper and uranium minerals precipitated as patinas as well as hydrocarbon traces in fault-parallel fractures, (Fig. 2.6D, E). In the southern area, the Loncoche fault cuts the Upper Cretaceous Neuquén Group strata (Fig. 2.6F); further south its displacement decreases and the Loncoche fault is no longer recognized in the field nor in the seismic data.

The Casa de Piedra (YPF, 1976) and Pampa Amarilla faults are minor N-striking, E-directed thin-skinned structures recognized locally, with lengths <3 km (Figs. 2.5, 2.6). The Pampa Amarilla thrust is probably a splay of the Loncoche thrust that takes over part of the shortening lost by this structure in the south of the study area. The Casa de Piedra thrust is developed exclusively west of an intrusive body recognized in the seismic data (Figs. 2.7C, 2.8) and as a dome in the surface (Figs. 2.5, 2.6). We interpret that the fault is the result of buttressing against the intrusive (Figs. 2.7C, 2.8).

2.4.2 Subsurface structure

Interpretation of subsurface data (seismic and wells; Figs. 2.7, 2.8, 2.10, Table 2.1) allowed us to determine the main structures at depth, linking them to surface geology. The reverse, NNW-striking, west-verging Los Cerrillos fault (Fig. 2.9) was already recognized by Giambiagi et al. (2009b) as an inverted normal fault, which forms part of the Palauco fault system (Fig. 2.2). It affects the basement and the Mesozoic deposits (Fig. 2.9), but it is covered by Quaternary deposits at surface. Wellbore data indicates that the Neuquén synrift basin stratigraphy shows important changes in thickness across the Los Cerrillos fault. In more detail, drill holes LCe x-1, LCe x-1002 and well 20 (Figs. 2.5, 2.8, 2.9 and Table 2.1) ended in the Upper Triassic-Lower Jurassic Pre-Cuyo synrift deposits after more than >400 m (reaching 826 m in well 20) of these rocks, but immediately to the west the drill hole ABu x-1 (Table 2.1) ended in the Permian-Triassic Choiyoi Group which is overlain by ~200 m of the Pre-Cuyo rocks.

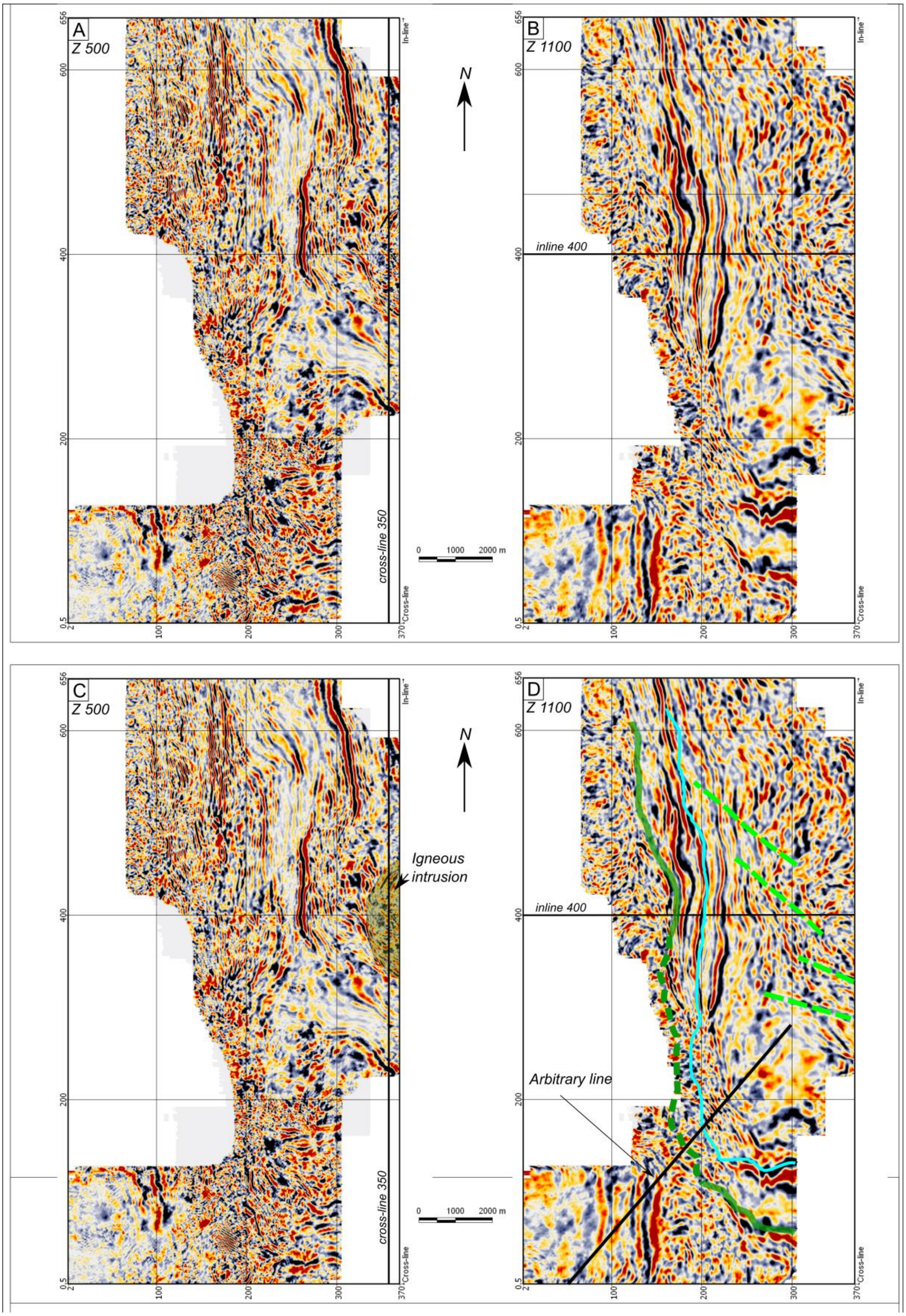

Figure 2.7: A) Uninterpreted time slice at z=500 ms. B) Uninterpreted time slice at z=1100 ms. C) Interpreted time slice at z=500 ms, the reflectors in the highlighted area are concentric to a high-noised core zone. This coincides in surface with the domed zone marked in the aerial image of Fig. 2.6A and the outcrops shown in Fig. 2.6G that we interpret as caused by an igneous intrusive in subsurface. D) Interpreted time slice at z=1100 ms, where a NW structure, called here Huemul lineament and other oblique structures are shown. Green and light blue lines indicate the Huitrin and Chachao formations top respectively. The cross-line and inline shown in Fig. 2.8 and the arbitrary line shown in Fig. 2.9 are marked.

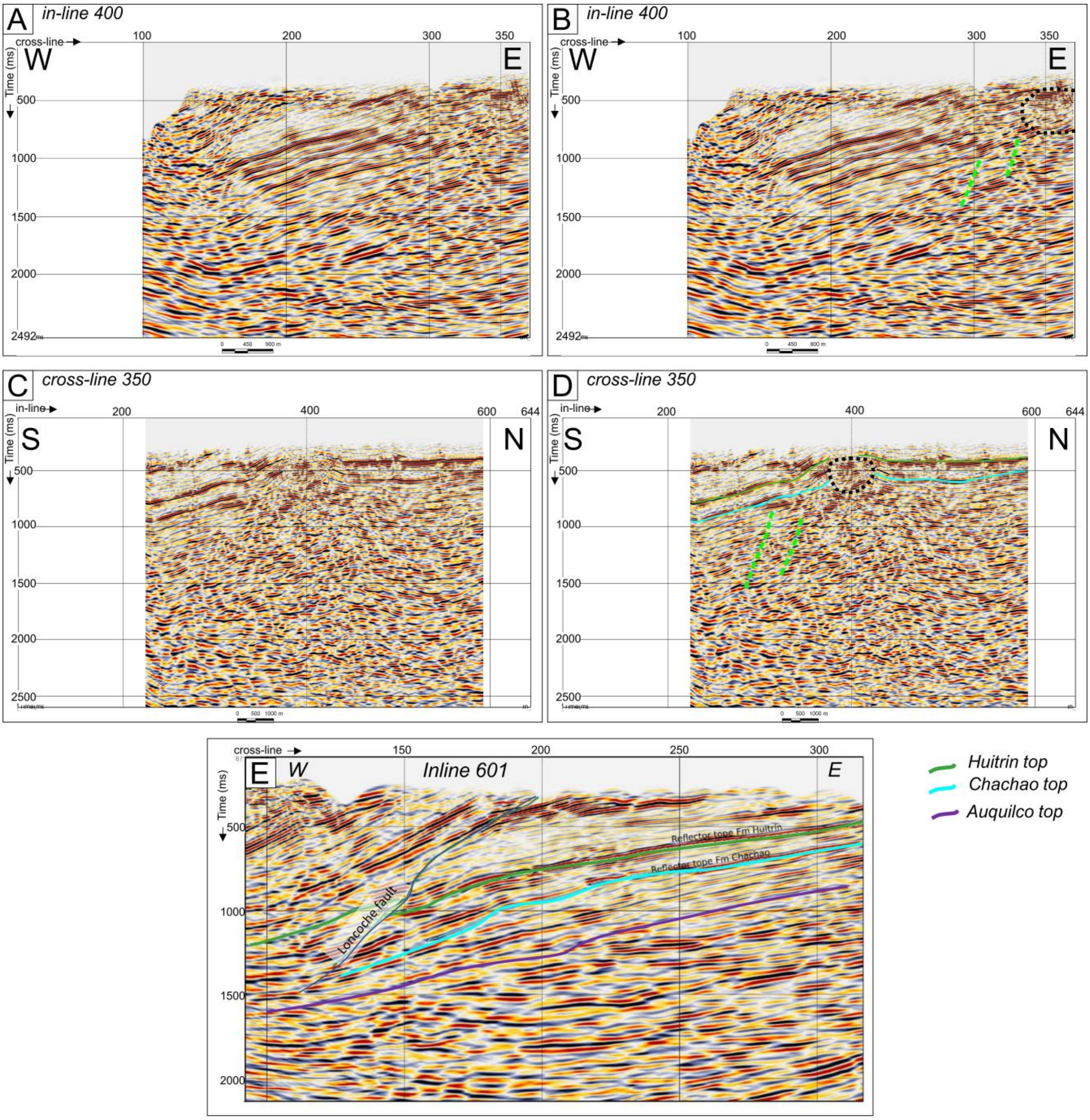

Figure 2.8 A) In-line 400 uninterpreted. B) In-line 400 showing the Huemul lineament (green dashed lines) and the intrusive (black dashed line). C) Cross-line 350 uninterpreted. D) Cross-line 350 showing the intrusive and the deformation it causes to the host rock. In green dashed lines the Huemul lineament is marked. E) In-line 601 showing the Loncoche thin-skinned fault cutting the sedimentary sequence of the Neuquén basin and detached along the Auquilco evaporites. Green, light blue and purple continuous lines indicate the Huitrin, Chachao and Auquilco formations top respectively.

The wedge geometry of synrift strata east of the Los Cerrillos fault (Fig. 2.9) suggests a half-graben controlled by this fault. We interpret that this fault was a synrift normal fault inverted during the Miocene. East of the Los Cerrillos fault, a minor blind structure, the Vega del Sol fault (Fig. 2.5), with similar attitude was recognized (YPF, 1995).

The subsurface expression of the Loncoche, Casa de Piedra and Pampa Amarilla faults could be determined from the seismic data. The Loncoche fault (Fig. 2.8E) affects the Neuquén Group in the surface and the shales of the Mendoza Group in subsurface, probably detaching along the evaporites of the Auquilco Formation towards the west. It is composed of a principal fault and a series of minor splays with moderate angles. The Pampa Amarilla and Casa de Piedra thrusts are affecting the upper section of the Mendoza Group and are probably detached along the shales of the Vaca Muerta Formation, though this is not clearly recognized in the seismic data. The dome located east of the Casa de Piedra fault is observed in the seismic data (Fig. 2.8) due to the outward radial dipping of the reflectors and a high-noise core. The PA x-2 wellbore, located in the eastern part of the dome, between Cerro Mirano and the Casa de Piedra fault (Fig. 2.5) cuts through >170 m of andesites from a depth of 416 m to the end of hole. We interpret that intrusion (named here Pampa Amarilla intrusive) produced doming of the Neuquén basin strata and that the Casa de Piedra fault is the result of buttressing against this rigid dome.

Time slices of the seismic data suggest that WNW- and NW-striking, subvertical structures are common in the northern sector of the study area, (Figs. 2.7, 2.8). The most important of these structures, named here Huemul lineament, is aligned with the Huemul mine and the Pampa Amarilla intrusive body (Figs. 2.5, 2.7).

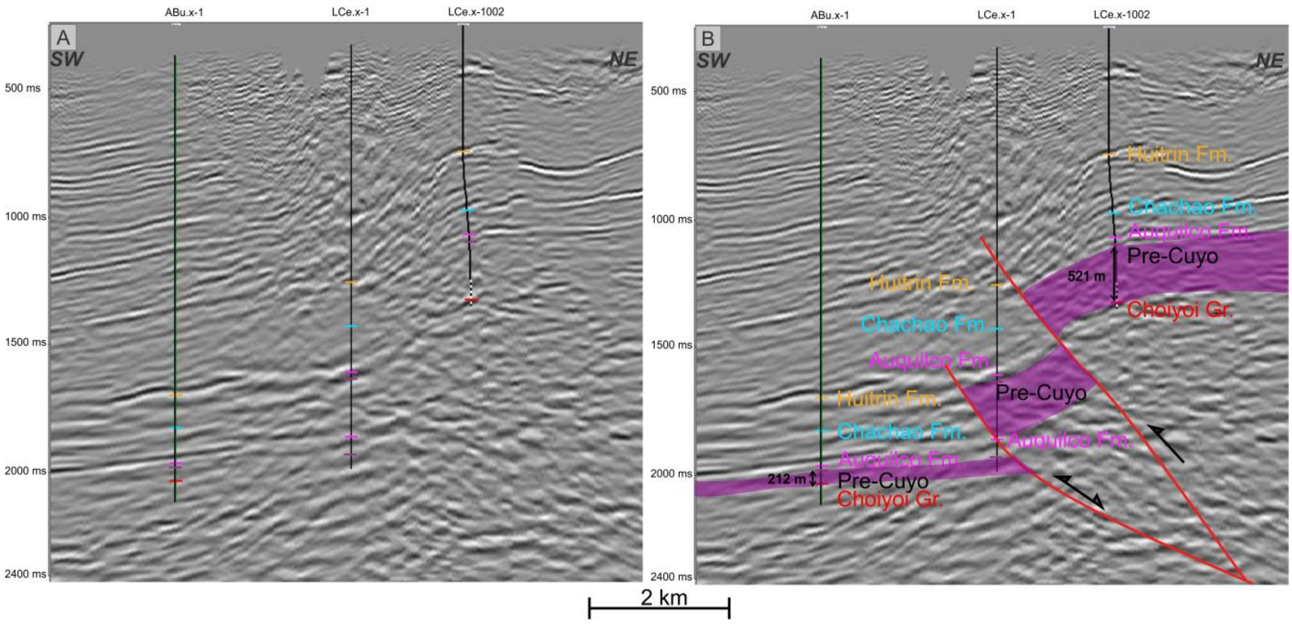

Figure 2.9: A) Uninterpreted arbitrary line oriented NE-SW (see map Fig. 2.5 and Fig 2.7D for location). B) Interpreted arbitrary line showing Los Cerrillos inverted normal fault that controlled the synrift thickness of Upper Triassic-Lower Jurassic Pre-Cuyo rocks. We interpret the uppermost fault as a hanging wall bypass.

Fm top depth	ABu.x-1	Fm top depth	LCe.x-1	Fm top depth	LCe.x-1002
922	Malargüe	1693	Huitrín	550	Rayoso
1160	Neuquén	1902	Agrio	659	Huitrín
2275	Huitrín	2191	Chachao	709	Agrio
2321	Agrio	2246	Vaca Muerta	1070	Chachao
2572	Vaca Muerta	2502	Auquilco	1112	Vaca Muerta
2888	Auquilco	2526	Pre-Cuyo	1296	Auquilco
2910	Pre-Cuyo	2944	Auquilco	1304	Lotena
3122	Choiyoi	3061	Pre-Cuyo	1330	Pre-Cuyo
3247	end of hole	3156	end of hole	1851	Choiyoi
				1901	end of hole
212	*thickness (m) of Pre-Cuyo*	*418*	*thickness (m) of Pre-Cuyo (minimum)*	*521*	*thickness (m) of Pre-Cuyo*

Table 2.1: The stratigraphy cut through the drill-holes plotted in the arbitrary seismic line in Fig. 2.9 is shown with indication of the total apparent thickness of the Upper Triassic-Lower Jurassic Pre-Cuyo synrift deposits.

2.4.3 Pseudo-3D structural model

Nine W-E cross sections were constructed, separated by approx. 2 km each (Figs. 2.5, 2.10), by integrating dip data, unit contacts and surface fault traces with well log data and the interpretation of the 3D seismic cube. We reconstructed the initial geometry of the units and pre-existing normal faults (Fig. 2.10), and used kinematic forward-modeling to build sequential cross-sections taking into account Neogene sedimentation and isostatic changes using the flexural method in MOVE ©.

The cross-sections were extrapolated into a pseudo-3D structural model (Fig. 2.11). This ensures that the proposed structural model is consistent along strike. Structures and formation tops were mapped throughout the study area producing 3D surfaces that permit the characterization of the main structural features, such as main faults with lateral variations in displacement, depth to formation tops, bedding attitude, etc.

The northern domain (cross-sections 1 to 6, Fig. 2.10) is characterized by structures with eastern vergence. The thin-skinned Loncoche fault was modelled with a detachment level in the Upper Jurassic Auquilco evaporite. Two minor fault splays show variable geometries and displacement in the different cross-sections as constrained by wellbore, seismic and surface data. This fault system decreases its displacement southward and is

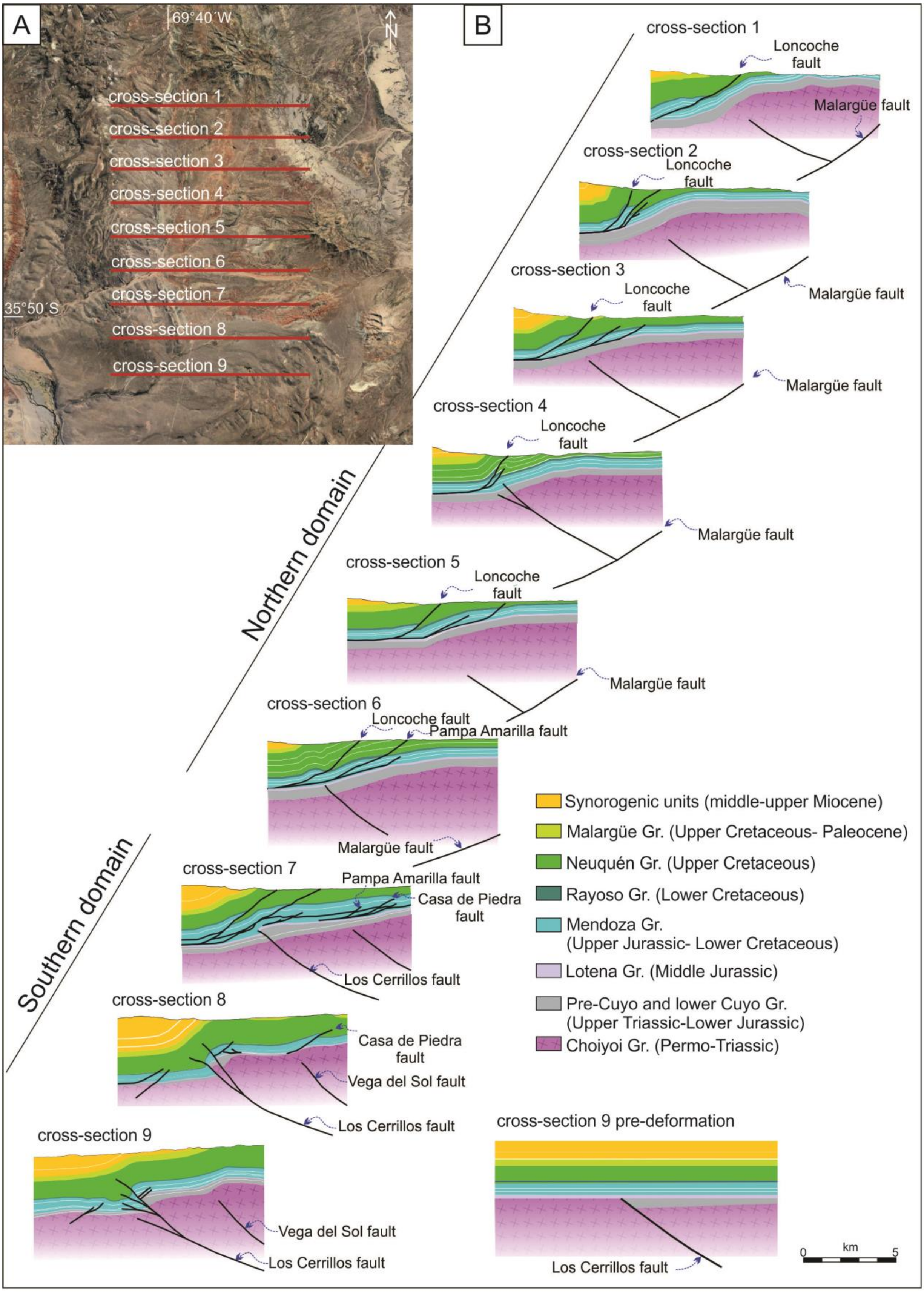

Figure 2.10: A) Google Earth image with location of W-E cross-sections in the Agua Botada area. B) Perspective view of the nine W-E cross-sections. The northern domain is characterized by the Malargüe anticline formed as consequence of reverse movement along the pre-existing Malargüe basement fault, and thin-skinned, east-directed thrusts. The southern domain is controlled by the inversion of the Los Cerrillos fault. In the lowermost right corner the predeformation section is shown.

absent south of cross-section 7 (Fig. 2.10). The deep seated Malargüe fault generates the Malargüe anticline in the north (sections 1–4) and also decreases its displacement towards the south. In our models, the high angle of the Loncoche fault is the result of tilting during folding related to the Malargüe fault.

The southern domain, in contrast, is characterized by a dominant western vergence (cross-sections 7 to 9, Fig. 2.10). The Los Cerrillos fault shows increasing complexity towards the south, with the development of fault splays, shortcut, bypass faults and minor backthrusts (Fig. 2.10). The Vega del Sol basement fault is recognized due to the anticline it forms in the Mesozoic cover. This fault increases its displacement towards the south.

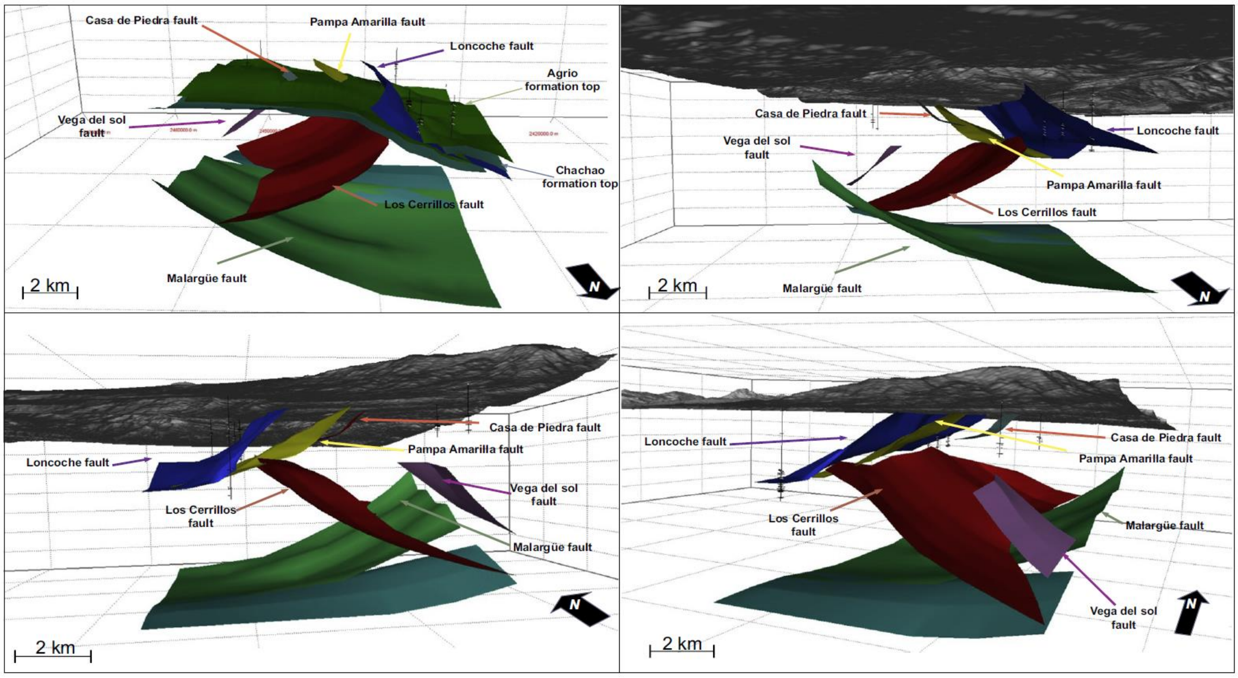

Figure 2.11: Different perspectives of the pseudo-3D model of the Agua Botada area. Upper green surfaces represent the top of the Chachao (dark green) and Agrio Formations (light green) of early Cretaceous age. Basement faults are the E-directed Malargüe fault, and W-directed Los Cerrillos and Vega del Sol faults. Thin-skinned E-directed faults are the Loncoche, Casa de Piedra and Pampa Amarilla faults.

2.4.4 Cenozoic intrusives and their relationship with structures

In order to study the relationship between the structural evolution of the Malargüe fold-and-thrust belt orogenic front and the Cenozoic igneous intrusions, we analysed the spatial distribution of sills and dykes at the surface, from Google Earth satellite images, and at subsurface based on wellbore data. During fieldwork, we described the relationship of intrusions with the host rock and with structures (Fig. 2.12A), and measured kinematic indicators on mesoscale faults affecting the intrusions and their wallrocks. The relative timing of intrusion of sills and dykes is not always clear throughout the study area: some dykes clearly post-date sills (e.g. Fig. 2.12B), while other dykes abut against sills (Fig. 2.12C). This latter could be the result of a pre-existing sill arresting the dyke or of synchronous emplacement with the dyke feeding the sill in the third dimension (Spacapan et al., 2016a). The similar composition of dykes and sills (Schiuma, 1994; Spacapan et al., 2016a, 2016b) suggests that all belong to the middle Miocene to Pliocene Huincán magmatic cycle (Nullo et al., 2002). Our observations indicate that intrusions in the Agua Botada area are older than the Loma Fiera Formation (i.e. sills and dykes do not intrude this Formation), which has provided ages ~10 Ma (Baldauf, 1997; Horton et al., 2016), but intrude synorogenic beds from the Agua de la Piedra Formation (16-10 Ma, Silvestro and Atencio, 2009). This stratigraphical constraint indicates that sills and dykes were emplaced during the 16-10 Ma period, before the main phase of folding in the Malargüe anticline constrained to <7 Ma by Silvestro et al. (2005).

Most previous works focused on sills emplaced in the Vaca Muerta and Agrio Formations (Schiuma, 1994; Rodriguez Monreal et al., 2009; Spacapan et al., 2016a, 2018). In addition to these, we surveyed those emplaced in the red shales of the Rayoso and Neuquén Groups (Fig. 2.6). Our observations are mostly consistent with those reported in the referenced works. Most sills have sharp contacts with the wallrock, with borders subparallel to the stratification of the wallrock (Fig. 2.12C). Most sill terminations are straight and abrupt (Fig. 2.12D), although wedge terminations were also observed (Fig. 2.6B). Sills are strongly controlled by rheological contrast, intruding shales but without affecting the more competent limestone, sandstone and conglomerate beds (Fig. 2.12B), as described in previous works (Spacapan et al., 2016a). The maximum observed thickness of sills is 70 m, while the maximum lengths reach 3000 m.

Subvertical dykes with andesitic to basaltic andesite composition and porphyritic textures intrude all Mesozoic units. Most dykes radiate from two subvolcanic centers located in the Mirano and Tronquimalal peaks (Figs. 2.5, 2.12E, F). These two centers have an ellipsoidal shape, elongated along the WNW trend. The measurement of the orientation of 37 dykes from satellite images shows a predominant WNW trend, with ENE-, E- and NW-striking dykes also frequent (Fig. 2.13). Thickness and length are highly variable, but show a linear relationship between both features and the dyke strikes. Dykes with ENE to WNW strikes are much longer and thicker than NW- to NE-striking dykes (Fig. 2.13).

To understand the relative timing between the Malargüe anticline and dyke and sill intrusion located at its backlimb, we unfolded and horizontalized the beds, taking the dykes as passive elements. By doing this, the dykes take a vertical to subvertical attitude (Fig. 2.13), suggesting that the intrusion occurred before the development of the anticline. This is consistent with the age constraints discussed at the beginning of this section.

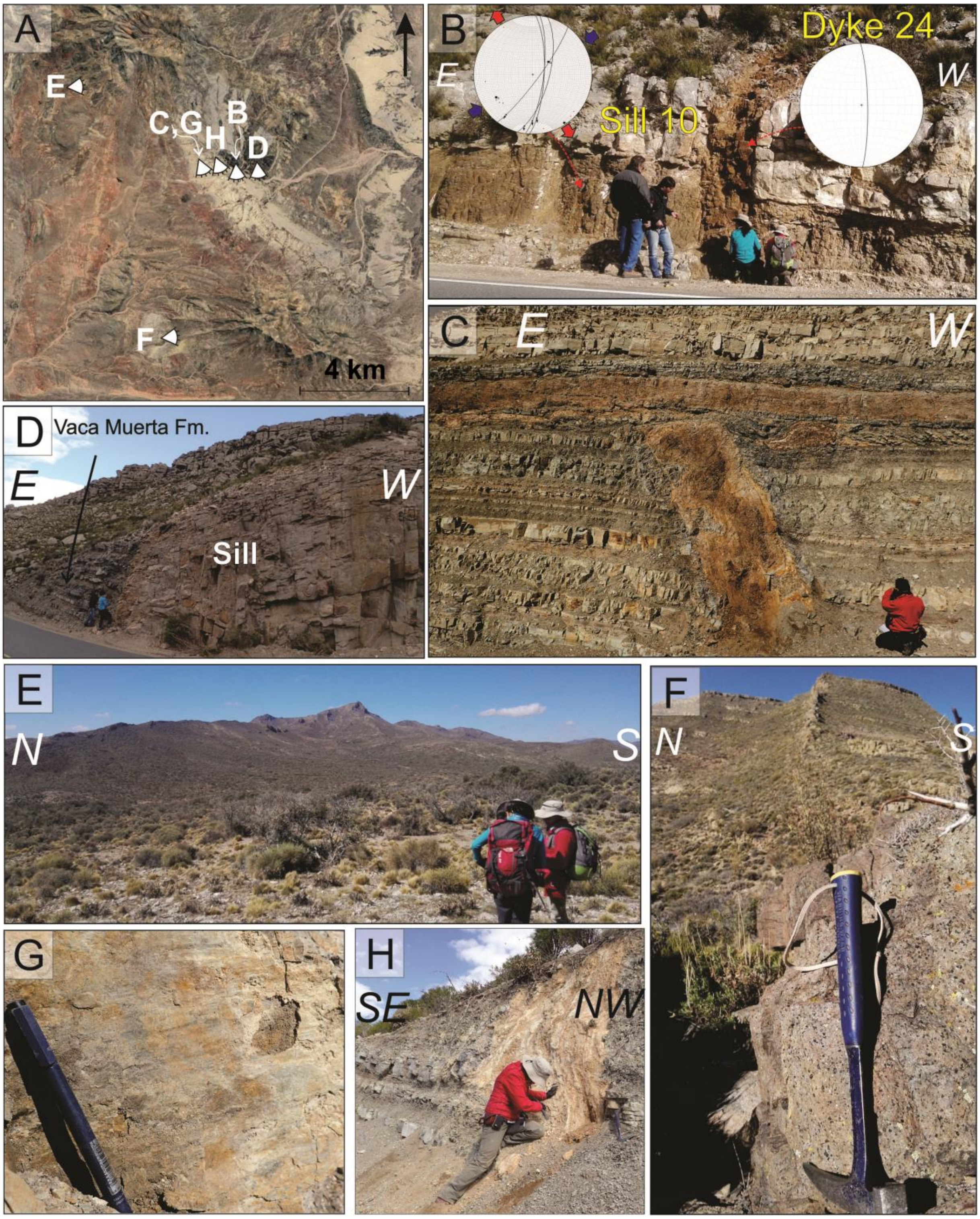

Figure 2.12: A) Aerial image (Google Earth) showing the location and orientation of the pictures described next. B) The dyke crosscuts a sill which is sheared with NNE dextral strike-slip faults subparallel to the dyke strike (GPS point AB dyke 24: 35°44'54.29"S 69°34'47.99"W). C) Dyke and sill intruding the Agrio Formation. The sill intrudes the pelitic layers of this unit due to low strength compared to the limestone beds. Apparently the dyke abuts against the sill (GPS point AB dyke 21: 35°44'55.48"S 69°35'16.80"W). This same outcrop was studied in detail by Spacapan et al. (2016a). D) Sharp contact between a sill and the Vaca Muerta Formation wallrock (GPS point AB sill 15 35°44'52.68"S 69°34'28.99"W). E) Photo looking eastward to the Mirano peak, the southernmost subvolcanic center, with radial dykes (GPS 35°48'S 69°36'W). F) Photo looking to the E pointing to the Tronquimalal peak with a dyke in the foreground which is radiated from the peak interpreted as subvolcanic center (GPS point AB dyke 34: 35°43'8.49"S 69°38'30.86"W). G) Subhorizontal striae and slip plane affecting a dyke, indicating strike-slip faulting (GPS point AB dyke 21: 35°44'55.48"S 69°35'16.80"W). H) Highly sheared and altered dyke intruding the Agrio Formation (GPS 35°45'1.19"S 69°34'53.89"W).

We studied the available oil-well logs of the area (Fig. 2.5) to determine the intervals where igneous rocks were cut through. These rocks correspond to andesites of aphanitic to porphyritic texture with different alteration degrees and hydrocarbon traces. The apparent thickness reaches a maximum of 40 m and the thickest intervals are hosted in the shales of the Vaca Muerta Formation and the evaporites of the Auquilco Formation. We compared the thickness of igneous rocks in the drill-holes with the distance to the two volcanic centers identified, Tronquimalal and Mirano peaks (Supplementary material). In the northern area (AB e-4, AB x-2, AB x-1, AB e-5; Fig. 2.5) there is a good correlation between the thickness of intrusives and the distance to the Tronquimalal neck, as well as in the central zone related to the Mirano neck; both necks show an associated swarm of dykes. In the southern area we did not recognize dykes outcropping in surface or necks, but there are some drill-holes (ABu x-1, LCe x-2 and well 18) that show high values of accumulated thickness of igneous rocks, such as the ABu x-1 accounting for >200 m (Supplementary material). We interpret that this is probably related to subhorizontal intrusives, sills, which are covered by the Cenozoic deposits.

Observations at the Agua Botada area show that the Loncoche fault (Fig. 2.5) acted as a magmatic conduit allowing the emplacement of a sill that grades to an inclined sheet intrusion along the fault (Fig. 2.6). Furthermore, uranium and copper minerals precipitated along the contact of the sill and the fault, and the sill as well as the sandstones of the Neuquén Group wallrock are impregnated with hydrocarbons (Fig. 2.6E), indicating a link between reverse faulting, intrusion and fluid flow. On the other hand, subvertical strike-slip faults locally control the emplacement of dykes, as already described by Spacapan (2016b). These dykes are heavily altered by hydrothermal fluids, with precipitation of fibers of hematite and calcite and hydrocarbon impregnation, which shows that fluid migration occurred during movement of these fractures. This suggests that the Loncoche reverse fault and the subvertical strike-slip faults have controlled magmatic emplacement and fluid and hydrocarbon migration. We will discuss this subject further in Section 2.5.2.

2.4.5 Kinematic analysis

Many intrusions in the Agua Botada area are affected by mesoscale faults with displacements <1 m. We measured fault slip data on 37 dykes and 22 sills and on Mesozoic rocks at 7 localities (Figs. 2.12, 2.13). A total of 87 fault plane-striation pairs with reliable sense of shear were measured. A dominant E- to ENE-directed shortening axis and subvertical extension axis is observed at sites close to the Loncoche fault (Fig. 2.6). In other sites, faults affect the interior of sills and dykes (Fig. 2.12G, H), as well as the contacts between dykes and wallrock. Overall, the NNE- to NE-trending faults show

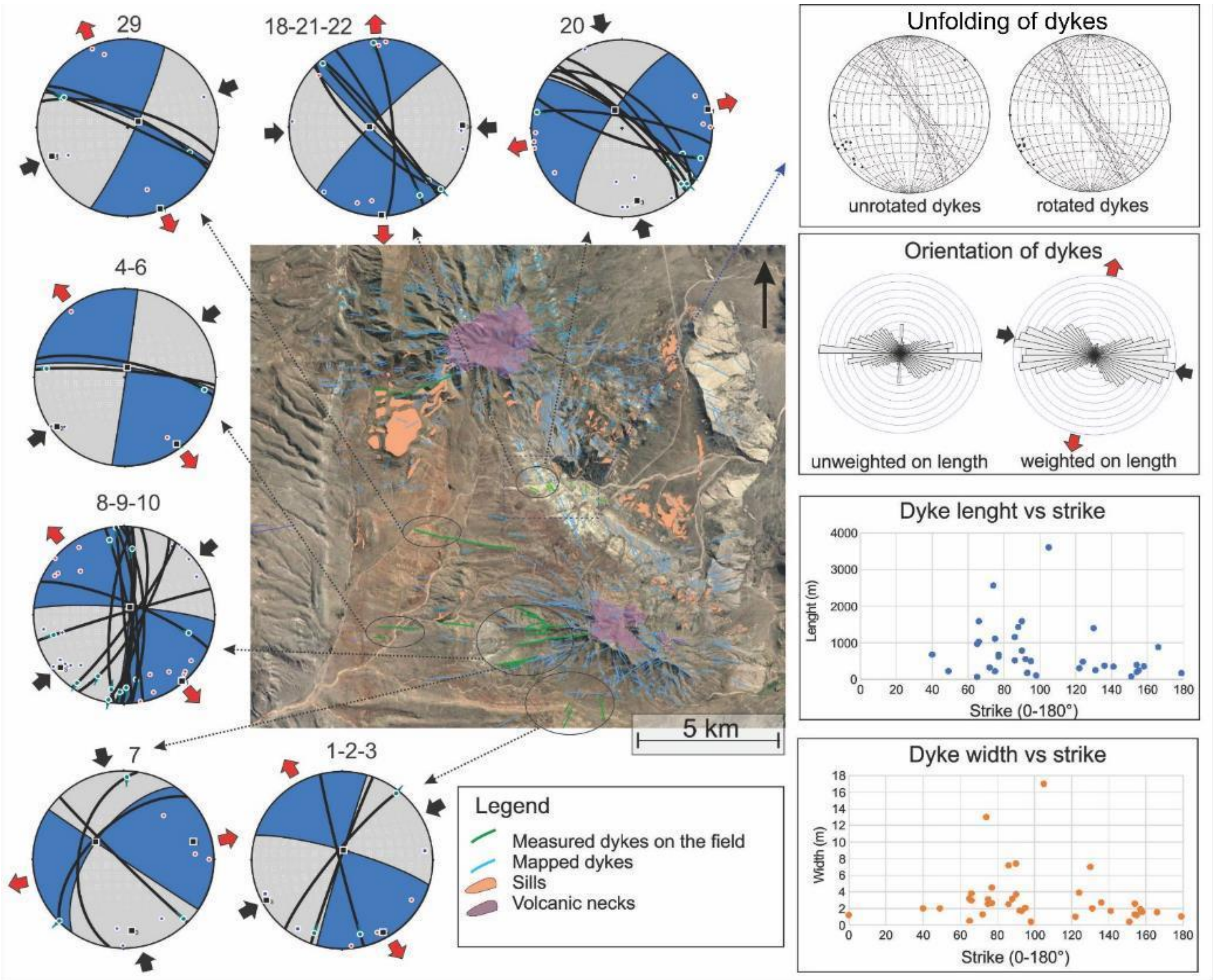

Figure 2.13: Kinematic data (green dots: striae data, blue dots: individual P-axes (contraction), red dots: individual T-axes (tension) obtained from the dykes in the area, showing that they are affected by strike-slip faulting. The unfolding performed in the dykes intruding the Mendoza Group in the backlimb of Malargüe anticline shows a better mechanical orientation when the data is restored to the horizontal position, indicating the dykes where intruded previous to the folding of Malargüe anticline, in agreement with geological data. The rose diagram includes both measured on field and mapped dykes, unweighted and weighted on length, showing a horizontal WNW oriented contraction (black arrows) and a NNE oriented extension (red arrows) at the time of intrusion. When compared the dyke length and width versus the strike, there is a correlation between the dimension of the intrusive and a roughly W to WNW strike.

dextral movements, while the WNW- to NW-striking faults show sinistral movements (Fig. 2.13). Most data are consistent, indicating a strike-slip regime with E- to NE-directed shortening and N- to SE-directed extension.

An exception to this is the dextral movement of two of the NW-striking dykes (7 and 20 in Fig. 2.13) in the western flank of the Malargüe anticline, indicating a ENE-directed extension axis perpendicular to the trend of the anticline, and NNW-directed shortening axis. Here we propose that the ENE extension and NNW contraction may be due to local deviations of the contractional direction maybe related to previous structures, similar to what is observed nowadays from wellbore breakouts (Guzmán et al., 2007). Another explanation is the dextral movement of NW-striking faults preceded the intrusion of the dykes, as suggested by Spacapan et al., (2016b).

2.5 Discussion

2.5.1 Controls on intrusions

The geometry and connectivity of magmatic intrusions is the result of the combination of tectonic and magmatic processes and the lithology and pre-existing structures of the host rock (Magee et al., 2018). Tectonic processes include the influence of active structures during magma intrusion, that act as magma conduits (Kalakay et al., 2001; Galland et al., 2007a, 2007b; Ferré et al., 2012; Martínez et al., 2018; van Wyk de Vries and van Wyk de Vries, 2018) and the role of the stress field (Nakamura, 1977; Takada, 1989; Kavanagh, 2018). Magmatic processes refer to size, depth and shape of the magma source, magma injection rate, buoyancy and viscosity (Galland et al., 2007a, 2007b, 2018). Lithology controls the rheology of the host rock (Kavanagh et al., 2017; Galland et al., 2018) and pre-existing structures are weak zones that can also act as preferential pathways for magma (Ferré et al., 2012).

Dyke intrusion is strongly influenced by stress and crustal heterogeneities (Kavanagh, 2018). It is well established that the opening direction of dykes is perpendicular to the local minimum principal stress $\sigma 3$ (Anderson, 1951; Fossen, 2010; Kavanagh, 2018). This local stress is determined by the interaction of magma pressure and tectonic stress. In radial dyke systems emplaced under neutral stress conditions, magmatic pressure is similar in all direction and dykes of all orientations are similar in length. In contrast, radial dyke systems emplaced under a regional tectonic stress are elongated in the direction of the maximum horizontal stress $\sigma Hmax$ and dykes of the same orientation are more abundant than dykes of other trends (Odé, 1957; Nakamura, 1977). Pre-existing structures in the host rock are weak planes that can be used for magma migration and emplacement in dykes, depending on the orientations of fractures with respect to the tectonic stress and on magmatic overpressure (Delaney et al., 1986).

The emplacement of sills is the result of the interaction of tectonic stress and mechanical layering of the host rock. Traditionally, opening perpendicular to $\sigma 3$ implying a vertical direction for the minimum stress has been proposed (Anderson, 1951; Hubbert and Willis, 1957). A recent review of sill complexes has shown that these are found in layered rocks under all stress regimes (Magee et al., 2016), which suggests that the presence of interfaces between rocks with different mechanical properties is the key factor (Galland et al., 2018). However, in some cases, sills have been documented in rocks with strong vertical mechanical discontinuities (bedding and foliation), where they were emplaced under local compressional conditions, which shows that the stress state controlled sill emplacement (Stephens et al., 2017). It seems that both mechanical layering of rocks and stress state can control sill emplacement, with one of these factors prevailing in some cases.

Magma supply for sills can be fed by a variety of structures, from dykes (Eide et al., 2016; Kavanagh et al., 2017) to inclined sheets connecting sills at different stratigraphic levels (Muirhead et al., 2012; Magee et al., 2016) to inclined sheets taking advantage of faults (Magee et al., 2013; Galland et al., 2007a, 2007b; Ferré et al., 2012).

Magmatic migration under contraction has been modelled by means of analogue modeling and compared with real examples in the Southern Central (Galland et al., 2007a, 2007b) and Northern Central Andes (Martínez et al., 2016, 2018) showing that thrusts and inverted faults could act as magma pathways even with considerably lateral migration in the shortening direction. In northern Chile basin inversion under Andean contraction is coeval with magma migration and this latter process influenced the geometry of the inverted faults and also the amount of shortening accommodate by the fault due to the role of igneous fluids as lubricants (Martínez et al., 2016, 2018). On the other hand, these authors showed that magma migration, under shortening, is controlled by its viscosity; when higher the viscosity, the magma migrates shorter distances laterally and it is confined provoking uplift (Martínez et al., 2018).

In the study area, previous works have emphasized the role of layering and rheology of host rocks on sill intrusions, with intrusion favoured in shale-dominated units and within these, in weak shale beds vs. strong sandstone beds (Spacapan et al., 2016a). Both within the study area and throughout the Malargüe fold-and-thrust belt, it has been proposed that sills and laccoliths were fed by inclined sheet magma migration along thrusts (Araujo et al., 2013; Schiuma and Llambías, 2014), with thrusts acting as magma conduits and feeding sills in favorable stratigraphic intervals. No conclusive evidence of sill feeding by dykes has been reported in the area (Spacapan et al., 2016a). Our observations in the Loncoche fault support the role of active thrusts as magma conduits. Fault planes of the Loncoche fault are intruded by inclined sheets and mineral fibers on minor faults developed on the intrusions (Fig. 2.6) indicate fault movement once the inclined sheets were emplaced, showing that the fault was active during this period and not a pre-existing weakness. This is consistent with the age constraints for intrusions and activity of the Loncoche fault which suggest that both were coetaneous (see Sections 2.4 and 2.5). On the other hand, the analysis of well data (Section 2.4.4) suggests that sills were also fed by the intrusive centers of the Cerros Mirano and Tronquimalal, in which case some of the sills could be fed by these cylindrical intrusions.

Dykes in the study area are radial systems developed from the magmatic centers of the Cerros Mirano and Tronquimalal, displaying a preferential E-W to ESE orientation, consistent with roughly E-W maximum horizontal stress σHmax (Fig. 2.13), which indicates a control of the regional tectonic stress on their emplacement. Previous works have proposed that NW-trending pre-existing strike-slip faults controlled dyke intrusions (Spacapan et al., 2016b). We observed that some of the outcrop-scale faults are developed within the dykes indicating that strike-slip fault movement took place after intrusion (Fig. 2.13). Field observations alone do not allow us to determine if these faults moved shortly after dyke emplacement or if they are largely posterior. We will discuss this issue further in the following section.

2.5.2 Stress state during the magmatic intrusion and relation with fluid migration

Recent works have documented that the state of stress can be complex in orogenic fronts and depart from the expected compressional stress field, with the minimum principal stress σ_3 horizontal leading to the development of normal and strike-slip faults (Lacombe et al., 2012; Tavani et al., 2015). Without neglecting other factors that influence the shape and mechanism of igneous intrusions, we propose that stress changes in the study area were an important factor determining the intrusion of dykes *vs.* sills.

The stress state and its changes in time in the study area are not well constrained. Guzmán et al. (2011) have studied the σ_{Hmax} directions in the Eocene to Oligocene from dyke trends, south of the study area, proposing a NE σ_{Hmax} for this period. During the Miocene, a change to E-W σ_{Hmax} took place and this remained until the present (Guzmán et al., 2007). The dominant contractional stress regime that led to crustal shortening and uplift of the Andes implies that $\sigma_{Hmax} = \sigma_1$, and the E-W direction was determined by the direction of plate convergence along the Argentina-Chile subduction zone (Pardo Casas and Molnar, 1987; Somoza, 1998; Norabuena et al., 1999). Local fluctuations to WNW or ESE σ_{Hmax} orientations have been suggested as the result of strain partitioning due to previous basement anisotropies (Branellec et al., 2015b) and topographic variations (Guzman et al., 2007; Mescua et al., 2014).

Our observations and previous works in nearby areas (Galland et al., 2007a, b; Araujo et al., 2013; Schiuma and Llambías, 2014) indicate that sill intrusions were fed by inclined sheets using thrusts as magmatic conduits. We documented continued activity of thrusts after magmatic intrusion at the Loncoche fault (Fig. 2.6). This suggests that sill intrusions took place in a compressive regime, where σ1 was horizontal with E-W trend and the vertical minimum principal stress favoured horizontal fracture opening. This indicates that in the study area, both stress state and mechanical layering acted as main factors that conditioned sill intrusion.

The plan-view elongated shape of the radial dykes is the result of an E-W σ_{Hmax}, which is most likely the unchanged σ_1 determined by plate convergence. The NW- to WNW-striking dykes are emplaced in strike-slip faults, that may be pre-existing faults as suggested by Spacapan et al. (2016b); however, fault slip data from small scale faults affecting the contact between dykes and wallrock, as well as the interior of the dykes, indicate that faults were reactivated after intrusion. Mechanical analysis shows that subvertical faults display low slip and dilation tendencies under horizontal compression, while in a vertical radial extension stress regime ($\sigma_2 = \sigma_3$), vertical fractures subparallel to σ_1 are likely to open, and vertical fractures oblique at low angles to σ_1 can open and shear (Stephens et al., 2017). This stress state has been indicated as one of the possible origins of the “σ_2 paradox” that produces strike-slip and normal faults in the frontal region of thrust wedges (Tavani et al., 2015) and can explain (i) the reactivation of pre-existing strike-slip faults with a dilation component to allow dyke emplacement, and (ii) the continued movement of the faults that produced small scale strike-slip faults. Field observations, as cross-cutting relationships between dykes and sills, similar composition, and that both are not intruding units younger than 10 Ma (Loma Fiera Fm.) suggest that dykes and sills were emplaced during the same time period (16-10 Ma, see section 2.4.4). We propose that during this period, the region was subjected to a stress regime with $\sigma_1 >> \sigma_2 \sim \sigma_3$. In this scenario, σ_2 and σ_3 could be interchanged producing alternating compression and strike-slip regimes (Zoback, 2010). Furthermore, this stress state has been recognized during the Pliocene-present in the orogenic front of the Malargüe fold-and-thrust belt (Mescua et al., 2019), which suggests that the stress state in the region was constant since the early Miocene to the present in the study area.

The circulation of hydrothermal fluids and hydrocarbons in the faults of the study area is demonstrated by (i) copper and uranium mineralizations associated to the sill emplaced in the Loncoche fault; (ii) hydrothermal alteration in dykes that present strike-slip shearing with growth of hydrothermal mineral fibers; (iii) hydrocarbon impregnations in both kinds of structures. These observations imply that active thrusts and strike-slip faults, including major structures and outcrop-scale faults, acted as fluid carriers. Hydrothermal fluids migrated through these fault zones, leading to alteration of igneous intrusions and host rock and to the precipitation of mineralizations, locally with economic interest such as in the Huemul mine. Hydrocarbons also migrated through the faults. Strike-slip faults affect sills that are hydrocarbon reservoirs in many oilfields in the region (Comeron et al., 2002; Witte et al., 2012; Schiuma and Llambías, 2014; Spacapan et al., 2016, 2017), suggesting that the development of strike-slip faults can enhance fracture connectivity and be an important factor in the migration of hydrocarbons into these reservoirs.

2.5.3 Tectonic and magmatic evolution of the study area

During the emplacement of dykes and sills, between 16 and 10 Ma, a foredeep area developed in the northern domain (Silvestro et al., 2005). The active structure during that period is interpreted by Silvestro et al. (2005) to be the Chacaico basement fault, located approx. 30 km towards the west (Fig. 2.4). Crosscutting relationships between dykes and sills, intruded during this period, indicate that they were synchronically emplaced. This suggests, a priori, that the magma intrusion was controlled by either a strike-slip/compression ($\sigma v=\sigma 2$ and $\sigma 2 \sim \sigma 3$) or a compression/strike-slip ($\sigma v=\sigma 3$ and $\sigma 2 \sim \sigma 3$) stress regime (Fig. 2.14A). We postulate that under this stress field regime pre-existing WNW- to E-striking structures were prone to dilate and were used as magma conduits.

After the deposition of the synorogenic deposits of the Loma Fiera Formation (approx 10 Ma, Fuentes et al., 2016), movement along the Doña Juana basement structure and associated thin-skinned thrusts and backthrusts generates the Sierra de la Ventana syncline (Fig. 2.4), as suggested by the lack of angular unconformities in the synorogenic units in the syncline and U/Th-He (AHe) thermochronological studies on apatite indicating a 8.9 to 7 Ma exhumation time for the Valenciana anticline (Bande et al., in press). During this period (10-7 Ma), a wedge-top depocenter is developed in the western sector of the Agua Botada area (Fig. 2.14B). The Loncoche fault represented the thrust front for that time. The eastward advance of the thrust system, suggest that the stress regime was a compressional one. This also correlates with the absence of dykes intruded during this period (10 -7 Ma) which may be influenced by this stress field. Under this stress field, at approx. 8 Ma, the Malargüe anticline started to develop, and continued its activity at least up to 1 Ma (Silvestro et al. 2005; Bande et al., in press). The Coyocho basalts (6.7-2.7 Ma) unconformably cover Cenozoic strata folded into the Sierra de la Ventana syncline, indicating the fossilization of the Loncoche fault after 7 Ma (Fig. 2.14C).

In the southern domain, during the first Miocene compressional period (16-10 Ma; Fig. 2.14D), active structures were localized in the inner sector of the Malargüe fold-and-thrust belt and in the Palauco fault system (Silvestro and Atencio, 2009). One of the faults of this system corresponds to the Los Cerrillos fault. Our model proposes that during this period and under a compressional stress regime, sills cut by the oil exploration wells were emplaced. The pre-existing Palauco system experienced a reactivation during the 11-8 Ma period (Fig. 2.14E) (Silvestro and Atencio, 2009) and during the last stage, since 7 Ma, the stress regime changed to a strike-slip one (Fig. 2.14F), as proposed by Mescua et al. (2019).

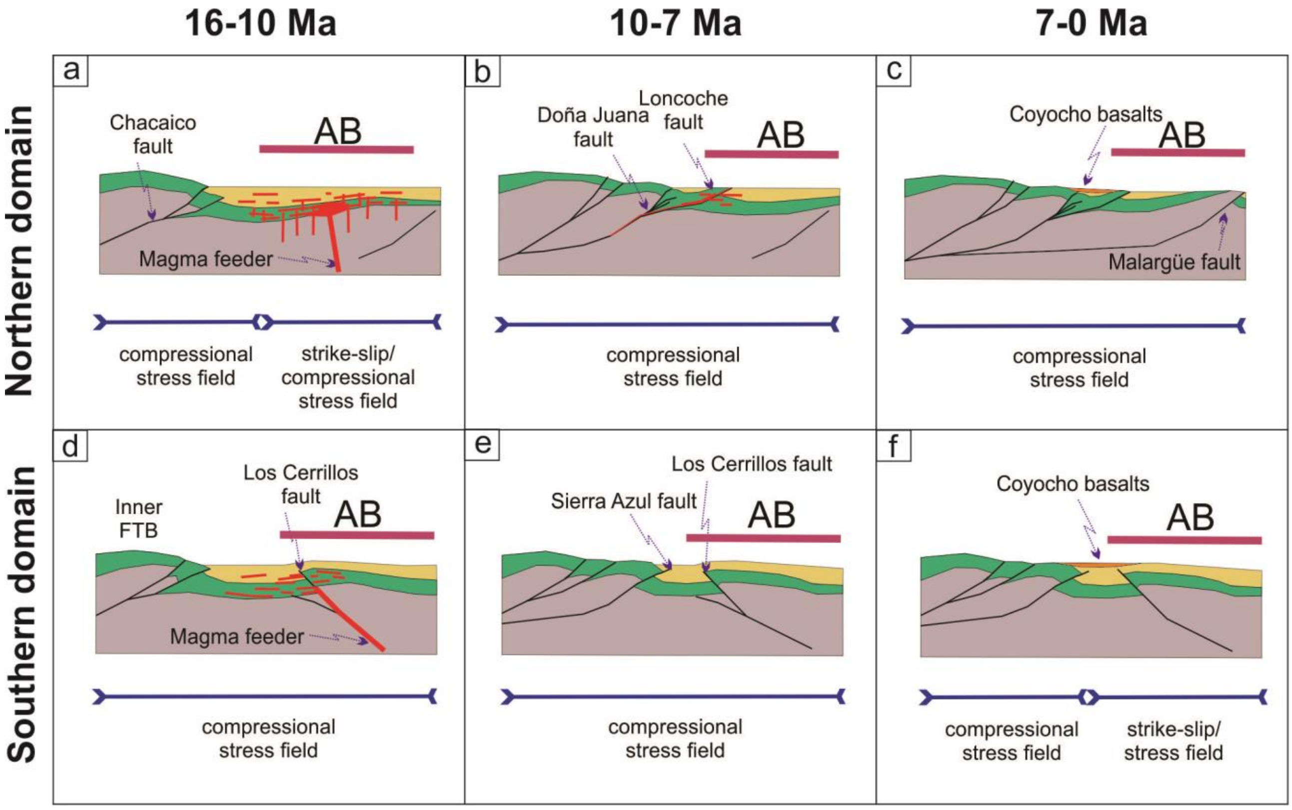

Figure 2.14: Structural evolution of the northern (A-C) and southern (D-F) domains of the Agua Botada (AB) area. A) At the beginning of contraction in the Malargüe fold-and-thrust belt, the AB area was subjected to a strike-slip/compression stress regime. Under this regime, sills and dykes intruded the Mesozoic beds and Neogene synorogenic strata of the Agua de la Piedra Formation. B) With the advance of the thrust front, at 10-7 Ma, the AB area was under compression, and few sills intruded the sedimentary sequences fed from the active thrusts. C) The thrust front reached the Malargüe anticline area at approx 8-7 Ma. The western AB area was unconformably covered by the Coyocho basalts. D) In the southern domain, the thrust front was located at the Los Cerrillos fault, during the 16-10 Ma period. The AB area was under a compressional stress field, and sills intruded the Mesozoic units, fed from the Los Cerrillos fault. E) During the 10-7 Ma period, the area was under compression, and the Sierra Azul fault developed. F) During the last stage, the stress field in the AB area changed to a strike-slip one, as documented by Mescua et al. (2019).

All these observations indicate that, in the study area: (i) sills are syn- or post-tectonic with respect to deformation of the western part of the study area, which started at 16 Ma (Silvestro and Atencio, 2009), (ii) sills and dykes were likely emplaced contemporaneously in the northern domain, with dykes emplaced shortly after sills and vice versa, but most intrusions predate the Loma Fiera Formation dated at 10 Ma; (iii) shearing of well-oriented dykes occurred before thin-skinned thrusting event (>10 Ma) under a strike-slip regime; (iv) the contraction and folding in the area, related to the Malargüe fault, took place after the main pulse of intrusion emplacement, coincident with the proposal of Silvestro and Atencio (2009) that indicates that the Malargüe anticline started to form at 7 Ma; and (V) there is no evidence of emplacement of dykes in the southern domain; instead, well logs indicate the presence of many igneous bodies, interpreted here as sills.

Taking into account that sill and dyke intrusion is favoured by the different stress fields acting in the region, this suggests that in the northern domain, between 16 and 10 Ma, the stress state fluctuated between compression/strike-slip and strike-slip/compression, in a way similar to that proposed at present for the orogenic front of the Malargüe fold-and-thrust belt to the north and south of the study area (Mescua et al., 2019). This is in accordance with tensile joint analysis carried out by Branellec et al. (2015b) indicating a N-S subhorizontal extensional direction during the pre-folding event. On the other hand, during that period, the southern domain was under pure compression and it is marked by the intrusion of sills.

2.6 Conclusions

Based on the structural characterization of dykes and sills in the framework of the evolution of the thrust front of the Malargüe fold-and-thrust belt, during the Miocene to Present, we infer the *in-situ* stress field acting at the time of intrusion. We propose that during the evolution of the thrust front, the local stress field changed from a compressional to a strike-slip/compressional one, favouring during this last stress field the synchronous emplacement of sills and dykes. We propose that the alternation of these stress regimes allowed hydrocarbon migration through thrusts and subvertical strike-slip faults as well. Previous NW-striking structures were not amenable to be inverted due to its high obliquity to the maximum principal stress in a compressional regime, but instead, they were prone to slip under a strike-slip/compressional regime; while WNW oriented previous structures were prone to dilate and acted as feeders from a magmatic source.

This interchange between both stress regimes is likely related to the similar values of the minimum ($\sigma 3$) and intermediate principal stress ($\sigma 2$) with an E-W oriented maximum principal stress ($\sigma 1$) according to the plate convergence vector.

Chapter III

3. Stress field and active faults in the orogenic front of the Andes in the Malargüe fold-and-thrust belt (35°-36°S)

Resumen

Integramos datos de campo y de pozos petroleros para discutir el campo de esfuerzos en el sector frontal de la faja plegada y corrida de Malargüe (Andes de Argentina). Las observaciones de superficie indican que los corrimientos N-S y las fallas de desplazamiento de rumbo de orientación NO a ONO y ESE están activas en el área de estudio. La inversión de los indicadores cinemáticos de fallas, combinada con los datos de ruptura u ovalización (*breakouts*) de la perforación y una prueba de fracturación (*mini-frac*) dentro del área de estudio, permiten constreñir un estado de esfuerzos del Cuaternario a reciente, que se caracteriza por un esfuerzo máximo subhorizontal, orientado E-O, y por esfuerzos intermedios y mínimos con magnitudes similares que se intercambian localmente, produciendo un escenario en el que las fallas inversas y las fallas de desplazamiento de rumbo se activan de manera alternativa. Se examinan además las implicancias de las estructuras reconocidas para el riesgo sísmico.

Abstract

We integrate field and wellbore data to discuss the stress field in the frontal sector of the Malargüe fold-and-thrust belt (Andes of Argentina). Surface observations indicate N-S thrusts and NW to WNW and ESE strike-slip faults are active in the study area. Inversion of fault kinematic indicators, combined with borehole breakout data and a mini-frac test within the study area, constrain the Quaternary to recent stress state, which is characterized by a subhorizontal, E-W oriented maximum stress, and by intermediate and minimum stresses with similar magnitudes that are locally interchanged, producing a setting in which reverse and strike-slip faults are alternatively active. The implications of the recognized structures for earthquake hazard are examined.

A version of this chapter was published in Tectonophysics by Mescua, J.F., Barrionuevo, M., Giambiagi, L., Suriano, J., Spagnotto, S., Stahlschmidt, E., de la Cal, H., Soto, J.L., Mazzitelli, M., 2019. Stress field and active faults in the orogenic front of the Andes in the Malargüe fold-and-thrust belt (35°–36°S).

3.1. Introduction

The development of fold-and-thrust belts in orogenic environments is the result of contraction, which is usually interpreted as a result of a compressional stress state, with the minimum principal stress (σ_3) in the vertical direction. In this stress regime, thrusts and reverse faults are active (Anderson, 1951) with trends sub-perpendicular to the horizontal maximum principal stress (σ_1). In particular, during advance of the orogenic wedge, the active frontal structures are usually assumed to be orogen parallel thrusts (e.g. Elliot, 1976; Chapple, 1978).

However, as Lacombe *et al.* (2010) and Tavani *et al.* (2015) noted, the occurrence of transversal structures (strike-slip or more rarely normal faults) in the frontal sector of fold-and-thrust belts is frequent. Field and microstructural analyses suggest that the intermediate principal stress (σ_2) is vertical during the development of these structures and the minimum principal stress (σ_3) is horizontal, giving place to what these authors call the "σ_2 paradox" (Tavani *et al.*, 2015).

In this work, we study the orogenic front of the Malargüe fold-and-thrust belt in the Andes of Argentina (35-36ºS, Fig. 3.1). The Pliocene-Quaternary stress state in this region is debated in recent works, with some researchers proposing an extensional regime (Ramos and Kay, 2006; Folguera *et al.*, 2008, 2009), while others reported active thrust faults (Silvestro *et al.*, 2005; Giambiagi *et al.*, 2008) suggesting compression.

We document N-trending thrusts that constitute the main structures in the study area, placing Cretaceous rocks over Quaternary deposits. Thrusts are locally displaced tens of meters by NW, WNW and ESE-trending strike-slip faults, some of which juxtapose Cretaceous rocks and Quaternary deposits. We explore the possible setting in which both kinds of structures could be active and their implications for seismic hazard.

3.2. Geologic setting

The Malargüe fold-and-thrust belt is a basement-involved belt developed in the eastern side of the Andes between 34° and 36°S (Fig. 3.1). In this region, the basement corresponds to the Late Permian-Early Triassic acidic volcanic rocks of the Choiyoi Group (Llambías *et al.*, 1993). The sedimentary cover consists of Late Triassic-Neogene deposits of the Neuquén basin, a retroarc basin filled with alternating marine and continental sediments that reach more than 6.000 m thick in the most important depocenters (Legarreta and Uliana, 1999). The evolution of the basin is characterized by a Late Triassic-Early Jurassic extensional event, during which depocenters controlled by

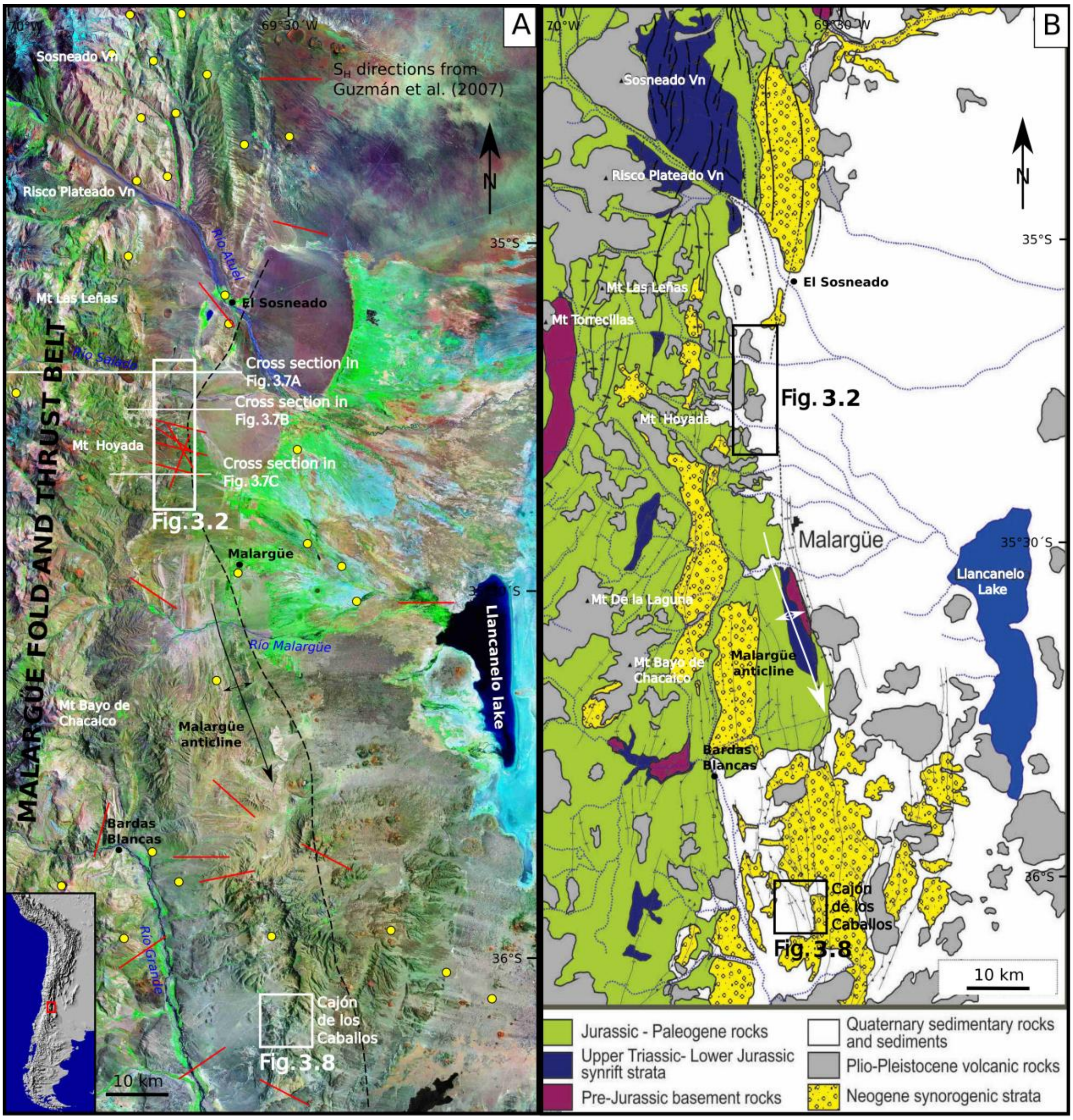

Figure 3.1. Location of the study area. A) LANDSAT ETM+ image (RGB742 band combination) of the orogenic front of the Malargüe fold-and-thrust belt. White boxes correspond to the areas where active faults were recognized in this work. The dashed line is the approximate location of the Malargüe fold-and-thrust belt orogenic front. Red lines indicate the maximum horizontal stress (S_H) determined by Guzmán *et al.* (2007) based on borehole breakout determinations. Yellow dots are upper crustal seismic events (depth ≤ 20 km) from the INPRES catalog (1999-2018; www.inpres.gob.ar), PDE catalog (1953-2018; https://earthquake.usgs.gov/data/pde.php), and Spagnotto et al. (2015). All events have magnitudes lower than 4.5. B) Geologic map based on Giambiagi et al. (2012).

NNE- and NNW-trending normal faults were developed at the latitude of the study area (Legarreta and Uliana, 1999; Giambiagi *et al.*, 2009). The Middle Jurassic-Early Cretaceous was dominated by thermal subsidence (Legarreta and Gulisano, 1989), with an episode of normal fault reactivation in the Late Jurassic (Cegarra and Ramos, 1996; Charrier *et al.*, 2017; Mescua *et al.*, 2008). During the Late Cretaceous, Andean uplift began and the Neuquén basin became a foreland basin (Mpodozis and Ramos, 1989;

Tunik *et al.*, 2010). The latest Cretaceous to Paleocene fill of the basin corresponds to the first Atlantic marine ingression (Legarreta and Uliana, 1999).

The final uplift of the Andes took place since 20 Ma, as recorded by Miocene to recent synorogenic deposits locally preserved within the thrust belt and the foreland basin (*e.g.* Silvestro *et al.*, 2005; Horton et al., 2016; Horton and Fuentes, 2016). This orogenic stage is characterized by a progression of deformation towards the foreland since the middle Miocene (Mescua *et al.*, 2014), with the main development of the orogenic front (Fig. 3.1) taking place since 7 Ma in the northern part of the study area (Malargüe anticline, Silvestro *et al.*, 2005). In the southern part of the study area, the orogenic front was uplifted earlier (17 Ma at Sierra de Palauco, Silvestro and Atencio, 2009). Out of sequence activity in thrusts of the inner sector of the belt took place although its age is not well constrained (Kozlowski *et al.*, 1993; Mescua *et al.*, 2014; Bande et al., 2020). The main structures along the orogenic front are thrusts and reverse faults, with associated fault-related folds. Dominant east-vergent basement structures transfer shortening to the cover with detachment levels in shale and gypsum units (Kozlowski *et al.*, 1993). Locally, west-vergent thrusts developed giving place to triangle zones (Manceda and Figueroa, 1995; Silvestro and Atencio, 2009). Traverse structures, oblique to the strike of the orogen, have been recognized throughout the belt. These faults are usually interpreted as structures developed during the Late Triassic-Early Jurassic extensional episode and inverted during Andean orogenesis (e.g. Yagupsky *et al.*, 2008; Bechis *et al.*, 2010). Boll *et al.* (2014) related WNW-trending faults to inherited structures and interpreted ENE faults as opening fractures parallel to the direction of maximum horizontal stress during Andean orogenesis, and proposed that these structures were active between the Late Cretaceous and the late Miocene.

The Pliocene to Quaternary stress field has been the subject of debate in recent works. Some researchers suggested extension as a result of orogenic collapse of the Andes, proposing active normal faults (Ramos and Kay, 2006; Folguera *et al.*, 2008, 2009). These authors propose that volcanism in the area, was sourced in the mantle with a geochemistry that indicates a rapid ascent with little interaction with the crust, under a extensional regime in which normal faults were the conduits for the magma (Ramos and Kay, 2006; Folguera et al., 2008; 2009). Farther east, in the San Rafael Block area they documented normal faults (Ramos et al., 2014). In contrast, Silvestro *et al.* (2005) indicate activity of the Malargüe fault and uplift of the Malargüe anticline between 7 and 1 Ma (Fig. 3.1), and Giambiagi *et al.* (2008) document thrusting of Paleocene rocks over Pleistocene deposits in the Sosneado fault near the town of El Sosneado (Fig. 3.1).

3.3. Methods

We consider that structures that affect Pliocene-Quaternary sediments are active faults. These structures were recognized from published maps and satellite images and verified in the field. During fieldwork, we determined the deformed units, measured bed orientations and measured kinematic indicators on minor faults (cm to m of displacement) associated with the thrusts and strike-slip faults. Kinematic data was obtained from slickensides (direction of movement) and displacement of marker beds, mineral growth lineations and Riedel fractures (sense of movement). At each station, measurements vary between n=5 and n=20.

Kinematic data from faults were analyzed using the FaultKin software (Allmendinger, 2001). The software calculates P (contraction) and T (tension) axes for each datum and uses Linked Bingham statistics to calculate the aggregate deformation axes λ_1, λ_2 and λ_3.

The directions of the stress field components were obtained from borehole breakout data (Cox, 1970; Bell and Gough, 1982; Zoback *et al.*, 1985), and from the inversion of kinematic indicators from minor faults (Angelier, 1975, 1984, 1990; Lacombe, 2012).

Borehole logging reports on three wells were used to identify sections with breakouts (Cox, 1970; Bell and Gough, 1982; Zoback *et al.*, 1985). Breakouts are sections of the wellbore deformed by the stresses acting on the walls. The direction of the long section of the elliptic borehole can be measured and is interpreted to indicate the minimum horizontal stress (S_{hmin}) direction. Data quality was characterized using the World Stress Map classification (Sperner *et al.*, 2003).

Kinematic indicators were inverted for stress using the T-TECTO software (Zalohar and Vrabec, 2007) and the methods outlined in Giambiagi *et al.* (2016). We obtained reduced stress tensors that record the orientation of the principal stress (σ_1, σ_2 and σ_3) and the stress ratio $\phi =[(\sigma_2-\sigma_3)/(\sigma_1-\sigma_3)]$. The stress ratio permits to classify the stress regime defining compressional, strike-slip and extensional regimes and transitional states between them when two of the main stresses are similar in magnitude.

In order to estimate the magnitudes of stress in the region, we combine a mini-frac test from an oilwell in the northern study area with geomechanical considerations, taking into account the results from the stress inversion. The mini-frac test provides a measurement of the value of σ'_3 (Zoback, 2010). In order to estimate σ'_1 we take into account the evidences of active faulting in the region. Considering that the friction coefficient (μ_s) of fractures limits the effective differential stress, and assuming μ_s= 0.6 (Jaeger and Cook, 1979; Byerlee, 1978), we can use the relation:

$$\sigma'1 / \sigma'3 \leq [(\mu^2+1)^{1/2}+\mu]^2 \sim 3.1$$

to estimate σ'_1 (Jaeger y Cook, 1979; Zoback y Townend, 2001).

On the other hand, we calculate the vertical stress σ_v integrating the densities of the rock column of a borehole with density log data and compare this value with the estimations of σ'_3 and σ'_1 to determine the current stress field.

With the determined stress field, we carried out a slip tendency analysis (Morris *et al.*, 1996) using the “Stress analysis” module implemented in the Move© software. This method consists of calculating the relationship between the normal and shear stress on planes of all orientations, obtaining a value between 0 and 1. Planes with a value of slip tendency over 0.6, the friction coefficient assumed as standard (Byerlee, 1978), correspond to planes that will slide, indicating active faults in the prescribed stress regime.

Finally, taking into account the active faults recognized in the region, we modeled the Coulomb static stress change produced on the structures by earthquakes on the major thrusts of the area. This change is defined as

$$\Delta\sigma_f = \Delta\tau_\beta - \mu' \Delta\sigma_\beta$$

where $\Delta\sigma_f$ is the change is Coulomb stress, $\Delta\tau_\beta$ is the change in shear stress, μ' is the effective coefficient of friction and $\Delta\sigma_\beta$ is the change in normal stress (King *et al.*, 1994).

We used the Coulomb 3.2 software (Toda *et al.*, 2005; Lin and Stein, 2004) to calculate stress changes using different faults as sources with earthquake magnitudes according to their length (Wells and Coppersmith, 1994; Wesnousky, 2008; Leonard, 2010), always assuming a friction coefficient μ_s= 0.6.

3.4. Active faults

3.4.1 Northern sector

In the northern sector of the study area (Fig. 3.2), we studied three sectors where active structures could be recognized and characterized. At Cerro Pencal (Figs. 3.2, 3.3),

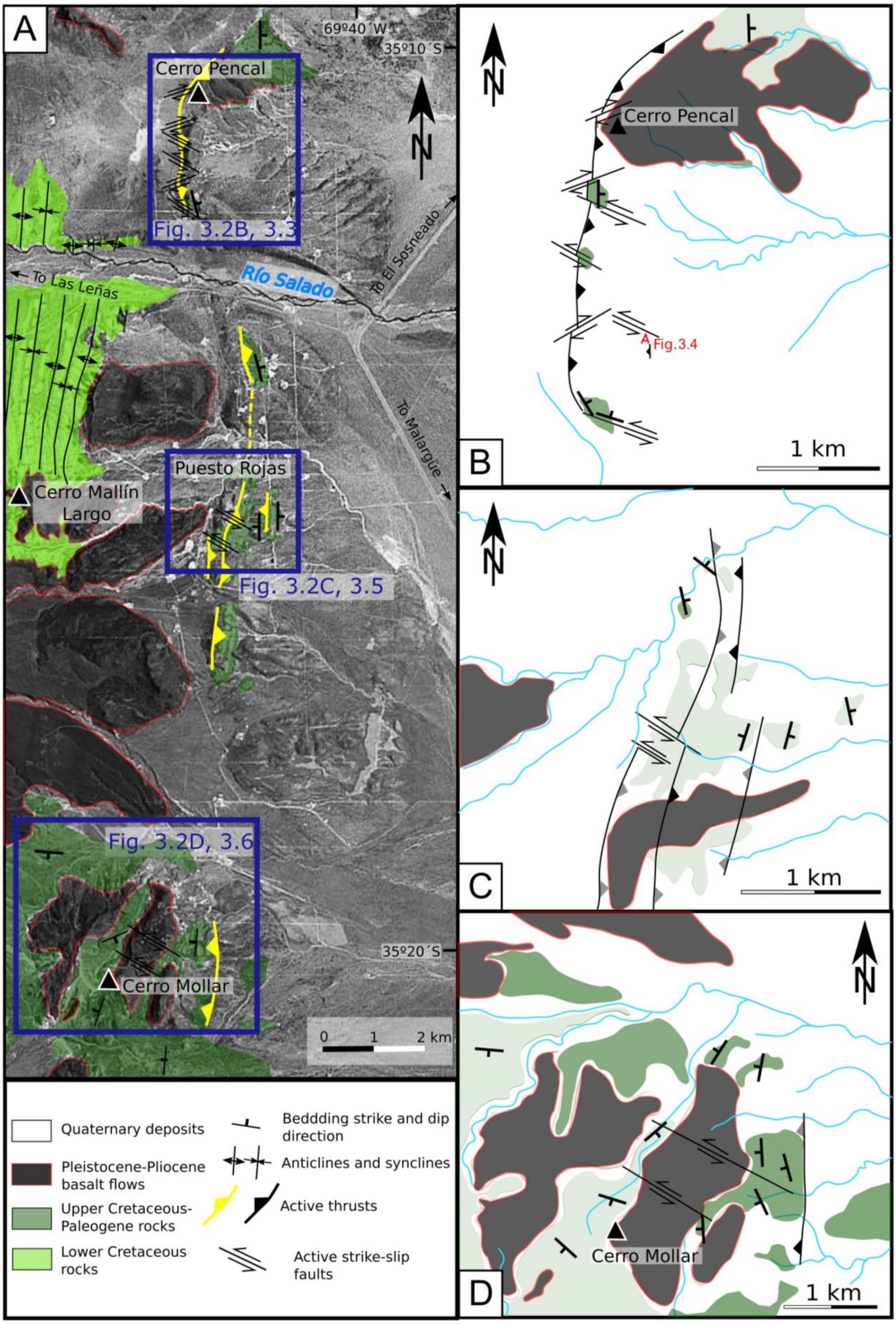

Figure 3.2: A) Location of northern study areas over LANDSAT ETM+ band 8, indicating the main active structures. Outcrops of Cretaceous to Pliocene rocks are shown, the rest of the study area is covered by Quaternary deposits. B,C,D) Geologic maps for the northern study areas.

an active N-S-striking low-angle backthrust places Upper Cretaceous redbeds of the Neuquén Group (Cenomanian-Campanian, Tunik et al., 2010) over Quaternary deposits, uplifting the Cerro Pencal hill (Figs. 3.2, 3.3). Quaternary deposits in the northern area correspond to polymictic conglomerates with subangular and subrounded clasts of up to 50 cm of diameter, locally containing larger clasts. Unfortunately no further constraints are available on the age of these deposits. The backthrust can be mapped for 5.5 km along strike, and its southern and northern ends are covered by alluvium. A minor east verging thrust affecting Quaternary deposits was also observed in this region (Fig. 3.4). The Cerro Pencal backthrust is segmented by 20 m-wide strike-slip fault zones composed of a series of minor subparallel faults (Fig. 3.3) with a few centimeters to 1.5 m of displacement, which accumulate tens of meters of displacement for the whole fault zone. Faults with WNW trend are sinistral, as shown by field relations and kinematic data (Fig. 3.3), while minor conjugate faults with ENE trend are dextral.

South of the Salado river, in Puesto Rojas (Fig. 3.2), a N-trending backthrust placing Upper Cretaceous redbeds over Quaternary deposits was also recognized, with a splay fault towards the west (Fig. 3.5). This structure could be the southern continuation of the Cerro Pencal backthrust, although it is uncertain if these structures constitute a single fault or two separate segments. The main fault strand can be recognized for 7 km along strike. The clearest evidence of recent activity of the strike-slip faults is found in Puesto Rojas, where WNW-trending sinistral fault juxtaposes mid-Cretaceous limestones (Huitrín Fm. of Albian age, Leanza, 2003) over Quaternary deposits (Fig. 3.5a). East of this structure, the same units are affected by an east-verging thrust (Fig. 3.5b). The easternmost active structure recognized in the area is an east-verging thrust that places Upper Cretaceous redbeds of the Neuquén Group over Quaternary (Fig. 3.5c). Associated with this structure, minor faults with 0.5 m of displacement affecting Late Cretaceous redbeds and Quaternary deposits also indicate active contraction and reverse faulting in this sector (Fig. 3.5d, e).

At Cerro Mollar (Figs. 3.2d and 3.6), mid-Cretaceous rocks are thrusted over Quaternary deposits along an east-verging structure. Poor exposure in this sector prevented us from determining the lateral extent of the fault. West of the thrust, WNW-trending faults corresponding to 40-50 m-wide zones of fracturing in Upper Cretaceous redbeds were observed. Analysis of kinematic data from these structures reveals a sinistral displacement, with minor or absent dip slip (Fig. 3.6).

The active thrusts that we recognized are linked to major blind reverse faults observed in seismic lines and wellbores (Kozlowski et al., 1993; Rojas and Radic, 2002),

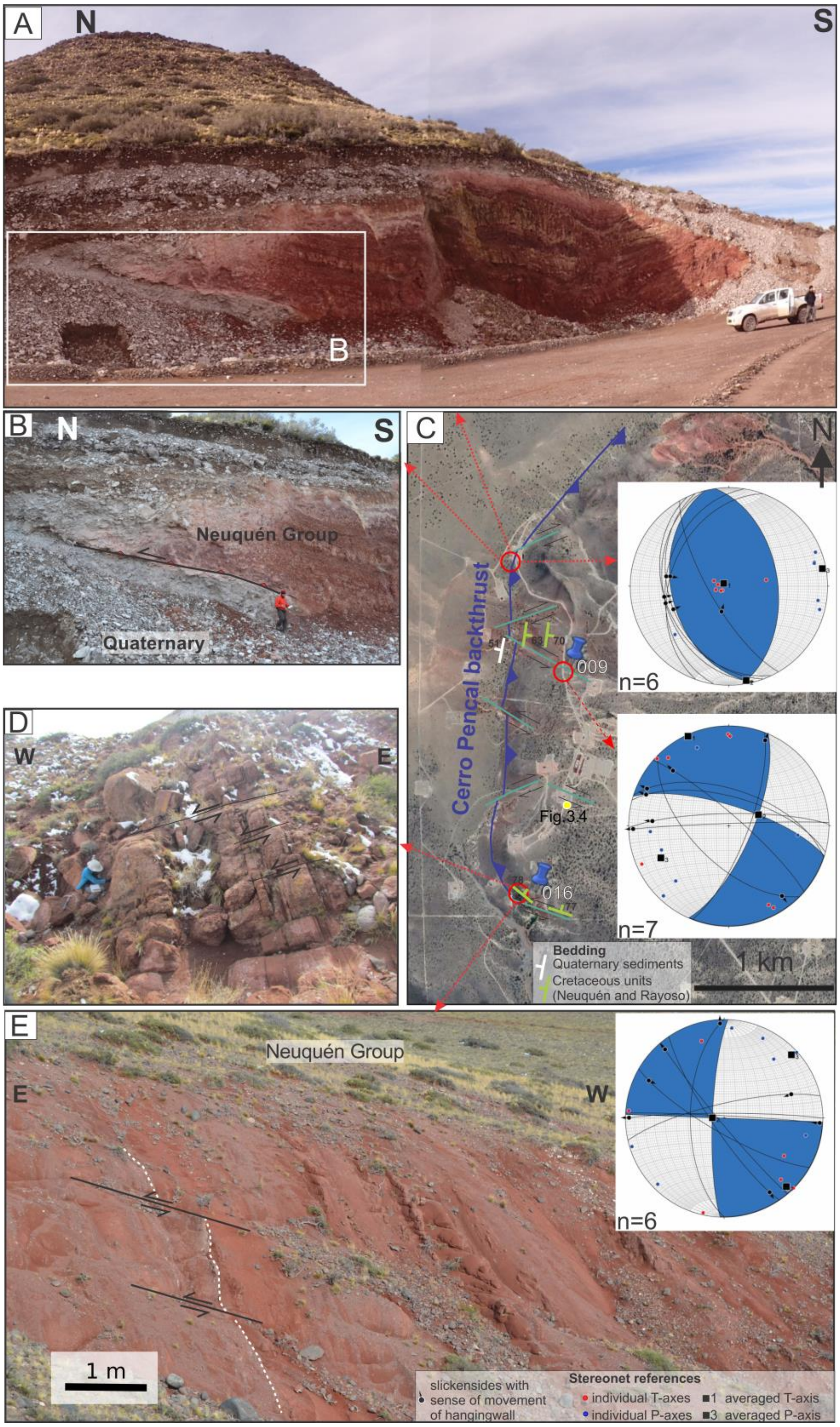

Figure 3.3: Active faults at Cerro Pencal, location in Fig. 3.2. A, B) Cerro Pencal backthust which places Late Cretaceous redbeds over Quaternary deposits. C) Mapped structures over Google Earth image, insets show kinematic data of minor faults indicating pure reverse movement of the Cerro Pencal backthrust and sinistral movement of the oblique strike-slip faults. The yellow dot indicates the location of Fig. 3.4. D, E) Strike-slip fault zones consisting of small faults with metric displacement. Inset in (E) shows kinematic data for the strike-slip faults.

the Malargüe (Fig. 3.1) and Puchenque (west of the study area) fault systems. These thick-skinned inverted Mesozoic normal faults are the main structures of the orogenic front of the Malargüe fold-and thrust belt at these latitudes (Fig. 3.7). The structural model proposed for the region suggests that these structures are also active.

***Figure 3.4**:* Minor east-verging thrust developed in Quaternary deposits at Cerro Pencal. Location in Figs. 3. 2B and 3. 5.

3.4.2 Southern sector

In the Cajón de los Caballos area (Figs. 3.1 and 3.8), poor exposures make the determination of cross-cutting relationship between structures difficult. Some N-trending thrusts in this sector (Fig. 3.8a) affect a volcaniclastic unit dated at 11-8 Ma (Loma Fiera Fm., Baldauf, 1993; Silvestro and Atencio, 2009; Horton et al., 2016). Traverse WNW- and ESE-striking lineaments were recognized on satellite images. Field observations indicate that these correspond to zones of fractures with strike-slip kinematic indicators (Fig. 3.8b). Cretaceous rocks are deformed close to the faults with beds rotated away from the regional N-trending attitudes. Satellite image interpretation suggests that strike-slip faults affect the younger rocks in the region (basalts dated at ca. 3-2 Ma, Silvestro and Atencio, 2009). We could only measure kinematic data on Late Cretaceous beds affected by WNW-trending strike-slip faults, showing sinistral displacement, and ESE-trending faults showing dextral movements (Fig. 3.8b). Based on the field data, we cannot determine if the thrusts are active structures or were active during the prolonged contractional history of this locality, which started at ~17 Ma (Silvestro and Atencio, 2009). Strike-slip structures, in contrast, affect Pliocene volcanic units, so we interpret them as active faults.

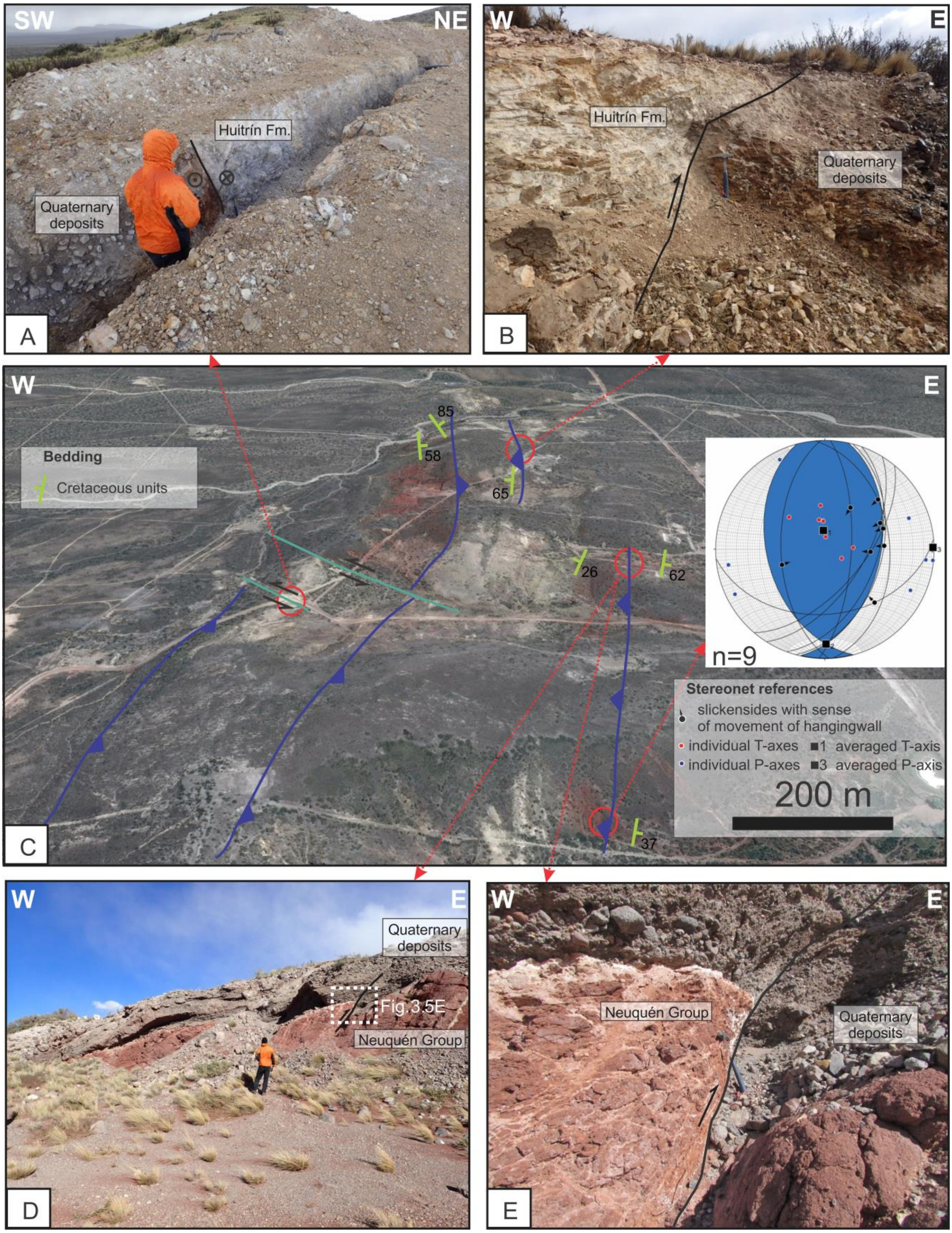

Figure 3.5: Active faults at Puesto Rojas, location in Fig. 3.2. A) Strike-slip fault affecting mid-Cretaceous rocks and Quaternary deposits. B) Thrust placing mid-Cretaceous limestones over Quaternary deposits. C) Mapped structures over Google Earth image. Inset shows kinematic data for a reverse fault zone consisting of minor thrusts. D, E) Minor faults with tens of cm of displacement associated with the thrust that uplifts Cretaceous rocks over Quaternary deposits.

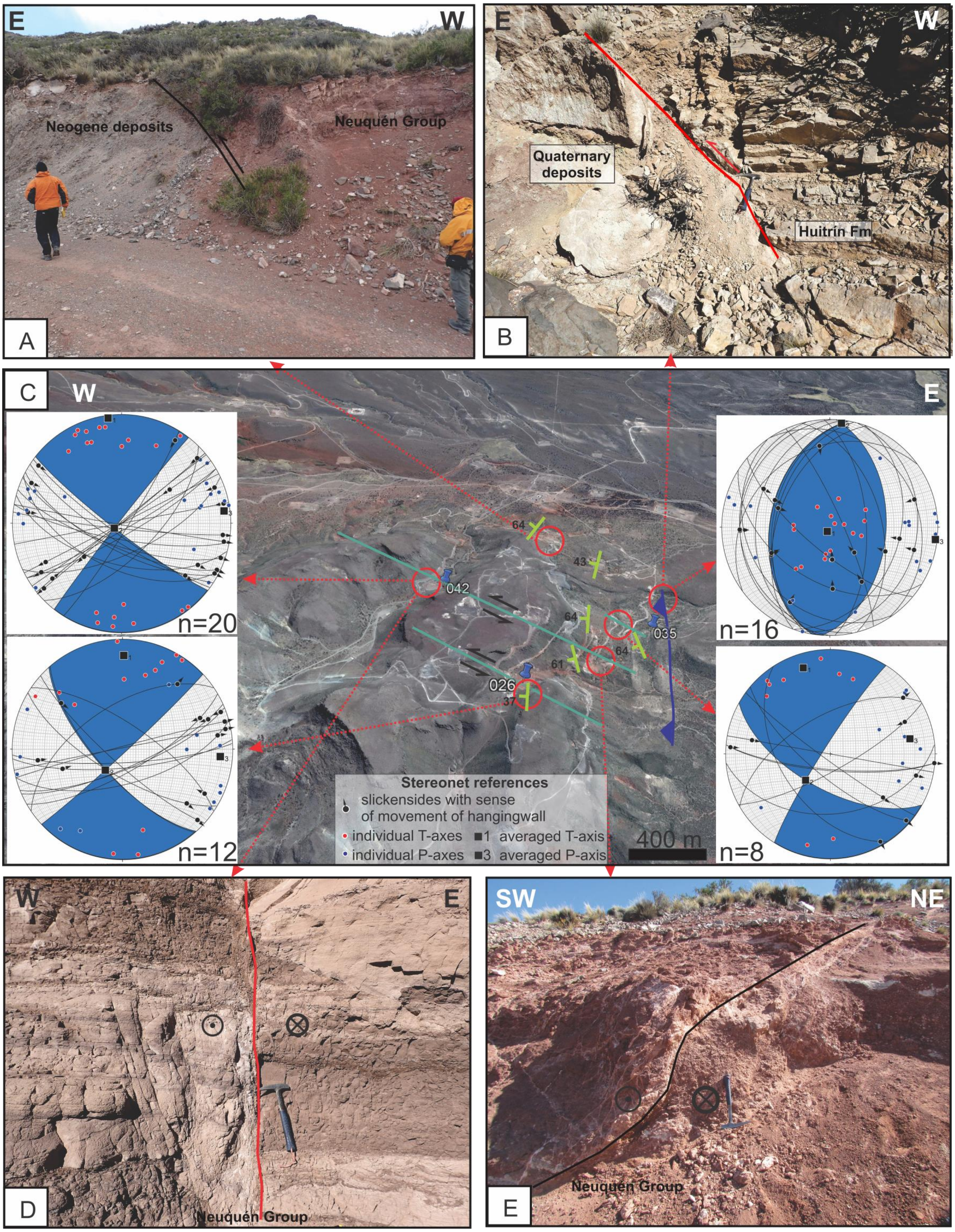

Figure 3.6. Active faults at Cerro Mollar, location in Fig. 3.2. A) Thrust placing Cretaceous redbeds over Quaternary deposits. B) Thrust placing mid-Cretaceous limestones over Quaternary deposits. C) Mapped structures over Google Earth image. Insets show kinematic data for reverse and sinistral faults. D, E) Strike-slip faults on Late Cretaceous redbeds

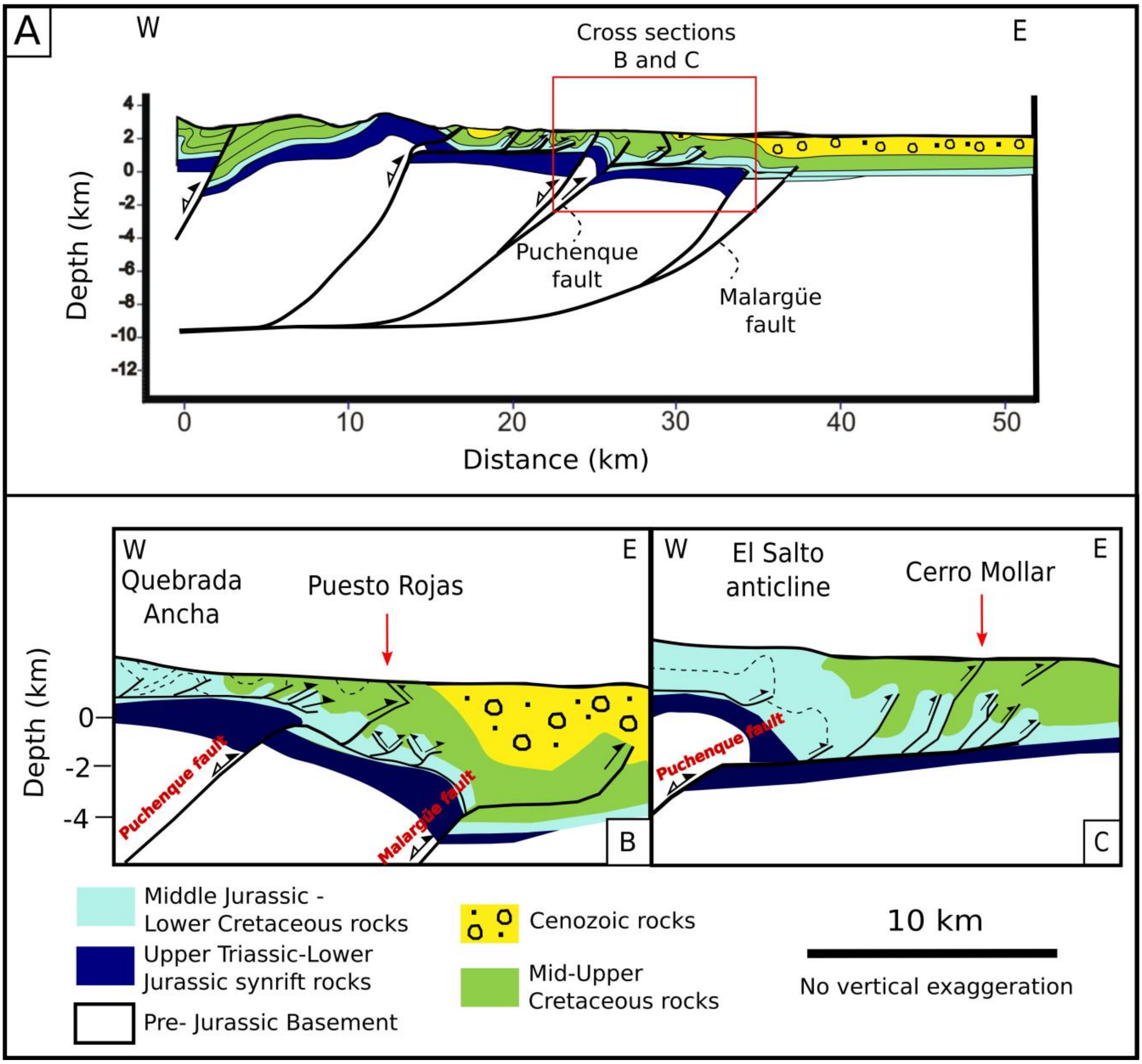

Figure 3.7. A) Regional cross-section across the Malargüe fold-and-thrust belt from Giambiagi et al. (2012). Note how the displacement on basement faults such as the Puchenque and Malargüe faults is transferred to thin-skinned thrusts that reach the surface in the study area. B, C) Cross-sections through the Puesto Rojas (B) and Cerro Mollar (C) sectors, showing the relationship between basement reverse faults and the active faults presented in this work, located with red arrows. Modified from Rojas and Radic (2002).

3.5. Kinematic analysis

Kinematic analysis of fault slip data was carried out on stations in all study areas (Figs. 3.3, 3.5, 3.6 and 3.8), and allowed us to characterize the movement of the mapped active faults.

Thrusts show pure dip-slip with a consistent E-W contraction direction. The P and T axes for each station are grouped in clusters indicating a well-defined contraction direction for this deformation. While some of the strike-slip faults affect Quaternary

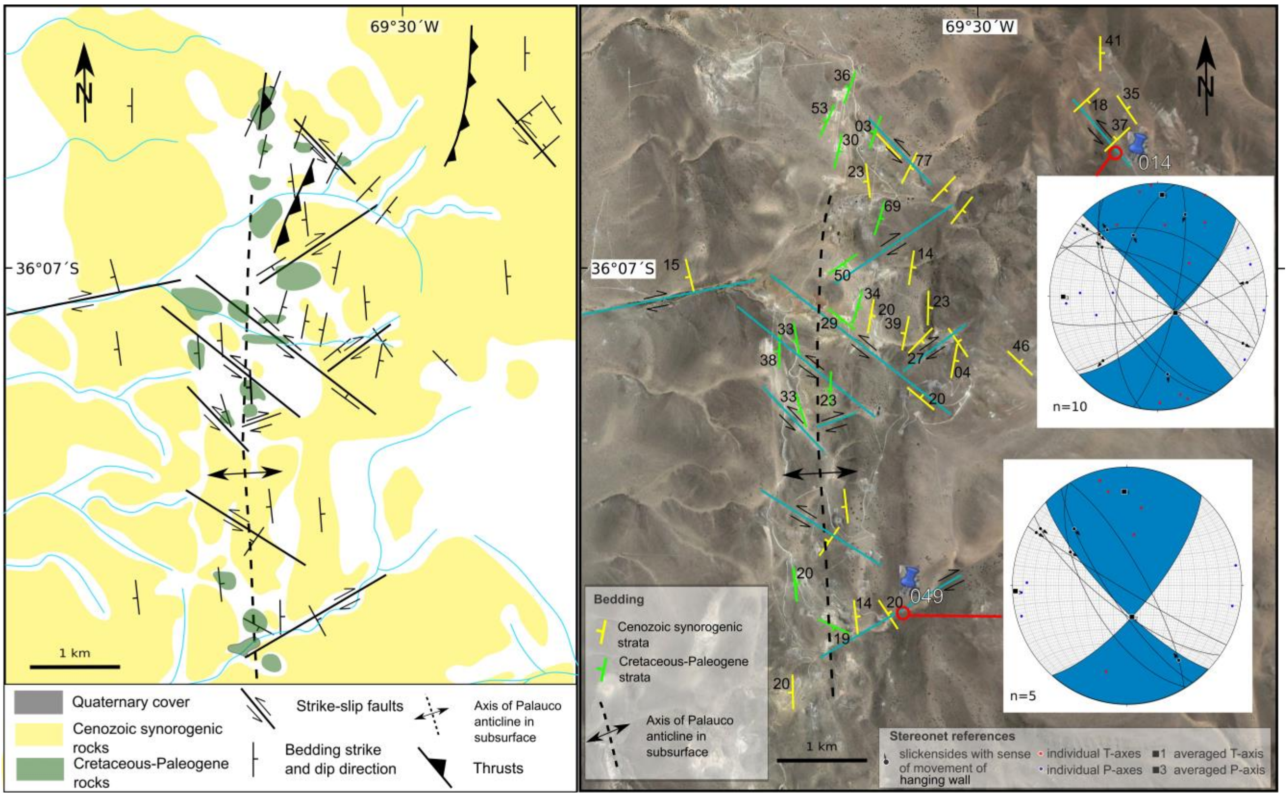

Figure 3.8. Active strike-slip faults in the Cajón de los Caballos, location in Fig. 3.2. (A) Geologic map of the Cajón de los Caballos area. (B) Mapped structures over Google Earth image. Insets show kinematic data for minor faults associated with two of the strike-slip faults..

deposits (Fig. 3.5a), most kinematic data from strike-slip faults were measured on structures that affect Cretaceous rocks. In order to analyze the possibility that these structures were ancient faults previous to folding in the region, we compared the kinematic results in the deformed (current) and unfolded state (Fig. 3.9). In the deformed state, all strike-slip kinematic data indicate NW or E-W contraction directions, with some dispersion of P and T axes in spite of which the fields of contraction and extension are well defined (Fig. 3.9). In contrast, the unfolded data show different deformations: for stations with shallow dipping strata (both stations at Cajón de los Caballos and station 42 at Cerro Mollar, locations in Figs. 3.6 and 3.8), the restoration does not change the kinematics of the faults. For stations with steeply dipping strata (stations 26 and 35 at Cerro Mollar and stations 9 and 16 at Cerro Pencal, locations in Figs. 3.3 and 3.6), the restored data indicate extension with NW to N extension directions.

We consider that the faults post-date folding because (i) the dependence of fault kinematics in the restored state on the current bedding dip (strike-slip for low dips and extension for high dips) suggests that the faults post-date folding; (ii) there are no indications of N-S extension between the Late Cretaceous and the Miocene in the region, and (iii) it seems unlikely that pre-folding faults with different kinematics and from different

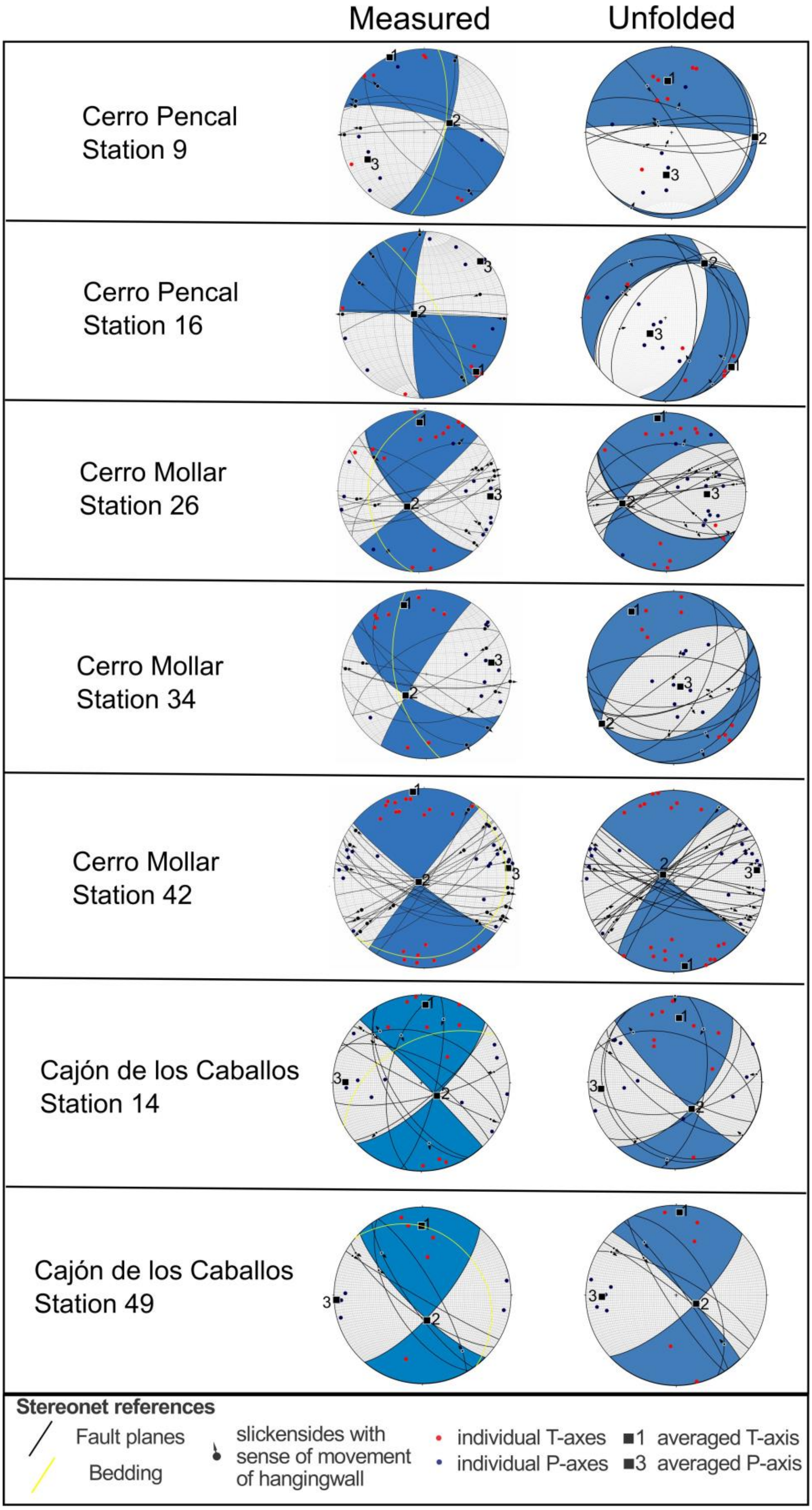

Figure 3.9: Kinematic fault-slip data for strike slip faults. For each station, the left stereonet shows the measured data and the right stereonet shows the data after bed unfolding. Note that all the measured data correspond to a compatible deformation with roughly E-W contraction, while the unfolded data produce different deformations depending on bedding dip at each stations, which indicates that the measured faults post-date the folding.

locations would be folded in such a way to produce kinematics consistent with a younger strike-slip deformation event recorded in the same localities.

We propose that both kinds of structures: N-trending thrusts and ESE- and WNW-trending strike-slip faults, were active during the Pliocene?-Quaternary to the present.

3.6. Stress state

3.6.1. Stress directions

We obtained principal stress axes directions from two independent sources: (i) maximum and minimum horizontal stress directions (S_{Hmax} and S_{hmin}) were measured from borehole breakouts in oil wells from the northern area; and (ii) the inversion of fault kinematic data (Angelier, 1975, 1984, 1990) which provides the direction of the three main stress axes and the stress ratio ϕ (see section 3.3. Methods).

Wellbore A

Unit	**Length (m)**	**S_H strike**	**Quality**
Avilé Member	40	78	D
Lower Agrio Formation	200	66	

Wellbore B

Unit	**Length (m)**	**S_H strike**	**Quality**
Avilé Member	82	88	D
Lower Agrio Formation	50	82	

Wellbore C

Unit	**Length (m)**	**S_H strike**	**Quality**
Avilé Member	44	97	D

Table 3.1 Borehole breakout data from the Cerro Pencal sector.

Borehole breakouts were measured in three wells in the northern part of the study area (Cerro Pencal; Fig. 3.2). While the quality of breakout data was low due to the short length of the analyzed well sections (class D in the classification of the World Stress Map project; Sperner *et al.*, 2003; see Table 3.1), the results are consistent with regional studies (Guzmán *et al.*, 2007, 2011; Guzmán and Cristallini, 2008) and those from inversion of fault kinematic data presented in this work, indicating E-W to ENE S_{Hmax} directions (Fig. 3.10).

Inversion of kinematic data for stress was carried out for three locations in Cerro Mollar, where we had the highest number of measurements. The results are shown in Figure 3.11 and Table 3.2. Stress directions are consistent with the kinematic P and T axes and with S_{Hmax} and S_{hmin} directions derived from borehole breakouts (Fig. 3.10). In addition to this, the stress ratio ϕ indicates similar magnitudes of σ_2 and σ_3 in one case (station 26, Table 3.2), while data from station 42 indicate a pure strike-slip regime and stations 35 and 36 indicate a pure reverse stress state.

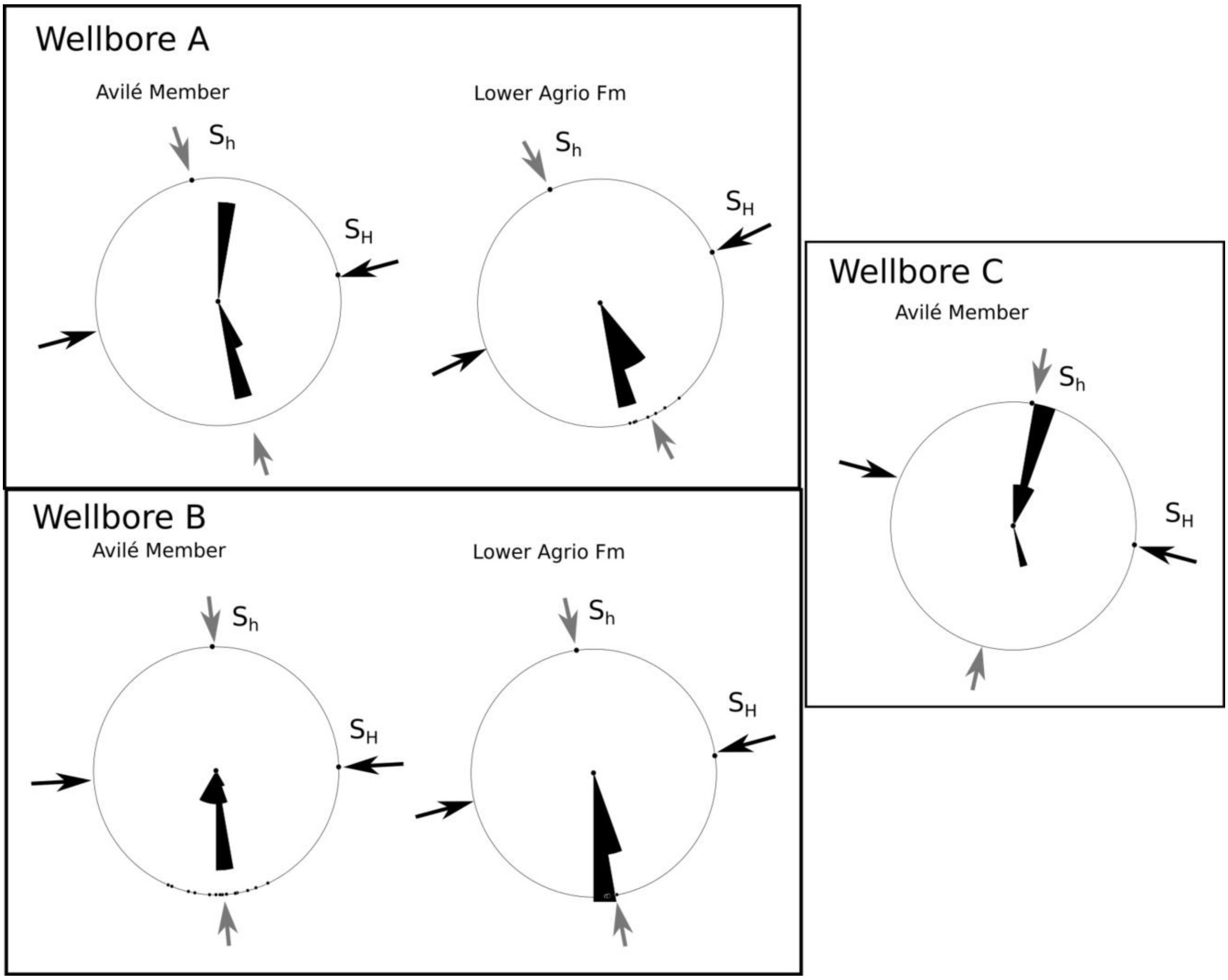

***Figure 3.10**:* Maximum (SH) and minimum (Sh) horizontal stress derived from borehole breakout data.

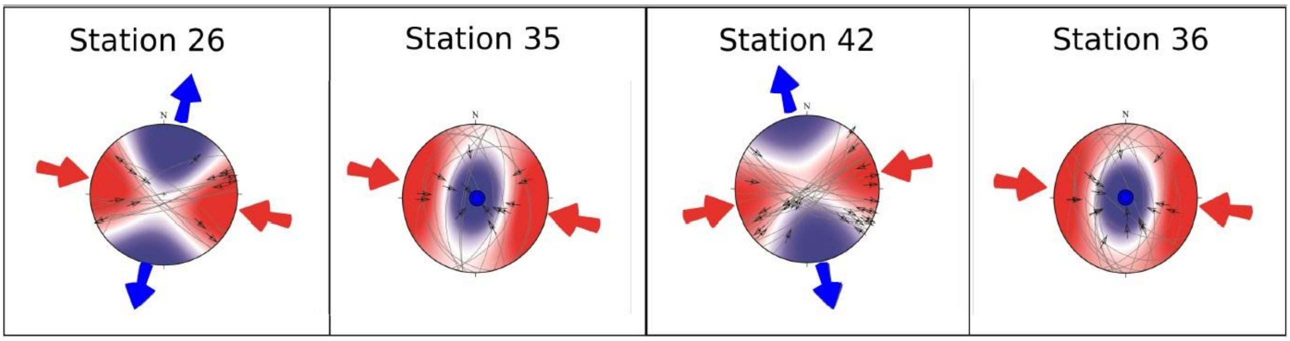

Figure 3.11: Stress inversion results. The direction of σ1 is shown in red arrows and the direction of σ3 in blue arrows. Location of stations in Fig. 3.6.

Site	Latitude	Longitude	n	nT	σ_1	σ_2	σ_3	ϕ	α	Regime
26	35°17'47,54''S	69°48'02,33''W	12	12	44/13	288/63	140/23	0,10	14	SL/R
35	35°19'48,84''S	69°42'03,17''W	18	20	272/2	3/25	178/64	0,60	27	R
36	35°19'45,31''S	69°41'55,22''W	16	16	277/0	187/2	21/88	0,69	20	R
42	35°19'42,02''S	69°42'56,51''W	21	25	248/2	358/84	158/6	0,50	17	SL

Table 3.2: Stress inversion of kinematic data. n= number of measurements used for the inversion; nT= total number of measurements; σ_1,σ_2,σ_3= principal stress axes; ϕ=(σ2-σ3)/(σ1-σ3); and α=misfit angle. Stress regimes are: SL/R=strike-slip/reverse; R/SL= reverse/strike-slip; SL=strike-slip.

3.6.2. Stress magnitudes

In order to better understand the stress state, we used wellbore data combined with geomechanical considerations to obtain the magnitude of stresses (see section 3.3 Methods). We calculated the vertical stress (σ_V) as a function of depth by integrating density data from wellbore profiling. The minimum principal stress magnitude was obtained from a mini-frac test (Zoback, 2010) carried out in a wellbore in the northern sector (Puesto Rojas) for a depth of 1277 m: σ_3=26 MPa (Fig. 3.12). At this same depth, the vertical stress from density data was σ_V=30.5 MPa.

Estimating the maximum stress σ_1 requires some assumptions. In our case study, since we know that there are active faults in the area, and assuming μ_s= 0.6 (see section 3.3 Methods), we obtain σ_1=80.6 MPa.

These results determine a stress state in which:

$$\sigma_3 = 26 \text{ MPa} < \sigma_2 = \sigma_V = 30.5 \text{ MPa} < \sigma_1 = 80.6 \text{ MPa}$$

and therefore $\sigma_3 \sim \sigma_2 << \sigma_1$.

This stress regime corresponds to a reverse/strike-slip faulting environment in which both kinds of structures are active due to small fluctuations in the values of σ_3 and σ_2 that interchange the orientation of the minimum and intermediate stresses (Zoback, 2010).

The determined stress magnitudes and the differential stress ($\sigma_1 - \sigma_3$ = 54.6 MPa) are consistent with estimations from frontal regions of other orogens (Lacombe, 2001; Beaudoin and Lacombe, 2018).

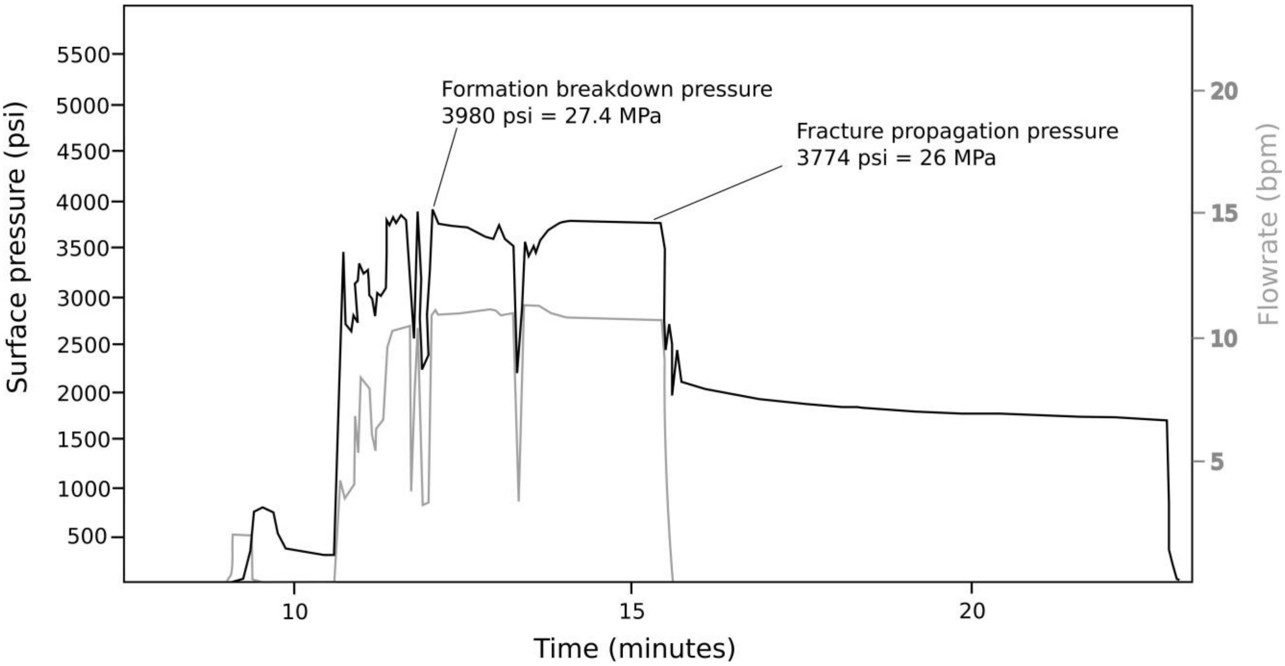

***Figure 3.12**:* Mini-frac test in a well of the Puesto Rojas area. The Fracture Propagation Pressure corresponds to the minimum principal stress magnitude (3774 psi=26 MPa).

3.7. Slip tendency analysis

Combining the results of sections 3.4 and 3.5, we carried out a slip tendency analysis (Morris *et al.*, 1996). As in the previous case, we assume μ_s= 0.6, which implies that we are not considering weak faults that may be inherited from the pre-Andean history. We analyzed two cases, corresponding to the two alternating stress states that we propose for the region.

In the reverse faulting regime, $\sigma_3 = \sigma_v = 26$ MPa; $\sigma_1 = 80.6$ MPa is horizontal with a direction parallel to the Nazca-South America convergence (N80ºE), based on breakout

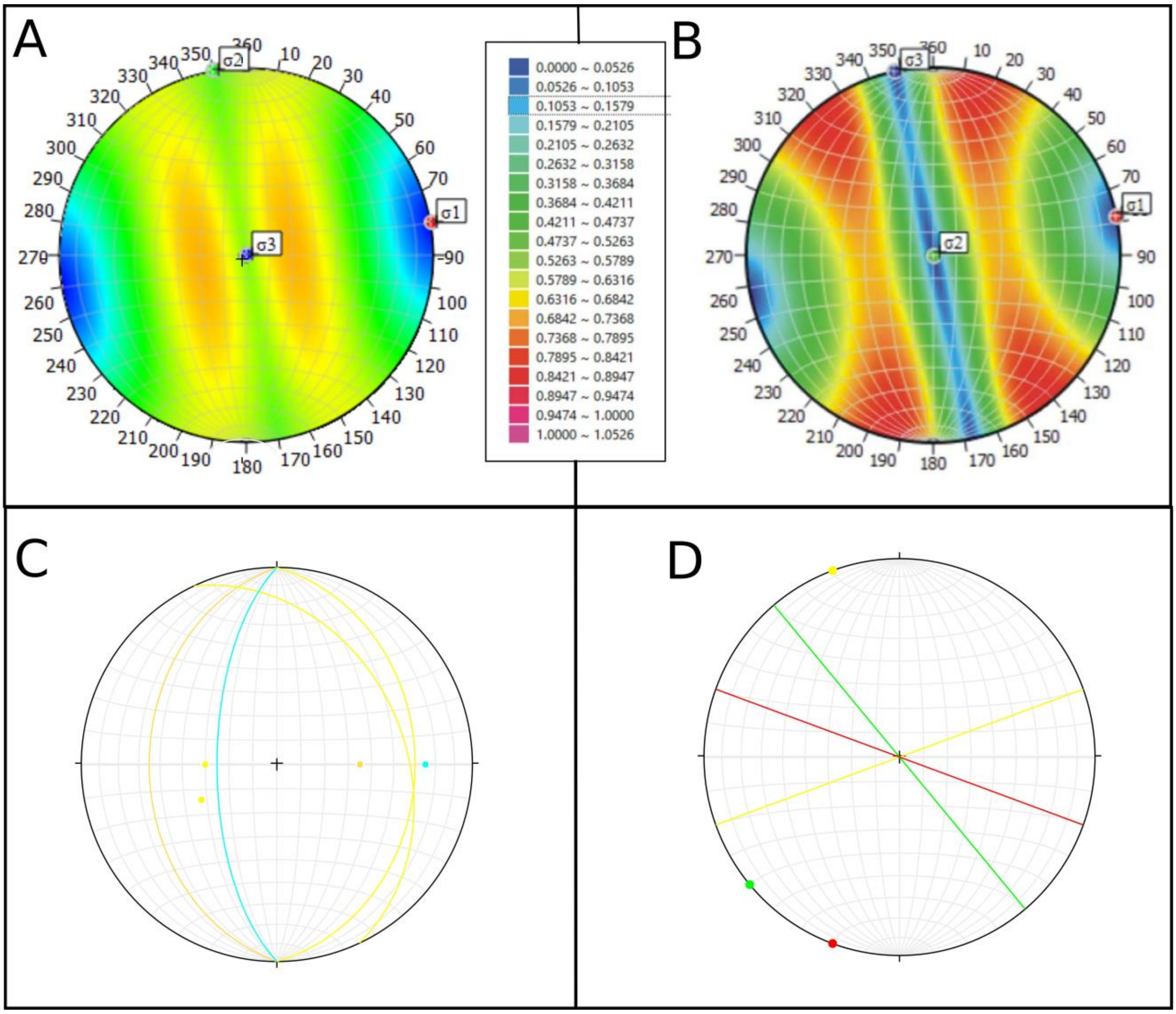

Figure 3.13. Results of slip tendency analysis. Colors indicate slip tendency value for fault plane poles. Faults with slip tendency>0.6 are active in the proposed stress field. (A) Reverse faulting regime with σ1 of azimuth 80º. (B) Strike-slip faulting regime with σ1 of azimuth 80º. (C) Thrust planes mapped in the study area, color coded to show their slip tendency in the compressional stress field. Note that high-angle reverse faults show low slip tendency (green color) suggesting that some mechanism has to act to produce their movement (e.g., high fluid pressure). Low angle reverse faults show high slip tendency (yellow color). (D) Strike-slip faults mapped in the study area, color coded to show their slip tendency in the strike-slip stress field. Sinistral, WNW faults show the highest slip tendency (red color). Dextral ESE faults also show high slip tendency (yellow), whereas sinistral NW faults show low slip tendency (green color). However these sinistral NW faults fall in the red field if σ1 has an azimuth of 110º, also observed in the study area.

data and the stress inversion for stations 35 and 36 (Fig. 3.11); and $\sigma_2 = 30.5$ MPa is horizontal and orthogonal to σ_1. In this stress state, N to NNW low-angle faults are active, consistent with the thrusts and backthrusts observed in the field (Fig. 3.13a,c).

In the strike-slip regime, σ_3 and σ_2 are interchanged, and therefore $\sigma_2 = \sigma_v = 30.5$ MPa and $\sigma_3 =26$ MPa is horizontal and orthogonal to σ_1 that remains in the same orientation and magnitude of the previous case as obtained in station 26. This stress state activates high angle WNW and ENE strike-slip faults, like the ones mapped in the field (Fig. 3.13b,d). The same stress magnitudes but with a ESE-trending σ_1, like the one obtained for station 42 (Fig. 3.11) activate NW trending faults.

This indicates that the Pliocene to recent activity of N-trending thrusts and WNW- and ESE-strike slip faults can be the result of a reverse/strike-slip faulting regime in the region. In addition to this, pre-existing faults with those orientations will likely be reactivated.

3.8. Coulomb stress variations

We calculated the static stress change in the faults of Cerro Pencal, Puesto Rojas and Cerro Mollar produced by the reverse faults mapped in the region, the Sosneado and Malargüe faults (Figs. 3.1 and 3.7), and the structures reported in this work. In particular, we analyzed the stress change on the strike-slip faults. With the Sosneado thrust or the Cerro Pencal and Puesto Rojas backthrusts as sources, static stress change was not favorable to reactivation of the strike-slip faults. In contrast, the static stress change produced by a M=6 earthquake on the Malargüe fault produced positive and important

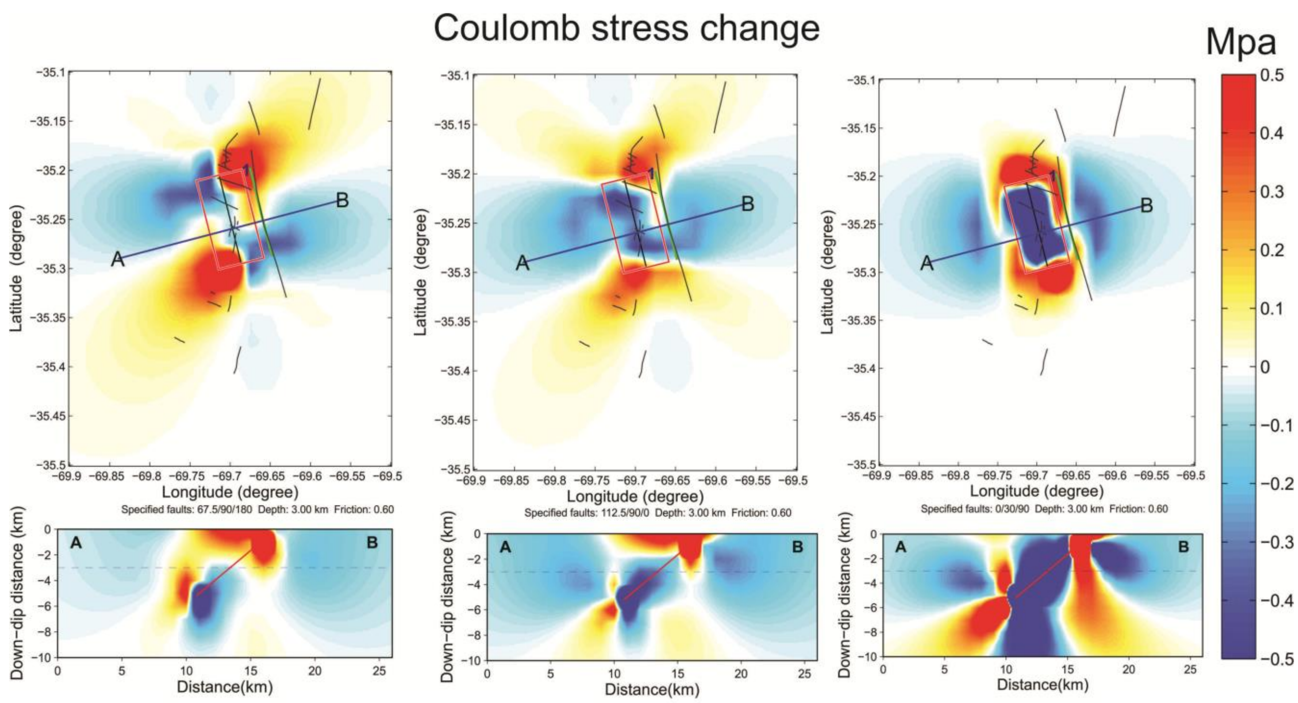

Figure 3.14:. Coulomb static stress change. In all cases the source is a Mw=6 earthquake on the Malargüe fault and the receptors are: (A) dextral faults (strike 67.5°, vertical), (B) sinistral faults (strike 112.5°, vertical), and (C) reverse faults (strike 0°, dip 30°).

values (higher than 0.3 MPa) on the strike-slip faults (Fig. 3.14). The highest values of static stress change on the studied faults are in dextral faults on the edges of the Malargüe fault, while values for the sinistral faults are also positive. This result suggests that seismic activity on the Malargüe fault favors seismicity on the strike-slip faults in the context of a reverse/strike-slip faulting regime (in the sense of Zoback, 2010).

3.9. Discussion

3.9.1. Tectonic implications

The stress field in the Andean retroarc is determined by a combination of the convergence of the Nazca and South American plates and topographic forces (Guzmán *et al.*, 2007): the general E-W trend of $S_H=\sigma_1$ is a response to the convergence direction, while topographic forces produce small rotations to ESE and WNW trends. Local deformation structures produce localized NNE to NNW trends (Guzmán *et al.*, 2007). Our results are consistent with the determinations of the orientation of S_H made by these authors in the frontal Malargüe fold-and-thrust belt.

The identification of active thrusts and strike-slip faults throughout the orogenic front of the Malargüe fold-and-thrust belt, and the relationship of these structures with the stress field, indicates that this region was not affected by an extensional collapse during the Pliocene-Quaternary as previously proposed by Ramos and Kay (2006) and Folguera *et al.* (2008, 2009). In contrast to this proposal, thrusts are active along parts of the orogenic front, indicating that the region is currently under compression.

The thrusts along the frontal Malargüe fold-and-thrust belt developed in the middle Miocene (~15 Ma, Silvestro *et al.*, 2005) and were episodically active since that time, accumulating significant displacement (more than 3 km according to Giambiagi *et al.*, 2009b). The thrusts are cross-cut by oblique strike-slip faults with tens of meters of displacement which postdate folding in thrust-related anticlines, and were likely active since the Pliocene-Quaternary.

The stress state determined from inversion of fault slip data and available well bore information (minifrac test) corresponds to a reverse/strike-slip faulting regime (Zoback, 2010) in which σ_2 and σ_3 have similar magnitudes and are locally exchanged, which leads to an alternation of the activity of both kinds of structures producing the "σ_2 paradox" defined by Tavani *et al.* (2015). Furthermore, a Coulomb static stress change analysis indicates that in this stress regime, activity on the basement N-trending reverse faults increases the likelihood of activation of the strike-slip faults. We therefore propose that strike-slip faults were active for short periods of time following earthquakes on the major reverse faults.

A model of the evolution of the region during the Miocene (Barrionuevo *et al.*, 2019) suggests that these variations in the stress regime are a long-term feature of the orogenic front and that the alternation between compression and strike-slip deformation took place intermittently in different sectors of the Malargüe area during the Neogene and Quaternary.

3.9.2. Implications for seismic hazard

The study area is located ~25 km away from the main city in southernmost Mendoza province, Malargüe, that has a population of over 26.000 according to the 2010 census. Important infrastructure related to oil extraction activities is found within the study area and its surroundings.

While there is no record of destructive local earthquakes in the study area, probably due to the recent permanent population (the city of Malargüe was founded in 1886), low-magnitude seismic activity has been detected in the region (Fig. 3.1). Instrumental seismicity is restricted to international or national networks (PDE and INPRES catalogs) and local seismic experiments located near the region (Spagnotto *et al.*, 2015). All the events with depths lower than 20 km have magnitudes M ≤ 4.5. Important activity has been observed in the Sosneado thrust (Fig. 3.1), already documented as an active structure by Giambiagi *et al.* (2008). Only a few events have been detected in the study area and can be the result of activity either on the Malargüe and Puchenque faults or on the oblique strike-slip faults.

In order to estimate the implications of the main active faults recognized in this work for seismic hazard, we determined the maximum possible earthquake magnitude for the thrusts from their surface length, based on the equations available in the literature (Wells and Coppersmith, 1994; Wesnousky, 2008; Leonard, 2010). We calculated the maximum moment magnitude (M_W) for the Cerro Pencal backthrust and the Puesto Rojas backthrust as separate structures, and also combined in case both can rupture as a single fault. The result shows potential M_W between 5.5 and 6.2 (Table 3.3), which suggests that these faults can generate moderate earthquakes that should be taken into account in seismic hazard and risk studies.

Fault	Surface length (m)	Maximum magnitude Wells and Coppersmith (1994)	Maximum magnitude Wesnousky (2008)	Maximum magnitude Leonard (2010)
Cerro Pencal backthust	5500	5.8	5.5	5.8
Puesto Rojas backthrust	7000	5.9	5.7	5.9
Cerro Pencal + Puesto Rojas backthrust	12500	6.2	6.2	6.2

Table 3.3: Maximum earthquake magnitude estimated from the surface length of thrusts in the study area.

3.10. Conclusions

We document active orogen parallel thrusts and oblique strike-slip faults in the orogenic front of the Malargüe fold-and-thrust belt, in the Andes between 35° and 36°S. Based on the available data, we propose that the Pliocene and Quaternary activity of both kinds of faults is the result of a reverse/strike-slip faulting regime in which $\sigma_3 \sim \sigma_2 << \sigma_1$. The lack of historical destructive earthquakes in the region is likely a reflection of the recent permanent population of the area and the long recurrence period of the structures, however, based on their surface length, we estimate that the thrusts can produce earthquakes of magnitude ~6.

Chapter IV

4. First approach to numerical modeling of the subduction system

Resumen

En este capítulo se presentan las técnicas, la configuración de los modelos y el enfoque que usamos para modelar el sistema de subducción. Se utilizó el código de elementos finitos/diferencias finitas llamado LAPEX-2D para simular la subducción de una losa prescripta cinemáticamente debajo de una placa continental. Esta configuración fue diseñada para centrarse en las características de la placa superior que inferimos son importantes en la forma en que el sistema se comporta bajo compresión. Aunque los resultados no fueron realistas, el trabajo involucrado es una parte relevante del proyecto de doctorado y el proceso de aprendizaje relacionado. Se continúa trabajando con *setups* donde la losa no está prescripta.

Abstract

In this chapter we present the techniques, models setup and modeling approach to model the subduction system. We used the finite-element/finite-difference code called LAPEX-2D to simulate a kinematically prescribed slab subducting below a continental plate. This setup was designed to focus on the upper-plate characteristics that we infer are important on how the system behaves under compression. Although results were not realistic the work involved is a relevant part of the doctoral project and its related learning process. We continue working with setups without the kinematic prescription of the slab.

4.1 Introduction

In general, the geological processes we want to model are on a temporal scale of 10^6-10^7 years (millions to tens of millions of years) and the spatial scale around 10^3 km in the horizontal scale and 10^2 km in the vertical (depth) scale. The subduction processes are intrinsically complex to model and many geological and physical aspects are still enigmatic due to our limited observations in both time and space. Besides, it is necessary to simulate complex rheologies, including elasticity, plasticity and viscosity (stress- and temperature-dependent). For this, two different approaches were attempted, the first one which simulates the subduction system, with both plates and its interface, and the second approach, modeling the upper plate behaviour under compression (see Chapter 5).

In this chapter, we introduce the first modeling approach, simulating the whole subduction system, using the code LAPEX-2D (Babeyko et al., 2002; Babeyko and Sobolev, 2005). Although we did not achieve a realistic simulation of the subduction system so far, the work involved is relevant as part of the learning process during the doctoral studies and implies a methodological progress. Furthermore, it will help guide next steps for the application of this code to simulate the subduction system.

4.2 LAPEX-2D

4.2.1 Methodology

LAPEX-2D (LAgrangian Particle Explicit) is a 2D, parallel, thermomechanical, finite-element/finite-difference method (Babeyko et al., 2002; Babeyko and Sobolev, 2005; Sobolev and Babeyko, 2005) which combines the explicit Lagrangian algorithm FLAC (Cundall and Board, 1988; Poliakov et al., 1993) with the particle-in-cell method (Sulsky et al., 1995; Moresi et al., 2003). The particles track material properties and the full stress tensor, minimizing numerical diffusion related to remeshing. This code allows the employment of realistic temperature- and stress-dependent, visco-elastic rheology combined with Mohr-Coulomb plasticity. The rheological material parameters we used in the models were taken from experimental studies (Table 4.1).

The code solves a coupled 2D system of conservation equations for momentum (Eq. 4.1), mass (Eq. 4.2) and energy (Eq. 4.3), together with rheological equations (Eqs. 4.4 and 4.5) for a Maxwell visco-elastic body with temperature and stress-dependent viscosity (Eq 4.4) and a Mohr-Coulomb failure criterion (Eq. 4.5) (Sobolev et al., 2006). Viscous deformation consists of competing dislocation, diffusion and Peierls creep mechanisms (Kameyama et al., 1999).

$$\frac{-\partial p}{\partial x_i} + \frac{\partial \tau_{ij}}{\partial x_j} + \rho g_i = 0, i = 1{,}2$$ Eq. 4.1

$$\frac{1}{K}\frac{dp}{dt} - \alpha\frac{dT}{dt} = \frac{-\partial v_i}{\partial x_i}$$ Eq. 4.2

$$\rho C_p \frac{dT}{dt} = \frac{\partial}{\partial x_i}\left[\lambda(x_i, T)\frac{\partial T}{\partial x_i}\right] + \tau_{ij}\left(\acute{\varepsilon}_{ij}^{v} + \acute{\varepsilon}_{ij}^{p}\right) + \rho A$$ Eq. 4.3

$$\frac{1}{2G}\frac{\acute{d}\tau_{ij}}{dt} + \frac{1}{2\eta}\tau_{ij} + \acute{\varepsilon}_{ij}^{p} = \acute{\varepsilon}_{ij}$$ Eq. 4.4

$$\frac{1}{\eta(\tau,T)} = \frac{1}{\eta dif(T)} + \frac{1}{\eta dis(\tau,T)} + \frac{1}{\eta p(\tau,T)}$$

$$\sigma_1 - \sigma_3 \frac{1+sin\phi}{1-sin\phi} + 2c\sqrt{\frac{1+sin\phi}{1-sin\phi}} = 0 \qquad \text{Eq 4.5}$$

$$g_s = \sigma_1 - \sigma_3$$

In the equations above Einstein summation applies and: xi are coordinates, t is time, vi velocities, *p* pressure, τ_{ij} is stress deviator, $\acute{\varepsilon}_{ij}$ is the strain-rate deviator, $\acute{\varepsilon}^{v}_{ij}$ viscous strain-rate deviator, $\acute{\varepsilon}^{p}_{ij}$ plastic strain-rate deviator, d/dt convective time derivative, $\hat{d}\,\tau_{ij}/dt$ Jaumann co-rotational deviatoric stress rate, ρ density, g_i gravity vector, K: bulk modulus, G: shear modulus, η: viscosity; ηdif: diffusion creep viscosity, ηdis: dislocation creep viscosity, ηp: Peierls creep viscosity, τ: square root of second invariant of stress tensor, R: gas constant, T: temperature, σ_1: maximum principal stress, σ_3: minimum principal stress, ϕ: angle of friction, *c*: cohesion, g_s: shear plastic flow potential, C_p: heat capacity, λ: heat conductivity; A: radioactive heat production.

Material properties Flow law	Wet quartzite (WQ)	Wet plagioclase (WP)	Columbia diabase (CD)	Dry olivine (OD)	Wet olivine (OW)
Phase	Felsic upper crust	Mafic continental lower crust	Mafic oceanic crust	Lithospheric mantle	Asthenosphere
Density[1], ρ_0 (kg/m^3)	2800	3000	3000	3300	3300
Heat expansion, α (K^{-1})	3.70E-05	2.70E-05	2.70E-05	3.00E-05	3.00E-05
Specific heat, C_p (kJkg^{-1}K^{-1})	1.2	1.2	1.2	1.2	1.2
Heat conductivity, k (WK^{-1}m^{-1})	2.5	2.5	2.5	3.3	3.3
Heat productivity, A (µWm^{-3})	1	0.3	0.3	0	0
Friction angle[2], φ (°)	30	30	30	30	30
Cohesion[2], C_0 (MPa)	20	40	40	40	40
Bulk modulus, K (GPa)[1]	55	63	63	122	122
Shear modulus, G (GPa)[1]	36	40	40	74	74
Dislocation creep pre-exponential factor, Bn (Pa^{-n}s^{-1})	8.57E-28	5.78E-15	1.37E-25	6.22E-16	2.03E-15
Dislocation creep activation energy, En (kJmol^{-1})	223	356	485	480	480
Dislocation creep activation volume Vn (cm^{3}mol^{-1})	0	0.3	0	11	11
Power law exponent[3], n	4	3	4.7	3.5	3.5
Difussion creep pre-exponential factor, Bd (Pa^{-n}s^{-1})	-/'	-/'	-/'	1.50E-09	1.00E-09
Difussion creep activation energy, Ed (kJmol^{-1})	-/'	-/'	-/'	375	335
Creep activation volume Vd (cm^{3}mol^{-1})	-/'	-/'	-/'	5	4
Peierls creep pre-exponential factor, Bp[3] (Pa^{-n}s^{-1})	-/'	-/'	-/'	6.85E-67	6.85E-67
Peierls creep activation energy, Ep[3] (kJmol^{-1})	-/'	-/'	-/'	540	540
Peierls creep activation volume Vp[3] (cm^{3}mol^{-1})	-/'	-/'	-/'	0	0
WQ: Gleason and Tullis, 1995; WP: Rybacki and Dresen, 2000; CD: Mackwell et al., 1998; OD and OW: Hirth and Kohlstedt, 2003.					

Table 4.1: Material parameters

4.2.2 Modeling setup

We tried different model box sizes, from 600 km in horizontal direction and 200 km in vertical direction (depth), to 1200 km in horizontal direction and 400 km in the vertical

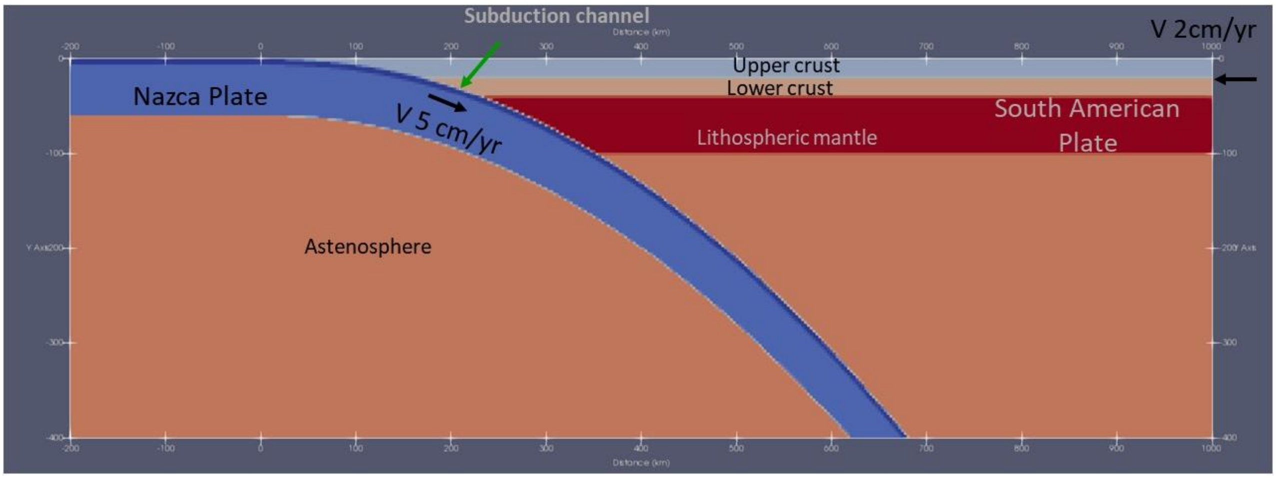

Figure 4.1: Model setup

direction (Figure 4.1) and a resolution of 4 km. In this approach we use a kinematically prescribed slab to avoid changes in velocities and subduction angle, since our focus was the influence of the upper-plate's characteristics in the deformation mode. For this, Dr Andrey Babeyko modified the code to implement this boundary condition. The subduction simulation with a prescribed slab allows for a realistic temperature distribution.

Based on Sobolev et al (2006), we used plastic strain-softening for felsic and mafic crust, reducing their cohesion and friction coefficient to a third when accumulated plastic strain (aps) changes from 1 to 2. They also used viscous strain softening, and the viscosity of continental crust is decreased by a factor of ten (log linearly) when finite strain changes from 0.5 to 1.0.

Regarding the interface between the oceanic slab and the continental plate, it was modelled following Sobolev et al. (2006) as a subduction channel using three finite elements with plastic rheology, with 2 elements on the oceanic side and one element in the continental side giving place to a 12 km-thick subduction channel with plastic rheology. Using two elements on the continental side provoked important continental subduction erosion, which we wanted to minimize in our models. These elements have lower cohesion (1 MPa) and friction coefficient (0.01) to allow plastic deformation in the interface. The friction coefficient value of 0.01 was used by Sobolev et al. (2006) for the models of the Southern Andes.

The yield stress is defined as the smallest of either the frictional (Mohr-Coulomb) stress:

$$\tau = c + \mu\sigma_n$$

or the temperature-dependent, viscous shear stress (Peacock, 1996)

$$\tau \;\; = \tau_0 exp\left(\frac{-T - T_0}{\Delta T}\right)$$

Where τ: stress norm defined as the square root of the second invariant of the stress tensor, *c*: cohesion, σ_n: normal stress, μ: effective friction coefficient of the subduction channel, *T* and T_0 (400°C) local and reference temperatures, τ_0 (30 MPa) and $\Delta T(75°C)$ are parameters which values are in brackets.

This approach was used by Sobolev et al. (2006) to simulate the shallow, low-temperature zone of the subduction channel with frictional (brittle) rheology with shear stress increasing with depth. At greater depths and higher temperatures, the viscous flow mechanism takes over and shear stress decreases with depth. The depth where frictional rheology changes to viscous rheology depends on the friction coefficient and it is larger where friction is lower.

4.3 Modeling results

We performed 50 model runs trying to find a realistic model to use as a reference and then to modify different parameters and test their influence on upper plate behaviour. As a first outcome, LAPEX-2D is a fast and light code; we ran simulations up to 20 Myr with the dimensions of 1200 x 400 km, and a resolution of 4 km, and took 300 minutes in 4 processors. Input files are easy to manipulate and to develop new model setups. The output is also light which allows its visualization and its smooth animation, using ParaView.

The modeling results were not realistic in some cases, probably due to the kinematically prescribed boundary condition imposed by the slab. This did not allow for example for isostatic compensation (Figure 4.2) developing an anomalously high depth of the trench.

Another issue was the unrealistic high resulting topography sustained by the prescribed slab (Figure 4.2). After 7 Myr a high topography was developed (Figure 4.3 A) and then at 8 Myr the slab changed its shape and the topography collapsed (Figure 4.3 B). We firstly inferred that the cause was related to the influence of the bottom boundary which in this model setup was 200 km depth. So, we decided to enlarge the model box to

400 km in Y-direction (depth). We obtained similar results in different tests (e.g. test-180615b Figure 4.4), even with bigger model boxes, such as 1200 x 400 km: after 7 Myr, the topography collapsed and the slab changed its shape.

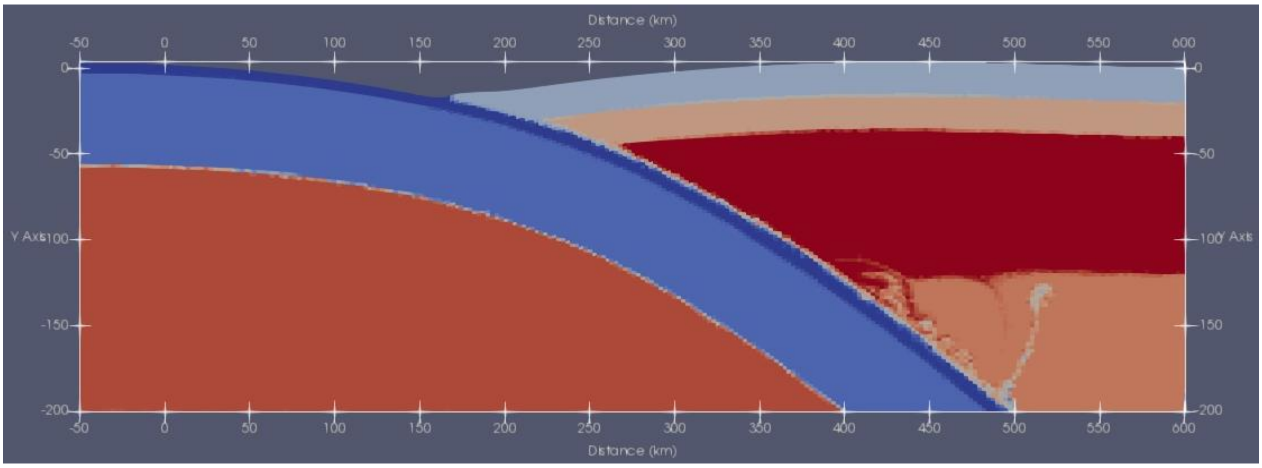

Figure 4.2: Example of model (test-170328d) with prescribed slab showing how the trench develops an anomalous depth of more than 15 km which we infer caused by the prescribed kinematic slab.

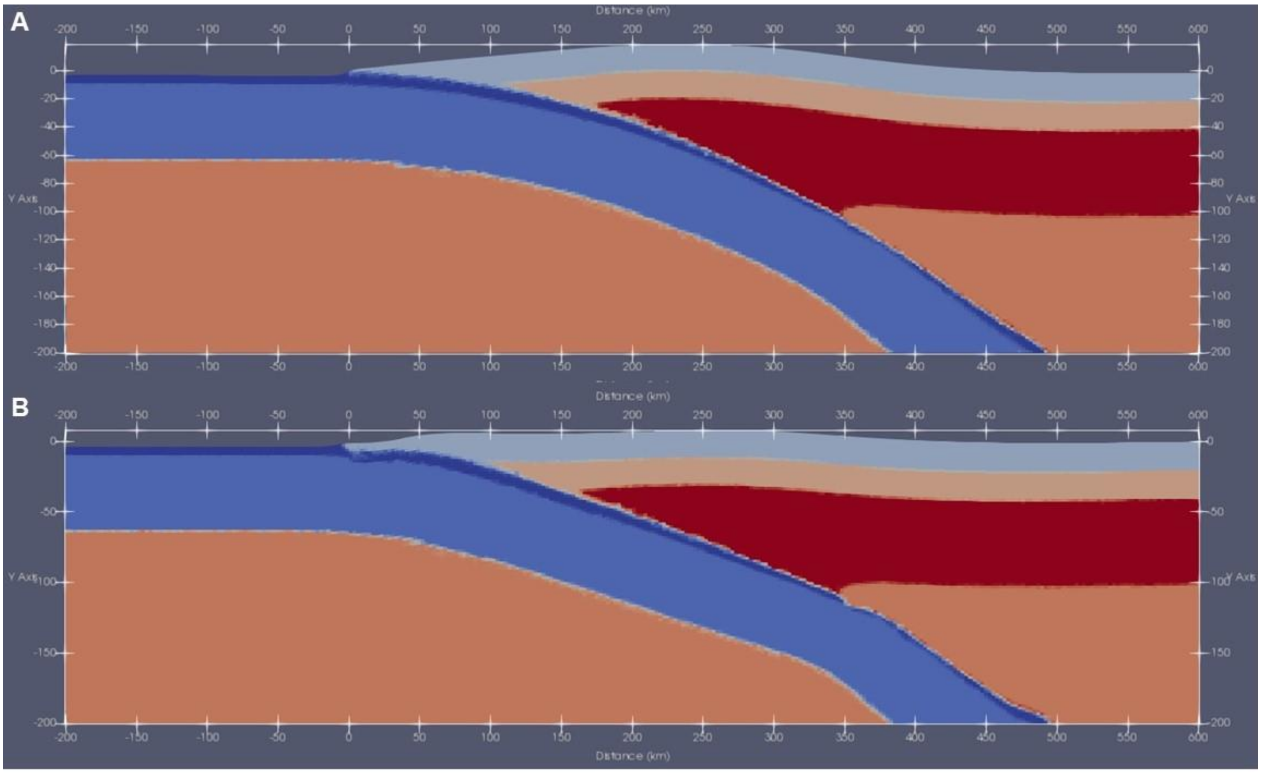

Figure 4.3: test-180514b model box 800 km x 200 km. A) At 7 Myr high topography is developed. B) At 8 Myr the boundary condition imposed by the prescribed slab geometry is broken and the topography collapses. In this model with 200 km depth, we infer that the bottom boundary influenced the behaviour of the slab.

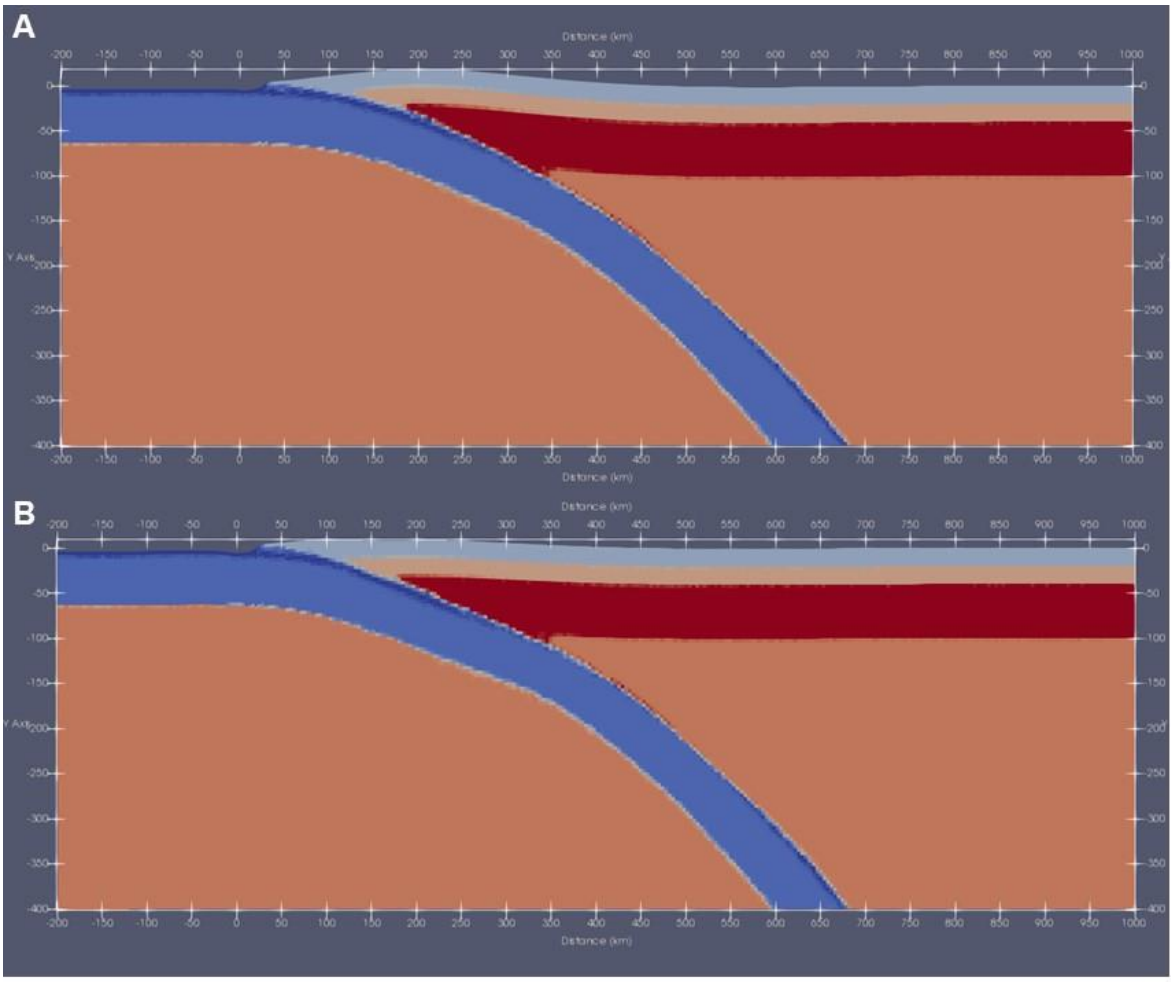

Figure 4.4: test-180615b model box 1200 km x 400 km. A) at 6.8 Ma, B) below at 7.2 Ma, the topography collapsed and the slab shape changes.

When using high friction coefficient (>0.05) in the subduction channel, the slab broke as in test-180518a (Figure 4.5) similarly to what was shown by Sobolev et al. (2006) when they used friction coefficient higher than 0.1 resulting in slab break-off. we tried with a bigger model box (1200 km x 400 km) and obtained same results (e.g. test-180620b, Figure 4.6).

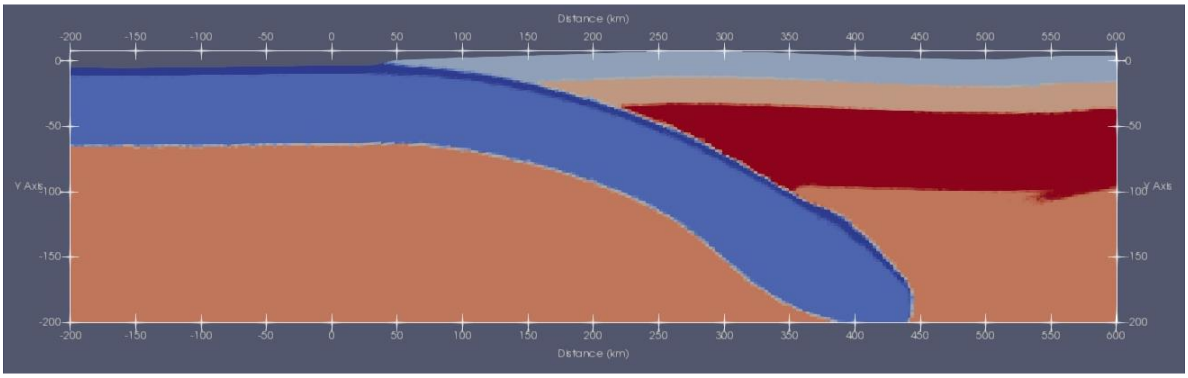

Figure 4.5: test-180518a at 1.2 Myr with high friction coefficient, produces slab break-off.

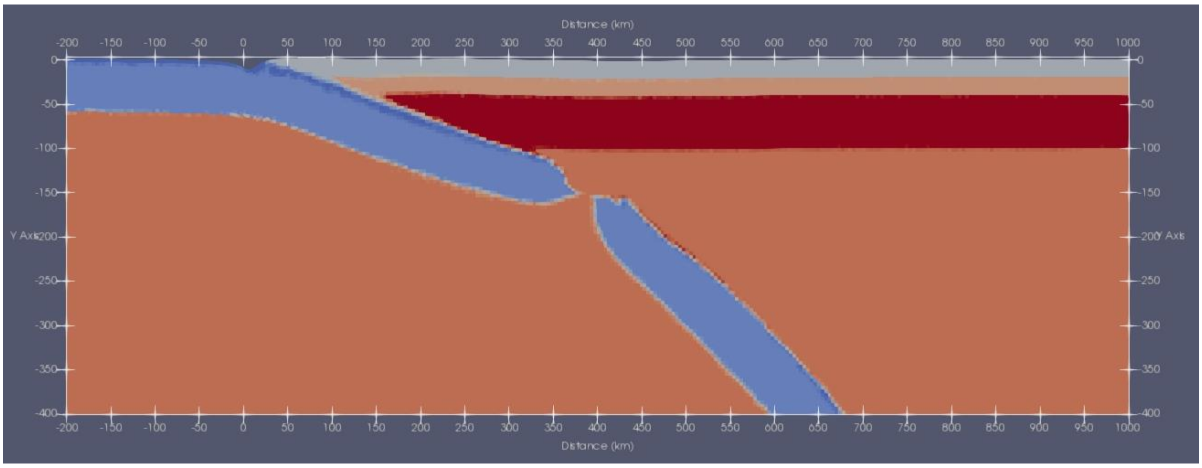

Figure 4.6: test-180620b with a bigger model box and higher friction coefficient (>0.05) that provokes slab break-off.

4.4 Conclusions and future work

Simulating the subduction process with a kinematically prescribed slab is quite complex and we did not achieve realistic results. The simplification allows for studying some parameters, such as upper-plate influence on deformation without the influence of slab-angle and velocities change. But in the cases we showed this was not a realistic approach. As shown by Sobolev et al. (2006), the friction coefficient in the subduction channel imposes an important control on the subduction system even in a prescribed slab, despite the model box size.

The kinematically prescribed slab imposes such a strong boundary condition allowing anomalous high topography until certain point when the prescribed geometry of the slab is abruptly modified.

Although these attempts were not successful, the subduction simulation allows for a realistic temperature distribution and its control on the rheology of materials. Furthermore, LAPEX-2D is a light code which permits the simulation of this complex system in relatively short computational time. Future work will be dedicated to testing new model setups without the prescribed slab to simulate the subduction system but focused on the upper-plate features that control the deformation mode.

Chapter V

5. The impact of inherited crustal features on the evolution of the Southern Central Andes: new insights from field observations and numerical modeling

Resumen

Los Andes Centrales del Sur, muestran una variación latitudinal en los patrones estructurales, donde entre 33° y 36°S se observan variaciones de segundo orden en la localización y acortamiento. Se ha propuesto que, además del buzamiento de la losa, el relleno de la trinchera y la edad de la placa oceánica, la resistencia de la placa superior impone un control importante sobre la construcción orogénica. Nos centramos en un segmento en el que la dinámica de subducción es prácticamente la misma en toda la provincia tectónica; por lo tanto, la influencia de los parámetros relacionados con la subducción puede no ser considerada, pero en el que las anisotropías a escala litosférica heredadas de eventos de deformación previos pueden jugar un papel fundamental en la deformación. Por ejemplo, la fase extensional regional del Mesozoico generó una corteza más delgada de lo normal con una composición más máfica al sur de los 35°S. Esto, a su vez, hizo a esta región más resistente a la deformación en el régimen compresivo andino cenozoico, resultando en un menor acortamiento. Este sector de los Andes está dominado por un modo de deformación simple o desacoplada entre la corteza superior e inferior. En este contexto integramos la información geológica y geofísica en dos transectas (33°40'S y 36°S), y usando modelado numérico geodinámico, simulamos diferentes configuraciones de la placa superior y evaluamos su control sobre el estilo de deformación. En contraste con el escenario de cizalla simple con litologías máficas dominantes, una composición más félsica de la corteza resulta en una deformación de cizalla pura. Nuestro estudio constituye el primer esfuerzo de modelado geodinámico para comprender los procesos de construcción de montañas en estas latitudes del orógeno. Los resultados obtenidos nos animan a concluir que la composición de la corteza inferior es un factor importante en el modo de deformación de la corteza de la placa superior en un orógeno de subducción. También es importante mostrar que las asimetrías en el límite litosfera-astenósfera de un orógeno no colisional con polaridad hacia el E promueven el establecimiento de estructuras de deformación vergentes al E asociadas a los despegues principales a escala cortical.

Abstract

The non-collisional Southern Central Andes show a latitudinal variation in structural patterns, where second-order variations in the localization and amount of shortening occur between 33° and 36°S. It has been proposed that besides slab dip, trench fill, and age of the oceanic plate the strength of the upper-plate imposes an important control on mountain building in this sector of the mountain belt. We focus on a segment where subduction dynamics are virtually the same throughout the tectonic province; thus, the influence of the subduction-related parameters can be neglected, but where inherited lithospheric-scale anisotropies from previous deformation events may play a pivotal role in guiding deformation. For example, a regional Mesozoic extensional phase generated a thinner-than-normal crust with more mafic composition south of 35°S. This, in turn, made this region more resistant to deformation in the Cenozoic Andean compressional regime, resulting in less shortening. This sector of the Andes is dominated by a simple-shear or uncoupled deformation mode between upper and lower crust. In this context we integrated geological and geophysical information into two transects (33°40'S and 36°S), and using geodynamic numerical modeling, we simulated different upper-plate configurations and assessed their control on the style of deformation. In contrast to the simple-shear scenario with dominant mafic lithologies, a more felsic composition of the crust results in pure-shear deformation. Our study constitutes the first geodynamic modeling effort to understand mountain-building processes at these latitudes of the orogen. The obtained results encourage us to conclude that the composition of the lower crust is an important factor in the mode of deformation in the crust of the upper plate in a subduction orogen. Importantly, we are also able to show that asymmetries in the lithosphere-asthenosphere boundary of of a non-collisional orogen with E-directed polarity promote the establishment of E-vergent deformation structures associated with principal, crustal-scale detachments.

5.1 Introduction

The Southern Central Andes (27-46°30'S) represent a typical subduction-related orogen that developed from the Late Cretaceous to the present day, where no terrane accretions have been documented since the Palaeozoic. It has been proposed that two main factors control deformation variations along the strike at a continental-scale: (i) subduction dynamics, i.e., slab dip, age of the oceanic subducted plate, presence of oceanic ridges, trench fill and convergence obliquity (Jarrard, 1986; Sobolev and Babeyko, 2005; Oncken et al., 2006; Schmidt et al., 2011). In addition, (ii) upper-plate

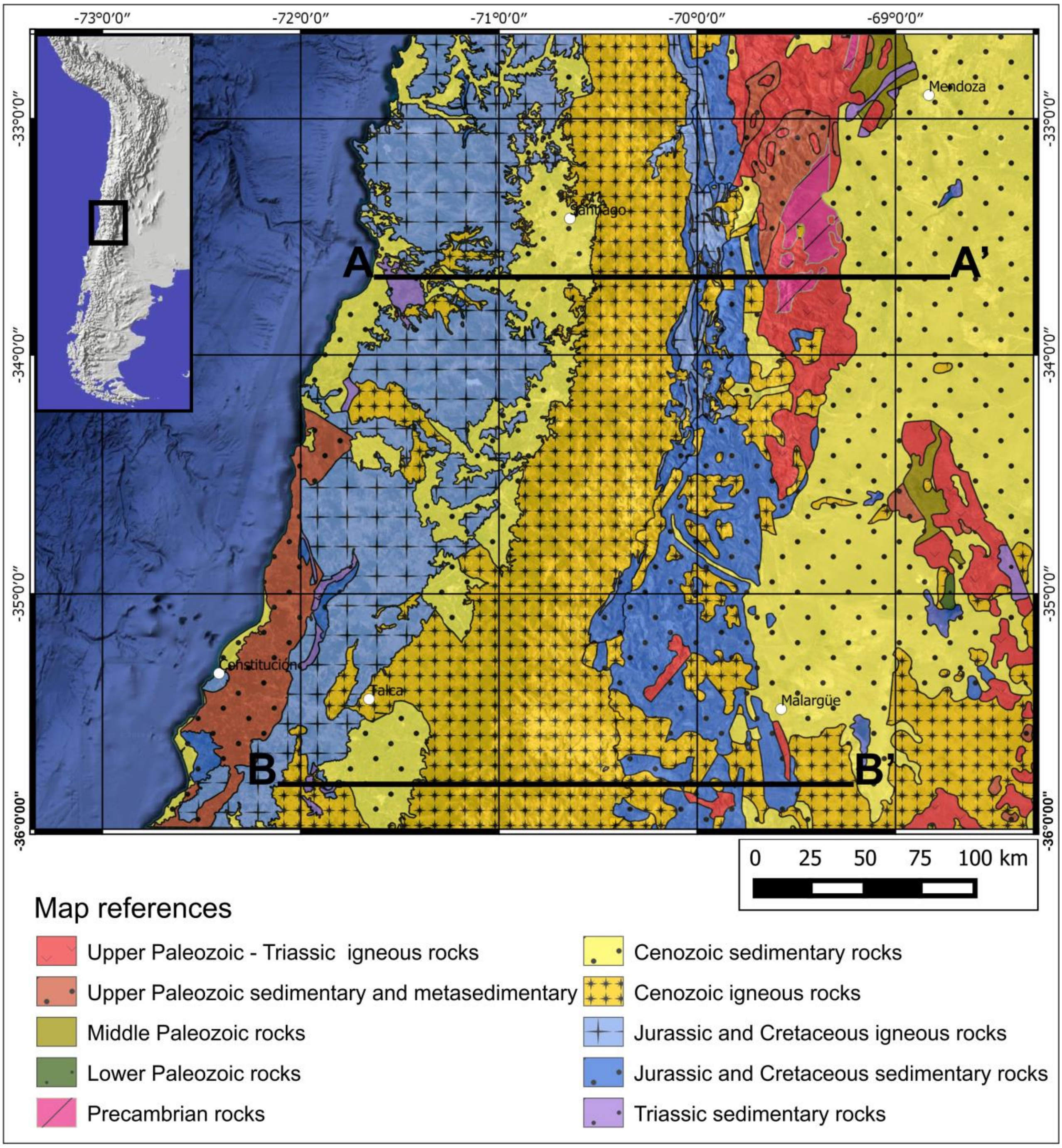

Figure 5.1: Geological map of the study area. Based on SEGEMAR (1997) and SERNAGEOMIN (2003). A-A': location of the cross-section at 33°40'S. B-B': location of the cross-section at 36°S

characteristics, such as the thermal state, lithospheric strength variations, rheological heterogeneities, and crustal and lithospheric thickness variation are thought to exert an important control on mountain building (Allmendinger et al., 1983; Kley et al., 1999; Ramos et al., 2002; Pearson et al., 2013).

In this chapter, we focused on the segment between 33° and 36°S (Figure 5.1), where second-order variations in the amount of shortening and its localization are observed (Giambiagi et al., 2012). According to these authors, the main difference in this area are variations in lithospheric strength, mainly influenced by the pre-Andean, i.e. pre-Cenozoic tectono-magmatic events. A Mesozoic extensional phase (cf. Chapter 1) left a thinner-than-normal crust, with a more mafic composition south of 35°S, which in turn resulted in higher lithospheric resistance to compression and less shortening, dominated by a simple-shear mode. In the simple-shear mode (Allmendinger and Gubbels, 1996) the loci of shortening in the upper and lower crust are decoupled, and separated laterally, while in the pure-shear mode the deformation of upper and lower crust occurs in the same crustal column and they are both coupled.

The principal aim of this chapter is to test the influence of upper-plate characteristics on the Cenozoic Andean deformation style and vergence of the orogenic system, using geodynamic numerical modeling with input data from field observations. As we are focussing on the narrow segment of the mountain belt with normal subduction, the dynamic parameters of subduction are similar along strike, and the subduction-setting variations can be neglected as a controlling factor with respect to the deformation patterns. Accordingly, we will focus on the control of upper-plate characteristics in the context of the structural evolution of an Andean-type orogenic system.

We integrate geological and geophysical information into two transects that best represent the orogenic deformation styles best (33°40'S and 36°S); these prototypes were compared with geodynamic numerical models, where different upper-plate configurations were established, analysing the resulting deformation style.

5.2 Geological setting

The study area has been under a protracted subduction setting since the Palaeozoic, which resulted in several periods of contractional and extensional deformation. These events created crustal heterogeneities prior to the Late Cretaceous-Quaternary Andean orogeny, which impacts on the lithospheric strength and the Cenozoic structural styles.

During the Paleozoic subduction history, the accretion of terranes to the margin of Gondwana resulted in the configuration of the continental lithosphere of the South American plate (Ramos et al., 1986). In the late Paleozoic, the subduction started again at a similar position as the present-day subduction of the oceanic Nazca plate and, in Early Permian, a contractional event resulted in the NW- to NNW-trending San Rafael orogenic belt. Postdating this event, widespread volcanism developed under extensional conditions from the Late Permian to Early Triassic; the corresponding rocks are grouped into the Choiyoi Group (Llambias et al., 1993; Sato et al., 2015). The extensional conditions continued during the Early-Middle Triassic, with the development of the continental Cuyo rift basin.

During the Late Triassic to Early Jurassic, the Neuquén basin formed in a backarc extensional setting beginning as a series of isolated depocenters that subsequently coalesced (Vergani et al., 1995). These NNE- to NNW-trending depocenters contain early synrift deposits of more than ~2 km of thickness north of 35°S, while south of this latitude, volcanic and volcaniclastic rocks were also deposited accounting for more than ~4 km of thickness. The Mesozoic transition between a passive rift (north of 35°S) and an active rift (south of 35°S) was associated with significant volcanism; this area coincides with the Sosneado-Melipilla lineament, a Paleozoic crustal anisotropy connected with the Melipilla anomaly in central Chile that represents a rigid crustal block to the south of the mentioned lineament (Yáñez et al., 1998). This suggests a strong lateral change in crustal strength (Giambiagi et al., 2012).

Following the synrift phase, during Middle Jurassic to Early Cretaceous, a sag phase superseded the extensional processes. At this time, the depocenters were linked and marine and continental sediments were deposited (Uliana and Biddle, 1988; Uliana and Legarreta, 1993). However, this sag phase was interrupted again by a brief period of extension during the Late Jurassic in the northern part of the basin (Mescua et al., 2014). In the Late Cretaceous, the onset of Andean shortening is recorded by coarse continental deposits in a foreland-basin setting (Vergani et al., 1995).

During the Neogene, synorogenic deposits with volcanic and volcaniclastic intervals fill intermontane and foreland basins that record the Andean shortening and uplift (Irigoyen et al., 2000; Giambiagi et al., 2003b; Silvestro et al., 2005; Buelow et al., 2018; among others). Volcanism was located along the Chilean slope of the Principal Cordillera between 33° and 35°S, during Early to Middle Miocene time until the Pliocene, when the arc migrated to the east to its current position at the border between Chile and Argentina (Stern and Skewes, 1995). South of 35°S, an eastward arc expansion occurred in the Middle to Late Miocene (Ramos and Folguera, 2011); in the Pliocene-Quaternary the magmatic arc was established in the Principal Cordillera, to the east or above the Miocene arc (Kay et al., 2006).

Late Cretaceous tectonism in the 33°40’ S transect accounts for 10 km of shortening; this led to crustal thickening, which generated a thicker crust (~40 km) in the western zone, where the Coastal Cordillera is located (Giambiagi et al., 2015). Regarding the 36° transect, the onset of contraction is inferred to have started in the Late Cretaceous; this process led to a similar configuration as in the 33°40’S zone with a thickened crust in the current forearc. According to geochemical data, from Early to Middle Miocene, the crust was relatively thin (< 40 km) between 33° and 35°S, due to Eocene-Early Miocene extension (Charrier et al., 2002); after the Early Miocene (21-16 Ma) main shortening event and by the Pliocene (e.g., Kay and Mpodozis, 2002), crustal thickness reached 50 km.

In the study area, the Aconcagua (32°30'-34°S) and Malargüe (34°-36°S) fold-and-thrust belts constitute the Principal Cordillera morphotectonic province, where most of the

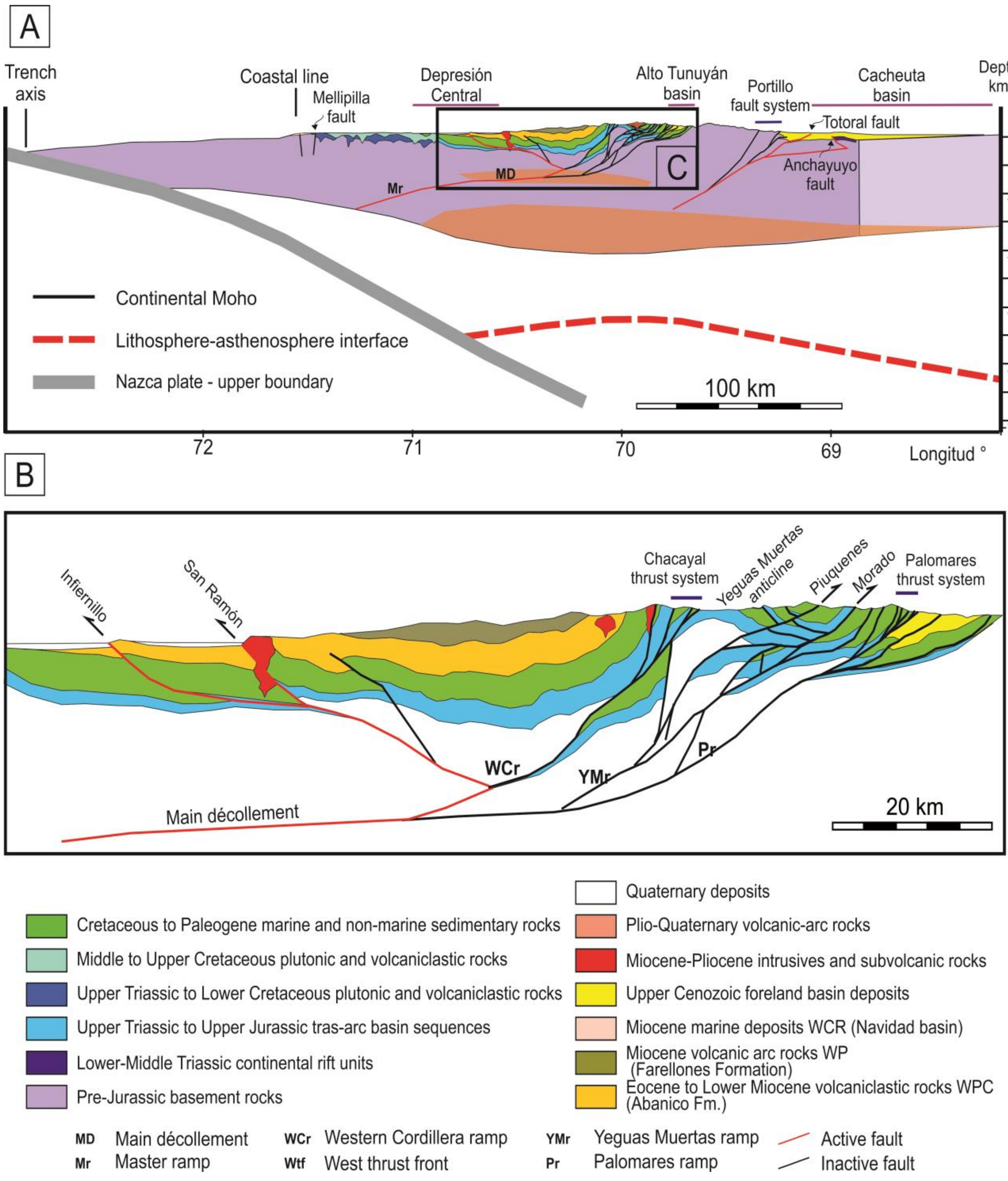

Figure 5.2: Cross-section at 33°40'S (modified from Giambiagi et al., 2015)

shortening is accommodated by a combination of thin- and thick-skinned structures. The basement of the Choiyoi Group is involved in the deformation of the Principal Cordillera south of 33°30'S. Furthermore, these thrust belts evolved over the thick (~4 km) Mesozoic deposits of the Neuquén Basin, which contain mechanically weak formations such as evaporites and mudstones that constitute detachment levels for the Andean deformation (Kozlowski et al., 1993; Manceda and Figueroa, 1995). In the northern zone, thick-skinned deformation in the Frontal Cordillera also absorbed part of the shortening. There is a marked decrease in shortening to the south, however, which traditionally was proposed as a result of geodynamic boundary conditions, such as slab angle and coupling between plates.

We focus on two segments, a northern one between 33° and 34°40'S which is represented by a complete transect (Figure 5.2) of the orogen at 33°40'S based on Giambiagi et al. (2015;), and a southern segment between 34°40'S and 36°S. The latter section is represented by a cross-section at 35°40'S (Figure 5.3), which was constructed based on my own data and prior research (e.g., Orts et al., 2012; Astaburuaga, 2014; Fennell et al., 2019;).

The northern segment (33°-34°40'S) includes the morphotectonic provinces of Principal Cordillera and the Frontal Cordillera. The Aconcagua fold-and-thrust belt, in the Principal Cordillera province, has been interpreted classically as a thin-skinned belt in its northern sectors (e.g., Ramos, 1988; Kozlowski et al., 1993; Ramos et al., 1996), but to the south, reactivated Mesozoic basement structures are involved in the deformation (Giambiagi et al., 2003a). The shortening estimates for this thrust belt are around 50 km at 33°40'S (Giambiagi et al., 2015) and 23 km at 34°40'S (Turienzo et al., 2012) in its eastern sector, while for the Western Principal Cordillera less than 10 km of Miocene shortening have been estimated (Turienzo et al., 2012; Giambiagi et al., 2015). To the east the Frontal Cordillera comprises a basement block of Choiyoi Group rocks that accounts for limited shortening (10 km); this unit abruptly ends south of 34°40'S. Farther east, limited inversion of Mesozoic faults accounts for less than 5 km in the Cerrilladas Pedemontanas (Giambiagi et al., 2015). The total Late Cretaceous to present-day shortening for this transect is approximately 70 km.

In the southern segment (34°40'-36°S), the Andes are comprised of the Principal Cordillera morphotectonic province, where the Malargüe fold-and-thrust belt absorbs most of the shortening involving the inversion of Mesozoic normal faults and newly formed Cenozoic thrusts in a hybrid thin- and thick-skinned deformation style (Kozlowski et al., 1993; Manceda and Figueroa, 1995; Mescua et al., 2014). The shortening estimates, from

Late Cretaceous to present day, at this latitude is around 25 km for the eastern flanks of the orogen and 15-20 km for the western areas, which results in a total of 40-45 km (Mescua et al., 2014).

Another difference between the two areas is the fact that the lower crust has a different composition. The emplacement of felsic Permian-Triassic magmas represented by the Choiyoi Group modified the bulk crustal composition to a more felsic character. Subsequently, Mesozoic extension in the Neuquén basin was localized in a narrow NNW-trending zone north of 35°, while south of 35°S, the rifting process was more intense with substantial thinning of the crust (Vergani et al., 1995; Giambiagi et al., 2012; Sigismondi, 2012). Mafic underplating also modified the lower crust south of 35°S (Kay et al., 1989; Llambias et al., 1993). It is conceivable that these processes may have strengthened the crust south of 35°S and thus prevented its deformation under compression (Giambiagi et al., 2012).

Regarding the main detachments that accommodate crustal shortening, there are two main group of models proposed according to their vergence: an E-vergent model (Ramos et al., 2004; Farías et al., 2010a; Astini and Dávila, 2010; Giambiagi et al., 2012; Turienzo et al., 2012; Buelow et al., 2018; among others) and a W-vergent model (Armijo et al., 2010; Riesner et al., 2018). In the latter group of models, Andean growth was postulated to have been W-directed, meaning that the deformation migrates from eastern belts, such as Cordillera Frontal to the west, which is also opposed to the E-vergent model that implies an E-directed growth of the orogen.

At crustal-scale, the major detachment underlying the belt is located between 10 and 12 km according to cross-section balancing and geophysical modeling (Manceda and Figueroa, 1995; Farías et al., 2010b; Tassara and Echaurren, 2012; Turienzo et al., 2012; Giambiagi et al., 2003a, 2012, 2015; Mescua et al., 2014).

Based on structural geology techniques and geophysical constraints, Giambiagi et al. (2012) presented several cross-sections for the eastern slope of the Andes and proposed that north of 35°S the deformation mode occurs in a pure-shear or coupled mode between upper and lower crustal deformation while to the south, it changes to a simple-shear or uncoupled mode.

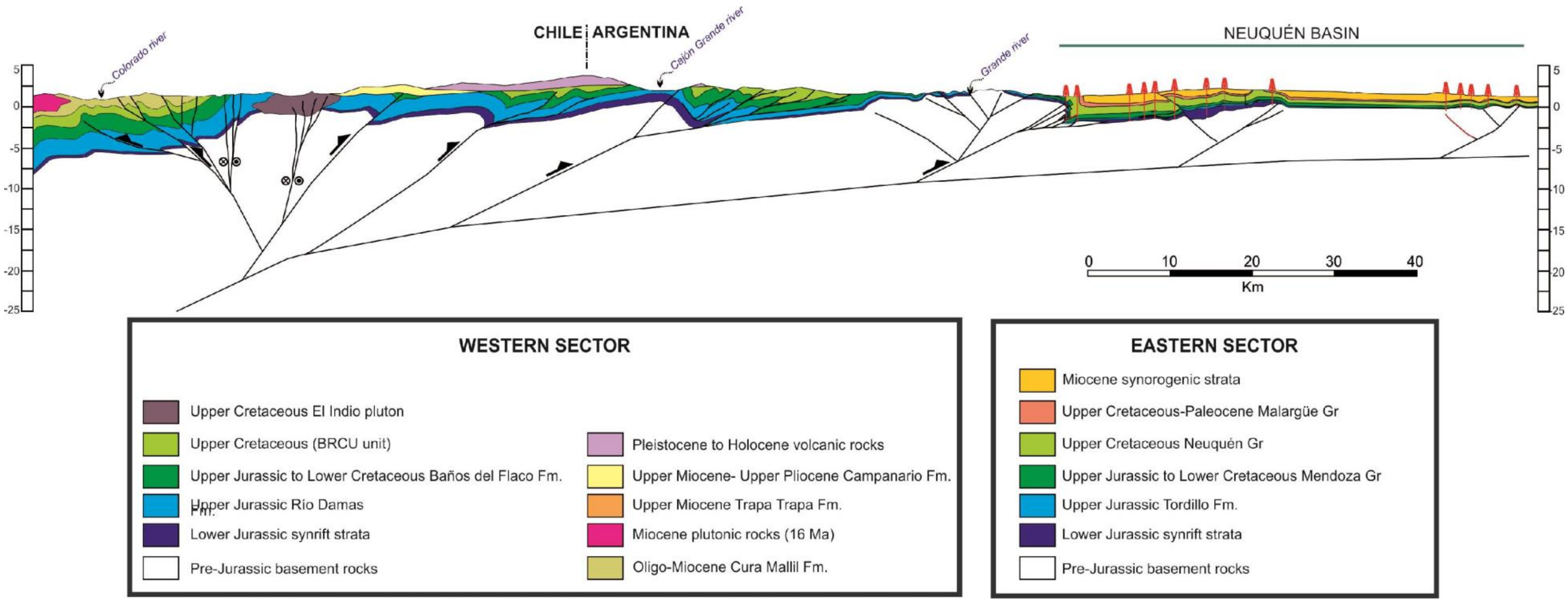

Figure 5.3: Cross-section at 36°S based on own data and from Orts et al., 2012, Astaburuaga, 2014, Giambiagi et al., 2012.

5.3 Methods

5.3.1 Geological methods

From the integration of surface data and geophysical evidence, a conceptual model was constructed for the Andes at 36°S. To construct this regional cross-section (Figure 5.3), we performed kinematic forward modeling in the frontal zone (See chapter 2) and considered the previous partial structural cross-section generated by other researchers (Orts et al., 2012; Astaburuaga, 2014; Fennell et al., 2019), as well as geophysical data (presented in chapter 2). For the frontal zone, which lies in the Neuquén basin area, we presented the tectonic evolution from the Miocene to the present-day in chapters 2 and 3. we included new seismic reflection data and oil-well logs to construct the cross-sections in that zone.

5.3.2 Numerical geodynamic modeling

We used ASPECT (Advanced Solver for Problems in Earth's ConvecTion; Kronbichler et al., 2012; Heister et al., 2017), a highly scalable geodynamic open-source code, to simulate the behaviour of the South American plate under contraction. Based on the present-day structure and the inferences about pre-Andean crustal configuration, we defined an initial setup for the sections at 33°40'S and 36°S, prior to the onset of Andean contraction.

The model box was 2D, with 500 km in the horizontal direction and 240 km in depth, with free-slip in both sides (in vertical direction) and a closed-bottom boundary. The top boundary condition is zero traction with a sticky air layer that approximates a free surface in a way that diminishes the grid distortion and the associated numerical instabilities. We applied a constant horizontal velocity, which in some setups was on both sides of the model and in other cases only on the right boundary.

The code solves the equations of conservation of momentum (Eq. 5.1), mass (Eq. 5.2) and energy (Eq. 5.3)

$$-\frac{\partial p}{\partial x_i} + \frac{\partial \tau_{ij}}{\partial x_j} + \rho g_i = 0, \ i = 1, 2 \qquad \text{Eq. 5.1}$$

$$\frac{1}{K}\frac{dp}{dt} - \alpha\frac{dT}{dt} = -\frac{\partial v_i}{\partial x_i} \qquad \text{Eq. 5.2}$$

$$\rho C_p \frac{dT}{dt} = \frac{\partial}{\partial x_i}\left[\lambda(x_i,T)\frac{\partial T}{\partial x_i}\right] + \tau_{ij}\left(\dot{\varepsilon}_{ij}^{v} + \dot{\varepsilon}_{ij}^{p}\right) + \rho A \qquad \text{Eq. 5.3}$$

Where the Einstein summation rule applies, and *xi* are coordinates, t: time, vi: velocities, *p:* pressure, τ_{ij} : stress deviator, $\dot{\varepsilon}_{ij}$: the strain-rate deviator, d/dt convective time derivative, ρ density, g_i gravity vector, K: bulk modulus, T: temperature, C_p: heat capacity, λ: heat conductivity; A: radioactive heat production.

These sets of equations are coupled with constitutive equations that describe the rheology of the rock under stresses. The code employs elasto-visco-plastic rheology and the deviatoric strain rate $\dot{\varepsilon}_{ij}$ is subsequently determined by elastic, viscous and plastic components:

$$\dot{\varepsilon}_{ij} = \dot{\varepsilon}_{ij}^{e} + \dot{\varepsilon}_{ij}^{v} + \dot{\varepsilon}_{ij}^{p} = \frac{1}{2G}\frac{\hat{\mathrm{d}}\,\tau_{ij}}{\mathrm{dt}} + \frac{1}{2\eta_{eff}}\tau_{ij} + \dot{\varepsilon}_{ij}^{p} \qquad \text{Eq. 5.4}$$

Where, $\dot{\varepsilon}_{ij}^{e}$ is the elastic strain-rate deviator, $\dot{\varepsilon}_{ij}^{v}$ the viscous strain-rate deviator, $\dot{\varepsilon}_{ij}^{p}$ the plastic strain-rate deviator, *G* the elastic shear modulus, $\hat{\mathrm{d}}\,\tau_{ij}/dt$ the Jaumann co-rotational deviatoric stress rate, and η_{eff} the effective viscosity. To calculate the effective viscosity, three competing mechanisms of creep were taken into account: diffusion, dislocation, and Peierls creep. In this setup at a given temperature and stress, the mechanism that produces the highest viscous strain rate becomes the dominant creep mechanism:

$$\dot{\varepsilon}_{eff}^{v} = \dot{\varepsilon}_d + \dot{\varepsilon}_n + \dot{\varepsilon}_p \qquad \text{Eq. 5.5}$$

Here $\dot{\varepsilon}_d$: diffusion creep, $\dot{\varepsilon}_n$: dislocation creep, $\dot{\varepsilon}_p$ Peierls creep, calculated as:

$$\dot{\varepsilon}_d = B_d \tau_{II} exp\left(-\frac{E_d}{RT}\right) \qquad \text{Eq. 5.6}$$

$$\dot{\varepsilon}_n = B_n \tau_{II}^{n}\ \ exp\left(-\frac{E_n}{RT}\right) \qquad \text{Eq. 5.7}$$

$$\dot{\varepsilon}_p = B_p exp\left[-\frac{E_p}{RT}\left(1-\frac{\tau_{II}}{\tau_p}\right)^q\right] \qquad \text{Eq. 5.8}$$

And the effective viscosity is calculated as:

$$\eta_{eff} = \frac{\tau_{II}}{2\dot{\varepsilon}^{v}_{eff}} \qquad \text{Eq. 5.9}$$

In the above, τ_{II} : stress tensor norm; R: gas constant, and the other parameters are material constants. Diffusion creep is dominant at very low strain rates or high temperatures (Babeyko et al., 2006). At typical geological strain rates (>10^{-15} s^{-1}) and moderate temperatures, the deformation in the mantle is mainly accommodated by the dislocation creep (power-law creep) (Babeyko et al., 2006). And Peierls creep becomes dominant at very high deviatoric stress (>500 MPa) (Babeyko et al., 2006).

In the upper crust, plastic deformation is responsible for faulting, and the Mohr-Coulomb criterion is applied:

$$\sigma_1 - \sigma_3 \frac{1+sin\phi}{1-sin\phi} + 2C_h\sqrt{\frac{1+sin\phi}{1-sin\phi}} = 0 \qquad \text{Eq. 5.10}$$

In this equation, σ_1: maximum principal stress, σ_3: minimum principal stress, ϕ: angle of friction, C_h: cohesion.

5.4 Numerical modeling setup

The model setup consists of a model box of 500 km width and 240 km of depth (Figure 5.4), with a variable resolution of 500 m per element in the upper crust (from 0-50 km), 1 km (from 50-100 km) and 5 km in the lower part of the model box. A sticky air layer of 10 km is added on top of the upper crust.

We computed two main model sets, one for the transect at 33°40’S (M33.4 models) and the second one for the transect at 36°S (M36 models). The main differences between both sets are (i) the estimated shortening (70 km for M33.4 vs. 45 km for M36), (ii) the initial crustal thickness across the orogen, and (iii) the crustal composition, based on geological constraints (see section 5.2).

For the model setup, we considered a thicker crust (~40 km) in the western zone, where the Coastal Cordillera is located, this represents the Late Cretaceous shortening event, accounting for 10 km of shortening in the 33°40’ S transect (Giambiagi et al., 2015). The 36° transect is not well constrained but presumably, the onset of contraction in the

Late Cretaceous led to a similar configuration as in the 33°40'S zone with a thickened crust in the current forearc.

The rheological parameters were taken from laboratory experiments (Table 5.1) for the different materials controlling the rheology of the model layers:

- Continental upper crust (CUC): Wet quartzite, WQ (Gleason and Tullis, 1995)
- Continental lower crust (CLC): mafic crust: Maryland dry diabase, MDD or Columbia diabase, CD (Mackwell et al., 1998); felsic crust: wet quartzite, WQ (Gleason and Tullis, 1995) or dry quartzite, DQ (Ranalli and Murphy, 1987)
- Continental lithospheric mantle (CLM): Dry olivine, DO (Hirth and Kohlstedt, 2003)
- Sublithospheric mantle (SLM): Wet olivine, WO (Hirth and Kohlstedt, 2003)

The temperature distribution is linear from the bottom of the lithosphere to the surface, and adiabatic between the LAB and the bottom of the model.

In total, four sets of simulations were performed, whose results are summarized below and in the Table 5.2.

Material properties Flow law	Wet quartzite (WQ)	Dry quartzite (DQ)	Maryland dry diabase (MDD)	Columbia diabase (CD)	Dry olivine (DO)	Wet olivine (WO)
Phase	Felsic crust	Felsic crust	Mafic crust	Mafic crust	Lithospheric mantle	Asthenosphere
Density, ρ_0 (kg/m^3)	2800	2800	3000	3000	3300	3300
Heat expansion, α (K^{-1})	3.70E-05	3.70E-05	2.70E-05	2.70E-05	3.00E-05	3.00E-05
Specific heat, C_p (kJkg^{-1}K^{-1})	1.2	1.2	1.2	1.2	1.2	1.2
Heat conductivity, k (WK^{-1}m^{-1})	2.5	2.5	2.5	2.5	3.3	3.3
Heat productivity, A (µWm^{-3})	1	1	0.3	0.3	0	0
Friction angle, φ (°)	30	30	30	30	30	30
Cohesion, C_0 (MPa)	20	20	40	40	40	40
Bulk modulus, K (GPa)	55	55	63	63	122	122
Shear modulus, G (GPa)	36	36	40	40	74	74
Dislocation creep pre-exponential factor, Bn (Pa^{-n}s^{-1})	8.57E-28	8.12E-20	5.78E-27	1.37E-25	6.22E-16	2.03E-15
Dislocation creep activation energy, En (kJmol^{-1})	223	156	485	485	480	480
Dislocation creep activation volume Vn (cm^{3}mol^{-1})	0	0	0.3	0	11	11
Power law exponent, n	4	2.4	4.7	4.7	3.5	3.5
Difussion creep pre-exponential factor, Bd (Pa^{-n}s^{-1})	-/'	-/'	-/'	-/'	1.50E-09	1.00E-09
Difussion creep activation energy, Ed (kJmol^{-1})	-/'	-/'	-/'	-/'	375	335
Creep activation volume Vd (cm^{3}mol^{-1})	-/'	-/'	-/'	-/'	5	4
Peierls creep pre-exponential factor, Bp (Pa^{-n}s^{-1})	-/'	-/'	-/'	-/'	6.85E-67	6.85E-67
Peierls creep activation energy, Ep (kJmol^{-1})	-/'	-/'	-/'	-/'	540	540
Peierls creep activation volume Vp (cm^{3}mol^{-1})	-/'	-/'	-/'	-/'	0	0

WQ: Gleason and Tullis, 1995; DQ: Ranalli and Murphy, 1987; MDD and CD: Mackwell et al., 1998; OD and OW: Hirth and Kohlstedt, 2003.

Table 5.1: Material parameters used in the models

M#	Model group	ICD depth (km)	Max. crustal thickness (km)	Vel. left (cm/yr)	Vel. right (cm/yr)	Sticky air thickness (km)	Lower crust material
1	A33.4	17	45	2	5	10	MDDf1
2	A36	12	40	2	5	10	MDDf1
3	B33.4	17	45	0.5	0.5	100	MDDf1
4	B33.4	17	45	0.5	0.5	10	MDDf1
5	B33.4	17	45	0	1	100	MDDf1
6	B33.4	17	45	0	1	10	MDDf1
7	B36	12	40	0.5	0.5	100	MDDf1
8	B36	12	40	0.5	0.5	10	MDDf1
9	B36	12	40	0	1	100	MDDf1
10	B36	12	40	0	1	10	MDDf1
11	C33.4	17	45	0.5	0.5	10	MDDf1
12	C33.4	17	45	0	1	10	MDDf1
13	C36	12	40	0.5	0.5	10	MDDf1
14	C36	12	40	0	1	10	MDDf1
15	D33.4	variable	40	0.5	0.5	10	MDDf1
19	D33.4	variable	40	0.5	0.5	10	DQf1
20	D33.4	variable	40	0.5	0.5	10	DQf5
21	D33.4	variable	40	0.5	0.5	10	WQf5
16	D33.4	variable	40	0	1	10	MDDf1
22	D33.4	variable	40	0	1	10	DQf1
23	D33.4	variable	40	0	1	10	DQf5
24	D33.4	variable	40	0	1	10	WQf5
17	D36	variable	40	0.5	0.5	10	MDDf1
31	D36	variable	40	0.5	0.5	10	CDf0.2
32	D36	variable	40	0.5	0.5	10	CDf1
33	D36	variable	40	0.5	0.5	10	MDDf0.2
37	D36	variable	40	0.5	0.5	10	CDf0.1
38	D36	variable	40	0.5	0.5	10	CDf0.05
18	D36	variable	40	0	1	10	MDDf1
34	D36	variable	40	0	1	10	CDf0.2
35	D36	variable	40	0	1	10	CDf1
36	D36	variable	40	0	1	10	MDDf0.2
39	D36	variable	40	0	1	10	CDf0.1
40	D36	variable	40	0	1	10	CDf0.05

Table 5.2: Model list with indication of the main characteristics of each group of models. Notice that the model numbers (M#) are non-correlative in D-group. ICD: Intracrustal discontinuity. Vel. Left and Vel. Right: velocities applied on the left and right sides of the model, respectively. Lower crust material: MDDf1 and MDDf0.2: Maryland dry diabase scale factor 1 or 0.2; DQf1: Dry quartzite scale factor 1; DQf5: Dry quartzite scale factor 5; WQf5: Wet quartzite scale factor 5. CD0.2, CDf1, CDf0.1, CDf0.05: Columbia diabase scale factor 0.05 to 1.

5.4.1 A-group models: high pushing velocities and linear LAB

The first model setup approach (A-group models; Figure 5.4 and Table 5.2) consisted of two cross-sections at 33°40'S (named A33.4) and 36°S (named A36), where the only difference between both was the crustal thickness with an ICD (intracrustal discontinuity) at 17 km and 12 km, and a maximum crustal thickness of 45 km and 40 km, for the northern and southern models, respectively. Both setups have an irregular Moho geometry attempting to simulate the initial crustal configuration before the Miocene shortening phase, as derived from geological and geophysical constraints. For both models, the lithosphere-asthenosphere boundary (LAB) is a line located at 60 km depth on the left side, and at 100 km on the right side. The horizontal velocities were only applied to the lithosphere and were 5 cm/yr from the left side and 2 cm/yr from the right side, which in total provides 7 cm/yr.

In these models, we used for the continental upper crust (CUC) the following lithologic components: wet quartzite; continental lower crust (CLC): Maryland dry diabase; continental lithospheric mantle (CLM): dry olivine and sublithospheric mantle (SLM): wet olivine (references in Table 5.1).

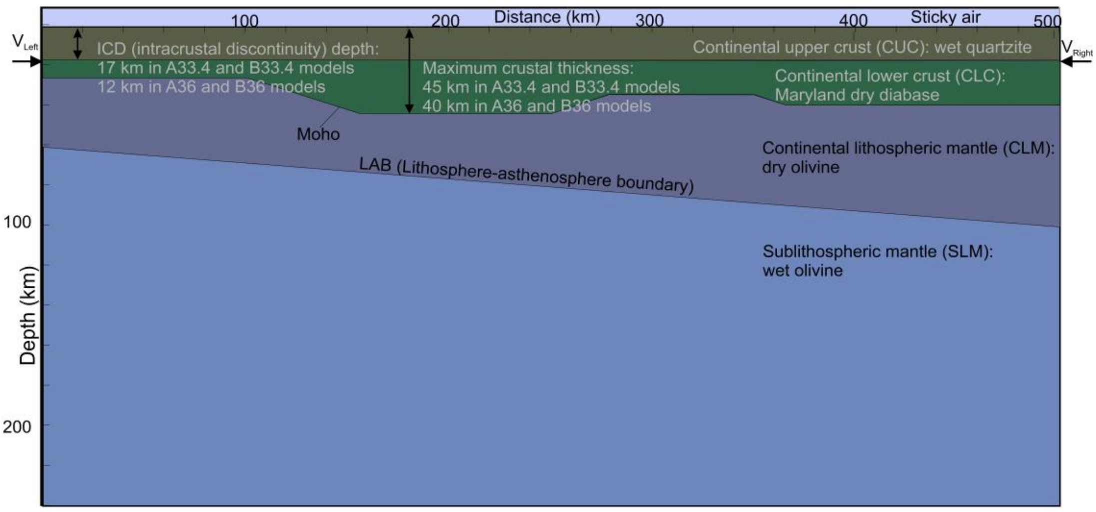

Figure 5.4: A- and B-group model setup with indication of the differences between models for 33.4°S and 36°S. VLeft and VRight are velocities applied on the left and right respectively and vary according to the setup (see section 5.4.1 and 5.4.2). For material parameters see Table 5.1.

5.4.2 B-group models: low pushing velocities and linear LAB

In the second set of models, we used the same geometry as in the A-group (Figure 5.4), and only the pushing velocities were modified. Two subsets of models were run, the first with 0.5 cm/yr from each side of the model box and the second with 1 cm/yr only from the right side. Each of these subsets was also modelled with a variation in the sticky air thickness from 10 km to 100 km to check the performance of the code to finish the simulation and converge in a reasonable time. In these models, the rheology was the same as in A-group: the continental upper crust (CUC): wet quartzite; continental lower crust (CLC): Maryland dry diabase; continental lithospheric mantle (CLM): dry olivine and sublithospheric mantle (SLM): wet olivine (Table 5.1).

5.4.3 C-group models: low pushing velocities and symmetric LAB

In this case, the Moho geometry was the same as in the previous model group (B-group) keeping the different ICD depth and crustal thickness that characterizes each transect: ICD 17 km and crustal thickness 45 km for 33° 40'S (named C33.4); ICD 12 km and crustal thickness 40 km for 36°S (named C36). The main difference in this group is the lithosphere-asthenosphere boundary (LAB) geometry (Figure 5.5), that was modified to replicate the geometry due to the mantle-wedge corner flow, with a thinner lithosphere where the corner flow was developed. This approach was taken to simulate the temperature distribution of the lithosphere and its strength according to its thickness.

In these models, the materials and rheology used are the same as in previous models: the continental upper crust (CUC): wet quartzite; continental lower crust (CLC): dry Maryland diabase; continental lithospheric mantle (CLM): dry olivine and sublithospheric mantle (SLM): wet olivine (Table 5.1).

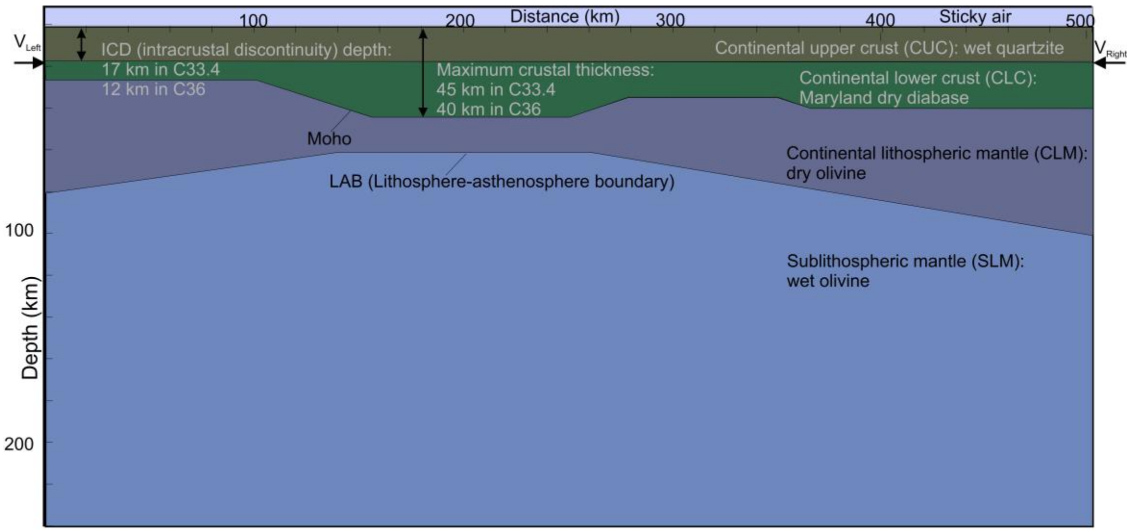

Figure 5.5: C-group model setup with indication of the differences between C33.4 and C36 models. For material parameters see Table 5.1.

5.4.4 D-group models: low pushing velocities and asymmetric LAB

After the simulations of the C-group models, the LAB geometry was changed to improve the lithosphere structure near the subduction zone. An asymmetric simplified LAB geometry attempts to replicate the lithospheric strength and heat distribution in the orogen to test its effect on deformation. We also changed the crust geometry based on the reconstructions by Giambiagi et al. (2015) for the Late Cretaceous (Figure 5.6).

Another variation introduced here is the lower crustal composition and hence its rheology. As mentioned before (see section 5.2), the crust was modified during pre-Andean tectonic evolution. For the 33°40’S model (named D33.4), a more felsic lower crust was inferred, while in the southern zone, it is assumed to be mafic. Therefore, the lower crustal material parameter was modified to be as a dry quartzite and a wet quartzite for the 33°40 model. We also tested variations of these materials applying a scale factor ***f*** (Sobolev et al., 2006; Currie and Beaumont, 2011; Liu and Currie, 2016; Wolf and Huismans, 2019) for the dislocation creep flow law, to account for uncertainties from extrapolation from laboratory experiments to nature. We use f=5 for a dry quartzite and for a wet quartzite. These values were chosen to simulate a more intermediate composition for the lower crust, thus a stronger rheology than a quartzite.

For the 36°S model (named D36), a mafic lower crust was assumed (see section 5.2) and we used a Maryland dry diabase and a Columbia diabase, the latter being weaker than the former (Table 5.3, Burov, 2011). Besides, we applied a scaling factor ***f*** of 0.2 and

1 for the Maryland diabase and 0.05, 0.1, 0.2 and 1 for the Columbia diabase to simulate the lower crust affected by temperature and melting in the arc zone.

Models at 33°40’S - D33.4				**Models at 36°S – D36**			
M#	**Vl0.5Vr0.5**	**M#**	**Vl0Vr1**	**M#**	**Vl0.5Vr0.5**	**M#**	**Vl0Vr1**
15	MDDf1	16	MDDf1	17	MDDf1	18	MDDf1
19	DQf1	22	DQf1	31	CDf0.2	34	CDf0.2
20	DQf5	23	DQf5	32	CDf1	35	CDf1
21	WQf5	24	WQf5	33	MDDf0.2	36	MDDf0.2
				37	CDf0.1	39	CDf0.1
				38	CDf0.05	40	CDf0.05

Table 5.3: Model list for D-group. MDDf1 and MDDf0.2: Maryland dry diabase scale factor 1 or 0.2; DQf1: Dry quartzite scale factor 1; DQf5: Dry quartzite scale factor 5; WQf5: Wet quartzite scale factor 5. CD0.2, CDf1, CDf0.1, CDf0.05: Columbia diabase scale factor 0.05 to 1.

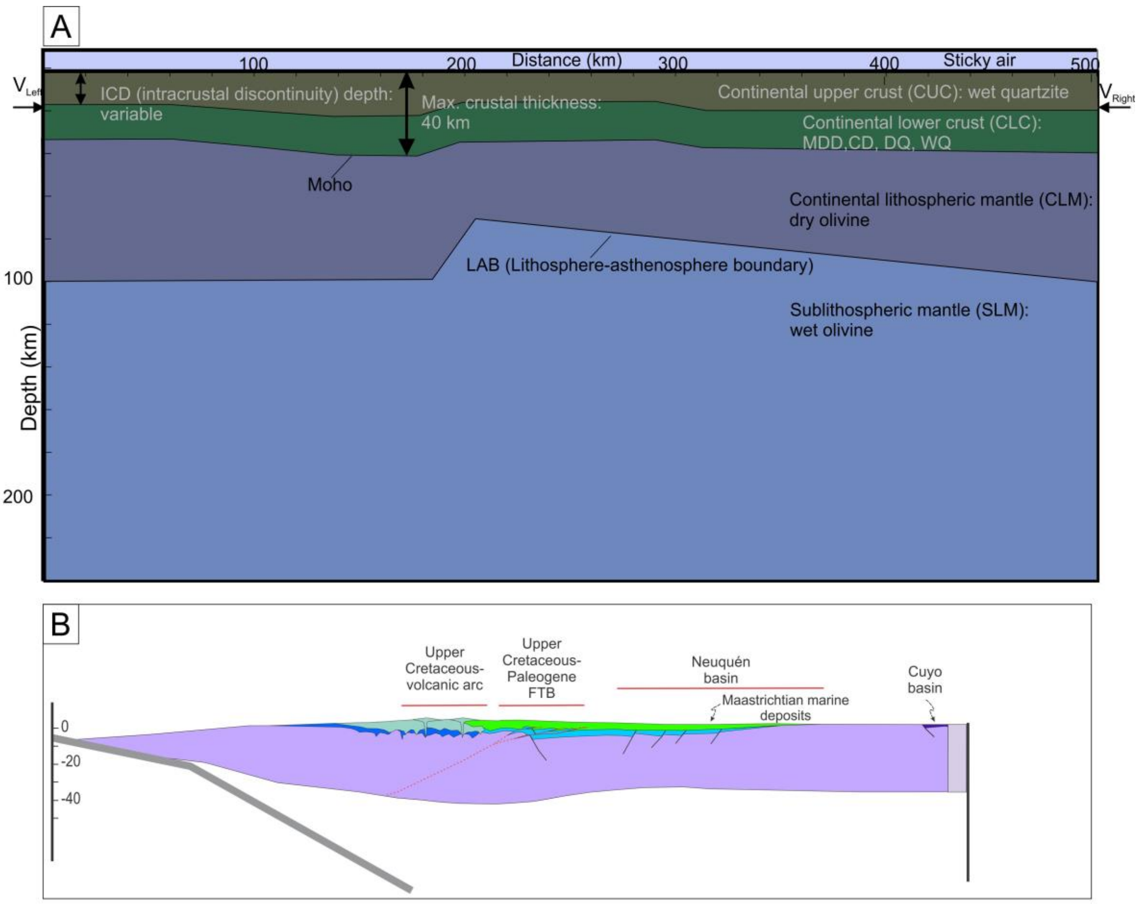

Figure 5.6: A) D-group model setup. Lower crust composition variations are detailed in Table 5.3 MDD: Maryland dry diabase, CD: Columbia diabase, DQ: Dry quartzite, WQ: Wet quartzite. B) Late Cretaceous-Early Paleocene reconstruction from Giambiagi et al. (2015) used to develop the initial model setup.

5.5 Results

We ran more than 60 models using the different setups described above and from that total 34 models are presented here since these are the ones that developed more realistic results.

5.5.1 A-group models (high pushing velocities)

From this first group of models, we observed that the deformation occurs where the lithosphere is thinner (near the left boundary), although the crust is thinner in the same zone. This latter factor increases the integral strength of the lithosphere when compared to a lithosphere with a thicker crust. We note, however, that the western (left) boundary of the model box combined with the thinnest lithosphere may also attract deformation

5.5.1a Model at 33°40’S (A33.4):

In this model, the deformation is focused on the left side of the model box (forearc) and despite some deformation is observed in the arc (x coordinates: 120-150 km) it is minor; even running the model for 2 Myr (model time), the deformation does not migrate to the east; instead the underthrusting of the lithosphere on the western border of the model occurred after ~30 km of shortening (Figure 5.7).

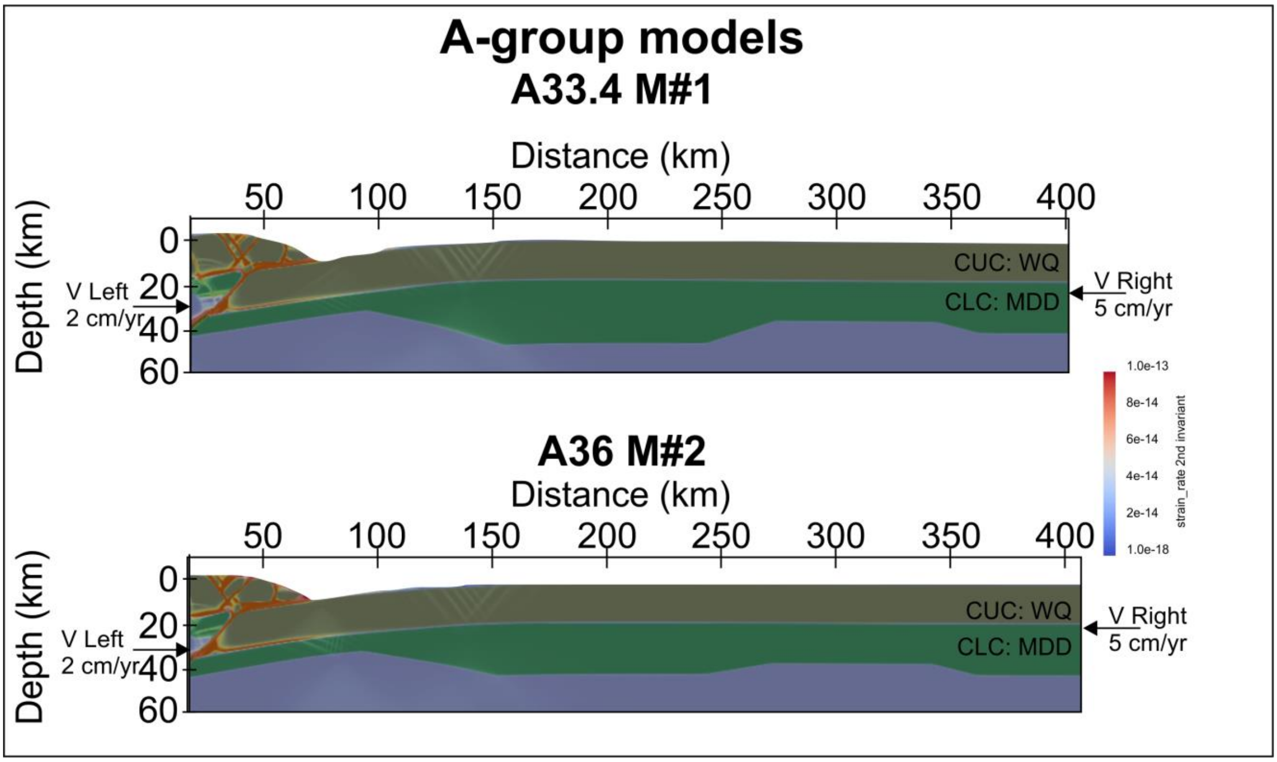

Figure 5.7: Models at 33°40’S (above) and at 36°S (below) after 30 km of shortening the deformation affects only the thinner part of the lithosphere in the left side of the model.

5.5.1b Model at 36°S (A36):

Similar to the Model 33°40°S, the deformation affects almost exclusively the left border of the model, with underthrusting of the eastern lithosphere to the west after 30 km of shortening (Figure 5.7).

5.5.2 B-group models (lower pushing velocities)

In these models, the deformation is also focused on the left side of the model where the lithosphere is thinner, but due to the lower pushing velocity (1 cm/yr vs. 7 cm/yr in A models), the strain rate is lower. Finally, after 50 to 70 km of shortening, an underthrusting of the crust is observed (Figure 5.8 and 5.9).

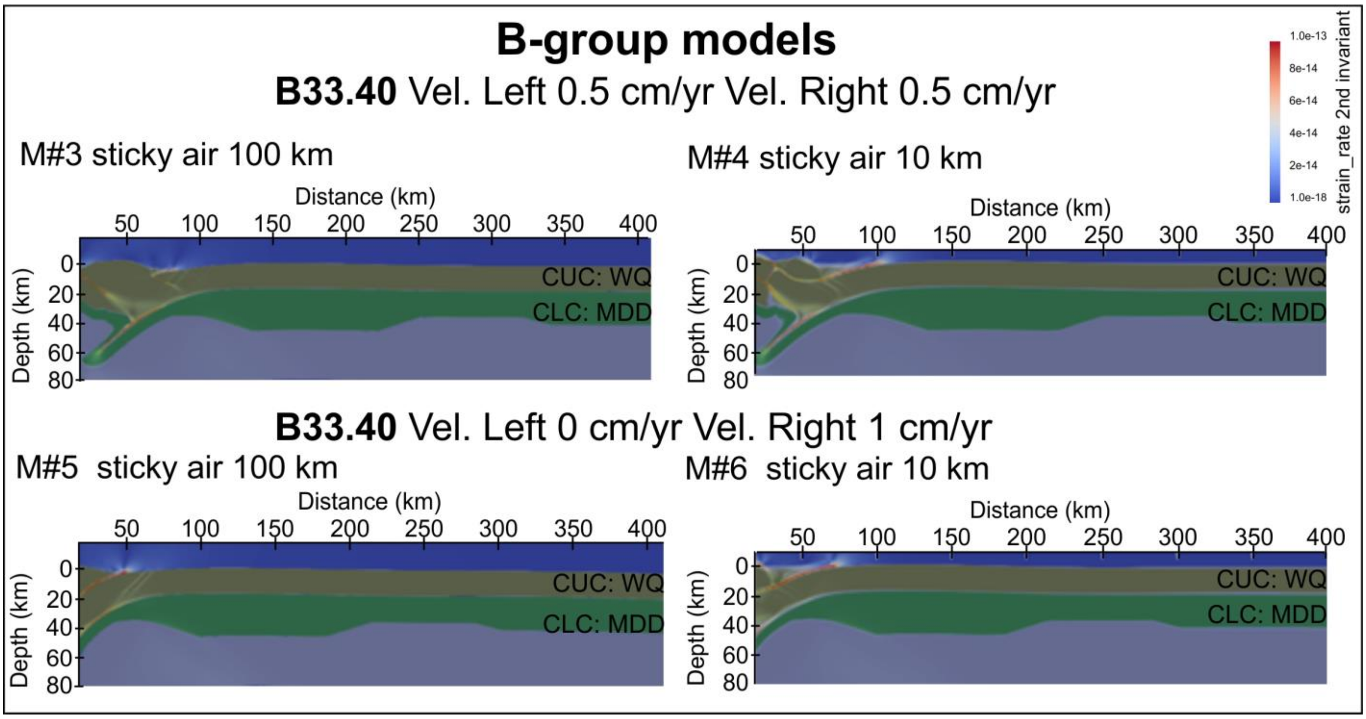

Figure 5.8: Model at 33.40°S, after 70 km of shortening. The deformation affects only the thinner part of the lithosphere in the left side of the model with an underthrusting of the crust.

5.5.2a Model at 33°40'S (B33.4):

When we compare the different setups for models at 33°40'S (B33.4), we observe that if the velocity is applied only on the right (East) boundary, the entire lithosphere moves farther to the left side (West). On this side, the effect of side boundary conditions is more pronounced (Figure 5.8 M#5 and #6), acting as a backstop for the underthrusted crust. Also, when comparing the influence of the sticky air thickness (M #3 vs. M #4 and M#5 vs. M#6), we noticed that, under a thin, sticky air, the deformation in the upper crust is more

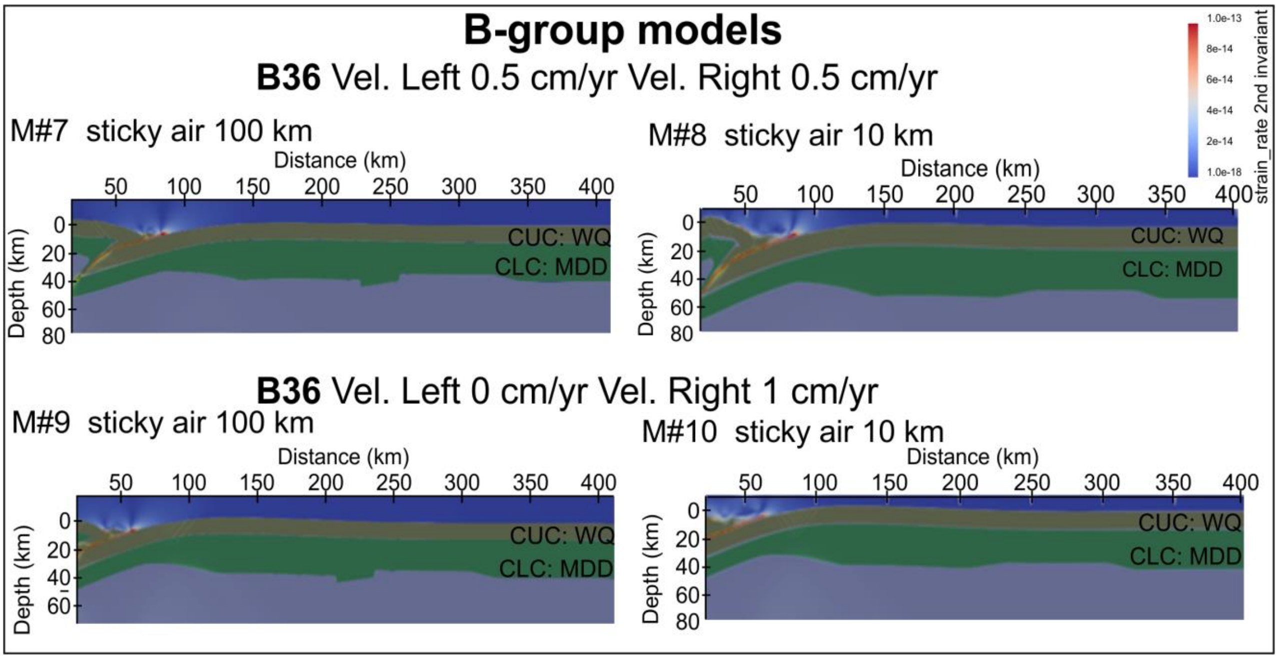

Figure 5.9: Model at 36°S, after 45 km of shortening. As in previous models, the deformation is focused in the thinner part of the lithosphere in the left side of the model.

complex, with several shear zones. In M#6, the upper crust is deformed by a detachment that does not cut the whole crust and it is disconnected from the detachment in the lower crust. In general, all of these models show that the main detachments are E-vergent.

5.5.2b Model at 36°S (B36):

Regarding models at 36°S, after 45 km of shortening an underthrusting of the crust is observed, but in these cases, the deformation is mostly concentrated in a main detachment that cuts the whole crust (e.g.,Figure 5.9 M#7); while in the equivalent model at 33°40'S (M#3), the deformation is more complex with a pair of main detachments. We interpret this as a result of a thicker mafic crust in the B36 models, which results in higher strength for the whole crust. In all of these B36 models, the main detachments are E-vergent.

The B-group models do not replicate the deformation patterns determined from geological and geophysical data in the Andes. One main conclusion is that the deformation is focused where the lithosphere is thinner (thus weaker), in this case, near to the left side of the model box.

5.5.3 C-group models (low pushing velocities and symmetric LAB)

5.5.3.a Models at 33°40’S: C33

In these models, the lithospheric thickness symmetrically varies across the strike. The deformation is focused where the lithosphere is thinner, between x-coordinates 150 to 250 km (Figure 5.10). This would replicate well the deformation in the arc region of the orogen, where due to corner flow, the lithosphere is thinner, and thus prone to be deformed under contraction. At the beginning of the model run (~5 km shortening), the deformation is visible in the upper crust as a pair of conjugate faults or shear zones that irradiate from a point in the ICD, which then continue downward, in very diffuse zones, reaching the LAB. After 40 km of shortening, the deformation is concentrated in a main detachment, which differs in its dip for the M#11 (E-vergent) and M#12 (W-vergent). We ran these models again, with the same setup to test whether the detachment’s vergence is randomly oriented and we found that this is the case. We interpret that this is due to the homogeneity of the crust and once the yield strength is reached the crust deforms randomly to the East or to the West.

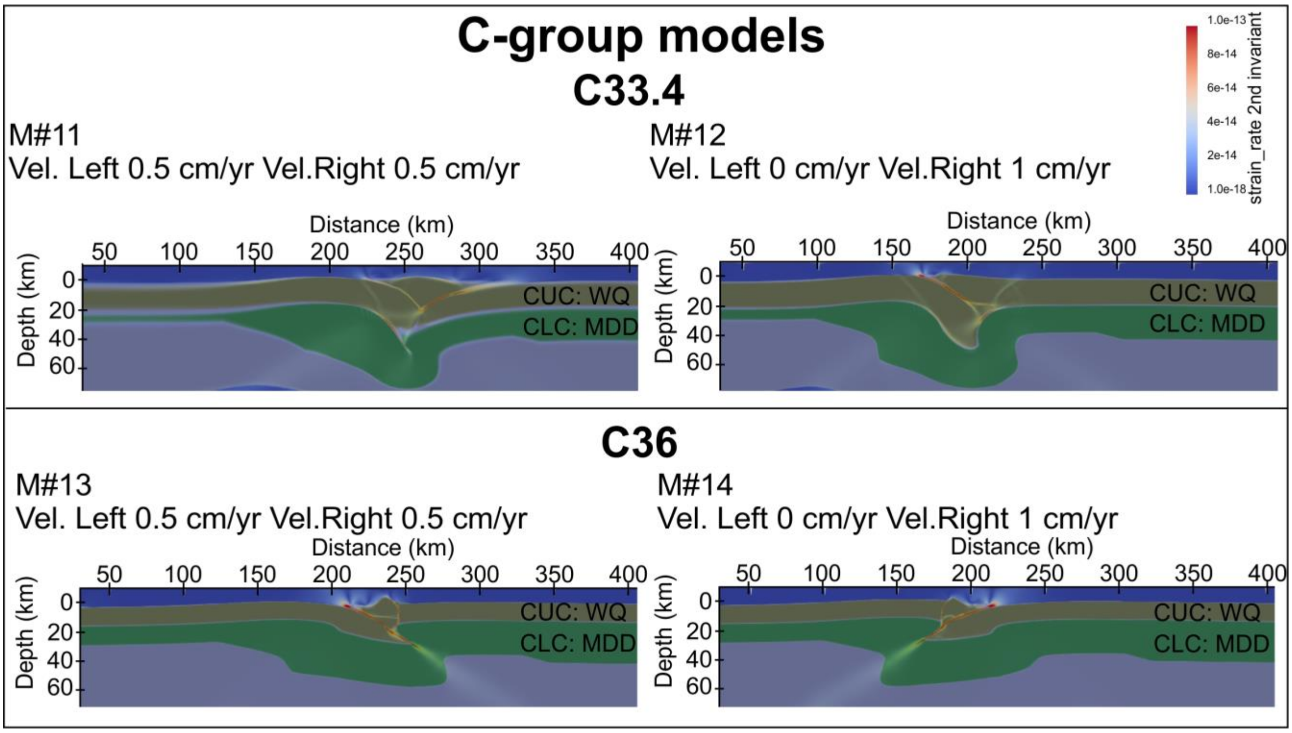

Figure 5.10: Vl0.5, Vl0: velocity on the left side 0.5 cm/yr or 0 cm/yr; Vr0.5, Vr1: velocity on the right side 0.5 cm/yr or 1 cm/yr.

These models do not replicate some of the orogenic features in the study area. For example, the crustal thickness is higher than the present-day estimations. After 70 km of shortening in the M#11 model, the crust reaches nearly 70 km of thickness, while according to Tassara and Echaurren (2012), it is 50 km.

5.5.3.b Models at 36° (C36):

Similarly, as in the C33.4 models, the vergence of the detachments does not seem to be controlled by velocity-boundary conditions. In these models, the upper crust is thinner compared to the C33.4 models and the deformation pattern is different (Figure 5.10).

We observe that the shear zone location is apparently controlled by the change of the geometry in the lower crust since the detachment cuts the lower crust in the area in which the thickness variation was established.

5.5.4 D-group models (low pushing velocities and asymmetric LAB)

5.5.4.a Models at 33°40’S (D33.4):

The first-order observation from these models is that there are no important differences whether the velocity is applied on both sides with 0.5 cm/yr (Vl0.5Vr0.5 models) or if it is applied only on the right side with 1 cm/yr (Vl0Vr1). The noticeable difference is that the whole lithosphere is displaced to the left side when the velocity is applied on the right boundary. When we change the material rheology in the lower crust, the deformation is quite different. When we use a mafic material as a diabase (Maryland dry diabase, Figure 5.11 models #15 and #16), the lower crust does not flow and the upper crustal detachment cuts the entire crust. This deformation mode is similar to the simple-shear mode, where upper crustal deformation is horizontally displaced with respect to lower crustal deformation. In the models with felsic and thus weaker composition of the lower crust (#19 to #24), the crust flows viscously, producing a widening of the crustal root. This deformation is aligned vertically with upper crustal deformation, as a pure-shear or coupled deformation mode.

In these models, the crust reaches a thickness of almost 60 km after 70 km of shortening, which correlates well with the actual structure of the orogen.

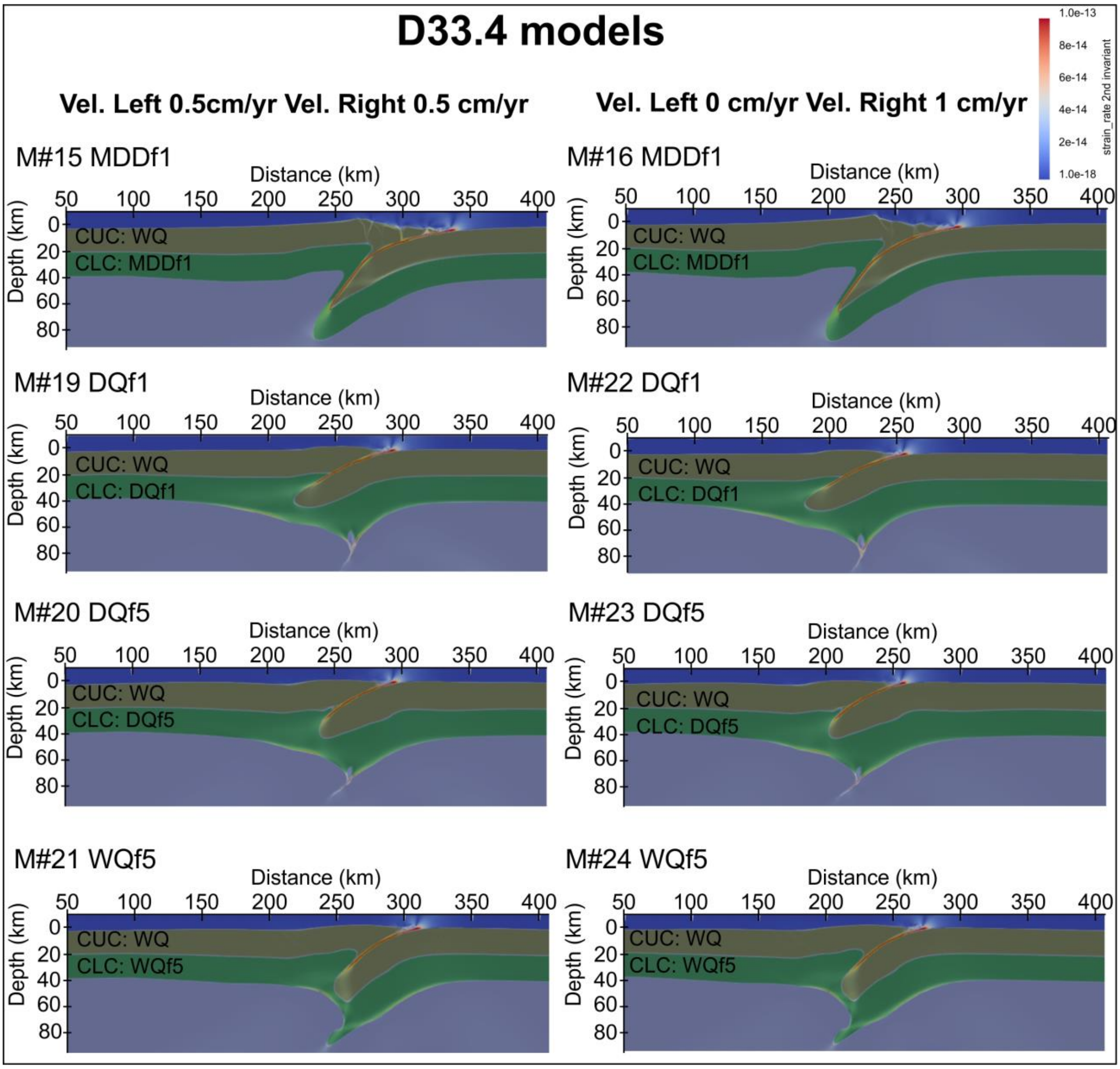

Figure 5.11: Model results after 70 km of shortening. MDDf1: Maryland dry diabase scale factor 1; DQf1: Dry quartzite scale factor 1; DQf5: Dry quartzite scale factor 5; WQf5: Wet quartzite scale factor 5. Vl0.5, Vl0: velocity on the left side 0.5 cm/yr or 0 cm/yr; Vr0.5, Vr1: velocity on the right side 0.5 cm/yr or 1 cm/yr.

5.5.4.b Models at 36° (D36):

Another inference we can make from D-group models (33.4 and 36) is with regards to the orogenic vergence. All of our models with the asymmetric LAB (Figure 5.6) produce E-vergent detachments (Figure 5.12), which is in accordance with the dominant geological models for the Andes. This could be interpreted as a result of the thicker and stronger lithosphere, to the left (West) of the thinner lithosphere in the model, in what is the forearc domain. This western domain is usually inferred to be a rigid block of cold and thick lithosphere, which acts as a backstop for the E-directed movement of the crust (Tassara and Yáñez, 2003). The asymmetry of the LAB generates a weaker zone than the surrounding that concentrates the deformation.

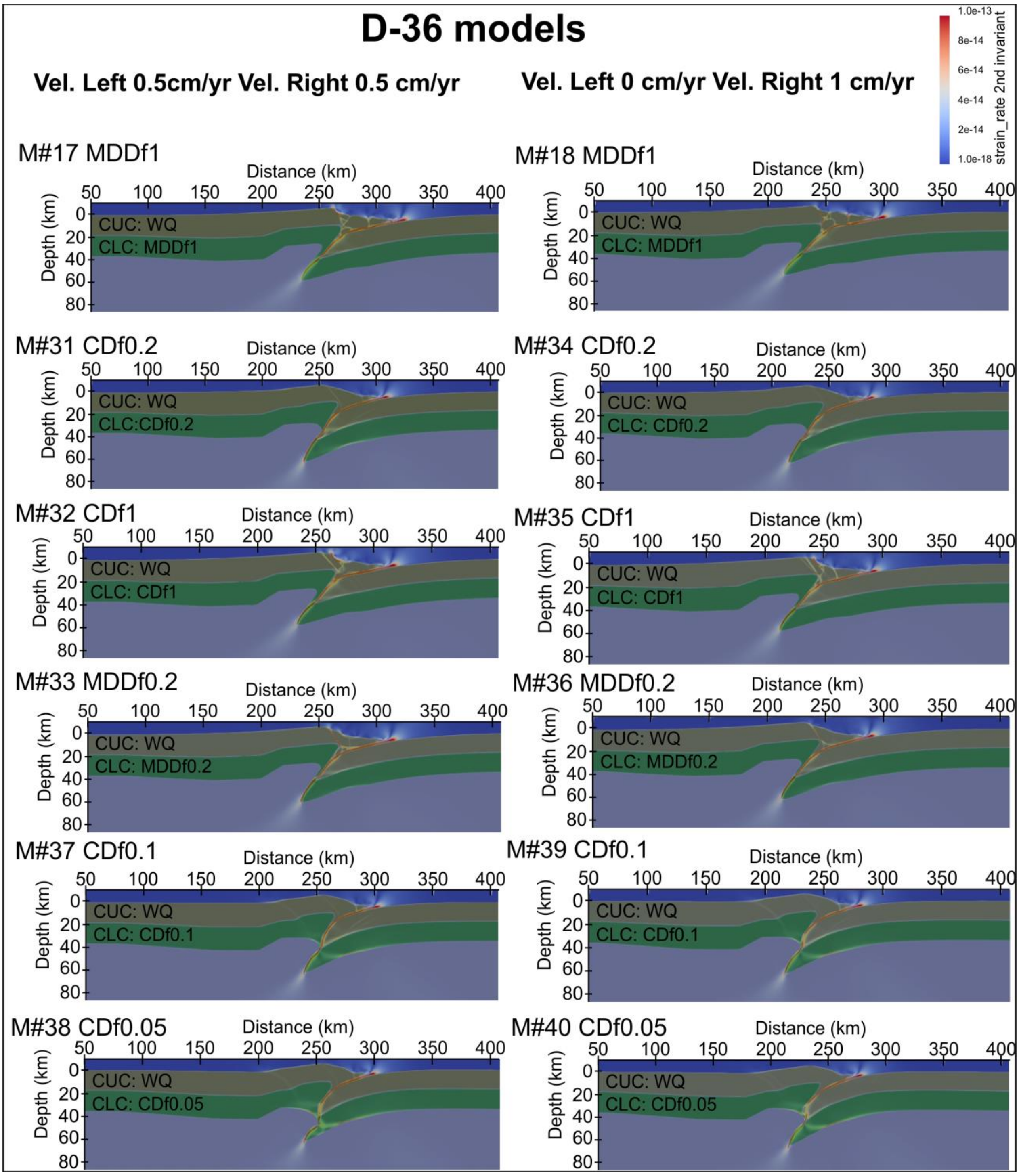

Figure 5.12: Model results after 45 km of shortening. MDDf1, MDDf0.2: Maryland dry diabase scale factor 1 or 0.2; CD0.2, CDf1, CDf0.1, CDf0.05: Columbia diabase scale factor 0.05 to 1. Vl0.5, Vl0: velocity on the left side 0.5 cm/yr or 0 cm/yr; Vr0.5, Vr1: velocity on the right side 0.5 cm/yr or 1 cm/yr.

5.6 Model limitations

In our models, we tested the influence of different crustal thickness and composition under contraction. The main issues of the first attempt (A-group models) are: (i) the velocities applied are not real, because not all of the subduction velocity is transferred as shortening to the upper plate, and (ii) the thin lithosphere on the left side is the weakest part of the model, so the deformation is focused there. In B-group models, the geometry was not realistic and the thin lithosphere on the left side localised the deformation. For C- and D-groups, although the lithosphere was thinner below the area that represents the magmatic arc, the lithospheric structure in the model is probably still too simple compared to the real structure.

The main simplification in our setup is that the simulation does not include the subduction system with an oceanic plate interacting with the continental plate and underlaying mantle. In particular, we focused on the deformation mode of the crust without considering the dynamic influence of corner flow. As Sobolev et al. (2006) demonstrated, corner flow is blocked when the lithospheric mantle is delaminated, and this causes changes in shortening rates. In our study area, the delamination process presumably had not yet occurred. Thus, we are able to assume that the influence of blocked corner flow with respect to shortening rates is not significant. Nevertheless, in future work, we plan to incorporate these processes and test their influence.

5.7 Discussion

It was proposed that high elastic thickness (Te) correlates with thin-skinned tectonics and low Te correlates with thick-skinned deformation; i.e., a weaker lithosphere allows for shortening of the entire crust while a stronger lithosphere resists deformation and shortening is localized only in a portion of the crust (Watts et al., 1995; Lacombe and Bellahsen, 2016;).

Mouthereau et al. (2013) suggested that the deformation mode correlates with the age of the lithosphere of the upper plate, hence its thermal state. Orogens formed in old, cold and stronger lithosphere (with a high-viscosity mantle) are characterized by large detachment faults that are usually rooted in a weak sedimentary cover where large amounts of shortening develop in a simple-shear mode. In contrasts, orogens formed in younger (i.e., Phanerozoic) lithosphere, which has higher geothermal gradients and a weaker mantle, are characterized by less shortening and thrust faults formed in the middle to lower crust, revealing that the deformation is distributed with brittle crustal thrust ramps in the upper crust. In contrast, flow occurs in the ductile middle-lower crust, in a pure-shear mode (Mouthereau et al., 2013; Lacombe and Bellahsen, 2016;). In our study region, the age of the South American lithosphere is similar in the northern and southern sectors, and thus its thermal state. The thermal state is also affected by the magmatism related to subduction, which is also similar in both sectors. Regarding the shortening, in the northern area shortening estimates are higher than in the southern area, although evidence for pure- and simple-shear deformation was reported for each area, respectively (Giambiagi et al., 2012) showing that for this case there is no clear correlation with the deformation mode and shortening estimates.

In the case of the Altiplano-Puna segment to the north, the pure- and simple-shear deformation mode is related to changes in the strength of the lithosphere related to the presence of thick sedimentary sequences in the foreland of Altiplano, where the Subandean System has evolved (Allmendinger and Gubbels, 1996). This scenario was tested by Babeyko and Sobolev (2005) employing numerical modeling. A similar approach was recently employed by Liu et al. (under review in Tectonics). For our studied Andean segment between 33 and 36ºS, the thickness of the sedimentary succession of the Neuquén basin is similar (~4 km), indicating that it is not the main control over the deformation mode. In this case, our tests show that a change in lower crustal composition and thus crustal strength affects the deformation mode, with an uncoupled or simple-shear deformation mode when the lower crust is mafic and rheologically stronger, and pure-shear deformation mode, when the lower crust is more felsic and consequently weaker.

According to our results, the vergence of the orogenic system with an eastward subduction polarity is controlled by the asymmetry of the LAB. The thick and strong lithosphere in the forearc acts as backstop inducing deformation directed to the East. Importantly, this is in accordance with the geological observations for the area.

5.8 Conclusions

We present here the first geodynamic models for the Andes at this latitude and conclude that the lower crust composition is an important factor controlling the deformation mode; felsic compositions allow for pure-shear deformation and more mafic for a simple-shear deformation. Another interesting conclusion is that the asymmetry of the LAB promotes E-vergent deformation of the main detachments.

Chapter VI

6. Conclusions and future perspectives

6.1 Conclusions

Here, the main points of this thesis are summarized:

From the integration of surface structural data, wellbore and seismic data, it is interpreted that during the Miocene-Pliocene evolution of the thrust front of the Malargüe fold-and-thrust belt (35°-36°S, Southern Central Andes), the local stress field changed from a compressional to a strike-slip/compressional one, likely related to similar values of the minimum (σ3) and intermediate (σ2) principal stress, with the maximum principal stress (σ1) oriented E-W according to the plate convergence vector. The strike-slip/compressional regime favoured the emplacement of sills and dykes. Previous NW-striking structures were not amenable to be inverted but instead they were prone to slip under the strike-slip/compressional regime. WNW-oriented structures were prone to dilate and act as magmatic feeders.

Based on inversion of fault slip data and wellbore minifrac test, we infer that the Pliocene to present-day activity of both reverse and strike-slip faults in the orogenic front of Malargüe fold-and-thrust belt is the result of a strike-slip/ compressional regime. In this regime, intermediate (σ2) and minimum (σ3) stresses have similar magnitudes ($\sigma3 \sim \sigma2 < \sigma1$) and are locally interchanged, producing a setting in which reverse and strike-slip faults are alternatively active.

Geodynamic numerical modeling was performed, using the code LAPEX-2D, of a whole subduction system setup with a kinematically prescribed subduction slab. This configuration does not replicate realistically the system but implies a methodological progress which can guide next steps of subduction systems modeling.

The first high-resolution geodynamic models of the Andes at 33°-36°S were run, simulating the continental lithosphere under contraction. It is concluded that the lower crust composition is an important factor controlling the deformation mode, resulting in pure-shear when felsic composition and simple-shear when more mafic. An interesting result is that the LAB asymmetry promotes E-vergent deformation of the main detachments, and this sheds lights on the present discussion of west- vs east-vergence of the Andean orogen.

6.2 Future perspectives

We are working on the completion of the orogen-scale transect at 36° which integrates surface and subsurface data. This would allow for a better understanding of the Andean evolution at this latitude and its comparison with other latitudes in the normal subduction zone.

As we mentioned above, the LAPEX-2D code is a light geodynamic code that demands low computational costs. This is a good point to continue using it in personal desktops. We are working on setups of the subduction system but without a kinematically prescribed slab. These setups allow for a realistic temperature distribution and the dynamic effects of the asthenospheric corner flow.

Regarding the code ASPECT, we are preparing new setups for lithosphere under compression with more realistic temperature distribution. As a subduction module for the code is being improved we want to test it for the Southern Central Andes configuration.

7. References

Aguirre-Urreta B., Tunik M., Naipauer M., Pazos P., Ottone G., Fanning M., Ramos V.A., 2011. Malargüe Group (Maastrichtian–Danian) deposits in the Neuquén Andes, Argentina: implications for the onset of the first Atlantic transgression related to Western Gondwana break-up. Gondwana Res 19:482–494.

Ahumada E.A., Costa C.H., 2009. Antithetic linkage between oblique Quaternary thrusts at the Andean front, Argentine Precordillera. J South Am Earth Sci 28:207–216.

Allmendinger, R. W. ,2001. FaultKinWinFull version 1.2.2. A program for analyzing fault slip data for Windows™ computers. [Available at http://www.geo.cornell. edu/ geology/faculty/RWA/programs.html, last accessed 19/4/2019]

Allmendinger, R.W., Gubbels, T. 1996. Pure and simple shear plateau uplift, Altiplano-Puna, Argentina and Bolivia: Tectonophysics 259: 1–13.

Allmendinger, R.W., Ramos, V.A., Jordan, T.E., Palma, M., Isacks, B.L., 1983. Paleogeography and Andean structural geometry, northwest Argentina. Tectonics 2, 1–16. https://doi.org/10.1029/TC002i001p00001

Allmendinger R.W., Figueroa D., Snyder D., Beer J., Mpodozis C., Isacks B.L., 1990. Foreland shortening and crustal balancing in the Andes at 30°S latitude. Tectonics 9:789–809.

Allmendinger, R.W., Jordan, T.E., Kay, S.M., Isacks, B.L., 1997. The evolution of the Altiplano-Puna Plateau of the Central Andes. Annual Reviews of Earth and Planetary Sciences, 25: 139-174.

Allmendinger, R. W., Cardozo, N., Fisher, D. M., 2012. Structural geology algorithms: Vectors and tensors. Cambridge University Press.

Alvarado P., Beck S., Zandt G., Araujo M., Triep E., 2005. Crustal deformation in the south-central Andes back-arc terranes as viewed from regional broad-band seismic wave form modelling. Geophys J Int. doi:10.111/j.1365-246X.2005.02759.

Alvarado P., Beck S., Zandt G., 2007. Crustal structure of the south-central Andes Cordillera and backarc region from regional wave form modeling. Geophys J Int 121:858–875.

Álvarez P.P., Godoy E., Aguirre-Urreta M.B., 1996. Jurásico marino de la Alta Cordillera de Chile Central, Región Metropolitana. En: XIII Congreso Geológico Argentino (Buenos Aires), Actas 5:181.

Anderson, E. M., 1951. The dynamics of faulting and dyke formation with applications to Britain. Hafner Pub. Co.

Angelier, J., 1975. Sur l'analyse de mesures recueillies dans des sites faillés : l'utilité d'une confrontation entre les méthodes dynamiques et cinématiques. C. R. Acad. Sci. Paris, Ser. D 281, 1805–1808.

Angelier, J., 1984. Tectonic analysis of fault slip data sets. J. Geophys. Res. 89 (B7), 5835–5848.

Angelier, J., 1990. Inversion of field data in fault tectonics to obtain the regional stress. III: a new rapid direct inversion method by analytical means. Geophys. J. Int. 103, 363–376.

Araneda M., Avendaño M., Merlo C., 2000. Modelo gravimétrico de la cuenca de Santiago, etapa III final. In: IX Congreso Geológico DE Chile (Puerto Varas) 404–408.

Araujo, V. S., Dimieri, L. V., Frisicale, M. C., Turienzo, M. M., Sánchez, N. P., 2013. Emplazamiento del cuerpo subvolcánico Laguna Amarga y su relación con las estructuras tectónicas andinas, sur de la provincia de Mendoza. Revista de la Asociación Geológica Argentina, 70(1), 40-52.

Arcila Gallego, P. A., 2010. Los depósitos sinorogénicos del sur de Mendoza y su relación con la faja plegada y corrida de Malargüe (35°-36° S), Mendoza. Argentina (Doctoral dissertation, Facultad de Ciencias Exactas y Naturales. Universidad de Buenos Aires).

Armijo, R., Rauld, R., Thiele, R., Vargas, G., Campos, J., Lacassin, R., Kausel, E. 2010. The West Andean Thrust, the San Ramón Fault and the seismic hazard for Santiago, Chile. Tectonics 29. TC2007.

Artabe, A. E., Morel, E. M., Spalletti, L. A., Brea, M., 1998. Paleoambientes sedimentarios y paleoflora asociada en el Triásico tardío de Malargüe, Mendoza. Revista Asociación Geológica Argentina, 53(4), 526-548.

Astaburuaga, D., 2014. Evolución estructural del límite Mesozoico-Cenozoico de la Cordillera Principal entre los 35 30′ y 36 S, Región del Maule, Chile. Dep. Geol. Univ. Chile (Msc. Thesis, 128 pp.).

Astini, R.A., Dávila, F.M., 2010. Comment on “The West Andean Thrust, the San Ramón Fault, and the seismic hazard for Santiago, Chile” by Rolando Armijo et al. Tectonics 29, n/a-n/a. https://doi.org/10.1029/2009TC002647
Aydin, A., 2000. Fractures, faults, and hydrocarbon entrapment migration and flow. Marine and Petroleum Geology 17, 797-814.
Azcuy, C.L., Caminos, R., 1987, Diastrofismo. En El sistema carbonífero en la República Argentina (Archangelsky, S., ed.), Academia Nacional de Ciencias, p. 239–252. Córdoba, Argentina.
Babeyko, A.Y. and Sobolev, S.V. , 2005. Quantifying different modes of the Late Cenozoic shortening in the Central Andes, Geology 33, 621–624.
Babeyko, A.Y., Sobolev, S. V., Trumbull, R.B., Oncken, O., Lavier, L.L., 2002. Numerical models of crustal scale convection and partial melting beneath the Altiplano-Puna plateau. Earth Planet. Sci. Lett. 199, 373–388. https://doi.org/10.1016/S0012-821X(02)00597-6
Babeyko, A.Y., Sobolev, S. V., Vietor, T., Oncken, O., Trumbull, R.B., 2006. Numerical Study of Weakening Processes in the Central Andean Back-Arc. Andes - Act. subduction orogeny 495–512. https://doi.org/10.1007/978-3-540-48684-8
Baldauf, P.E., 1997. Timing of the uplift of the Cordillera Principal, Mendoza Province, Argentina [Ph.D. thesis]: Washington, D.C., George Washington University, 356 p.
Baldis, B. A. J., G. Chebli, 1969. Estructura profunda del área central de la Precordillera sanjuanina, IV, J. Geol. Argent., 1, 47-66.
Baldis, B. A., Peralta, S. H., 1999. Silúrico y Devónico de la Precordillera de Cuyo y Bloque de San Rafael. En Geología Argentina (Caminos, R.; editor). Servicio Geológico y Minero Argentino, Instituto de Geología y Recursos Minerales, Anales 29 (10): 215-238, Buenos Aires.
Balgord, E. A., Carrapa, B., 2016. Basin evolution of Upper Cretaceous–Lower Cenozoic strata in the Malargüe fold-and-thrust belt: northern Neuquén Basin, Argentina. Basin Research, 28(2), 183-206.
Bande, A., Boll, A., Fuentes, F., Horton B., Stockli, D. F., (in press) Thermochronological constraints on the exhumation of the Malargüe fold-thrust belt, southern Central Andes. In: Opening and closure of the Neuquén Basin in the Southern Andes, Diego Kietzmann and Andrés Folguera (eds)
Barazangi, M. Isacks, B. L. Spatial distribution of earthquakes and subduction of the Nazca plate beneath South America. Geology 4, 686–692 (1976).
Barrientos S., Vera E., Alvarado P., Monfret T., 2004. Crustal seismicity in central Chile. J S Am Earth Sci 16:759–768.
Barton, C.A., Zoback, M.D. Moos, D., 1995. Fluid flow along potentially active faults in crystalline rock. Geology 23, 683-686.
Bastías H., Tello G.E., Perucca L.P., Paredes J.D., 1993. Peligro sísmico y neotectónica. En: Ramos VA (ed) Geología y recursos naturales de la provincia de Mendoza. Relatorio XII Congreso Geológico Argentino 6(1):645–658.
Beaudoin, N., Lacombe, O., 2018. Recent and future trends in paleopiezometry in the diagenetic domain: Insights into the tectonic paleostress and burial depth history of fold-and-thrust belts and sedimentary basins. Journal of Structural Geology, 114: 357-365.
Bechis, F., Giambiagi, L., García, V., Lanés, S., Cristallini, E., Tunik, M., 2010. Kinematic analysis of a transtensional fault system: The Atuel depocentre of the Neuquén Basin, Central Andes, Argentina: Journal of Structural Geology, v. 32, p. 886–899, doi:10.1016/j.jsg .2010.03.009.
Bechis, F., Cristallini, E. O., Giambiagi, L. B., Yagupsky, D. L., Guzmán, C. G., García, V. H., 2014. Transtensional tectonics induced by oblique reactivation of previous lithospheric anisotropies during the Late Triassic to Early Jurassic rifting in the Neuquén basin: insights from analog models. Journal of Geodynamics, 79, 1-17.
Bechis, F., Giambiagi, L. B., Tunik, M., Suriano, J., Mescua, J. F., Lanés, S., (in press) Tectono-stratigraphic evolution of the Atuel depocenter during the Late Triassic to Early Jurassic rift stage, Neuquén basin, west-central Argentina. In: Opening and closure of the Neuquén Basin in the Southern Andes, Diego Kietzmann and Andrés Folguera (eds)
Bell, J.S., Gough D.I., 1982. The use of borehole breakouts in the study of crustal stress, U.S. Geol. Surv. Open File Rep., 82-1075, 539 – 557.
Bense, F.A., Löbens, S., Dunkl, I., Wemmer, K., Siegesmund, S., 2013. Is the exhumation of the Sierras Pampeanas only related to Neogene flat-slab subduction? Implications from a multi-

thermochronological approach. J. South Am. Earth Sci. 48, 123–144. https://doi.org/10.1016/j.jsames.2013.09.002.
Bermúdez, A., Delpino, D., 1989. La provincia basáltica andino cuyana (35°-37°LS). Revista de la Asociación Geológica Argentina, 44: 35-55.
Bermúdez, A., Delpino, D., Frey, F., Saal, A., 1993. Basaltos de retroarco extraandinos. En: Ramos, V.A. (ed). Relatorio Geología y Recursos Naturales de la Provincia de Mendoza. Relatorio XII Congreso Geológico Argentino: Buenos Aires, Servicio Geológico Minero Argentino (SEGEMAR), Abstracts, v. 1, p. 161–172.
Bettini, F., 1982. Complejos efusivos terciarios presentes en las Hojas 30c y 32b (Puntilla del Huincán y Chos Malal), del sur de Mendoza y Norte del Neuquén, Argentina. In Actas V Congreso Latinoamericano de Geología 5: 79-114.
Bodenbender, G., 1911. Constitución geo- lógica de la parte meridional de La Rioja y regiones limítrofes. Academia Nacional de Ciencias, Boletín 19:1-220, Córdoba.
Boll, A., Alonso, J., Fuentes, F., Vergara, M., Laffitte, G., Villar, H., 2014. Factores controlantes de las acumulaciones de hidrocarburos en el sector norte de la Cuenca Neuquina, entre los ríos Diamante y Salado, provincia de Mendoza, Argentina. IX Congreso de Exploración y Desarrollo de Hidrocarburos, Actas: 3-44.
Bordonaro, O., 1999. Cámbrico y Ordovícico de la Precordillera y Bloque de San Rafael. En Geología Argentina (Caminos, R.; editor). Servicio Geológico y Minero Argentino, Instituto de Geología y Recursos Minerales, Anales 29 (8): 189-204, Buenos Aires.
Bracaccini, O., 1946. Contribución al conocimiento geológico de la Precordillera Sanjuanino-Mendocina. Boletín de Informaciones Petroleras 23(258): 81-105; (260): 259- 74; (261): 361-384; (262): 455-473; (263): 22-35; (264): 103-125 y (265): 171- 192.
Bracaccini, O., 1960. Lineamientos principales de la evolución estructural de la Argentina. Petrotecnia, Revista Instituto Argentino del Petróleo 10(6): 57-69.
Branellec, M., Callot, J. P., Aubourg, C., Nivière, B., Ringenbach, J. C. 2015a. Matrix deformation in a basement-involved fold-and-thrust-belt: a case study in the central Andes, Malargüe (Argentina). Tectonophysics, 658, 186-205.
Branellec, M., Callot, J. P., Nivière, B., Ringenbach, J. C., 2015b. The fracture network, a proxy for mesoscale deformation: constraints on layer parallel shortening history from the Malargüe fold and thrust belt, Argentina. Tectonics, 34(4), 623-647.
Branellec, M., Nivière, B., Callot, J. P., Ringenbach, J. C., 2016. Mechanisms of basin contraction and reactivation in the basement-involved Malargüe fold-and-thrust belt, Central Andes (34–36 S). Geological Magazine, 153(5-6), 926-944.
Brüggen, J., 1950. Fundamentos de la Geología de Chile. Instituto Geográfico Militar, Santiago 374.
Buchanan, A., Kietzmann, D., Palma, R., 2016. Evolución paleoambiental de la Formación Remoredo (Jurásico Inferior) en el depocentro Malargüe, Cuenca Neuquina Surmendocina. Revista de la Asociación Geológica Argentina, 74(2), 163-178.
Buelow, E. K., Suriano, J., Mahoney, J. B., Kimbrough, D. L., Mescua, J. F., Giambiagi, L. B., & Hoke, G. D. (2018). Sedimentologic and stratigraphic evolution of the Cacheuta basin: Constraints on the development of the Miocene retroarc foreland basin, south-central Andes. Lithosphere, 10(3), 366-391.
Burd, A.I., Booker, J.R., Mackie, R., Favetto, A., Pomposiello, M.C., 2014. Three- dimensional electrical conductivity in the mantle beneath the Payun Matru Volcanic Field in the Andean back-arc of Argentina near 36. 5 S: Decapitation of a mantle plume by resurgent upper mantle shear during slab steepening? Geophys. J. Int. 1, 1e12.
Burov, E.B., 2011. Rheology and strength of the lithosphere. Mar. Pet. Geol. 28, 1402–1443. https://doi.org/10.1016/j.marpetgeo.2011.05.008
Byerlee, J. 1978. Friction of rocks. Pure and Applied Geophysics 116, 615–26.
Cahill T., Isacks B.L., 1992. Seismicity and shape of the subducted Nazca plate. J Geophys Res 97:17503–17529
Caminos, R., 1965. Geología de la vertiente oriental del Cordón del Plata, Cordillera Frontal de Mendoza. Rev Asoc Geol Argentina 20(3):351–392.
Casa, A., Cortéz, J.M., Borgnia, M., 2010. Evidencias de deformación pleistocena en el sistema de fallas de La Carrera (32°40′–33°15′S), Cordillera Frontal de Mendoza. Rev Asoc Geol Argentina 67:91–104.

Cawood. P.A., 2005. Terra australis Orogen: Rodinia breakup and development of the pacific and Iapetus margins of Gondwana during the Neoproterozoic and Paleozoic. Earth Science Reviews 69: 249-79.

Cegarra M.I., Ramos V.A. (1996) La faja plegada y corrida del Aconcagua. In Ramos VA (ed) Geología de la región del Aconcagua, provincias de San Juan y Mendoza. Subsecretaría de Minería de la Nación, Dirección Nacional del Servicio Geológico, Anales 24:387-422.

Chapple,W.M., 1978. Mechanics of thin-skinned fold-and-thrust belts. Geol. Soc. Am. Bull. 89 (8), 1189–1198.Charrier R, Pinto L, Rodríguez MP (2007) Tectonostratigraphic evolution of the Andean orogen in Chile. In Moreno T,, Gibbons W (eds) The Geology of Chile. The Geological Society: 21-114.

Charrier, R., 1979. El Triásico de Chile y regiones adyacentes de Argentina: una reconstrucción paleogeográfica o y paleoclimática. Comunicaciones 26, 1-37.

Charrier, R., Baeza, O., Elgueta, S., Flynn, J, Gans, P., Kay, S.M., Muñoz, N., Wyss, A,, Zurita, E., 2002. Evidence for Cenozoic extensional basin development and tectonic inversion south of the flat-slab segment, southern Central Andes, Chile (33°–36°S.L.). J South Am Earth Sci 15:117–139.

Charrier, R., Bustamante, M., Comte, D., Elgueta, S., Flynn, J.J., Iturra, N., Muñoz, N., Pardo, M., Thiele, R., Wyss, A.R., 2005. The Abanico Extensional Basin: regional extension, chronology of tectonic inversion and relation to shallow seismic activity and Andean uplift. Neues Jb Geol Paläontol Abh 236:43–77.

Charrier, R., Pinto, L., Rodríguez, M., 2007. Tectonostratigraphic evolution of the Andean Orogen in Chile. En: Gibbonds W, Moreno T (eds) The geology of Chile. Geological Society London, Special Publications pp 21–116.

Charrier, R., Farías, M., Maksaev, V., 2009. Evolución tectónica, paleogeográfica y metalogénica durante el Cenozoico en los Andes de Chile norte y central e implicaciones para las regiones adyacentes de Bolivia y Argentina. Rev Asoc Geol Argentina 65:5–35.

Charrier, R., Ramos V.A., Tapia, F., Sagripanti L., 2015. Tectono-stratigraphic evolution of the Andean Orogen between 31 and 37°S (Chile and Western Argentina). En: Geodynamic Processes in the Andes of Central Chile and Argentina. Sepúlveda S. A., Giambiagi L. B., Moreiras S. M., Pinto L., Tunik M., Hoke G.D., Farías M. (eds) Geological Society, London, Special Publications. Vol. 399. Pp: 13-61.

Chiaramonte, L., Ramos, V. A., & Araujo, M. (2000). Estructura y sismotectónica del anticlinal Barrancas, cuenca Cuyana, provincia de Mendoza. Revista de la Asociación Geológica Argentina, 55(4), 309-336.

Cisneros, H., Bastias, H., 1993. Neotectónica del borde oriental del Bloque de San Rafael. En: XII Congreso Geológico Argentino (Mendoza), 270–276.

Cobbold, P. R., Rossello, E. A., 2003. Aptian to recent compressional deformation, foothills of the Neuquén Basin, Argentina. Marine and Petroleum Geology, 20(5), 429-443.

Combina, A., Nullo, F., 2005. Tertiary volcanism and sedimentation in the southern Cordillera Principal, Mendoza, Argentina. In International Symposium on Andean Geodynamics (ISAG) 6:174-177.

Combina, A. M., Nullo, F., 2011. Ciclos tectónicos, volcánicos y sedimentarios del Cenozoico del sur de Mendoza-Argentina (35-37 S y 69 30'W). Andean Geology, 38(1), 198-218.

Comeron, R., González, J.M., Schiuma, M., 2002. Los Reservorios de las Rocas Ígneas Intrusivas. 5° Congreso de Exploración y Desarrollo de Hidrocarburos, IAPG, Rocas reservorio de las cuencas Productivas de la Argentina, p. 559-582, Mar del Plata, Argentina.

Cortés, J.M., Cegarra, M., 2004. Plegamiento cuaternario transpresivo en el piedemonte suroccidental de la Precordillera sanjuanina. Rev Asoc Geol Argentina, Special Publication 7:68–75.

Cortés, J.M., Vinciguerra, P., Yamín, M., Pasini, M.M., 1999. Tectónica cuaternaria de la region andina del Nuevo Cuyo (28°–38°LS). En: Caminos R (ed) Geología Argentina, Segemar Anales 29:760–778.

Cortés, J.M., Casa, A., Pasini, M., Yamin, M., Terrizzano, C., 2006. Fajas oblicuas de deformación neotectónica en Precordillera y Cordillera Frontal (31°30′–33°30′LS). Controles paleotectónicos. Rev Asoc Geol Argentina 61:639–646.

Costa, C., Vita-Finzi, C., 1996. Late Holocene faulting in the southeast Sierras Pampeanas of Argentina. Geology 24:1127–1130.

Costa, C., Gardini, C., Diederix, H., Cortés, J.M., 2000. The Andean orogenic front at sierra de las Peñas-Las Higueras, Mendoza, Argentina. J S Am Earth Sci 13:287–292
Costa, C., Murillo, M., Sagripanti, G., Gardini, C., 2001. Quaternary intraplate deformation in the southern Sierras Pampeanas, Argentina. J Seismol 5:399–409.
Cox, J.W. (1970), The high resolution dipmeter reveals dip – related borehole and formation characteristics, Trans. SPWLA Annu. Logging Symp., 11, 3–6.
Cox, S.F., 2005. Coupling between deformation, fluid pressures, and fluid flow in ore-producing hydrothermal systems at depth in the crust. Economic Geology 100th Anniversary Volume, 39-75.
Cristallini, E.O., Ramos, V.A., 1995. Structural cross-section of Río San Juan. En: Ramos, V.A. (Ed.), Field Guide to the Geology of Precordillera Folded and Thrust Belt (Central Andes). ICL-COMTEC-AGA, Buenos Aires
Cristallini, E., Ramos, V.A., 2000. Thick-skinned and thin-skinned thrusting in La Ramada Fold and Thrust belt: crustal evolution of the High Andes of San juan, Argentina (32°SL). Tectonophys 317:205–235.
Cristallini, E., Mosquera, A., Ramos, V.A., 1995. Estructura de la Alta Cordillera de San Juan. Rev Asoc Geol Argentina 49(1–2):165–183.
Cundall, Board, M., 1988. A Microcomputer Program for Modeling Large-Strain Plasticity Programs, in: PROCEEDINGS OF THE SIXTH INTERNATIONAL CONFERENCE ON NUMERICAL METHODS IN GEOMECHANICS, 11-15 APRIL 1988, INNSBRUCK, AUSTRIA. VOLUMES 1-3. Publication of: Balkema (AA). pp. 2101–2108.
Currie, C.A., Beaumont, C., 2011. Are diamond-bearing Cretaceous kimberlites related to low-angle subduction beneath western North America? Earth Planet. Sci. Lett. 303, 59–70. https://doi.org/10.1016/j.epsl.2010.12.036
Delaney, P. T., Pollard, D. D., Ziony, J. I., McKee, E. H., 1986. Field relations between dikes and joints: Emplacement processes and paleostress analysis. Journal of Geophysical Research: Solid Earth, 91(B5), 4920-4938.
Dellapé, D., Hegedus, A., 1995. Structural inversion and oil occurrence in the Cuyo basin of Argentina. Petroleum Basins of South America. En: Tankard A, Suárez R, Welsink H (eds) Am Assoc Petrol Geol Bulletin 62:369–367.
del Rey, A., Deckart, K., Arriagada, C., Martínez, F., 2016. Resolving the paradigm of the late Paleozoic–Triassic Chilean magmatism: Isotopic approach. Gondwana Res. 37, 172–181. https://doi.org/10.1016/j.gr.2016.06.008.
Di Giulio, A., Ronchi, A., Sanfilippo, A., Tiepolo, M., Pimentel, M., Ramos, V.A., 2012. Detrital zircon provenance from the Neuquén Basin (south-central Andes): Cretaceous geodynamic evolution and sedimentary response in a retroarc-foreland basin. Geology, 40: 559-562.
Dimieri, L. V. 1997). Tectonic wedge geometry at Bardas Blancas, southern Andes (36 S), Argentina. Journal of Structural Geology, 19(11), 1419-1422.
Donnadieu, F. Merle, O., 1998. Experiments on the indentation process during cryptodome intrusions: New insights into Mount St. Helens deformation. Geology, 26, 79–82.
Du Toit, A.L., 1937. Our wandering continents. An hypothesis of continental drifting. Oliver & Boyd, 366 p., London.
Eide, C.H., Schofield, N., Jerram, D.A., Howell, J.A., 2016. Basin-scale architecture of deeply emplaced sill complexes: Jameson Land, East Greenland. Journal of the Geological Society, doi:10.1144/jgs2016-018.
Elliott, D., 1976. The motion of thrust sheets. J. Geophys. Res. 81 (5), 949–963.
Elgueta, S., Charrier, R., Thiele, R., 1999. Volcanogenic sedimentation model for the Miocene Farellones Formation, Andean Cordillera, Central Chile. En: IV International Symposium of Andean Geodynamics (Göttingen), Germany, pp 228–231.
Encinas, A., Le Roux, J.P., Buatois, L.A., Nielsen, S.N., Finger, K.L., Fourtanier. E., Lavenu, A., 2006. Nuevo esquema estratigráfico para los depósitos marinos mio-pliocenos del área de Navidad (33°–34°S). Chile central. Rev Geol Chile 33(2):221–246.
Faccenna, C., Becker, T.W, Conrad, C.P., Husson, L., 2013. Mountain building and mantle dynamics. Tectonics 32, 80-93.
Farías, M., Charrier, R., Carretier, S., Martinod, J., Fock, A., Campbell, D., Cáceres, J., Comte, D., 2008. Late Miocene high and rapid surface uplift and its erosional response in the Andes of central Chile (33°–35°S). Tectonics. doi:10.1029/2006TC002046.

Farías, M., Vargas, G., Tassara, A., Carretier, S., Baize, S., Melnick, D., Bataille, K., 2010. Land-Level changes produced by the Mw 8.8 2010 Chilean earthquake. Science. doi:10.1126/science.1192094.
Farías, M., Comte, D., Charrier, R., Martinod, J., 2010a. Crustal-scale structural architecture of the Central Chile Andes based on 3D seismic tomography, seismicity, and surface geology: Implications for mountain building in. Tectonics 57–78.
Farías, M., Comte, D., Charrier, R., Martinod, J., David, C., Tassara, A., Tapia, F., Fock, A., 2010b. Crustal-scale structural architecture in central Chile based on seismicity and surface geology: Implications for Andean mountain building. Tectonics 29. https://doi.org/10.1029/2009TC002480
Fennell, L. M., Folguera, A., Naipauer, M., Gianni, G., Rojas Vera, E. A., Bottesi, G., Ramos, V. A., 2017. Cretaceous deformation of the southern Central Andes: synorogenic growth strata in the Neuquén Group (35° 30′–37° S). Basin Research, 29, 51-72.
Fennell, L.M., Iannelli, S.B., Encinas, A., Naipauer, M., Valencia, V., Folguera, A., 2019. Alternating contraction and extension in the Southern Central Andes (35°–37°S). Am. J. Sci. 319, 381–429. https://doi.org/10.2475/05.2019.02
Ferré, E., Galland, O., Montanari, D., Kalakay, T., 2012, Granite magma migration and emplacement along thrusts: International Journal of Earth Sciences, p. 1-16.
Fock, A., 2005. Cronología y tectónica de la exhumación en el Neógeno de los Andes de Chile central entre los 33° y los 34° S, Tesis para optar al grado de Magíster en Ciencias, Mención Geología, Memoria para optar al título de Geólogo, Departamento de Geología, Universidad de Chile, Santiago, pp179.
Fock, A., Charrier, R., Farías, M., Muñoz, M., 2006. Fallas de vergencia Oeste en la Cordillera Principal de Chile Central: Inversión de la cuenca de Abanico (33°–34°S). Rev Asoc Geol Argentina, Special Publication 10:48–55.
Folguera, A., Zárate, M., 2011. Neogene sedimentation in the Argentine foreland between 34°30′S and 41°S and its relation to the Andes evolution. En: Salfity, JA, Marquillas R A (eds) Cenozoic geology of the Central Andes of Argentina: Salta, SCS Publisher, p 123–134.
Folguera, A., Etcheverría, M., Pazos, P., Giambiagi, L.B., Cortés, J.M., Fauqué, L., Fusari, C., Rodríguez, M.F., 2004. Descripción de la Hoja Geológica Potrerillos (1:100.000). Subsecretaría de Minería de la Nación, Dirección Nacional del Servicio Geológico, p 262.
Folguera, A., Bottessi, G., Zapata, T., Ramos, V.A., 2008. Crustal collapse in the Andean backarc since 2 Ma: Tromen volcanic plateau, Southern Central Andes (36°40′-37°30′S). Tectonophysics, 459: 140-160.
Folguera, A., Naranjo, J.A., Orihashi, Y., Sumino, H., Nagao, K., Polanco, E., and Ramos, V., 2009, Retroarc volcanism in the northern San Rafael block (34°–35°30′S), southern Central Andes: Occurrence, age, and tectonic setting: Journal of Volcanology and Geothermal Research, v. 186, p. 169–185, doi:10.1016 /j.jvolgeores.2009.06.012.
Folguera, A., Gianni, G., Sagripanti, L., Rojas Vera, E., Novara, I., Colavitto, B., Alvarez, O., Orts, D., Giménez, M., Introcaso, A., Ruiz, F., Martínez, P., Ramos, V.A., 2015. A review about the mechanisms associated with active deformation, regional uplift and subsidence in southern South America. Journal of South America Earth Sciences 64 (2): 511-524.
Folguera, A., Naipauer, M., Sagripanti, L., Ghiglione, M.C., Orts, D., Giambiagi, L., 2016. An introduction to the Southern Andes (33-50ºS): Book structure. En Folguera, A., Naipauer, M., Sagripanti, L., Ghiglione, M., Orts, D. y Giambiagi L. (eds.) Growth of the Southern Andes, Springer Earth System Sciences, 1-8, Amsterdam.
Fosdick, J. C., Reat, E. J., Carrapa, B., Ortiz, G., & Alvarado, P. (2017). Retroarc basin reorganization and aridification during Paleogene uplift of the southern central Andes. Tectonics, 36, 493–514. https://doi.org/10.1002/2016TC004400
Fossen, H., 2010, Structural geology, Cambridge University Press.
Franzese, J. R., Spalletti, L. A. 2001. Late Triassic–early Jurassic continental extension in southwestern Gondwana: tectonic segmentation and pre-break-up rifting. Journal of South American Earth Sciences, 14(3), 257-270.
Franzese, J., Spalletti, L., Pérez, I.G., Macdonald, D., 2003. Tectonic and paleoenvironmental evolution of Mesozoic sedimentary basins along the Andean foothills of Argentina (32°-54°S). J. South Am. Earth Sci. 16, 81–90. https://doi.org/10.1016/S0895-9811(03)00020-8

Fuentes, F., Horton, B. K., Starck, D., Boll, A. 2016. Structure and tectonic evolution of hybrid thick- and thin-skinned systems in the Malargüe fold–thrust belt, Neuquén basin, Argentina. Geological Magazine, 153(5-6), 1066-1084.

Fuentes, F., Horton, B.K., 2020. The Andean Foreland Evolution of the Neuquén Basin: A Discussion. Springer International Publishing. https://doi.org/10.1007/978-3-030-29680-3_14

Galland, O., Hallot, E., Cobbold, P.R., Ruffet, G., de Bremond d'Ars, J., 2007a. Volcanism in a compressional Andean setting: A structural and geochronological study of Tromen volcano (Neuquén province, Argentina). Tectonics, 26, TC4010, doi:10.1029/2006TC002011.

Galland, O., Cobbold, P. R., de Bremond d'Ars,J. Hallot, E., 2007b. Rise and emplacement of magma during horizontal shortening of the brittle crust: Insights from experimental modeling, J. Geophys. Res., 112, B06402, doi:10.1029/2006JB004604.

Galland, O., Bertelsen, H.S., Eide, C.H., Guldstrand, F., Haug, O.T., Leanza, H.A., Mair, K., Palma, O., Planke, S., Rabbel, O., ROgers, B., Schmiedel, T., Souche, A., Spacapan, J., 2018. Storage and transport of magma in the layered crust - Formation of sills and related flat-lying intrusions. In Buchardt, S. (ed.) Volcanic and Igneous Plumbing Systems, Elsevier: 113-138.

Gansser, A., 1973. Facts and theories on the Andes. Journal of the Geological Society 129: 39-131.

García, V.H., Casa, A.L., 2015. Quaternary tectonics and seismic potencial of the Andean retrowedge at 33°–34°S. En: Sepúlveda SA, Giambiagi LB, Moreiras SM, Pinto L, Tunik M, Hoke GD, Farías M (eds) Geodynamic Processes in the Andes of Central Chile and Argentina. Geol Soc London, Special Publication 399:311–327.

Giambiagi, L., Ramos, V.A., 2002. Structural evolution of the Andes in a transitional zone between flat and normal subduction (33°30′–33°45′S), Argentina and Chile. J South Am Earth Sci 15 (1):101–116.

Giambiagi, L. B., Alvarez, P. P., Godoy, E., Ramos, V. A., 2003a. The control of pre-existing extensional structures on the evolution of the southern sector of the Aconcagua fold and thrust belt, southern Andes. Tectonophysics, 369(1-2), 1-19.

Giambiagi, L. B., Ramos, V. A., Godoy, E., Alvarez, P. P., Orts, S., 2003b. Cenozoic deformation and tectonic style of the Andes, between 33 and 34 south latitude. Tectonics, 22(4).

Giambiagi, L., Bechis, F., García, V., Clark, A. H., 2008. Temporal and spatial relationships of thick- and thin-skinned deformation: A case study from the Malargüe fold-and-thrust belt, southern Central Andes. Tectonophysics, 459(1-4), 123-139.

Giambiagi LB, Tunik M, Barredo S, Bechis F, Ghiglione M, Alvarez P, Drosina M (2009a). Cinemática de apertura del sector norte de la cuenca Neuquina. Revista de la Asociación Geológica Argentina 65(2):278-292.

Giambiagi, L., Ghiglione, M., Cristallini, E., and Bottesi, G., 2009b. Kinematic models of basement/cover interactions: Insights from the Malargüe fold and thrust belt, Mendoza, Argentina: Journal of Structural Geology, v. 31, p. 1443–1457, doi: 10.1016/j.jsg.2009.10.006.

Giambiagi, L.B., Mescua, J.F., Bechis, F., Martínez, A., Folguera, A., 2011. Pre-Andean deformation of the Precordillera southern sector, Southern Central Andes. Geosphere 7(1), 1-21.

Giambiagi, L.B., Mescua, J.F., Bechis, F., Tassara, A. and Hoke, G., 2012. Thrust belts of the Southern Central Andes: along strike variations in shortening,topography, crustal geometry and denudation. GSA Bulletin, 124 (7/8): 1339-1351.

Giambiagi, L., Alvarez, P., Spagnotto, S., 2015. Temporal variation of the stress field during the construction of the central Andes: Constrains from the volcanic arc region (22–26°S), Western Cordillera, Chile, during the last 20 Ma., 2016. Tectonics, 35 (9): 2014-2033.

Giambiagi, L., Tassara, A., Mescua, J., Tunik, M., Álvarez, P., Godoy, E., Greg, H., Pinto L., Spagnotto, S., Porras, H., Tapia, F., Jara, P., Bechis, F., García, V., Suriano, J. and Pagano, S., 2015. Evolution of shallow and deep structures along the maipo-tunuyán transect (33° 40´S): from the pacific coast to the andean foreland. En: Geodynamic Processes in the Andes of Central Chile and Argentina. Sepúlveda, S., Giambiagi, L., Moreiras, S.M., Pinto, L., Tunik, M., Hoke, G. y Farías, M. (Eds). Geological Society of London, Special Publication 399: 63-82.

Giambiagi, L., Mescua, J., Bechis, F., Hoke, G., Suriano, J., Spagnotto, S., Moreiras, S., Lossada, A., Mazzitelli, M., Toural Dapoza, R., Folguera, A., Mardonez, D., Pagano, D., 2016. Cenozoic orogenic evolution of the Southern Central Andes (32-36°S). En Folguera, A., Naipauer, M.,

Sagripanti, L., Ghiglione, M., Orts, D. y Giambiagi L. (eds.) Growth of the Southern Andes, Springer Earth System Sciences, 63-98, Amsterdam.
Giambiagi, L., Álvarez, P.P., Creixell, C., Mardonez, D., Murillo, I., Velásquez, R., Lossada, A., Suriano, J., Mescua, J., Barrionuevo, M., 2017. Cenozoic Shift From Compression to Strike-Slip Stress Regime in the High Andes at 30°S, During the Shallowing of the Slab: Implications for the El Indio/Tambo Mineral District. Tectonics 36, 2714–2735. https://doi.org/10.1002/2017TC004608.
Giampaoli, P., Dajczgewand, D., Dzelalija, F., 2002. La estructura del sector externo de la faja plegada y corrida de Malargüe a la latitud del río Salado, cuenca neuquina surmendocina, Argentina. In Congreso Geológico Argentino, 15, Actas (Vol. 3, pp. 168-173).
Gleason, G.C., Tullis, J., 1995. A flow law for dislocation creep of quartz aggregates determined with the molten salt cell. Tectonophysics 247, 1–23. https://doi.org/10.1016/0040-1951(95)00011-B
Godoy, E., Yañez, G., Vera, E., 1999. Inversion of an Oligocene volcano-tectonic basin and uplifting of its superimposed Miocene magmatic arc in the Chilean Central Andes: first seismic and gravity evidences. Tectonophys 306(2):217–336.
Godoy, E., Schilling, M., Solari, M., Fock, A., 2009. Carta Rancagua. Escala 1:100.000: Santiago, Servicio Nacional de Geología y Minería. Serie Geología Básica n° 118:50.
González Bonorino, F., 1950. Algunos problemas geológicos de las Sierras Pampeanas. Asociación Geológica Argentina, Revista 5(3): 81-110.
González Díaz E.F., 1964. Rasgos geológicos y evolución geomorfológica de la Hoja 27d (San Rafael) y zona occidental vecina (Provincia de Mendoza). Rev Asoc Geol Argentina 19:151–188.
Gordillo, C., Lencinas, A. N., 1979. Sierras Pampeanas de Córdoba y de San Luis. En: Turner, J. C. M. (Ed.):Segundo Simposio Geología Regional Argentina, pp. 577-650. Academia Nacional de Ciencias, Córdoba.
Granado, P., & Ruh, J. B. (2019). Numerical modeling of inversion tectonics in fold-and-thrust belts. Tectonophysics, 763, 14–29. https://doi.org/10.1016/j.tecto.2019.04.033
Groeber, P., 1946. Observaciones geológicas a lo largo del meridiano 70. Hoja Chos Malal. Revista de la Asociación Geológica Argentina. 1: 178-208.
Gulisano, C. A., 1981. El Ciclo Cuyano en el norte de Neuquén y sur de Mendoza. In Congreso Geológico Argentino 8: 579
Gutiérrez, N., Hinojosa, L., Le Roux, J.P., Pedroza, V., 2013. Evidence for an Early-Middle Miocene age of the Navidad Formation (central Chile): Paleontological, paleoclimatic and tectonic implications. Andean Geol 40(1):1–26.-592.
Guzmán, C., Cristallini, E., Bottesi, G., 2007. Contemporary stress orientations in the Andean retroarc between 34 S and 39 S from borehole breakout analysis. Tectonics, 26(3).
Guzmán, C., Cristallini, E., 2009. Contemporary stress orientations from borehole breakout analysis in the southernmost flat-slab boundary Andean retroarc (32º44´ and 33º 40´S). Journal of Geophysical Research 114 (B2):B02406. doi: 10.1029/2007JB005505.
Guzmán, C., Cristallini, E., García, V., Yagupsky, D., Bechis, F., 2011. Evolución del campo de esfuerzos horizontal desde el Eoceno a la actualidad en la Cuenca Neuquina. Revista de la Asociación Geológica Argentina 68 (4): 542 - 554.
Haney, M., Snieder, R., Sheiman, J. and Losh, S., 2005. A moving fluid pulse in a fault zone. Nature, 437, 46, doi:10.1038/437046a.
Heredia, N., Farias, P., García-Sansegundo, J., Giambiagi, L., 2012. The basement of the Andean Frontal Cordillera in the Cordón del Plata (Mendoza, Argentina): Geodynamic evolution. Andean Geol 39(2):242–257.
Hernando, I. R., Franzese, J. R., Llambias, E. J., Petrinovic, I. A., 2014. Vent distribution in the Quaternary Payún Matrú Volcanic Field, western Argentina: Its relation to tectonics and crustal structures. Tectonophysics, 622, 122-134.
Hervé, F., Munizaga, F., Parada, M.A., Brook, M., Pankhurst, R., Snelling, N.J., Drake, R., 1988. Granitoids of the Coastal Range of central Chile: geochronology and geologic setting. J South Am Earth Sci 1:185–194.
Hildreth, W., Moorbath, S., 1988. Crustal contributions to arc magmatism in the Andes of Central Chile. Contributions to Mineralogy and Petrology, v. 98, pp. 455-489.

Hirth, G., Kohlstedt, D.L., 2003. Rheology of the Upper Mantle and the Mantle Wedge : A View from the Experimentalists upper mantle . We first analyze experimental data to provide a critical review of flow. Geophys. Monogr. Ser. 138, 83–105. https://doi.org/10.1029/138GM06

Hoke, G., Graber, N.R., Mescua, J.F., Giambiagi, L., Fitzgerald, P., Metcalf, J., 2015. Near pure surface uplift of the Argentine Frontal Cordillera: insights from (U–Th)/He thermochronometry and geomorphic analysis. En: Sepúlveda S, Giambiagi L, Pinto L, Moreiras S, Tunik M, Hoke G, Farías M (eds) Geodynamic Processes in the Andes of Central Chile and Argentina. Geol Soc London, Special Publications 399:383–399.

Horton, B. K., Fuentes, F., Boll, A., Starck, D., Ramirez, S. G., Stockli, D. F., 2016. Andean stratigraphic record of the transition from backarc extension to orogenic shortening: A case study from the northern Neuquén Basin, Argentina. Journal of South American Earth Sciences, 71, 17-40.

Horton, B.K., Fuentes, F., 2016. Sedimentary record of plate coupling and decoupling during growth of the Andes. Geology 44, 647–650. https://doi.org/10.1130/G37918.1

Hubbert, M., Willis, D.G., 1957. Mechanics of hydraulic fracturing. Transactions of Society of Petroleum Engineers of AIME, 210, 153-163.

Instituto Nacional de Prevención Sísmica (INPRES), 1985. El terremoto de Mendoza, Argentina del 26 de enero de 1985, Informe general, San Juan: p 137.

Instituto Nacional de Prevención Sísmica (INPRES), 2016. Terremotos históricos ocurridos en la República Argentina. En: http://www.inpres.gov.ar/seismology/historicos.html.

Irigoyen, M.V., Buchan, K.L., Brown, R.L., 2000. Magnetostratigraphy of Neogene Andean foreland-basin strata, lat. 33°S, Mendoza Province Argentina. Geol Soc Am Bull 112:803–816.

Isacks, B.L., 1988. Uplift of the Central Andean Plateau and bending of the Bolivian orocline. Journal of Geophysical Research 93(B4), 3211–3231.

Isacks, B., Jordan, T., Allmendinger, R. W., Ramos, V. A., 1982. La segmentacion tectonica de los Andes Centrales y su relacionn con la placa de Nazca subductada, Vth Congreso Latinoamericano de Geologia, Univ. de Buenos Aires, Buenos Aires.

Jaeger, J.C., Cook, N., 1979. Fundamentals of Rock Mechanics. London: Chapman and Hall, 593 pp.

Jara, P., Charrier, R., 2014. Nuevos antecedentes estratigráficos y geocronológicos para el Meso-Cenozoico de la cordillera Principal de Chile entre 32° y 32°30′S: Implicancias estructurales y paleogeográficas. Andean Geol 41(1):174–209.

Jara, P., Likerman, J., Winocur, D., Ghiglione, M., Cristallini, E., Pinto, L., Charrier, R., 2015. Role of basin width variation in tectonic inversion: insight from analogue modelling and implications for the tectonic inversion of the Abanico Basin, 32º–34ºS, Central Andes. En Geodynamic Processes in the Andes of Central Chile and Argentina.

Jarrard, R. D., 1986. Relations among subduction parameters. Reviews of Geophysics, 24(2), 217-284.

Jordan, T. E., Allmendinger, R. W., 1986. The Sierras Pampeanas of Argentina; a modern analogue of the Rocky Mountain foreland deformation. American Journal of Science, 286:737-764.

Jordan, T.E., Isacks, B.L., Allmendinger, R.W., Brewer, J.A., Ramos, V.A., Ando, C.J., 1983 a. Andean tectonics related to geometry of subducted Nazca plate: Geological Society of America Bulletin 94:341-361.

Jordan, T.E., Isacks, B., Ramos, V.A., Allmendinger, R.W., 1983 b. Mountain building in the Central Andes. Episodes 1983(3): 20-26.

Jordan, T.E., Allmendinger, R.W., Damanti, J.F., Drake, R.E., 1993. Chronology of motion in a complete thrust belt: The Precordillera, 30-31°S, Andes Mountains. J. Geol. 101: 135–156.

Kalakay, T. J., John, B. E., Lageson, D. R., 2001. Fault-controlled pluton emplacement in the Sevier fold-and-thrust belt of southern Montana, J. Struct. Geol., 23, 1151 – 1165.

Kadinsky-Cade, K., Reilinger, R., Isacks, B., 1985. Surface deformation associated with the November 23, 1977, Caucete, Argentina, earthquake sequence, J. Geophys. Res., 90(B14), 12,691–12,700, doi:10.1029/JB090iB14p12691.

Kameyama, M., Yuen, D.A., Karato, S.I., 1999. Thermal-mechanical effects of low-temperature plasticity (the Peierls mechanism) on the deformation of a viscoelastic shear zone. Earth Planet. Sci. Lett. 168, 159–172. https://doi.org/10.1016/S0012-821X(99)00040-0

Kaus, B.J.P., Popov., A.A., Baumann, T.S., Püs.k, A.E., Bauville, A., Fernandez, N., Collignon, M., 2016. Forward and inverse modeling of lithospheric deformation on geological timescales. NIC Symposium, Proceedings 48.

Kavanagh, J., Rogers, B.D., Boutelier, D., Cruden, A.R., 2017. Controls on sill and dyke-sill hybrid geometry and propagation in the crust: The role of fracture toughness. Tectonophysics 698: 109-120.

Kavanagh, J., 2018. Mechanisms of magma transport in the upper crust: dyking. In Buchardt, S. (ed.) Volcanic and Igneous Plumbing Systems, Elsevier: 55-88.

Kay, S. M., Kurtz, A., 1995. Magmatic and tectonic characterization of the El Teniente Region, internal report, Corp Nac Cobre, Santiago, Chile, p 80.

Kay, S.M., Abbruzzi, J.M., 1996. Magmatic evidence for Neogene lithospheric evolution of the central Andean “flat-slab” between 30°S and 32°S. Tectonophys 259:15–28

Kay, S.M., Ramos, V.A., 1996. El magmatismo cretácico de las Sierras de Córdoba y sus implicancias tectónicas. 13° Congreso Geológico Argentino y 3° Congreso Exploración de Hidrocarburos, Actas 3: 453-464, Buenos Aires.

Kay, S.M., Mpodozis, C., 2002. Magmatism as a probe to the Neogene shallowing of the Nazca plate beneath the modern Chilean flat-slab: Journal of South American Earth Sciences, v. 15, p. 39–57, doi:10.1016/ S0895-9811(02)00005-6.

Kay, S.M., Ramos, V.A., Mpodozis, C., Sruoga, P., 1989. Late Paleozoic to Jurassic silicic magmatism at the Gondwana margin: analogy to the Middle Proterozoic in North America? Geology 17, 324–328. https://doi.org/10.1130/0091-7613(1989)017<0324:LPTJSM>2.3.CO;2

Kay, S.M., Mpodozis, C., Ramos, V.A., Munizaga, F., 1991. Magma source variations for mid to late Tertiary volcanic rocks erupted over a shallowing subduction zone and through a thickening crust in the Main Andean Cordillera (28˚–33˚S). En: Harmon, R.S. and Rapela, C. (eds) Andean Magmatism and its Tectonic Setting, Geological Society of America

Kay, S.M., Godoy, E., Kurtz, A., 2005. Episodic arc migration, crustal thickening, subduction erosion, and magmatism in the south-central Andes: Geological Society of America Bulletin, v. 117, no. 1–2, p. 67–88, doi: 10.1130/B25431.1.

Kay, S.M., Burns, M., Copeland, P., Mancilla, O., 2006. Upper Cretaceous to Holocene magmatism and evidence for transient Miocene shallowing of the Andean subduction zone under the northern Neuquén Basin. En: Kay, S.M., and Ramos, V.A. (eds.). Evolution of an Andean Margin: A Tectonic and Magmatic View from the Andes to the Neuquén Basin (35°–39°S lat): Geological Society of America Special Paper 407, p. 19–60.

Keidel, J., 1916. La geología de las Sierras de la Provincia de Buenos Aires y sus relaciones con las montañas de Sudáfrica y Los Andes. Ministerio de Agricultura de La Nación, Sección Geología, Mineralogía y Minería, Anales XI(3): 1-78, Buenos Aires.

King, G., Stein, R., Lin, J., 1994. Static stress changes and the triggering of earthquakes. Bulletin of the Seismological Society of America, 84(3): 935-953.

Kleiman, L.E., Japas, M.S., 2009. The Choiyoi volcanic province at 34°–36°S (San Rafael, Mendoza, Argentina): Implications for the Late Paleozoic evolution of the southwestern margin of Gondwana. Tectonophys 473:283–299.

Kley, J., Monaldi, C.R., Salfity, J.A., 1999. Alongstrike segmentation of the Andean foreland: Causes and consequences. Tectonophysics 301:75–94.

Kokogián, D.A., Fernández Seveso, F., Mosquera, A., 1993. Las secuencias sedimentarias triásicas. En Geología y Recursos Naturales de Mendoza (ed. V.A. Ramos), pp. 65-78. XII Congreso Geológico Argentino y Congreso de Exploración de Hidrocarburos, Relatorio.

Kokogian, D., Spalleti, L., Morel, E., Artabe, A., Martínez, R., Alcober, O., Milana, J., Zavattieri, A., Papú, O. 1999. Los depósitos continentales Triásicos. En Geología Argentina (Caminos, R.; editor). Servicio Geológico y Minero Argentino, Instituto de Geología y Recursos Minerales, Anales 29 (15): 377-398, Buenos Aires .

Kozlowski, E., Manceda, R., Ramos, V.A., 1993, Estructura, In Ramos, V.A. (ed.) Geología y Recursos Naturales de Mendoza: 12 Congreso Geológico Argentino y 2 Congreso de Exploración de Hidrocarburos, Relatorio, p. 235–256.

Kurtz, A., Kay, S.M., Charrier, R., Farrar, E., 1997. Geochronology of Miocene plutons and exhumation history of the El Teniente region, Central Chile (34°–35°S). Rev Geol Chile 24(1):75–90.

Lacombe, O., 2001. Paleostress magnitudes associated with development of mountain belts: insights from tectonics analyses of calcite twins in the Taiwan foothills. Tectonics, 20(6): 834-849.

Lacombe, O., 2012. Do fault slip data inversions actually yield “paleostresses” that can be compared with contemporary stresses? A critical discussion. Comptes Rendus Geoscience, 344: 159-173.

Lacombe, O., Tavani, S., Soto, R., 2012. An introduction to the Tectonophysics special issue “Into the deformation history of folded rocks”. Tectonophysics 576–577, 1–3.

Lacombe, O., Bellahsen, N., 2016. Thick-skinned tectonics and basement-involved fold-thrust belts: Insights from selected Cenozoic orogens, Geological Magazine. https://doi.org/10.1017/S0016756816000078

Lagorio, S.L. 2008. Early Cretaceous alkaline volcanism of the Sierra Chica de Córdoba (Argentina): Mineralogy, geochemistry and petrogenesis. Journal of South American Earth Sciences 26(2): 152-171.

Lamb, S., Davis, P,. 2003. Cenozoic climate change as a possible cause for the rise of the Andes. Nature 425 (6960):792–797.

Langer, C. J., Hartzell, S., 1996. Rupture distribution of the 1977 western Argentina earthquake, Phys. Earth Planet. Int., 94, 121–132.

Leanza, H.A. 2003. Las sedimentitas huitrinianas y rayosianas (Cretácico inferior) en el ámbito central y meridional de la cuenca Neuquina, Argentina. Servicio Geológico y Minero Argentino, Serie Contribuciones Técnicas, Geología, 2:1-31

Legarreta, L. and Gulisano, C.A., 1989. Análisis estratigráfico secuencial de la cuenca Neuquina (Triásico superior- Terciario inferior). In G. Chebli y L. Spalletti (eds.), Cuencas Sedimentarias Argentinas. Facultad de Ciencias Naturales, Universidad Nacional de Tucumán, Correlación Geológica Serie 6: 221-243, Tucumán.

Legarreta, L., and Uliana, M.A., 1999, El Jurásico y Cretácico de la Cordillera Principal y la cuenca Neuquina. 1. Facies sedimentarias, in Caminos, R., ed., Geología Argentina: Servicio Geológico y Minero Argentino, Instituto de Geología y Recursos Minerales, Anales, v. 29, p. 399–416.

Legarreta, L., Kokogian, D.A., Dellapé, D.A., 1992. Estructuración terciaria de la Cuenca Cuyana: ¿Cuánto de inversión tectónica? Rev Asoc Geol Argentina 47(1):83–86.

Leonard, M., 2010. Earthquake fault scaling: Self-consistent relating of rupture length, width, average displacement, and moment release. Bull. Seismol. Soc. Am. 100, 1971–1988. https://doi.org/10.1785/0120090189.

Levina, M., Horton, B.K., Fuentes, F., Stockli, D.F., 2014. Cenozoic sedimentation and exhumation of the foreland basin system preserved in the Precordillera thrust belt (31-32°S), southern central Andes, Argentina. Tectonics 33, 1659–1680.

Limarino, C.O., Spalletti, L.A., 2006. Paleogeography of the upper Paleozoic basins of southern South America: an overview. Journal of South American Earth Sciences, 22: 134-155.

Litvak, V. D., Poma, S., & Kay, S. M. (2007). Paleogene and Neogene magmatism in the Valle del Cura region: new perspective on the evolution of the Pampean flat slab, San Juan province, Argentina. Journal of South American Earth Sciences, 24(2-4), 117-137.

Litvak, V. D., Spagnuolo, M. G., Folguera, A., Poma, S., Jones, R. E., Ramos, V. A., 2015. Late Cenozoic calc-alkaline volcanism over the Payenia shallow subduction zone, South-Central Andean back-arc (34° 30′–37° S), Argentina. Journal of South American Earth Sciences, 64, 365-380.

Liu, S., Currie, C.A., 2016. Farallon plate dynamics prior to the Laramide orogeny: Numerical models of flat subduction. Tectonophysics 666, 33–47. https://doi.org/10.1016/j.tecto.2015.10.010

Llambías EJ, Sato AM (1990) El batolito de Colanguil (29°-31°S) Cordillera Frontal Argentina: estructura y marco tectonico. Rev Geol Chile 17:89–108

Llambías, E.J., Kleiman, L.E., and Salvarredi, J.A., 1993, El magmatismo gondwánico, in Ramos, V.A., ed., Geología y Recursos Naturales de Mendoza: 12 Congreso Geológico Argentino y 2 Congreso de Exploración de Hidrocarburos, Relatorio, p. 53–64.

Llambías, E.J., Bertotto, G.W., Risso, C., Hernando, I., 2010. El volcanismo cuaternario en el retroarco de Payenia: una revisión. Revista de la Asociación Geológica Argentina, 67(2): 278-300.

López, M.G., Sola, P., 1981. Manifestaciones volcánicas alcalinas de los alrededores de Las Chacras y de la región de Villa Mercedes - Chaján, provincias de San Luis y Córdoba. 8º Congreso Geológico Argentino, Actas 4: 967-978.

López, V., Gregori, D.A., 2004. Provenance and evolution of the Guarguaraz Complex, Cordillera Frontal, Argentina. Gondwana Research, 7(4): 1197-1208.

Lossada, A.C., Giambiagi, L., Hoke, G.D., Fitzgerald, P.G., Creixell, C., Murillo, I., Mardonez, D., Velásquez, R., Suriano, J., 2017. Thermochronologic Evidence for Late Eocene Andean Mountain Building at 30°S. Tectonics 36, 2693–2713. https://doi.org/10.1002/2017TC004674

Lossada, A. C., Giambiagi, L., Hoke, G., Mescua, J., Suriano, J., & Mazzitelli, M. (2018). Cenozoic Uplift and Exhumation of the Frontal Cordillera Between 30° and 35° S and the Influence of the Subduction Dynamics in the Flat Slab Subduction Context, South Central Andes. In The Evolution of the Chilean-Argentinean Andes (pp. 387-409). Springer, Cham.

Löbens, S., Bense, F.A., Wemmer, K., Dunkl, I., Costa, C.H., Layer, P., Siegesmund, S., 2011. Exhumation and uplift of the Sierras Pampeanas: Preliminary implications from K-Ar fault gouge dating and low-T thermochronology in the Sierra de Comechingones (Argentina). Int. J. Earth Sci. 100, 671–694. https://doi.org/10.1007/s00531-010-0608-0.

Mackaman-Lofland, C., Horton, B.K., Fuentes, F., Constenius, K.N., Ketcham, R.A., Capaldi, T.N., Stockli, D.F., Ammirati, J., Alvarado, P., Orozco, P., 2020. Andean Mountain Building and Foreland Basin Evolution During Thin- and Thick-Skinned Neogene Deformation (32–33°S). Tectonics 39, e2019TC005838. https://doi.org/10.1029/2019TC005838

Mackwell, S.J., Zimmerman, M.E., Kohlstedt, D.L., 1998. High-temperature deformation of dry diabase with application to tectonics on Venus. J. Geophys. Res. Solid Earth 103, 975–984. https://doi.org/10.1029/97jb02671

Magee, C., Jackson, C.A., Schofield, N., 2013. The influence of normal fault geometry on igneous sill emplacement and morphology. Geology 41: 407-401.

Magee, C., Muihead, J., Karvelas, A., Holford, S., Jackson, C., Bastow, I, Schofield, N., Stevenson, C., McLean, C., McCarthy, W., Shtuckert, O., 2016. Lateral magma flow in mafic sill complexes. Geosphere, 12: 809-841.

Magee, C., Muirhead, J. D., Schofield, N., Walker, R. J., Galland, O., Holford, S. P., Spacapan, J. B., Jackson, C. A. L., McCarthy, W., 2018, Structural signatures of igneous sheet intrusion propagation: Journal of Structural Geology, https://doi.org/10.1016/j.jsg.2018.07.010.

Maksaev, V., Munizaga, F., Zentilli, M., Charrier, R., 2009. Fission track thermochronology of Neogene plutons in the Principal Andean Cordillera of central Chile (33–35°S): Implications for tectonic evolution and porphyry Cu-Mo mineralization. Andean Geol 36(2):153–171.

Manceda, R., Figueroa, D., 1995. Inversion of the Mesozoic Neuquén rift in the Malargüe fold and thrust belt, Mendoza, Argentina. In: Tankard, A. J., Suárez, R., Welsink, H. (Eds.), Petroleum Basins of South America, American Association of Petroleum Geologists Memoir, 62 (1995), pp. 369-382.

Mardonez, D., 2019. Interacción entre processos superficiales y profundos a lo largo de la transecta La Serena – Jachal, 30°S. PhD thesis. Universidad Nacional de Córdoba.

Martin, M. W., Clavero, J., Mpodozis, C., Cuitiño, L., 1995. Estudio geológico de la Franja El Indio, Cordillera de Coquimbo. Servicio Nacional de Geología y Minería (SERNAGEOMIN), Santiago, Registered Report IR-95-6.

Martínez, F., Bonini, M., Montanari, D., Corti, G., 2016. Tectonic inversion and magmatism in the Lautaro Basin, northern Chile, Central Andes: a comparative approach from field data and analog models. J. Geodyn. 94–95, 68–83.

Martínez, F., Montanari, D., Del Ventisette, C., Bonini, M., & Corti, G. ,2018. Basin inversion and magma migration and emplacement: Insights from basins of northern Chile. Journal of Structural Geology, 114(October 2017), 310–319. https://doi.org/10.1016/j.jsg.2017.12.008.

Massone, H.J., Calderón, M., 2008. P-T evolution of metapelites from the Guarguaraz complex, Argentina: evidence for Devonian crustal thickening close to the western Gondwana margin. Revista Geológica de Chile, 35(2): 215-231.

Mazzitelli, M. (2019). Estudio de la Interacción entre procesos someros y profundos en la transecta ubicada a los 32ºS, a la altura del Cerro Mercedario, Provincia de San Juan, Argentina. PhD thesis, Universidad Nacional de La Plata.

Mathieu, L., van Wyk de Vries, B., Holohan, E.P., Troll, V.R., 2008. Dykes, cups, saucers and sills: Analogue experiments on magma intrusion into brittle rocks. Earth and Planetary Science Letters, 271, 1–13.

McQuarrie, N. 2002. The kinematic history of the central Andean fold-thrust belt, Bolivia: Implications for building a high plateau. Geological Society of America Bulletin, 114(8), 950-963.

McGroder, M.F., Lease, R.O., Pearson, D.M., 2015. Along-strike variation in structural styles and hydrocarbon occurrences, Subandean fold-and-thrust belt and inner foreland, Colombia to Argentina, in: Geodynamics of a Cordilleran Orogenic System: The Central Andes of Argentina and Northern Chile. Geological Society of America, p. 2016. https://doi.org/10.1130/2015.1212(05)

Melchor, R., Casadío, S., 2000. Hoja Geológica 3766-I, Santa Isabel. Servicio Geológico Minero Nacional, Boletín 344:43.

Mescua, J.F., Giambiagi, L.B., Bechis, F., 2008. Evidencias de tectónica extensional en el Jurásico tardío (Kimeridgiano) del suroeste de la provincia de Mendoza. Revista de la Asociación Geológica Argentina, 63(4): 512-519.

Mescua, J.F., Giambiagi, L., 2012. Fault inversion vs. new thrust generation: a case study in the Malargüe fold-and-thrust belt Andes of Argentina. J Struct Geol 35:51–63.

Mescua, J. F., Giambiagi, L. B., Ramos, V. A., 2013. Late Cretaceous Uplift in the Malargüe fold-and-thrust belt (35 S), southern Central Andes of Argentina and Chile. Andean Geology, 40(1).

Mescua, J. F., Giambiagi, L. B., Tassara, A., Giménez, M.& Ramos, V. A., 2014. Influence of pre-Andean history over Cenozoic foreland deformation: structural styles in the Malargüe fold-and-thrust belt at 35° S, Andes of Argentina. Geosphere 10, 585–609.

Mescua, J., Giambiagi, L., Barrionuevo, M., Tassara, A., Mardonez, D., Mazzitelli, M., Lossada, A., 2016. Basement composition and basin geometry controls on upper-crustal deformation in the Southern Central Andes (30-36ºS). Geological Magazine. En: Tectonic evolution and mechanics of basement-involved fold-thrust belts.

Mescua J. F., Sruoga P., Giambiagi L., Suriano J., Barrionuevo M. And Spagnotto S, 2019. Links between magmatic arc behavior and upper plate deformation in the Malargüe Andes. LASI VI.

Moreiras, S.M., Giambiagi, L., Spagnotto, S., Nacif, S., Mescua, J., Toural, R., 2014. El frente orogénico activo de los Andes centrales a la latitud de la ciudad de Mendoza (32°50S–33°S). Andean Geol 41(2):261–342.

Moresi, L., Dufour, F., Mühlhaus, H.-B., 2003. A Lagrangian integration point finite element method for large deformation modeling of viscoelastic geomaterials. J. Comput. Phys. 184, 476–497. https://doi.org/10.1016/S0021-9991(02)00031-1

Morris, A., Ferrill, D., Brent Henderson, D., 1996. Slip tendency analysis and fault reactivation. Geology, 24: 275-278.

Mosquera, A. Ramos, V.A. 2006. Intraplate deformation in the Neuquén Basin. En: Kay, S.M. & Ramos, V.A. (Eds.): Evolution of Andean margin: A tectonic and magmatic view from the Andes to the Neuquén Basin (35°–39° S latitude). Geological Society of America, Special Paper 407: 97-124.

Mouthereau, F., Watts, A.B., Burov, E., 2013. Structure of orogenic belts controlled by lithosphere age. Nat. Geosci. 6, 785–789. https://doi.org/10.1038/ngeo1902

Mpodozis, C., Cornejo, P., 1988. Hoja Pisco Elqui, IV Región de Coquimbo. Servicio Nacional de Geología y Minería, Santiago, Carta Geológica de Chile, 68, 1:250.000.

Mpodozis, C., Ramos, V.A., 1989. The Andes of Chile and Argentina. En: Ericksen, G.E., Cañas Pinochet, M.T. y Reinemud, J.A. (Eds.): Geology of the Andes and its relation to Hydrocarbon and Mineral Resources, Circumpacific Council for Energy and Mineral Resources, Earth Sciences Series 11: 59-90, Houston.

Mpodozis, C., Cornejo, P., 2012. Cenozoic Tectonics and Porphyry Copper Systems of the Chilean Andes. Geology and genesis of major copper deposits and districts of the world: a tribute to Richard H. Sillitoe. Soc Econ Geol, Boulder, 329–360.

Muirhead, J., Airoldi, G., Rowland, J., White, J., 2012. Interconnected sills and inclined sheet intrusions control shallow magma transport in the Ferrar large igneous province, Antarctica. Geol. Soc Am. Muñoz, M., Fuentes, F., Vergara, M., Aguirre, L., Nyström, J.O., Féraud, G., Demant, A., 2006. Abanico East Formation: petrology and geochemistry of volcanic rocks behind the Cenozoic arc front in the Andean Cordillera, central Chile (33°50′S). Rev Geol Chile 33:109–140.

Muñoz, M., Charrier, R., Fanning, C.M., Maksaev, V., Deckart, K., 2012. Zircon trace element and O-Hf isotope analyses of mineralized intrusions from El Teniente Ore Deposit, Chilean Andes: Constraints on the source and magmatic evolution of porphyry Cu-Mo related magmas. J Petrol 53:1091–1122.

Murillo, I., Velásquez, R., & Creixell, C. (2017). Geología de las áreas Guanta–Los Cuartitos y Paso de Vacas Heladas, regiones de Atacama y Coquimbo, with explanatory text. Carta Geológica de Chile. Serv. Nac. Geol. Min., Santiago.Bull., 124: 162-180.

Nakamura, K., 1977. Volcanoes as possible indicators of tectonic stress orientation—principle and proposal. Journal of Volcanology and Geothermal Research, 2(1), 1-16.

Nasi, C., Moscoso, R., Maksaev, V., 1990. Hoja Guanta, Regiones de Atacama y Coquimbo. Servicio Nacional de Geología y Minería, Santiago, Carta Geológica de Chile 67.

Norabuena, E. O., Dixon, T. H., Stein, S., Harrison, C. G., 1999. Decelerating Nazca-South America and Nazca-Pacific plate motions. Geophysical Research Letters, 26(22), 3405-3408.

Nullo, F. E., Stephens, G. C., Otamendi, J., Baldauf, P. E., 2002. El volcanismo del Terciario superior del sur de Mendoza. Revista de la Asociación Geológica Argentina, 57(2), 119-132.

Nullo, F. E., Stephens, G., Combina, A., Dimieri, L., Baldauf, P., Bouza, P., Zanettini, J. C. M., 2005. Hoja geológica 3569-III/3572-IV Malargüe, provincia de Mendoza. Servicio Geológico Minero Argentino. Instituto de Geología y Recursos Minerales.

Nyström, J.O., Parada, M.A., Vergara, M., 1993. Sr- Nd isotope composition of Cretaceous to Miocene volcanic rocks in central Chile: A trend towards a MORB signature and a reversal with time. II Int Symp Andean Geodynamics, París, pp 411–414.

Odé, H. 1957. Mechanical analysis of the dike pattern of the Spanish Peaks area, Colorado. Bull. Geol. Soc. Am., 68: 567-576.

Oliveros, V., González, J., Vargas, M. E., Vásquez, P., Rossel, P., Creixell, C., ... & Bastias, F. (2018). The early stages of the magmatic arc in the Southern Central Andes. In The Evolution of the Chilean-Argentinean Andes (pp. 165-190). Springer, Cham.

Oncken, O., Hindle, D., Kley, J., Elger, K., Victor, P., Schemann, K., 2006. Deformation of the Central Andean upper plate system – facts, fiction and constraints for plateau models. En The Andes – active subduction orogeny (eds. O. Oncken, G. Chong, G. Franz, P. Giese, H.J. Gotze, V.A. Ramos, M.R. Strecker, P. Wigger), pp. 3-28, Springer.

Ortiz, A., Zambrano, J. J., 1981. La provincia geológica Precordillera oriental, Congr. Geol. Argent. Actas 8th, 3, 59-74.

Orts, D. L., Folguera, A., Giménez, M., Ramos, V. 2012. Variable structural controls through time in the Southern Central Andes (~ 36ºS). Andean Geology, 39(2), 220-241.

Pagano, D.S., Galliski, M.A., Márquez-Zavalía, M.F., 2014. Emplacement of the La Peña alkaline igneous complex, Mendoza, Argentina (33°S): Implications for the early Miocene tectonic regime in the retroarc of the Andes. J S Am Earth Sci 50:48–66.

Pardo-Casas, F., Molnar, P., 1987. Relative motion of the Nazca (Farallon) and South American plates since Late Cretaceous time. Tectonics, 6(3), 233-248.

Peacock, S.M., 1996. Thermal and petrologic structure of subduction zones, in: Geophysical Monograph Series. https://doi.org/10.1029/GM096p0119

Pearson, D.M., Kapp, P., DeCelles, P.G., Reiners, P.W., Gehrels, G.E., Ducea, M.N., Pullen, A., 2013. Infl uence of pre-Andean crustal structure on Cenozoic thrust belt kinematics and shortening magnitude: Northwestern Argentina. Geosphere 9, 1766–1782. https://doi.org/10.1130/GES00923.1

Pérez, D.J., 2001. Tectonic and unroofing history of Neogene Manantiales foreland basin deposits, Cordillera Frontal (32°30′S), San Juan Province, Argentina. J South Am Earth Sci 14:693–705

Pérez, D.J., Ramos, V.A., 1996. Los depósitos sinorogénicos. En: Ramos V.A (ed) Geología de la Región del Aconcagua. Provincias de San Juan y Mendoza. Dirección Nacional del Servicio Geológico, Anales 24(11):387–422.

Pineda, G., & Emparán, C. (2006). Geología del área de Vicuña-Pichasca, Región de Coquimbo, Carta Geológica de Chile, Serie Geología Básica (sheet 97). Santiago, Chile: Serv. Nac. Geol. Min.

Piquer, J., Castelli, J.C., Charrier, R., Yáñez, G., 2010. El Cenozoico del alto río Teno, Cordillera Principal, Chile central: estratigrafía, plutonismo y su relación con estructuras profundas. Andean Geol 37:32–53.

Polanski, J., 1964. Descripción de la Hoja 25a, Volcán San José, provincia de Mendoza, Dirección Nacional de Geología y Minería, Buenos Aires 98: p 1–94.
Polanski, J., 1972. Carta Geológica Económica de la República Argentina escala 1:200,000, Descripción geológica de la hoja 24 a-b Cerro Tupungato, provincia de Mendoza. Buenos Aires, Dirección Nacional de Geología y Minería, p 110.
Poliakov, A.N.B., Cundall, P.A., Podladchikov, Y.Y., Lyakhovsky, V.A., 1993. An Explicit Inertial Method for the Simulation of Viscoelastic Flow: An Evaluation of Elastic Effects on Diapiric Flow in Two- and Three- Layers Models, in: Flow and Creep in the Solar System: Observations, Modeling and Theory. Springer Netherlands, Dordrecht, pp. 175–195. https://doi.org/10.1007/978-94-015-8206-3_12
Ramos, V.A., 1988. The tectonics of the Central Andes: 30° to 33° S latitude. En Processes in continental lithospheric deformation (Clark, S.P., et al., eds.), Geological Society of America Special Paper 218: 31–54.
Ramos, V.A., 1999 a. Plate tectonic setting of the Andean Cordillera. Episodes, 22:3,183-190.
Ramos, V.A., 1999 b. Rasgos estructurales del territorio argentino. 1. Evolución tectónica de la Argentina. En Geología Argentina (Caminos, R.; editor). Servicio Geológico y Minero Argentino, Instituto de Geología y Recursos Minerales, Anales 29 (24): 715-784. Buenos Aires.
Ramos, V.A., Kay, S.M., 2006. Overview of the tectonic evolution of the southern Central Andes of Mendoza and Neuquén (35°–39°S latitude), in: Evolution of an Andean Margin: A Tectonic and Magmatic View from the Andes to the Neuquen Basin (35°-39°S Lat). Geological Society of America, pp. 1–17. https://doi.org/10.1130/2006.2407(01)
Ramos, V.A., Folguera, A., 2011. Payenia volcanic province in the Southern Andes: An appraisal of an exceptional Quaternary tectonic setting: Journal of Volcanology and Geothermal Research, v. 201, p. 53–64, doi:10.1016/j.jvolgeores.2010.09.008.
Ramos, V.A., Jordan, T.E., Allmendinger, R.W., Mpodozis, C., Kay, S.M., Cortés, J.M., Palma, M., 1986. Paleozoic terranes of the central Argentine-Chilean Andes. Tectonics 5, 855-880.
Ramos, V.A., Vujovich, G.I., 1995. Descripción de la Hoja Geológica San Juan (1:250,000). Dirección Nacional del Servicio Geológico, Buenos Aires.
Ramos V.A., Aguirre-Urreta, B., Alvarez, P., Cegarra, M., Cristallini, E., Kay, S.M., Lo Forte, G.L., Pereyra, F.X., Pérez, D.J., 1996 a. Geología de la región del Aconcagua, provincias de San Juan y Mendoza. Dirección Nacional del Servicio Geológico, Buenos Aires, Anales 24:510.
Ramos, V.A., Cegarra, M.I., Cristallini, E., 1996 b. Cenozoic tectonics of the High Andes of west-central Argentina (30–36°S latitude): Tectonophysics, v. 259, p. 185–200.
Ramos, V.A., Dallmeyer, R.D., Vujovich, G., 1998. Time constraints on the Early Palaeozoic docking of the Precordillera, central Argentina.En The Proto-Andean Margin of Gondwana (eds. R.J Pankhurst and C.W. Rapela), pp.143-158. Geological Society. London, Special Publications no. 142.
Ramos, V.A., Cristallini, E., Pérez, D.J., 2002. The Pampean flat-slab of the Central Andes. J South Am Earth Sci 15:59–78.
Ramos, V.A., Zapata, T., Cristallini, E., Introcaso, A., 2004. The Andean Thrust System-Latitudinal Variations in Structural Styles and Orogenic Shortening. En K. R. McClay (ed.), Thrust tectonics and hydrocarbon systems. AAPG Memoir 82: 30– 50.
Ramos, V.A., Litvak, V., Folguera, A., Spagnuolo, M., 2014. An Andean tectonic cycle: From crustal thickening to extension in a thin crust (34°–37°SL). Geosc Frontiers 5:351–367.
Ranalli, G., Murphy, D.C., 1987. Rheological stratification of the lithosphere. Tectonophysics 132, 281–295. https://doi.org/10.1016/0040-1951(87)90348-9
Richter, P.P., Ring, U., Willner, A.P., Leiss, B., 2007. Structural contacts in subduction complexes and their tectonic significance: the Late Paleozoic coastal accretionary wedge of central Chile. J Geol Soc London 164:203–214.
Riesner, M., Lacassin, R., Simoes, M., Carrizo, D., Armijo, R., 2018. Revisiting the Crustal Structure and Kinematics of the Central Andes at 33.5°S: Implications for the Mechanics of Andean Mountain Building. Tectonics 37, 1347–1375. https://doi.org/10.1002/2017TC004513
Rivano, S., Sepulveda, P., 1991. Hoja Illapel, Región de Coquimbo. Servicio Nacional de Geología y Minería, Santiago, Carta Geológica de Chile 1: 250.000: p 132.
Rivano, S., Godoy, E., Vergara, M., Villarroel, R., 1990. Redefinición de la Formación Farellones en la Cordillera de los Andes de Chile Central (32°–34°S): Rev Geol Chile 17:205–214.

Rodríguez, M. (2013). Cenozoic uplift and exhumation above the southern part of the flat-slab subduction segment of Chile (28.5–32°S) (PhD thesis). Chile: Universidad de Chile.
Rodriguez, M.P., Pinto Lincoñir, L., Encinas, A., 2012. Cenozoic erosion in the Andean forearc in Central Chile (33°–34°S): Sediment provenance inferred by heavy mineral studies. En: Rasbury ET, Hemming SR, Riggs NR (eds) Mineralogical and Geochemical Approaches to Provenance. Geol Soc of America, Special Paper 487:141–162.
Rodriguez Monreal, F., Villar, H. J., Baudino, R., Delpino, D., Zencich, S., 2009. Modeling an atypical petroleum system: A case study of hydrocarbon generation, migration and accumulation related to igneous intrusions in the Neuquen Basin, Argentina. Marine and Petroleum Geology, 26(4), 590-605.
Rojas, L., Radic, J.P., 2002. Estilos de deformación del basamento y de la cobertura sedimentaria en la faja plegada y fallada de Malargüe en el área de Puesto Rojas, Mendoza, Argentina. 15° Congreso Geológico Argentino, Actas 2: 224-229.
Rolleri, E.O., 1969. Rasgos tectóncios generales del valle de Matagusanos y de la zona entre San Juan y Jocolí, Provincia de San Juan, República Argentina. Asociación Geológica Argentina, Revista 24(4): 408- 412.
Russo, R., Silver, P.G., 1996. Cordillera formation, mantle dynamics and the Wilson cycle. Geology 24(6), 511-514.
Rybacki, E., Dresen, G., 2000. Dislocation and diffusion creep of synthetic anorthite aggregates. J. Geophys. Res. Solid Earth 105, 26017–26036. https://doi.org/10.1029/2000jb900223
Salfity, J., Gorustovich, S.A., 1984. Paleogeografía de la cuenca del Grupo Paganzo, Paleozoico superior. Asociación Geológica Argentina, Revista 38(3- 4)(1983): 437-453.
Sato, A.M., Llambías, E.J., Basei, M., Castro, C.E., 2015. Three stages in the late Paleozoic to Triassic magmatism of Southwestern Gondwana, and the relationships with the volcanogenic events in coeval bains. Journal of South American Earth Sciences 63, 48-69.
Schellart, W.P., Freeman, J., Stegman, D.R., Moresi, L., May, D.A., 2007. Evolution and diversity of subduction zones controlled by slab width. Nature 446, 308-311.
Schiuma, M. F., 1994. Intrusivos del valle del Río Grande, provincia de Mendoza, su importancia como productores de hidrocarburos (Doctoral dissertation, Facultad de Ciencias Naturales y Museo).
Schiuma, M. F., Llambías E. J., 2014. Importancia de los Sills Como Reservorios en la Cuenca Neuquina del Sur de Mendoza. 9° Congreso de Exploración y Desarrollo de Hidrocarburos, IAPG, Trabajos Técnicos I, p. 331-349, Mendoza, Argentina
Schmidt, S., Hetzel, R., Kuhlmann, J., Mingorance, F., Ramos, V.A., 2011. A note of caution on the use of boulders for exposure dating of depositional surfaces. Earth Planet. Sci. Lett. 302, 60–70. https://doi.org/10.1016/j.epsl.2010.11.039
SEGEMAR. 1997. Mapa Geológico de la República Argen- tina, Escala 1:2.500.000. Servicio Geológico y Minero Argentino.
SERNAGEOMIN. 2003. Mapa Geológico de Chile, Escala 1:1.000.000. Servicio Nacional de Geología y Minería, Publicación Geológica Digital no. 4.
Selles, D., Gana, P., 2001. Mapa geológico del área Talagante-San Francisco de Mostazal, Santiago de Chile, escala 1:100.000. Servicio Nacional de Geología y Minería, Santiago: p 99.
Seoane Borracer, F. N, Rocha, E., Armisen, M. R., Olivieri, G. A., Periale, S. L., Manceda, R. E. 2018. Proyecto exploratorio Pincheira, faja plegada y corrida de Malargüe, Cuenca Neuquina, provincia de Mendoza. In 10 Congreso de exploración y desarrollo de hidrocarburos, 75-90.
Siame, L. L., Sébrier, M., Bellier, O., Bourlès, D., Costa, C., Ahumada, E. A., Gardini, C. E. , Cisneros, H., 2015. Active basement uplift of Sierra Pie de Palo (Northwestern Argentina): Rates and inception from 10Be cosmogenic nuclide concentrations. Tectonics, 34, 1129–1153. doi: 10.1002/2014TC003771.
Sielfeld, G., Lange, D., & Cembrano, J. (2019). Intra-Arc Crustal Seismicity: Seismotectonic Implications for the Southern Andes Volcanic Zone, Chile. Tectonics, 38(2), 552-578.
Sigismondi, M.E., 2012. Estudio de la deformación litosférica de la cuenca Neuquina: estructura termal, datos de gravedad y sísmica de reflexión 381.
Silvestro, J., Atencio, M., 2009. La cuenca cenozoica del río Grande y Palauco: edad evolución y control estructural, faja plegada de Malargüe. Revista de la Asociación Geológica Argentina, 65(1): 154-169.

Silvestro, J., Kraemer, P., Achilli, F., Brinkworth, W. 2005. Evolución de las cuencas sinorogénicas de la Cordillera Principal entre 35-36 S, Malargüe. Revista de la Asociación Geológica argentina, 60(4), 627-643.
Sobolev, S. V., & Babeyko, A. Y., 2005. What drives orogeny in the Andes?. Geology, 33(8), 617-620.
Sobolev, S. V, Babeyko, A.Y., Koulakov, I., Oncken, O., 2006. Mechanism of the Andean orogeny: insight from numerical modeling, in: The Andes. Springer, pp. 513–535.
Somoza, R., 1998. Updated Nazca (Farallon)—South America relative motions during the last 40 My: implications for mountain building in the central Andean region. Journal of South American Earth Sciences, 11(3), 211-215.
Spacapan, J.B., Galland, O., Leanza, H., Planke, S., 2016a. Igneous sill and finger emplacement mechanism in shale-dominated formations: a field study at Cuesta del Chihuido, Neuquén Basin, Argentina. Journal of the Geological Society, doi.org/10.1144/jgs2016-056
Spacapan, J.B., Galland, O., Leanza, H. Planke, S., 2016b. Control of strike-slip fault on dyke emplacement and morphology. Journal of the Geological Society, 173, 573-576.
Spacapan, J. B., Palma, J. O., Galland, O., Manceda, R., Rocha, E., D'Odorico, A., Leanza, H. A., 2018. Thermal impact of igneous sill-complexes on organic-rich formations and implications for petroleum systems: A case study in the northern Neuquén Basin, Argentina. Marine and Petroleum Geology, 91, 519-531.
Spagnotto, Silvana; Triep, Enrique; Giambiagi, Laura; Lupari, Marianela 2015 Triggered seismicity in the andean arc region via static stress variation by the Mw=8.8, february 27, 2010, Maule earthquake. Journal of South American Earth Sciences. vol. 63 p. 36 - 47.
Spagnuolo, M.G., Litvak, V.D., Folguera, A., Bottesi, G., Ramos, V., 2012. Neogene magmatic expansion and mountain building processes in the southern Central Andes, 36–37°S, Argentina: Journal of Geodynamics, v. 53, p. 81–94, doi:10.1016/j.jog.2011.07.004.
Spalletti, L. A.,1997. Sistemas deposicionales fluvio-lacustres en el rift triásico de Malargüe (sur de Mendoza, República Argentina). In: Anales de la Academia Nacional de Ciencias Exactas, Físicas y Naturales, 49, 109-124.
Sperner, B., Müller, B., Heidbach, O., Delvaux,D., Reinecker, J., Fuchs, K., 2003. Tectonic stress in the Earth's crust: Advances in the World Stress Map Project. In New Insights Into Structural Interpretation and Modeling, edited by D. Nieuwland, Geol. Soc. Spec. Publ., 212, 101 – 116.
Spikings, R., Dungan, M., Foeken, J., Carter, A., Page, L., Stuart, F., 2008. Tectonic response of the central Chilean margin (35–38°S) to the collision and subduction of heterogeneous oceanic crust: a thermochronological study. J Geol Soc London 165:941–995.
Sruoga, P., Rubinstein, N.A., Etcheverría, M.P., Cegarra, M., Kay, S.M., Singer, B., Lee, J., 2008. Estadío inicial del arco volcánico neógeno en la Cordillera Principal de Mendoza (35°S). Rev Asoc Geol Argentina 63(3):469–545.
Sruoga, P., Rubinstein, N.A., Etcheverría, M.P., Cegarra, M., 2009. Volcanismo neógeno y mineralización asociada, Cordillera Principal, Mendoza (35°S). XII Congreso Geológico de Chile (Santiago de Chile): p 4.
Stein, J. E., Ghiglione, M. C., Hlebszevitsch, J. C., 2018. Estructuras y entrampamientos plio-pleistocenos (tardíos) en la plataforma deformada mendocina, Lindero de Piedra, Cuenca Neuquina In 10 Congreso de exploración y desarrollo de hidrocarburos, 111-123
Stelzner, A., 1873. Comunicaciones al Prof. H.B. Geinitz. Neues Jarbuch für Mineralogie, Geologie und Paläeontologue. Trad por R. Kittl, 1966 en Academia Nacional de Ciencias, Boletín 45:115-150, Buenos Aires.
Stephens, T.L., Walker, R.J., Healy, D., Bubeck, A., England, R.W., McCaffrey, K., 2017. Igneous sills record far-field and near-field stress interactions during volcano construction: Isle of Mull, Scotland. Earth and Planetary Science Letters 478: 159-174.
Stern, C., 2004. Active Andean volcanism: its geologic and tectonic setting. Rev Geol Chile 31 (2):161–206.
Stern, C.R., Skewes, M.A., 1995. Miocene to Present magmatic evolution at the northern end of the Andean Southern volcanic zone: Central Chile: Revista Geológica de Chile, v. 22, p. 261–271.
Stern, C.R., Moreno, H., López-Escobar, L., Clavero, J., Lara, L., Naranjo, J.A., Parada, M.A., Skewes, M., 2007. Chilean volcanoes. En Moreno, T. and Gibbons, W. (eds.) The Geology of Chile. The Geological Society, 148-179, London.

Strecker, M.R., Alonso, R.N., Bookhagen, B., Carrapa, B., Hilley, G.E., Sobel, E.R., Trauth, M.H., 2007. Tectonics and Climate of the Southern Central Andes. Annu. Rev. Earth Planet. Sci. 35, 747–787. https://doi.org/10.1146/annurev.earth.35.031306.140158.

Strecker, M.R., Alonso, R., Bookhagen, B., Carrapa, B., Coutand, I., Hain, M.P., Hilley, G.E., Mortimer, E., Schoenbohm, L., Sobel, E.R., 2009. Does the topographic distribution of the central Andean Puna Plateau result from climatic or geodynamic processes? Geology 37, 643–646. https://doi.org/10.1130/G25545A.1

Sulsky, D., Zhou, S.-J., Schreyer, H.L., 1995. Application of a particle-in-cell method to solid mechanics. Comput. Phys. Commun. 87, 236–252. https://doi.org/10.1016/0010-4655(94)00170-7

Suriano, J., Mardonez, D., Mahoney, J.B., Mescua, J.F., Giambiagi, L.B., Kimbrough, D., Lossada, A., 2017. Uplift sequence of the Andes at 30°S: Insights from sedimentology and U/Pb dating of synorogenic deposits. J. South Am. Earth Sci. 75, 11–34. https://doi.org/10.1016/j.jsames.2017.01.004

Takada, A., 1989. Magma transport and reservoir formation by a system of propagating cracks. Bulletin of Volcanology, 52(2), 118-126.

Tapia, F., Farías, M., Astaburugada, D., 2012. Deformación cretácica-paleocena y sus evidencias en la cordillera de los Andes de Chile Central (33.7–36°S). XI Congreso Geológico de Chile (Antofagasta), pp 232–234.

Tassara, A., Yáñez, G., 2003. Relación entre el espesor elástico de la litósfera y la segmentación tectónica del margen andino (15-47°S). Revista Geológica de Chile 32, 159-186.

Tassara, A., Götze, H.-J., Schmidt, S., Hackney, R., 2006. Three-dimensional density model of the Nazca plate and the Andean continental margin. Journal of Geophysical Research 111, B09404,

Tassara, A., Echaurren, A., 2012. Anatomy of the Andean subduction zone: Three-dimensional density model upgraded and compared against global-scale models. Geophys. J. Int. 189, 161–168. https://doi.org/10.1111/j.1365-246X.2012.05397.x

Tavani, S., Storti, F., Lacombe, O., Corradetti, A., Muñoz, J.A., Mazzoli, S., 2015. A review of deformation pattern templates in foreland basin systems and fold-and-thrust belts: Implications for the state of stress in the frontal regions of thrust wedges. Earth Science Reviews, 141:82-104.

Terrizzano, C.M., Fazzito, S.Y., Cortés, J.M., Rapalini, A.E., 2010. Studies of Quaternary deformation zones through geomorphic and geophysical evidence: a case in the Precordillera Sur, Central Andes of Argentina. Tectonophysics 490:184–196.

Thomas, W.A., Astini, R.A., 1996. The Argentine Precordillera: a traveler from the Ouachita embayment of North American Laurentia. Science, 273: 752-757.

Triep, E., 1987. La falla activada durante el sismo principal de Mendoza de 1985 e implicancias tectónicas. X Congreso Geológico Argentino (San Miguel de Tucumán). Actas 1:199–202.

Tunik, M., 2003. Interpretación paleoambiental de la Formación Saldeño (Cretácico superior), en la Alta Cordillera de Mendoza, Argentina. Rev de la Asoc Geol Argentina 58:417–433.

Tunik, M., Folguera, A., Naipauer, M., Pimentel, M., Ramos, V. A., 2010. Early uplift and orogenic deformation in the Neuquén Basin: constraints on the Andean uplift from U–Pb and Hf isotopic data of detrital zircons. Tectonophysics, 489(1-4), 258-273.

Turienzo, M. M., 2010. Structural style of the Malargüe fold-and-thrust belt at the Diamante River area (34 30′–34 50′ S) and its linkage with the Cordillera Frontal, Andes of central Argentina. Journal of South American Earth Sciences, 29(3), 537-556.

Turienzo, M. M., Dimieri, L., Frisicale, C., Araujo, V. Sanchez, N., 2012. Cenozoic structural evolution of the Argentinean Andes at 34º40`S: A close relationship between thick and thin-skinned deformation. Andean Geology, 39(2), 317-357.

Uliana, M. A., Biddle, K. T., 1988. Mesozoic-Cenozoic paleogeographic and geodynamic evolution of southern South America. Revista Brasileira de geociencias, 18(2), 172-190.

Uliana, M. A., Biddle, K. T., Cerdan, J., 1989. Mesozoic Extension and the Formation of Argentine Sedimentary Basins: Chapter 39: Analogs.

Uliana, M. A., Legarreta, L., 1993. Hydrocarbons Habitat in a Triassic-To-Cretaceous Sub-Andean Setting: Neuquén Basin, Argentina. Journal of Petroleum Geology, 16(4), 397-420.

Uliana, M. A., Arteaga, M. E., Legarreta, L., Cerdán, J. J., Peroni, G. O., 1995. Inversion structures and hydrocarbon occurrence in Argentina. Geological Society, London, Special Publications, 88(1), 211-233.

V.A., eds., Evolution of an Andean margin: A tectonic and magmatic view from the Andes to the Neuquén Basin (35°–39°S lat), Geological Society of America Special Paper 407, p. 1–18, doi: 10.1130/2006.2407(01).

Valencio, D. A., Linares, E., Creer, K., 1969. Paleomagnetismo y edades geológicas de algunos basaltos terciarios y cuartarios de Mendoza y Neuquén. IVº Jornadas Geológicas Argentinas. Actas, 2, 397-415.

van Wyk de Vries, B., van Wyk de Vries, M., 2018. Tectonics and volcanic and igneous plumbing systems. In Buchardt, S. (ed.) Volcanic and Igneous Plumbing Systems, Elsevier: 167-189.

Vásquez, P., Glodny, J., Franz, G., Frei, D., Romer, R.L., 2011. Early Mesozoic plutonism of the Cordillera de la Costa (34°-37°s), Chile: Constraints on the onset of the Andean Orogeny. J. Geol. 119, 159–184. https://doi.org/10.1086/658296.

Vergani, G. D., Tankard, A. J., Belotti, H. J., Welsink, H. J., 1995. Tectonic evolution and paleogeography of the Neuquén Basin, Argentina. In: Tankard, A.J., Suárez, R, Welsink H. J. (Eds.): Petroleoum basins of South America. American Association of Petroleum Geologists, Memoir 62: 383-402.

Vergara, M., Charrier, R., Munizaga, F., Rivano, S., Sepulveda, P., Thiele, R., Drake, R., 1988. Miocene volcanism in the central Chilean Andes (31°30′S–34°35′S). J South Am Earth Sci 1:199–209.

Vergara, M., Levi, B., Nyström, J.O., 1995. Jurassic and Early Cretaceous island arc volcanism, extension and subsidence in the Coast Range of central Chile. Geol Soc Am Bulletin 107:1427–1440.

Vergara, M., Morata, D., Hickey-Vargas, R., 1999. Cenozoic tholeiitic volcanism in the Colbún area, Linares Precordillera, Central Chile (35°35′–36°S). Rev Geol Chile 26(1):23–41.

Villar, L.M., Zappettini, E.O., 2000. El Complejo alcalino Paleógeno de Puesto La Peña. Simposio Internacional Magmatismo Andino. IX Congreso Geológico de Chile, Actas 2:697–701.

Von Gosen, W., 1992. Structural evolution of the Argentine Precordillera: the Río San Juan section. Journal of Structural Geology, 14(6): 643–667.

Walcek, A., Hoke, G., 2012. Surface uplift and erosion of the southernmost Argentine Precordillera. Geomorphology 153–154:156–168.

Wall, R., Gana, P., Gutiérrez, A., 1996. Mapa geológico del área de San Antonio- Melipilla, regiones de Valparaíso, Metropolitana y del Libertador General Bernardo O'Higgins. Servicio Nacional de Geología y Minería, mapa 1:100.000. Santiago 2:20.

Watts, A.B., Lamb, S.H., Fairhead, J.D., Dewey, J.F., 1995. Lithospheric flexure and bending of the Central Andes. Earth Planet. Sci. Lett. https://doi.org/10.1016/0012-821X(95)00095-T

Wells, D.L., Coppersmith, K.J., 1994. Empirical relationships among magnitude, rupture length, rupture width, rupture area and surface displacements. Bull. Seismol. Soc. Am. 84, 974–1002.

Wesnousky, S.G., 2008. Displacement and geometrical characteristics of earthquake surface ruptures: Issues and implications for seismic-hazard analysis and the process of earthquake rupture. Bull. Seismol. Soc. Am. 98, 1609–1632. https://doi.org/10.1785/0120070111.

Willner, A.P., 2005. Pressure-temperature evolution of a Late Paleozoic paired metamorphic belt in north-central Chile (34°–35°30′S). J Petrol 46(9):1805–1833. doi:10.1093/petrology/egi035

Winocur, D. A., Litvak, V. D., & Ramos, V. A. (2015). Magmatic and tectonic evolution of the Oligocene Valle del Cura basin, main Andes of Argentina and Chile: evidence for generalized extension. Geological Society, London, Special Publications, 399(1), 109-130.

Witte, J., Bonora, M., Carbone, C., Oncken, O., 2012. Fracture evolution in oil-producing sills of the Rio Grande Valley, northern Neuquén Basin, Argentina. AAPG bulletin, 96(7), 1253-1277.

Wolf, S.G., Huismans, R.S., 2019. Mountain building or backarc extension in ocean-continent subduction systems - a function of backarc lithospheric strength and absolute plate velocities. J. Geophys. Res. Solid Earth 2018JB017171. https://doi.org/10.1029/2018JB017171

Yagupsky, D., Cristallini, E., Fantín, J., Zamora Valcarce, G., Botessi, G., and Varadé, R., 2008, Oblique half-graben inversion of the Mesozoic Neuquén rift in the Malargüe fold and thrust belt, Mendoza, Argentina: New insights from analogue models: Journal of Structural Geology, v. 30, p. 839–853, doi: 10 .1016 /j .jsg .2008 .03 .007.

Yáñez, G. A., Ranero, C. R., von Huene, R., Díaz, J., 2001. Magnetic anomaly interpretation across the southern central Andes (32°-34°S): The role of the Juan Fernandez Ridge in the late Tertiary evolution of the margin. Journal of Geophysical Research 106: 6325–6345.

Yáñez, G., Cembrano, J., 2004. Role of viscous plate coupling in the late Tertiary Andean tectonics. Journal of Geophysical Research 109, B02407,doi:10.1029/2003JB002494.

Yáñez, G.A., Gana, P., Fernández, R., 1998. Origen y significado geológico de la anomalía Melipilla: Chile Central: Revista Geológica de Chile, v. 25, no. 2, p. 175–198.

Yáñez, G., Ranero, C.R., von Huene, R., Díaz, J., 2001. Magnetic anomaly interpretation across the southern central Andes (32º-34ºS): The role of the JuanFernandez Ridge in the late Tertiary evolution of the margin. Journal of Geophysical Research 106(B4), 6325-6345.

Yañez, G., Cembrano, J., Pardo, M., Ranero, C., Sellés, D., 2002. The Challenger-Juan Fernandez-Maipo major tectonic transition of the Nazca-Andean subduction system at 33– 34°: Geodynamic evidence and implications. J South Am Earth Sci 15:23–38.

YPF (1995). Unpublished internal report: Informe final de pozo NVS.x-1 Vega del Sol.

YPF. (1976). Unpublished internal report: Plano Geológico Zona Pampa Amarilla-Agua Botada.

Yrigoyen, M., 1993. Los depósitos sinorogénicos terciarios. En: Ramos V (ed) Geología y Recursos Naturales de Mendoza. Relatorio del XII Congreso Geológico Argentino y II Congreso de Exploración de Hidrocarburos:123–148.

Zalohar, J., and M. Vrabec (2007), Paleostress analysis of heterogeneous fault-slip data: the Gauss method, J. Struct. Geol., 29, 1798–1810.

Zapata, T., Brissón, I., Dzelalija, F., 1999. The role of basement in the Andean fold and thrust belt of the Neuquén Basin. Thrust tectonics, 99, 122-124.

Zappettini, E.O., Villar, L.M., Hernández, L.B., Santos, J.O., 2013. Geochemical and Isotopic Constraints on the Petrogenesis of the Puesto La Peña Undersaturated Potassic Complex, Mendoza Province, Argentina. Geodynamic Implications, Lithos 162–163:301–316.

Zoback, M., Moss, D.,Mastin, L.G., Anderson R.N., 1985. Well bore breakouts and in situ stress, J. Geophys. Res., 90, 5523 – 5530.

Zoback, M., Townend, J., 2001. Implications of hydrostatic pore pressures and high crustal strength for the deformation of intraplate lithosphere. Tectonophysics, 336: 19-30.

Zoback, M., 2010. Reservoir geomechanics. Cambridge University Press, 449 p. Cambridge.

Zurita, E., Muñoz, N., Charrier, R., Harambour, P.S., Elgueta, S., 2000. Madurez termal de la materia orgánica de la Formación Abanico = Coya Machalí, Cordillera Principal, Chile Central: resultados e interpretación. IX Congreso Geológico de Chile (Puerto Varas): 726–730.

8. Supplementary material

Supplementary material: Igneous rocks thickness in oil-well logs and distance to necks

Drill hole			Neuquén Group		Rayoso		Huitrin		Agrio		Chachao		Vaca Muerta		Auquilco		La Manga		Lotena		Cuyo Group		Remoredo		*Accum. in Mendoza Group*		Total thickness		Distance to the closest neck	
W	C	E	*A*	*R*	*Appa*	*Real*	*Appa*	*Real*	*Appa*	*Real*	*Appa*	*Real*	*Appa*	*Real*	*Appa*	*Real*	*Appa*	*Real*	*Appa*	*Real*	*Appa*	*Real*	*Appa*	*Real*	***Appa***	***Real***	***Appa***	***Real***		
AB e-4			15	13	6	5	0	0	14	13	16	15	34	32	43	43	12	12	10	10					***64***	***59***	**150**	**141**	5.6	Tronquimalal peak
AB x-2			0	0	0	0	0	0	42	38	0	0	58	50	46	46	4	4	0	0					***100***	***88***	**150**	**138**	7.2	
AB x-1			63	55			0	0	22	20	0	0	46	42	21	21	9	8	6	6					***68***	***62***	**167**	**151**	6.5	
AB e-5			0	0	0	0	0	0	44	34	0	0	40	36	0	0	0	0	8	7					***84***	***70***	**92**	**77**	8.7	
	AB e-3		0	0	0	0	0	0	30	29	0	0	56	54	3	3	8	8							***86***	***83***	**97**	**94**	7.5	Mirano peak
	PA x-6		59	55	0	0	0	0	22	21	0	0	80	75	0	0	0	0	0	0					***102***	***96***	**161**	**151**	5.8	
		PA x-2	0	0	0	0	0	0	43	43	0	0	133	133	0	0	0	0	0	0					***175***	***175***	**175**	**175**	2.1	
		PA x-1	0	0	0	0	12	12	0	0	0	0	89	89	0	0	0	0	0	0					***89***	***89***	**101**	**101**	3.6	
	LCe x-1		0	0	0	0	0	0	8	4	0	0	30	13	0	0	0	0	0	0			16	15	***38***	***17***	**54**	**31**	9.9	
		Well 13	26	26	0	0	0	0	0	0	29	29	24	24	0	0	0	0	0	0					***53***	***53***	**79**	**79**	6.7	
ABu x-1			0	0	0	0	0	0	25	25	4	4	156	155	18	18	0	0	0	0			18	18	***185***	***184***	**221**	**220**	12.4	
	LCe x-2		0	0	0	0	0	0	12	12	0	0	66	66	2	2	0	0	0	0			0	0	***78***	***78***	**80**	**80**	11.6	
		Well 18	0	0	0	0	0	0	10	10	26	25	42	42	0	0	0	0	0	0	47	47			***78***	***77***	**125**	**123**	8.9	

A: apparent thickness.

R: real thickness

In red real thickness not calculated due to poor quality diplogs

Drill-hole	Real thickness	Distance to closest neck: Tronquimalal peak	Distance to closest neck: Mirano peak
AB e-4	140.5	5.6	
AB x-2	138.1	7.2	
AB x-1	151.3	6.5	
AB e-5	76.9	8.7	
AB e-3	94.1		7.5
PA x-6	151.3		5.8
PA x-2	175.0		2.1
PA x-1	101.0		3.6
LCe x-1	31.2		9.9
Well 13	79.0		6.7
ABu x-1	219.9		12.4
LCe x-2	80.0		11.6
Well 18	123.5		8.9

Distance to the closest neck vs accumulated igneous rock thickness